

Institute of Chemistry  
Physical Chemistry

---

# DNA origami substrates as a versatile tool for surface-enhanced Raman scattering (SERS)

**Doctoral thesis (cumulative)**  
in fulfilment of the requirements for the degree  
**“doctor rerum naturalium”**  
**(Dr. rer. nat.)**  
in the discipline “Physical Chemistry”

submitted to the  
Faculty of Science  
of the University of Potsdam

by  
Julia Prinz

Potsdam, August 2016

Published online at the  
Institutional Repository of the University of Potsdam:  
URN urn:nbn:de:kobv:517-opus4-104089  
<http://nbn-resolving.de/urn:nbn:de:kobv:517-opus4-104089>

*Meinen wundervollen Eltern gewidmet*

NATURE IS FULL OF INFINITE CAUSES  
THAT HAVE NEVER OCCURED IN EXPERIENCE.

LEONARDO DA VINCI

1. Gutachter: JProf. Dr. Ilko Bald
2. Gutachter: Prof. Dr. Tim Liedl
3. Gutachter: apl. Prof. Dr. Michael Kumke

Tag der Disputation: 05.01.2017

## Danksagung

Die vorliegende Arbeit entstand am Institut für Chemie der Universität Potsdam im Fachgebiet Physikalische Chemie in der Arbeitsgruppe von Herrn JProf. Dr. Ilko Bald.

Zum Gelingen dieser Arbeit haben viele Menschen auf unterschiedlichste Weise beigetragen, denen ich hiermit meinen Dank aussprechen möchte.

Zunächst bedanke ich mich recht herzlich bei Herrn JProf. Dr. Ilko Bald für die Möglichkeit, meine Dissertation zu diesem spannenden Thema in seiner Arbeitsgruppe anfertigen zu dürfen. Desweiteren bin ich sehr dankbar für das in mich gesetzte Vertrauen, die unzähligen hilfreichen Diskussionen, das freundschaftliche Arbeitsklima innerhalb der Gruppe und nicht zuletzt für das stets offen stehende Büro, das ich immer mit mindestens einer guten Idee mehr verlassen habe.

Bei Herrn apl. Prof. Dr. Michael Kumke und Herrn Prof. Dr. Tim Liedl bedanke ich mich recht herzlich für die Erstellung der Zweitgutachten.

Herrn Dr. Sascha Eidner möchte ich danken für die Hilfe und Überwindung sämtlicher aufgetretener Computerprobleme (ohne die ich jetzt vermutlich noch nicht an diesem Punkt wäre).

Weiterhin danke ich der gesamten AG Löhmannsröben für ein durchweg sehr angenehmes und freundschaftliches Arbeitsklima und die Hilfsbereitschaft jedes Einzelnen.

Dr. Aleksandar Matković, Jelena Pešić und Dr. Radoš Gajić danke ich für ihre Gastfreundschaft in Belgrad und die gemeinsamen Erlebnisse, an die ich sehr gerne zurückdenke.

Ein großer Dank gilt allen, die in den letzten Jahren für einen schönen Arbeitsalltag mit kreativen Mittags- und Kaffeepausen gesorgt haben und mit denen ich auch außerhalb der Uni Zeit bei gemeinsamen Spieleabenden, Laufrunden und Badminton-Matches verbringen durfte. Ein großes Dankeschön insbesondere an Antonia, Christian, Dennis, Eric, Jenny, Kenny, Lisa, Lydi, Nicole, Phillip, Robin, Selina, Steffi, Sven, Till, Uschi und Youngeun.

Ein besonderer Dank gilt dabei meinen grandiosen Büromitbewohnern, Lydi und Youngeun, die täglich für gute Stimmung im 0.10 gesorgt haben und einfach immer für eine Überraschung gut waren.

Allen meinen Freunden außerhalb der Uni danke ich von ganzem Herzen für alles Erlebte und das, was wir noch zusammen erleben werden. Insbesondere danke ich euch für euer Verständnis und die Unterstützung in den letzten Monaten. Und dafür, dass ihr mich auch in stressigen Phasen so oft zum Lachen gebracht habt. Es ist einfach schön zu wissen, dass ich immer auf euch zählen kann.

Ein ganz besonderer Dank gilt meiner Familie.

Ohne eure Liebe und Unterstützung wäre das alles gar nicht möglich gewesen.

Danke, Mama und Papa. Für den Weg, den ihr mir geebnet habt und die Werte, die ihr mir vermittelt habt, werde ich für immer dankbar sein.

Danke, Stefan. Für eine wundervolle gemeinsame Kindheit, unsere ganz besondere Verbundenheit und ganz einfach dafür, dass du immer da bist.

Danke, Suse. Dafür, dass du mich jeden Tag daran erinnerst, was das Wichtigste im Leben ist. Und für alles andere. Dich an meiner Seite zu haben, ist das größte Geschenk.

DANKE



## Abstract

Surface-enhanced Raman scattering (SERS) is a promising tool to obtain rich chemical information about analytes at trace levels. However, in order to perform selective experiments on individual molecules, two fundamental requirements have to be fulfilled. On the one hand, areas with high local field enhancement, so-called “hot spots”, have to be created by positioning the supporting metal surfaces in close proximity to each other. In most cases hot spots are formed in the gap between adjacent metal nanoparticles (NPs). On the other hand, the analyte has to be positioned directly in the hot spot in order to profit from the highest signal amplification. The use of DNA origami substrates provides both, the arrangement of AuNPs with nm precision as well as the ability to bind analyte molecules at predefined positions.

Consequently, the present cumulative doctoral thesis aims at the development of a novel SERS substrate based on a DNA origami template. To this end, two DNA-functionalized gold nanoparticles (AuNPs) are attached to one DNA origami substrate resulting in the formation of a AuNP dimer and thus in a hot spot within the corresponding gap. The obtained structures are characterized by correlated atomic force microscopy (AFM) and SERS imaging which allows for the combination of structural and chemical information.

Initially, the proof-of principle is presented which demonstrates the potential of the novel approach. It is shown that the Raman signal of 15 nm AuNPs coated with dye-modified DNA (dye: carboxytetramethylrhodamine (TAMRA)) is significantly higher for AuNP dimers arranged on a DNA origami platform in comparison to single AuNPs. Furthermore, by attaching single TAMRA molecules in the hot spot between two 5 nm AuNPs and optimizing the size of the AuNPs by electroless gold deposition, SERS experiments at the few-molecule level are presented.

The initially used DNA origami-AuNPs design is further optimized in many respects. On the one hand, larger AuNPs up to a diameter of 60 nm are used which are additionally treated with a silver enhancement solution to obtain Au-Ag-core-shell NPs. On the other hand, the arrangement of both AuNPs is altered to improve the position of the dye molecule within the hot spot as well as to decrease the gap size between the two particles. With the optimized design the detection of single dye molecules (TAMRA and cyanine 3 (Cy3)) by means of SERS is demonstrated. Quantitatively, enhancement factors up to  $10^{10}$  are estimated which is sufficiently high to detect single dye molecules.

In the second part, the influence of graphene as an additional component of the SERS substrate is investigated. Graphene is a two-dimensional material with an outstanding combination of electronical, mechanical and optical properties. Here, it is demonstrated that single layer graphene (SLG) replicates the shape of underlying non-modified DNA origami substrates very well, which enables the monitoring of structural alterations by AFM imaging. In this way, it is shown that graphene encapsulation significantly increases the structural stability of bare DNA origami substrates towards mechanical force and prolonged exposure to deionized water.

Furthermore, SLG is used to cover DNA origami substrates which are functionalized with a 40 nm AuNP dimer. In this way, a novel kind of hybrid material is created which exhibits several advantages compared to the analogue non-covered SERS substrates. First, the fluorescence background of dye molecules that are located in between the AuNP surface and SLG is efficiently reduced. Second, the photobleaching rate of the incorporated dye molecules is decreased up to one order of magnitude. Third, due to the increased photostability of the investigated dye molecules, the performance of polarization-dependent series measurements on individual structures is enabled. This in turn reveals extensive information about the dye molecules in the hot spot as well as about the strain induced within the graphene lattice.

Although SLG can significantly influence the SERS substrate in the aforementioned ways, all those effects are strongly related to the extent of contact with the underlying AuNP dimer.



## Zusammenfassung

Desoxyribonukleinsäure (*engl. deoxyribonucleic acid (DNA)*) ist nicht nur Träger der Erbinformation, sondern wird auch seit den frühen 80er Jahren als Gerüstmaterial in der Nanotechnologie verwendet. Im Jahr 2006 wurde die bis dato entwickelte DNA-Nanotechnologie durch die Erfindung der sogenannten DNA Origami-Technik weiter revolutioniert. Diese erlaubt die Konstruktion vielfältiger zwei- und dreidimensionaler Strukturen durch gezielte DNA-Selbstassemblierung. Basierend auf der grundlegenden Watson-Crick Basenpaarung innerhalb eines DNA-Doppelstrangs können die gewünschten Zielstrukturen dabei mit hoher Genauigkeit vorhergesagt werden.

Neben der Entwicklung vielfältiger DNA-Konstrukte eignen sich DNA Origami-Substrate zudem hervorragend zur Bindung funktionaler Einheiten mit der Präzision im Bereich von Nanometern. Somit lassen sich beispielsweise Goldnanopartikel (AuNPs) präzise anordnen. Dies ist von höchstem Interesse im Zusammenhang mit der oberflächenverstärkten Ramanstreuung (*engl. surface-enhanced Raman scattering (SERS)*). SERS basiert darauf, die naturgemäß schwache Ramanstreuung eines Analyten um mehrere Größenordnungen zu verstärken, indem der Analyt nahe einer Metalloberfläche positioniert wird. Die Verstärkung der Ramanstreuung beruht hierbei hauptsächlich auf der Wechselwirkung des Analyten mit dem elektromagnetischen Feld der Metalloberfläche und kann im Zwischenraum zweier benachbarter Metallstrukturen besonders stark ausgeprägt sein.

Die vorliegende kumulative Dissertation beschäftigt sich mit der Entwicklung einer DNA Origami-basierten Sensoroberfläche für die Anwendung von SERS-Experimenten. Hierbei werden jeweils zwei AuNPs in gezieltem Abstand an ein DNA Origami-Substrat gebunden und das verstärkte Ramansignal eines Analyten im Zwischenraum des AuNP-Dimers detektiert. Zunächst wird das allgemeine Prinzip in Form eines Wirksamkeitsnachweises vorgestellt, in welchem der Farbstoff Carboxytetramethylrhodamin (TAMRA) als Analyt verwendet wird. Die darauf aufbauenden Experimente zielen auf eine Verringerung der Nachweisgrenze bis hin zur Einzelmoleküldetektion ab. Im Zuge dessen werden vielseitige Optimierungsschritte durchgeführt, die die Größe, die Anordnung sowie die Ummantelung der AuNPs mit einer dünnen Silberschicht betreffen. Es wird gezeigt, dass durch die Optimierung aller Parameter die Detektion einzelner TAMRA- und Cyanin 3 (Cy3)-Moleküle mittels SERS möglich ist.

Weiterhin wird Graphen, ein erst im Jahr 2004 entdecktes Material bestehend aus einer einzigen Schicht Kohlenstoffatome, als weiterer Bestandteil der untersuchten Nanostrukturen eingeführt. Graphen zeichnet sich durch eine bislang einzigartige Kombination aus optischen, elektronischen und mechanischen Eigenschaften aus und hat sich daher innerhalb kürzester Zeit zu einem vielfältigen Forschungsschwerpunkt entwickelt. In der vorliegenden Dissertation wird zunächst die erhöhte strukturelle Stabilität von Graphen bedeckten DNA Origami-Substraten im Hinblick auf mechanische Beanspruchung sowie auf die Inkubation in deionisiertem Wasser demonstriert. In weiterführenden Betrachtungen werden auch DNA Origami-Substrate, die mit AuNP-Dimeren funktionalisiert sind, mit Graphen bedeckt, und somit eine neuartige Hybridstruktur erzeugt. Es wird gezeigt, dass Graphen den Fluoreszenzuntergrund der untersuchten Farbstoffmoleküle deutlich reduziert und zusätzlich deren Photostabilität gegenüber der eintreffenden Laserstrahlung effektiv verbessert.



## Publications

- C. HECK, J. PRINZ, A. DATHE, V. MERK, O. STRANIK, W. FRITZSCHE, J. KNEIPP, I. BALD, “Gold nanolenses self-assembled by DNA origami”, *submitted manuscript*.
- J. PRINZ, A. MATKOVIĆ, J. PEŠIĆ, R. GAJIĆ, I. BALD, “Hybrid Structures for Surface-Enhanced Raman Scattering: DNA Origami/Gold Nanoparticle Dimer/Graphene”, *Small* **12**, 5458–5467 (2016).
- J. OERTEL, A. KELLER, J. PRINZ, B. SCHREIBER, R. HÜBNER, J. KERBUSCH, I. BALD, K. FAHMY, “Anisotropic metal growth on phospholipid nanodiscs via lipid bilayer expansion”, *Sci. Rep.* **6**, 26718 (2016).
- J. PRINZ, C. HECK, L. ELLERIK, V. MERK, I. BALD, “DNA origami based Au–Ag-core–shell nanoparticle dimers with single-molecule SERS sensitivity”, *Nanoscale* **8**, 5612–5620 (2016).
- A. MATKOVIĆ, B. VASIĆ, J. PEŠIĆ, J. PRINZ, I. BALD, A. R. MILOSAVLJEVIĆ, R. GAJIĆ, “Enhanced structural stability of DNA origami nanostructures by graphene encapsulation”, *New J. Phys.* **18**, 025016 (2016).
- S. VOGEL, J. RACKWITZ, R. SCHÜRMAN, J. PRINZ, A. R. MILOSAVLJEVIĆ, M. RÉFRÉGIERS, A. GIULIANI, I. BALD, “Using DNA Origami Nanostructures to Determine Absolute Cross Sections for UV Photon-Induced DNA Strand Breakage”, *J. Phys. Chem. Lett.* **6**, 4589–4593 (2015).
- C. HECK, L. OLEJKO, J. PRINZ, R. SCHÜRMAN, I. BALD, „Molekulare Prozesse untersucht im DNA-Nanolabor – DNA-Nanostrukturen für die Analytik“, *GIT Labor-Fachzeitschrift* **11/2014**, 25–27 (2014).
- J. PRINZ, B. SCHREIBER, L. OLEJKO, J. OERTEL, J. RACKWITZ, A. KELLER, I. BALD, “DNA Origami Substrates for Highly Sensitive Surface-Enhanced Raman Scattering”, *J. Phys. Chem. Lett.* **4**, 4140–4145 (2013).

*Press release from 16<sup>th</sup> December 2013:*

„Goldene Falle: Hochempfindliches System kann einzelne Moleküle nachweisen“  
Helmholtz Zentrum Dresden Rossendorf  
<http://www.hzdr.de/db/Cms?pNid=99&pOid=40525> (August 2016).

*English media echo from 16<sup>th</sup> December 2013:*

“Golden trap: Highly sensitive system to detect individual molecules”  
Science Daily®

<https://www.sciencedaily.com/releases/2013/12/131216142624.htm> (August 2016).

## Poster contributions

- J. PRINZ, L. ELLERIK, I. BALD, “DNA origami substrates functionalized with Au-Ag-core-shell nanoparticles for highly sensitive surface-enhanced Raman scattering”, *Molecular Plasmonics*, May **2015**, Jena, Germany.
- J. PRINZ, B. SCHREIBER, L. OLEJKO, J. OERTEL, J. RACKWITZ, A. KELLER, I. BALD, “DNA Origami Substrates for Highly Sensitive Surface-Enhanced Raman Scattering”, *Surface-Enhanced Spectroscopies*, August **2014**, Chemnitz, Germany.
- J. PRINZ, C. HECK, B. SCHREIBER, L. OLEJKO, J. OERTEL, A. KELLER, V. MERK, J. KNEIPP, I. BALD, “DNA origami substrates for highly sensitive surface-enhanced Raman scattering”, *Bunsentagung - 113<sup>th</sup> General Assembly for the German Bunsen Society for Physical Chemistry*, May **2014**, Hamburg, Germany.
- J. PRINZ, B. SCHREIBER, L. OLEJKO, J. OERTEL, J. RACKWITZ, A. KELLER, I. BALD, “DNA Origami Substrates for Highly Sensitive Surface-Enhanced Raman Scattering”, *DNA-Based Nanotechnology: Digital Chemistry*, May **2014**, Dresden, Germany.
- J. PRINZ, R. SCHÜRMAN, I. BALD, “Correlated SERS and AFM imaging to investigate DNA strand breaks at a single-molecule level”, *10<sup>th</sup> Symposium Confocal Raman Imaging*, September **2013**, Ulm, Germany.
- J. RACKWITZ, J. PRINZ, I. BALD, “Novel approaches to study low-energy electron-induced damage to DNA oligonucleotides”, *2<sup>nd</sup> NANO-IBCT Conference*, May **2013**, Sopot, Poland.
- I. BALD, J. PRINZ, B. SCHREIBER, A. KELLER, “Surface-enhanced Raman spectroscopy using gold nanoparticles arranged on DNA origami substrates”, *2<sup>3rd</sup> Lecture Conference on Photochemistry*, October **2012**, Potsdam, Germany.

## Oral presentations

- J. PRINZ, A. MATKOVIĆ, J. PEŠIĆ, R. GAJIĆ, I. BALD, “Hybrid structures for surface-enhanced Raman scattering (SERS): DNA origami / gold nanoparticle dimer / graphene”, *DNA Nanotechnology*, May **2016**, Jena, Germany.
- J. PRINZ, C. HECK, L. ELLERIK, I. BALD, “DNA origami substrates for single-molecule SERS”, *Biomolecular nanostructures for the study of biophysical and biochemical processes*, October **2015**, Potsdam, Germany.
- J. PRINZ, L. ELLERIK, I. BALD, “DNA origami substrates functionalized with Au-Ag-core-shell nanoparticles for highly sensitive SERS”, *DNA Mitteldeutschland*, May **2015**, Jena, Germany.

# Contents

<b>List of abbreviations</b>	<b>xiii</b>
<b>1. Introduction</b>	<b>1</b>
<b>2. Theoretical background</b>	<b>5</b>
2.1. Raman scattering . . . . .	5
2.1.1. Classical approach to Raman scattering . . . . .	6
2.1.2. Raman cross sections . . . . .	7
2.2. Plasmonics . . . . .	8
2.2.1. Optical properties of metals . . . . .	8
2.2.2. Localized surface plasmon resonance (LSPR) . . . . .	10
2.2.3. Coupling of LSPR . . . . .	12
2.3. Surface-enhanced Raman scattering (SERS) . . . . .	14
2.3.1. Enhancement mechanisms . . . . .	14
2.3.2. SERS enhancement factors . . . . .	16
2.3.3. Competing effects in SERS . . . . .	16
2.3.4. Single-molecule-SERS (sm-SERS) . . . . .	19
2.4. DNA nanotechnology . . . . .	20
2.4.1. Deoxyribonucleic acid (DNA) . . . . .	20
2.4.2. DNA as building block for materials . . . . .	21
2.4.3. Arrangement of AuNPs on DNA origami . . . . .	25
2.5. Graphene . . . . .	27
2.5.1. Electronic, optical and mechanical properties . . . . .	27
2.5.2. Raman scattering of graphene . . . . .	28
<b>3. Materials and methods</b>	<b>31</b>
3.1. List of chemicals and DNA strands . . . . .	31
3.2. Sample preparation . . . . .	33
3.2.1. Synthesis of DNA origami substrates . . . . .	33
3.2.2. Coating of AuNPs with ssDNA . . . . .	36
3.2.3. Determination of DNA surface coverage on AuNPs . . . . .	37
3.2.4. AuNP-DNA origami hybridization . . . . .	37
3.2.5. Pre-treatment of Si substrates . . . . .	38
3.2.6. Adsorption of DNA origami substrates or DNA origami-AuNP hybrids . . . . .	38
3.2.7. Electroless silver deposition . . . . .	38
3.2.8. Mechanical exfoliation of graphene . . . . .	39
3.2.9. Introducing a marker . . . . .	39
3.3. Methods . . . . .	39
3.3.1. SERS imaging . . . . .	39
3.3.2. Atomic force microscopy (AFM) imaging . . . . .	41
3.3.3. UV-Vis absorption measurements . . . . .	41
3.3.4. Fluorescence measurements . . . . .	42

3.3.5. Scanning electron microscope (SEM) imaging . . . . .	42
<b>4. Discussion</b>	<b>43</b>
4.1. Main manuscripts . . . . .	43
4.2. Side projects . . . . .	53
<b>5. Summary and outlook</b>	<b>55</b>
<b>6. Manuscripts</b>	<b>57</b>
6.1. Proof-of-principle . . . . .	59
6.2. Single-molecule-SERS . . . . .	71
6.3. Enhanced structural stability due to graphene . . . . .	91
6.4. DNA origami–AuNP dimer–graphene hybrid structures . . . . .	103
6.5. UV photon-induced DNA strand breakage . . . . .	117
6.6. Metallized phospholipid nanodiscs . . . . .	129
6.7. Gold nanolenses . . . . .	143
<b>A. Appendix</b>	<b>165</b>
<b>Bibliography</b>	<b>171</b>

# List of abbreviations

The abbreviations below refer to all chapters except chapter 6 (Manuscripts).

$\hat{\alpha}$ .....	polarizability (tensor)
$\hat{\alpha}_0$ .....	polarizability (tensor) for equilibrium coordinates
$\hat{\alpha}_{\text{NP}}$ .....	polarizability (tensor) for a nanoparticle
$\hat{\alpha}_{\text{sphere}}$ .....	polarizability (tensor) for a spherical nanoparticle
$\beta$ .....	deflection angle
$\gamma$ .....	collision frequency
$\epsilon_\infty$ .....	dielectric function of the constant background
$\epsilon_0$ .....	dielectric function of vacuum ( $\epsilon_0 \approx 8.854 \times 10^{-12} \text{ F m}^{-1}$ )
$\epsilon_m$ .....	dielectric function of the surrounding medium
$\epsilon(\omega)$ .....	complex dielectric function
$\varepsilon(\lambda)$ .....	molar decadic extinction coefficient
$\eta$ .....	radiation efficiency
$\theta$ .....	angle between a specific point and the center of the hot spot
$\kappa$ .....	shape factor ( $\kappa = 2$ for a spherical particle)
$\lambda$ .....	wavelength
$\lambda_{\text{D}}$ .....	Debye-length
$\lambda_{\text{exc}}$ .....	wavelength of the exciting laser light
$\lambda_{\text{LSPR, AgNP}}$ .....	wavelength of the LSPR frequency for a silver nanoparticle
$\lambda_{\text{LSPR, AuNP}}$ .....	wavelength of the LSPR frequency for a gold nanoparticle
$\nu_0$ .....	frequency of the incident laser light
$\nu_k$ .....	frequency of a molecular vibration with the normal mode $k$
$\nu_0 - \nu_k$ .....	frequency of STOKES scattering
$\nu_0 + \nu_k$ .....	frequency of anti-STOKES scattering
$\pi$ .....	bonding mode, transverse polarization
$\pi^*$ .....	anti-bonding mode, transverse polarization
$\rho$ .....	bonding mode, longitudinal polarization
$\rho^*$ .....	anti-bonding mode, longitudinal polarization
$\rho_-$ .....	bonding mode, Ag shell
$\rho_+$ .....	anti-bonding mode, Ag shell
$\rho_{--}$ .....	bonding mode, Au-Ag-core-shell NP
$\rho_{-+}$ .....	anti-bonding mode, Au-Ag-core-shell NP
$\sigma$ .....	cross section
$\sigma_{\text{F}}$ .....	fluorescence cross section
$\sigma_{\text{R}}$ .....	Raman cross section
$\sigma_{\text{R,ads}}$ .....	Raman cross section of molecules adsorbed on a metal surface
$\sigma_{\text{R,free}}$ .....	Raman cross section of non-adsorbed molecules
$\sigma_{\text{RR}}$ .....	resonant Raman cross section
$d\sigma_{\text{R}}/d\Omega$ .....	absolute differential Raman cross section
$\tau$ .....	relaxation time
$\Phi_{\text{pb}}$ .....	photobleaching quantum yield
$\Phi_{\text{r}}$ .....	radiative quantum yield

$\Psi_1 + \Psi_2$ .....	in-phase coupling, symmetric dielectric fields
$\Psi_1 - \Psi_2$ .....	out-of-phase coupling, antisymmetric dielectric fields
$\omega_0$ .....	angular frequency
$\omega_L$ .....	angular frequency of the incoming laser radiation
$\omega_{\text{LSPR}}$ .....	frequency of the localized surface plasmon resonance
$\omega_P$ .....	plasma frequency
$\omega_S$ .....	angular frequency of the scattered light
$\Omega$ .....	variable that defines the direction of scattered light
$b$ .....	thickness of the absorbing substance
$c$ .....	concentration
$d$ .....	diameter of a nanoparticle
$d_{\text{gap}}$ .....	gap size between two nanoparticles
$d_{\text{mol.-met.}}$ .....	distance between molecule and metal surface
$e$ .....	charge of one electron
$e^-$ .....	electron
$E$ .....	energy
$E(\lambda)$ .....	extinction
$E_F$ .....	FERMI level
$E_{\text{thr, Ag}}$ .....	energy threshold for inter-band transitions in Ag
$E_{\text{thr, Au}}$ .....	energy threshold for inter-band transitions in Au
$\vec{E}$ .....	electric field
$\vec{E}_0$ .....	amplitude of the electric field
$\vec{E}(z, \omega)$ .....	electric field at point $z$ in presence of a metal surface
$\vec{E}_0(z, \omega)$ .....	electric field at point $z$ in absence of a metal surface
$\text{EF}_F$ .....	enhancement factor in a fluorescence experiment
$\text{EF}_{\text{SERS}}$ .....	enhancement factor in a SERS experiment
$\text{EF}_{\text{sm-SERS}}^{\text{min}}$ .....	minimum enhancement factor for single-molecule detection
$h$ .....	PLANCK'S constant ( $h = 6.626 \times 10^{-34}$ J s)
$h^+$ .....	hole
$I_L(\omega_L)$ .....	laser intensity
$I_{\text{Raman}}$ .....	overall Raman intensity
$I_{\text{SERS}}$ .....	overall SERS intensity
$\text{Im}$ .....	imaginary term
$k$ .....	normal vibrational mode
$k_B$ .....	BOLTZMANN'S constant ( $k_B = 1.38 \times 10^{-23}$ J K $^{-1}$ )
$k_{\text{nr}}$ .....	rate constant for non-radiative processes
$k_{\text{pb}}$ .....	photobleaching rate constant
$k_r$ .....	rate constant for radiative processes
$l$ .....	angular momentum
$m$ .....	mass
$n_a$ .....	number of atoms
$n_e$ .....	number of free electrons per unit volume
$n_{\text{ph}}$ .....	number of emitted photons per excitation cycle
$N_0$ .....	number of molecules in the vibrational level $v = 0$
$N_1$ .....	number of molecules in the vibrational level $v = 1$
$N_{\text{Raman}}$ .....	number of molecules involved in a Raman experiment
$N_{\text{SERS}}$ .....	number of molecules involved in a SERS experiment
$\vec{P}$ .....	dipole moment
$Q_k$ .....	normal mode coordinate of the normal vibrational mode $k$



$Q_k^0$ .....	amplitude of the normal mode coordinate of $k$
$r$ .....	radius of a nanoparticle
Re .....	real term
$t$ .....	time
$T$ .....	temperature
$v$ .....	vibrational energy level ( $v = 0,1,2,\dots$ )
$V$ .....	volume
$\dot{x}$ .....	velocity of electron motion
$\ddot{x}$ .....	acceleration of electron motion
4-ABT .....	4-aminobenzenethiol
A .....	adenine
AB .....	absorption
AFM .....	atomic force microscopy
Ag .....	silver
AgNP .....	silver nanoparticle
Au .....	gold
AuDG hybrid .....	DNA origami-gold nanoparticle dimer-graphene hybrid
AuND .....	gold nanodisc
AuNL .....	gold nanolens
AuNP .....	gold nanoparticle
BiASERS .....	bi-analyte surface-enhanced Raman scattering
BLG .....	bilayer graphene
BSPP .....	Bis( <i>p</i> -sulfonatophenyl)phenylphosphine dehydrate dipotassium salt
C .....	cytosine
CCD .....	charge-coupled device
CoP .....	cobalt phthalocyanine
CT .....	charge transfer
Cu .....	copper
CVD .....	chemical vapour deposition
Cy3 .....	cyanine 3
Cy5 .....	cyanine 5
DDA .....	discrete dipole approximation
DDT .....	DL-dithiothreitol
DMPG .....	(1,2-dimyristoyl- <i>sn</i> -glycero-3-phospho-1'- <i>rac</i> -glycerol)
DNA .....	deoxyribonucleic acid
dsDNA .....	double-stranded DNA
DX .....	double-crossover motif
EBL .....	electron beam lithography
ETD .....	Everhart-Thornley detector
EF .....	enhancement factor
ES .....	electrostatic
EtOH .....	ethanol
F .....	fluorescence
FDTD .....	finite-difference time-domain
FLG .....	few-layer graphene
G .....	guanine
GERS .....	graphene-enhanced Raman scattering
GSND .....	Au-Ag-core-shell nanodumbbell
HOPG .....	highly-oriented pyrolytic graphite

HPLC	high performance liquid chromatography
HWP	half-wave plate
I-Gain	integral gain
IC	internal conversion
IR	infrared
IR*	internal relaxation
ISC	intersystem crossing
kb	kilobase
kbp	kilobase pair
LFIEF	local field intensity enhancement factor
LNA	locked nucleic acid
LOD	limit of detection
LSPR	localized surface plasmon resonance
<b>M1–M7</b>	manuscripts 1–7
M13mp18	genome of bacteriophage M13mp18
MEA	mercaptoethylamine
MeOH	methanol
Mg <sup>2+</sup>	magnesium ion
MgCl <sub>2</sub>	magnesium chloride
MIBK	methyl isobutyl ketone
NA	numerical aperture
NaCl	sodium chloride
ND	nanodisc
NP	nanoparticle
nt	nucleotide
P-Gain	proportional gain
PB	photobleaching
PCR	polymerase chain reaction
PEG	polyethylene glycol
PNA	peptide nucleic acid
R6G	rhodamine 6G
RNA	ribonucleic acid
ROXS	Reducing and Oxidizing System
S	sulphur
$S_0$	singlet ground electronic state
$S_n$	singlet electronic state of level $n$
SDS	sodium dodecyl sulfate
SE	secondary electron
SEF	surface-enhanced fluorescence
SEM	scanning electron microscopy
SERS	surface-enhanced Raman scattering
Si	silicon
SiC	silicon carbide
SiO <sub>2</sub>	silicon dioxide
SLG	single-layer graphene
sm	single-molecule
sm-SERS	single-molecule surface-enhanced Raman scattering
S/N	signal-to-noise
SPP	surface plasmon polariton

ssDNA .....	single-stranded DNA
T .....	thymine
$T_1$ .....	first triplet state
TAE .....	Tris-acetate-EDTA buffer
TAMRA .....	carboxytetramethylrhodamine
TLG .....	tri-layer graphene
TX .....	three-domain motif
UV .....	ultraviolet
Vis .....	visible



# 1

## Introduction

Nanotechnology is everywhere. And we encounter its effects throughout our daily lives: ranging from skin care products, over clothes and sports goods to cars, smartphones and computers. In all cases, nanomaterials are used as additives to common products resulting in beneficial properties such as increased electronic capability or higher mechanical stability. Additionally, nanoparticles (NPs) are highly promising in the field of medical applications, for instance, to specifically combat cancer cells by means of drug delivery or heat generation<sup>[1]</sup>. Since nanotechnology is already strongly anchored in countless fields, it is unambiguously a key technology of the future.

Besides the huge influence of nanotechnology on materials of our daily lives, it also opened new doors for analytical applications. For instance, Raman spectroscopy, a widely used analytical method, strongly profits from nanomaterials. In particular, Raman scattering is an inelastic scattering effect providing rich chemical information, while at the same time, it is hampered by very low Raman cross sections that are directly reflected in weak signal intensities. This drawback has been overcome by the development of surface-enhanced Raman scattering (SERS), an effect that was first observed by FLEISCHMANN *et al.* in 1974<sup>[2]</sup> and shortly afterwards correctly interpreted by JEANMAIRE *et al.*<sup>[3]</sup>. Basically, SERS relies on enhancing the Raman scattering signal of an analyte by placing it in close vicinity to a metal surface. Especially high field enhancements are generated in the gap between adjacent metal NPs<sup>[4,5]</sup>. However, the detection of single molecules by means of SERS is particularly challenging for several reasons. On the one hand, so-called “hot spots” have to be created that provide a sufficiently high field enhancement. On the other hand, the analyte molecule has to be placed directly in the hot spot in order to benefit from the highest field enhancement. Nevertheless, several techniques for single-molecule-SERS (sm-SERS) have been developed such as the ultralow concentration approach<sup>[6,7]</sup>, the bianalyte technique<sup>[8]</sup>, as well as NP dimers connected by bifunctional linkers<sup>[9,10]</sup>. However, these approaches either suffer from insufficient control over the hot spot formation and complex statistical analysis or from the lack of further functionalization.

With the invention of the DNA origami technique by ROTHEMUND in 2006<sup>[11]</sup> a tool was created that allows for the attachment of functional units with nm precision. In this way both, gold nanoparticles (AuNPs) and analyte molecules can be assembled at predefined positions making DNA origami predestined templates for SERS applications.

Consequently, the present thesis focuses on the development of a DNA origami-based platform

for the reliable detection of analytes by means of SERS. Thus, strategies from the field of material science are applied for analytical interests. The work includes several optimization steps towards detection limits, structural stability of the DNA origami templates as well as photostability of the analyte molecules. Throughout the whole thesis, SERS measurements are accompanied by correlated atomic force microscopy (AFM) in order to combine chemical and structural information.

In manuscript 1 (**M1**<sup>1</sup>) the proof-of-principle is presented by introducing the basic approach of DNA origami templates as substrates for SERS. Herein, triangular DNA origami substrates are functionalized with AuNP dimers of up to 15 nm. As Raman reporter molecule the well-established dye carboxytetramethylrhodamine (TAMRA) is used which is either bound to the AuNPs or to the DNA origami substrate. By optimizing the gap size and hence the hot spot, TAMRA is successfully detected at a few-molecule level.

In manuscript 2 (**M2**<sup>2</sup>) the initial DNA origami-AuNP structures introduced in **M1** are optimized in multiple ways aiming at sufficiently high field enhancements for single-molecule detection. In this context, the geometrical arrangement of the AuNPs is changed, larger AuNPs with a diameter of 60 nm are used and the interparticle distance is significantly decreased. Furthermore, a silver enhancement approach is applied in order to obtain Au-Ag-core-shell NPs providing higher field enhancements compared to bare AuNPs. In this way the successful detection of single analyte molecules (TAMRA and cyanine 3 (Cy3)) placed in the center between the two AuNPs is demonstrated. Additionally, the SERS performance of the optimized structures is quantified by estimating enhancement factors (EFs).

In the context of single-molecule detection it is particularly interesting to gain additional information about the conformation of the molecule within the hot spot. Therefore, a series of SERS measurements with varying polarization angles of the incoming and the scattered light is required. However, SERS measurements are frequently accompanied by photobleaching of the Raman dyes caused by the laser exposure. Recently, graphene was demonstrated to efficiently reduce the photobleaching of dye molecules in close vicinity and thereby stabilize the SERS signal over a prolonged period of time<sup>[12,13]</sup>. For this reason, the impact of graphene as an additional component to the developed SERS substrate is tested.

Initially, the encapsulation of bare DNA origami substrates by graphene is presented in manuscript 3 (**M3**<sup>3</sup>). Herein, the replication ability of graphene as well as its influence on the structural stability of the underlying DNA origami substrates is investigated.

Finally, in manuscript 4 (**M4**<sup>4</sup>) the individual components introduced in **M1–M3**, that is, a DNA origami template, a AuNP dimer and a single layer of graphene, are combined within one hybrid material. In this way the unique properties of the individual building blocks are efficiently merged resulting in highly beneficial SERS substrates. The impact of the graphene layer on the optical properties of the novel hybrid structures is extensively studied. In this context, the SERS performance, the appearance of the fluorescence background as well as the photostability of the dye molecules are subjects of research. Additionally, a deeper insight of the interplay between the graphene layer and the underlying structures is gained

---

<sup>1</sup> [**M1**] J. Prinz, B. Schreiber, L. Olejko, J. Oertel, J. Rackwitz, A. Keller, I. Bald, “DNA Origami Substrates for Highly Sensitive Surface-Enhanced Raman Scattering”, *J. Phys. Chem. Lett.* **4**, 4140–4145 (2013).

<sup>2</sup> [**M2**] J. Prinz, C. Heck, L. Ellerik, V. Merk, I. Bald, “DNA origami based Au-Ag-core-shell nanoparticle dimers with single-molecule SERS sensitivity”, *Nanoscale* **8**, 5612–5620 (2016).

<sup>3</sup> [**M3**] A. Matković, B. Vasić, J. Pešić, J. Prinz, I. Bald, A. Milosavljević, R. Gajić, “Enhanced structural stability of DNA origami nanostructures by graphene encapsulation”, *New J. Phys.* **18**, 025016 (2016).

<sup>4</sup> [**M4**] J. Prinz, A. Matković, J. Pešić, R. Gajić, I. Bald, “Hybrid Structures for Surface-Enhanced Raman Scattering: DNA Origami/Gold Nanoparticle Dimer/Graphene”, *Small* **12**, 5458–5467 (2016).

---

by polarization-dependent SERS measurements.

In addition to the four main manuscripts (**M1–M4**), DNA origami as substrates for ultraviolet (UV) photon-induced DNA strand breakage (**M5**<sup>5</sup>) are briefly discussed. Moreover, another facet of SERS substrates is pointed out in **M6**<sup>6</sup>, by demonstrating the SERS activity of gold nanodiscs (AuNDs) synthesized on the basis of phospholipids. Finally, DNA origami templates are presented as substrates for the assembly of plasmonic gold nanolenses (AuNLs) (**M7**<sup>7</sup>).

---

<sup>5</sup> [**M5**] S. Vogel, J. Rackwitz, R. Schürman, J. Prinz, A. R. Milosavljević, M. Réfrégiers, A. Giuliani, I. Bald, “Using DNA Origami Nanostructures to Determine Absolute Cross Sections for UV Photon-Induced DNA Strand Breakage”, *J. Phys. Chem. Lett.* **6**, 4589–4593 (2015).

<sup>6</sup> [**M6**] J. Oertel, A. Keller, J. Prinz, B. Schreiber, R. Hübner, J. Kerbusch, I. Bald, K. Fahmy, “Anisotropic metal growth on phospholipid nanodiscs via lipid bilayer expansion”, *Sci. Rep.* **6**, 26718 (2016).

<sup>7</sup> [**M7**] C. Heck, J. Prinz, A. Dathe, V. Merk, O. Stranik, W. Fritzsche, J. Kneipp, I. Bald, “Gold nanolenses self-assembled by DNA origami”, *submitted manuscript*.





# 2

## Theoretical background

### 2.1. Raman scattering

In 1928 RAMAN observed the so-called *Raman effect*<sup>[14]</sup> which is a form of inelastic light scattering representing the basis of today's Raman spectroscopy.

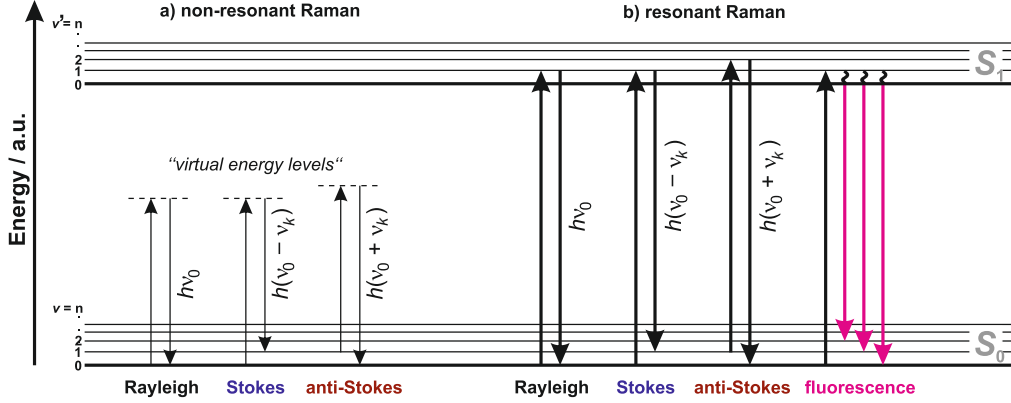
Basically, upon light-matter interactions elastic as well as inelastic scattering processes may occur, which are schematically depicted in Figure 2.1. Both processes are initiated by the absorption of an incident photon with the energy  $h\nu_0$  resulting in a transition of the molecule from the singlet ground electronic state  $S_0$  to a higher energy level. Depending on the wavelength  $\lambda_{\text{exc}}$  of the incoming laser light different types of energy levels may be populated. On the one hand, non-resonant excitation (Figure 2.1 **a**) leads to a transition to so-called “virtual energy levels”<sup>[15]</sup>. On the other hand, on the condition that the energy of the incoming laser light is in resonance with one (or more) electronic transition(s) of the molecule, higher singlet electronic states  $S_n$  are populated<sup>[16]</sup> (Figure 2.1 **b**). For both, non-resonant and resonant Raman processes, subsequent relaxation of the molecule to the electronic ground state  $S_0$  (to a vibrational level ( $v = 0, 1, 2, \dots$ )) causes the emission of another photon whose energy can be identical ( $h\nu_0$ ; elastic RAYLEIGH scattering) or different ( $h(\nu_0 \pm \nu_k)$ ; inelastic RAMAN scattering) from the energy of the incident photon<sup>[15]</sup>. Additionally, in the case of resonant excitation the molecule can be radiatively deactivated in terms of fluorescence which represents a competing path to Raman scattering (Figure 2.1 **b**). Since fluorescence cross sections  $\sigma_F$  typically exceed resonant Raman cross sections  $\sigma_{RR}$  by approximately 6 orders of magnitude the detection of Raman signals is often hampered upon resonant excitation<sup>[16]</sup> (see sections 2.1.2 and 2.3.3 for detailed considerations).

Depending on the involved (vibrational) energy levels the inelastic Raman scattering is classified in STOKES scattering and anti-STOKES scattering which significantly differ in their observed intensities. This is caused by the BOLTZMANN-distribution of the population density for different vibrational levels<sup>[17]</sup>:

$$\frac{N_1}{N_0} = e^{\frac{-\Delta E}{k_B T}} \quad (2.1)$$

where  $N_0$  and  $N_1$  are the numbers of molecules in the vibrational levels  $v = 0$  and  $v = 1$ ,  $\Delta E$  [J] is the energy difference between the two levels,  $T$  [K] is the temperature and  $k_B$  is the BOLTZMANN's constant ( $k_B = 1.38 \times 10^{-23}$  J K<sup>-1</sup>). Considering a room temperature of  $T = 300$  K, the lowest vibrational level ( $v = 0$ ) of the  $S_0$  state is almost entirely populated,

facing a population of less than 1% for the next vibrational level ( $v = 1$ )<sup>[17]</sup>. Thus, STOKES scattering is usually far more intense compared to anti-STOKES scattering and consequently analyzed in most Raman experiments<sup>[15]</sup>. However, according to equation 2.1 the population of the vibrational level  $v = 1$  and thus the intensity of the anti-STOKES scattering increases with increasing temperature. Ultimately, in comparison to RAYLEIGH scattering the intensity of Raman scattering is several orders of magnitude lower (approximately  $10^{-6}$  of the incident laser light<sup>[15]</sup>) which is reflected in extremely low Raman cross sections  $\sigma_R$  (see section 2.1.2 for detailed discussion).



**Figure 2.1.: Energy diagram illustrating basic processes in (a) non-resonant and (b) resonant Raman scattering.** For non-resonant excitation “virtual energy levels” are populated whereas in resonant Raman experiments the excitation wavelength matches an electronic transition resulting in the competing appearance of fluorescence which often hampers the detection of the pristine Raman signal.  $h$ : PLANCK’S constant ( $h = 6.626 \times 10^{-34}$  J s),  $\nu_0$ : frequency of the incident laser light,  $(\nu_0 - \nu_k)$ : frequency of STOKES scattering,  $(\nu_0 + \nu_k)$ : frequency of anti-STOKES scattering,  $S_0$ : singlet ground electronic state,  $S_1$ : singlet first electronic state,  $v = 0, 1, 2, \dots$ : vibrational energy levels.

### 2.1.1. Classical approach to Raman scattering

Although a full description of the Raman process requires quantum theoretical concepts, the basic principle is also accessible in terms of a classical and phenomenological approach<sup>[18]</sup>. At a starting point, the electric field  $\vec{E}$  [V m<sup>-1</sup>] of the incident laser light induces a dipole moment  $\vec{P}$  [C m] within the probed molecule which is proportional to its polarizability  $\hat{\alpha}$  (equation 2.2)<sup>[19]</sup>. Herein,  $\hat{\alpha}$  [C m<sup>2</sup> V<sup>-1</sup>] is a tensor of rank two with nine elements<sup>[18]</sup>.

$$\vec{P} = \hat{\alpha} \cdot \vec{E} \quad (2.2)$$

The oscillating electric field  $\vec{E}$  in turn is described by its amplitude  $\vec{E}_0$  [V m<sup>-1</sup>], its angular frequency  $\omega_0$  [s<sup>-1</sup>] or the corresponding frequency  $\nu_0$  [Hz] and the time  $t$  [s] as<sup>[20]</sup>:

$$\vec{E} = \vec{E}_0 \cos(\omega_0 t) = \vec{E}_0 \cos(2\pi\nu_0 t) \quad (2.3)$$

Consequently, the induced dipole moment is given by equation 2.4.

$$\vec{P} = \hat{\alpha} \cdot \vec{E}_0 \cos(2\pi\nu_0 t) \quad (2.4)$$

Considering a molecule with  $N_a$  atoms ( $N_a \geq 2$ ) yields  $3N_a - 6$  (or  $3N_a - 5$  for linear molecules) normal vibrational modes  $k$  describing linearly independent vibrations of the atoms around their equilibrium positions<sup>[18]</sup>. For a given normal vibrational mode  $k$  the displacement of each

atom upon vibration is then described by the corresponding normal mode coordinate  $Q_k$ <sup>[20]</sup>. As the result of molecular vibrations the molecular and electronic structure of the molecule is affected which leads to a slight perturbation of the polarizability  $\hat{\alpha}$ <sup>[20]</sup>. This is approximated on the basis of a TAYLOR expansion (around the equilibrium position  $Q_k = 0$ )<sup>[18]</sup>:

$$\hat{\alpha}(Q_k) = \hat{\alpha}_0 + \left( \frac{\partial \hat{\alpha}}{\partial Q_k} \right)_{Q_k=0} Q_k + \frac{1}{2} \left( \frac{\partial^2 \hat{\alpha}}{\partial Q_k^2} \right)_{Q_k=0} Q_k^2 + \dots \quad (2.5)$$

Herein, the molecular vibration for a given normal mode  $k$  can be described by a harmonic oscillation in terms of the normal mode coordinates  $Q_k$  with the amplitude  $Q_k^0$ , the frequency  $\nu_k$  [Hz] and the time  $t$  [s]<sup>[20]</sup>:

$$Q_k = Q_k^0 \cdot \cos(2\pi\nu_k t) \quad (2.6)$$

For small oscillations equation 2.5 can be reduced to the first two terms governing the induced dipole moment  $\vec{P}$  as<sup>[18]</sup>:

$$\vec{P} = \left[ \hat{\alpha}_0 + \left( \frac{\partial \hat{\alpha}}{\partial Q_k} \right)_{Q_k=0} Q_k^0 \cos(2\pi\nu_k t) \right] \vec{E}_0 \cos(2\pi\nu_0 t) \quad (2.7)$$

Trigonometric transformation yields equation 2.8 which is composed of the RAYLEIGH term correlated to the incident frequency  $\nu_0$  and the RAMAN term including the frequency shifts for STOKES scattering ( $\nu_0 - \nu_k$ ) and anti-STOKES scattering ( $\nu_0 + \nu_k$ ), respectively<sup>[20]</sup>.

$$\vec{P} = \underbrace{\hat{\alpha}_0 \vec{E}_0 \cos(2\pi\nu_0 t)}_{\text{RAYLEIGH}} + \underbrace{\frac{1}{2} \left( \frac{\partial \hat{\alpha}}{\partial Q_k} \right)_{Q_k=0} Q_k^0 \vec{E}_0 [\cos(2\pi(\nu_0 + \nu_k)t) + \cos(2\pi(\nu_0 - \nu_k)t)]}_{\text{RAMAN}} \quad (2.8)$$

Equation 2.8 yields the classical selection rule for Raman scattering, that is, that Raman scattering exclusively occurs if the polarizability of a given normal vibrational mode changes during the vibration<sup>[15]</sup>:

$$\left( \frac{\partial \hat{\alpha}}{\partial Q_k} \right)_{Q_k=0} \neq 0 \quad (2.9)$$

Basically, this condition is fulfilled for vibrations that are symmetrical with respect to the molecule's centre of symmetry<sup>[15]</sup>. As a general rule non-polar functional groups are in most cases Raman-active whereas for the detection of polar functional groups infrared (IR) spectroscopy, being the complementary approach to Raman spectroscopy, is the method of choice<sup>[21]</sup>.

### 2.1.2. Raman cross sections

The concept of cross sections  $\sigma$  has been introduced in order to compare the efficiency of different optical processes that are directly correlated to an excitation with incident light<sup>[18]</sup>. Geometrically, it can be understood in terms of an imaginary area surrounding a certain molecule. The larger the area (which is equal to a high cross section) the higher is the probability of an interaction with an incident photon.

Typical Raman cross sections  $\sigma_R$  are on the order of  $10^{-30}$  cm<sup>2</sup> per molecule for non-resonant excitation<sup>[22]</sup>. On the contrary, characteristic fluorescence cross sections  $\sigma_F$  are within the range of  $10^{-17}$ – $10^{-16}$  cm<sup>2</sup><sup>[23]</sup> and thus exceed Raman cross sections by up to 14 orders of magnitude.

Basically, the Raman cross section depends on the excitation wavelength, the investigated

vibrational mode as well as on the refractive index of the surrounding medium. Furthermore, the intrinsic low Raman cross sections  $\sigma_R$  can be directly influenced by the following factors:

- **Resonant excitation:** Upon resonant excitation of one of the molecule's electronic transitions (see Figure 2.1) the Raman cross section  $\sigma_R$  can be increased by a factor of at least  $10^4$ <sup>[18]</sup> and is then referred to as the resonant Raman cross section  $\sigma_{RR}$ . Since the laser wavelength can be chosen to be resonant with different electronic transitions, a high selectivity of investigated states is obtained. Ultimately, resonant excitation results in an improved signal-to-noise (S/N) ratio and thus leads to a decreased limit of detection (LOD).
- **Charge transfer processes:** If the analyte molecule is adsorbed on a metal surface (in most cases gold (Au) or silver (Ag)) charge transfer (CT) processes may occur, resulting in an altered Raman cross section  $\sigma_{R,ads}$  in comparison to non-adsorbed molecules  $\sigma_{R,free}$ <sup>[24]</sup>. This effect is further discussed in section 2.3.1.

It has to be mentioned, that Raman cross sections are often given in units of  $\text{cm}^2$  and refer to a molecule with a randomly-averaged orientation<sup>[18]</sup>. However, in order to completely describe the scattering process the direction of scattered photons also has to be considered. This is realized in the definition of the absolute differential Raman cross section  $d\sigma_R/d\Omega$  [ $\text{m}^2 \text{sr}^{-1}$ ] which additionally includes the radiation profile. In this definition  $\Omega$  is a variable that defines the direction of scattered light with respect to the incident laser beam<sup>[18]</sup>. Usually, the values for absolute differential Raman cross sections are given for STOKES scattering but can also be revealed for the anti-STOKES process<sup>[18]</sup>.

## 2.2. Plasmonics

### 2.2.1. Optical properties of metals

The optical properties of metals can widely be described by the *Plasma model* which considers a gas of free electrons moving relatively to a fixed background of positive ion cores if an electromagnetic field is applied<sup>[25]</sup>. The oscillation of the free electrons is damped due to mutual collisions which is characterized by the collision frequency  $\gamma$  [ $\text{rad s}^{-1}$ ] (or its reciprocal relaxation time  $\tau$  [s]). The motion of each electron within the free-electron gas is then described by equation 2.10<sup>[25]</sup>.

$$m\dot{x} + m\ddot{x} = -e\vec{E} \quad (2.10)$$

where  $m$  [kg] and  $e$  [A s] are the mass and the charge of one electron and  $\vec{E}$  [ $\text{V m}^{-1}$ ] is the applied electric field.  $\dot{x}$  [ $\text{m s}^{-1}$ ] and  $\ddot{x}$  [ $\text{m s}^{-2}$ ] describe the velocity and the acceleration of the electron motion.

Assuming harmonic time dependence for  $\vec{E}$ , a particular solution of equation 2.10 is given by  $x(t) = x_0 e^{-i\omega t}$ <sup>[25]</sup>. Within the classical framework based on MAXWELL's equation the complex dielectric function  $\epsilon(\omega)$  for the free-electron gas is obtained<sup>[18]</sup>:

$$\epsilon(\omega) = \epsilon_\infty \left( 1 - \frac{\omega_P^2}{\omega^2 + i\gamma\omega} \right) \quad (2.11)$$

where  $\epsilon_\infty$  is the dielectric function of the constant background arising from fixed ions.  $\omega$  [ $\text{s}^{-1}$ ] is the angular frequency of light and  $\omega_P$  [ $\text{s}^{-1}$ ] is the *plasma frequency* which in turn is related to the number of free electrons per unit volume  $n_e$  [ $\text{m}^{-3}$ ], to their mass  $m$  [kg] and to the

dielectric function of vacuum  $\epsilon_0$  ( $\epsilon_0 \approx 8.854 \times 10^{-12} \text{ F m}^{-1}$ ) as<sup>[18,25]</sup>:

$$\omega_P = \sqrt{\frac{n_e e^2}{m \epsilon_0 \epsilon_\infty}} \quad (2.12)$$

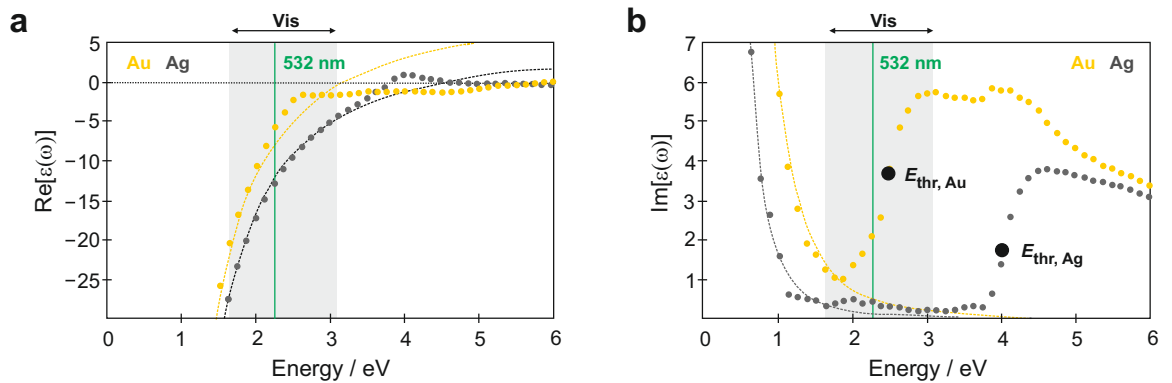
Equation 2.11 is also known as the DRUDE model<sup>[26]</sup> and can be separated in real (Re) and imaginary (Im) terms according to  $\epsilon(\omega) = \epsilon_1(\omega) + i\epsilon_2(\omega)$ <sup>[18]</sup>:

$$\text{Re}[\epsilon(\omega)] = \epsilon_1(\omega) = \epsilon_\infty \left( 1 - \frac{\omega_P^2}{\omega^2 + \gamma} \right) \quad (2.13)$$

$$\text{Im}[\epsilon(\omega)] = \epsilon_2(\omega) = \frac{\epsilon_\infty \omega_P^2 \gamma}{\omega(\omega^2 + \gamma^2)} \quad (2.14)$$

Figure 2.2 shows the behaviour of (a)  $\text{Re}[\epsilon(\omega)]$  and (b)  $\text{Im}[\epsilon(\omega)]$  for Au and Ag as a function of energy theoretically determined by the DRUDE model (equation 2.11). Additionally, the experimentally obtained dielectric functions are plotted for both metals (Figure 2.2, dots). As can be seen in Figure 2.2 a over a wide energy range,  $\text{Re}[\epsilon(\omega)]$  is similar for Au and Ag which implies that the electronic densities for both metals are comparable<sup>[27]</sup>. Moreover, the fact that  $\text{Re}[\epsilon(\omega)]$  exhibits large negative values within the visible range of the electromagnetic spectrum is the origin of the plasmonic properties of Au and Ag (among other metals)<sup>[27]</sup>. This relation is further discussed in section 2.2.2.

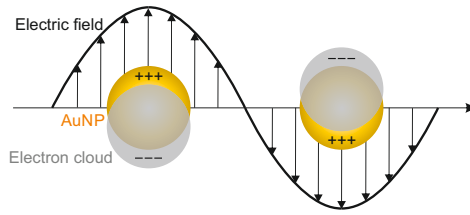
In contrast, the imaginary part  $\text{Im}[\epsilon(\omega)]$  (Figure 2.2 b) is related to the absorption properties of a metal<sup>[25]</sup>. Below 2.0 eV  $\text{Im}[\epsilon(\omega)]$  is similar for Au and Ag. However, above 2.0 eV  $\text{Im}[\epsilon(\omega)]$  rapidly increases for Au and exhibits a characteristic double-humb structure which is caused by the appearance of inter-band transitions between valence and conduction bands<sup>[27]</sup>. Figure 2.2 b clearly displays the energy thresholds for inter-band transitions in Au ( $E_{\text{thr, Au}}$ ) and Ag ( $E_{\text{thr, Ag}}$ ) at approximately 2.4 eV and 4.0 eV, respectively. Consequently, excitations in the visible range of the electromagnetic spectrum exclusively lead to intra-band transitions for Ag and to both, intra- and inter-band transitions for Au. This behaviour causes the discrepancies between calculations for  $\text{Im}[\epsilon(\omega)]$  based on the DRUDE model (Figure 2.2, lines) and experimental data (Figure 2.2, dots).



**Figure 2.2.: Dielectric functions  $\epsilon(\omega)$  for Au and Ag.** The real (a) and imaginary (b) parts of the experimentally determined dielectric functions  $\epsilon(\omega)$ <sup>[28]</sup> are plotted (yellow and grey dots) and compared to the theoretical data based on the DRUDE model (equation 2.11). (Figure adapted and modified from ref. <sup>[25]</sup>.)

### 2.2.2. Localized surface plasmon resonance (LSPR)

As mentioned before, the negative real part of the dielectric function  $\text{Re}[\epsilon(\omega)]$  is directly connected to the appearance of plasmons – an optical phenomenon which is generally defined as the collective oscillation of the surface conduction electrons excited by electromagnetic radiation<sup>[29]</sup>. Depending on their propagation ability as well as on their spatial confinement two types of plasmons are distinguished. On the one hand, surface plasmon polaritons (SPP) occur at flat interfaces between a dielectric material and a conductor and they can propagate in x- and y-directions for distances of up to hundreds of microns<sup>[25,29]</sup>. This type of plasmon is not discussed in detail. On the other hand, localized surface plasmon resonances (LSPR) result from excitation of surface conduction electrons in nanostructures whose diameter is much smaller compared to the incident laser wavelength<sup>[25]</sup>. The induced collective oscillation is non-propagating due to the spatial confinement to the NP surface which is illustrated in Figure 2.3<sup>[29]</sup>.



**Figure 2.3.: Excitation of the LSPR in a spherical AuNP.** The incident laser light induces a plasmon that is oscillating around the AuNP due to local confinement. (Figure adapted and modified from ref.<sup>[29]</sup>.)

To characterize the electromagnetic field surrounding the metal sphere, an electrostatic (ES) approximation can be applied which gives reasonable results for NPs smaller than 100 nm<sup>[25]</sup>. For larger NPs scattering is gaining in importance and thus more realistic results can be obtained by MIE theory<sup>[18]</sup>. Within the ES-approximation it is assumed that the electromagnetic field remains constant over the volume of the interacting NP since the radius  $r$  of the NP is much smaller compared to the wavelength  $\lambda$  of the light<sup>[25]</sup>. The dipolar polarizability  $\hat{\alpha}_{\text{NP}}$  for a NP with arbitrary geometry is then given by<sup>[30]</sup>:

$$\hat{\alpha}_{\text{NP}} = (1 + \kappa)V \frac{\epsilon(\omega) - \epsilon_{\text{m}}}{\epsilon(\omega) + \kappa\epsilon_{\text{m}}} \quad (2.15)$$

where  $V$  [m<sup>3</sup>] is the volume of the NP,  $\epsilon_{\text{m}}$  is the dielectric function of the surrounding medium and  $\kappa$  is a shape factor. In the case of a spherical particle it is  $\kappa = 2$  and thus<sup>[30]</sup>:

$$\hat{\alpha}_{\text{sphere}} = 4\pi r^3 \frac{\epsilon(\omega) - \epsilon_{\text{m}}}{\epsilon(\omega) + 2\epsilon_{\text{m}}} \quad (2.16)$$

From equation 2.16 it is obvious that the polarizability for a metal sphere becomes maximum for the condition that  $|\epsilon(\omega) + 2\epsilon_{\text{m}}|$  is a minimum. Since  $\epsilon(\omega)$  is a complex number,  $\epsilon(\omega) = -2\epsilon_{\text{m}}$  cannot exactly be complied but a resonance appears for  $\text{Re}[\epsilon(\omega)] = -2\epsilon_{\text{m}}$ <sup>[27]</sup>. The magnitude of the resulting polarizability  $\hat{\alpha}_{\text{sphere}}$  is then determined by the imaginary part  $\text{Im}[\epsilon(\omega)]$ <sup>[27]</sup>. Moreover, the frequency corresponding to the resonance is referred to as *dipolar LSPR frequency*  $\omega_{\text{LSPR}}$ <sup>1</sup>. For a sphere described by the DRUDE model (equation 2.11) the resonance

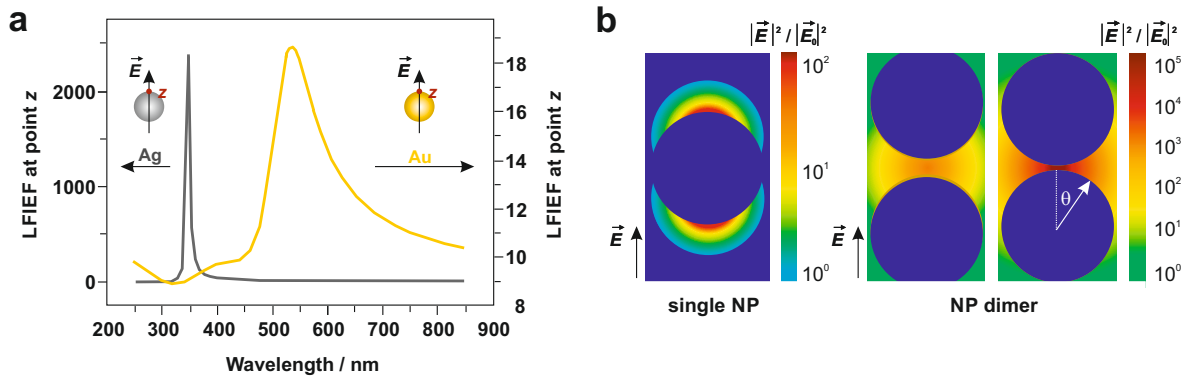
<sup>1</sup> In principle, dipolar as well as multipolar resonances can be excited within metal NPs. Both terms are related to the angular momentum  $l$  and are further discussed in section 2.2.3. Unless otherwise stated, the *LSPR* is referred to the dipolar resonance for the subsequent discussion.

criterion is fulfilled at  $\omega_{\text{LSPR}} = \frac{\omega_{\text{P}}}{\sqrt{3}}$  [25].

As a consequence of exciting the LSPR frequency  $\omega_{\text{LSPR}}$ , the electromagnetic field in the vicinity of the metal surface is influenced. This is quantified in terms of the local field intensity enhancement factor (LFIEF) which compares the intensity of the electromagnetic field at a specific point  $z$  in presence ( $\vec{E}(z, \omega)$ ) and absence ( $\vec{E}_0(z, \omega)$ ) of the metal surface (equation 2.17) [27]. The value of the LFIEF defines whether the electric field at position  $z$  is enhanced (LFIEF  $> 1$ ) or quenched (LFIEF  $< 1$ ) due to the presence of the metal.

$$\text{LFIEF}(z, \omega) = \frac{|\vec{E}(z, \omega)|^2}{|\vec{E}_0(z, \omega)|^2} \quad (2.17)$$

In Figure 2.4 **a** the LFIEF for a Au and a Ag sphere as a function of the incident laser wavelength is shown (the different scales have to be considered). For both metals a resonance peak appears at their corresponding LSPR frequency  $\omega_{\text{LSPR}}$ . The different appearances for the two metal spheres, that is, a sharp peak in the case of Ag and a much broader one for Au can be explained by the influence of the imaginary parts  $\text{Im}(\epsilon(\omega))$  of the metal's dielectric functions [27]. As illustrated in Figure 2.2 **b** the influence of  $\text{Im}(\epsilon(\omega))$  is much higher for Au than for Ag at their corresponding LSPR frequencies  $\omega_{\text{LSPR}}$ , both located within the visible range of the electromagnetic spectrum ( $\lambda_{\text{LSPR, AuNP}} \approx 520 \text{ nm}$  [31];  $\lambda_{\text{LSPR, AgNP}} \approx 420 \text{ nm}$  [32]). Additionally, the maximum LFIEF for the Ag sphere is approximately 130 times higher and also blue-shifted with respect to the Au sphere.



**Figure 2.4.: LFIEF and hot spots.** (a) The LFIEF at point  $z$  is depicted for a Au and a Ag sphere in the ES-approximation as a function of the incident laser wavelength. The corresponding NP sizes are in the range of 10 nm and hence much smaller compared to the incident wavelength [18,27]. (b) The localization of hot spots is qualitatively illustrated for a single NP and a NP dimer with two different gap sizes. The LFIEF values are estimated based on considerations for 30 nm silver nanoparticles (AgNPs) in water and an excitation wavelength of  $\lambda_{\text{exc}} = 428 \text{ nm}$  [22]. (Figure **a** adapted and modified from ref. [27].)

In addition to the choice of the metal, the LSPR frequency  $\omega_{\text{LSPR}}$  as well as the LFIEF can be tuned by many factors of which the most relevant for the present thesis are briefly discussed:

- **Size effects:** Spherical NPs  $< 20 \text{ nm}$  are mainly absorbing [33]. With increasing size the scattering is increased leading to increasing radiation losses. Therefore, the LSPR is damped which is expressed in a broadening and a red-shift of the LSPR peak [27]. In the case of Ag spheres an increase of the NP size leads to a dramatic decrease of the LFIEF caused by radiation losses. In contrast, due to the intrinsic optical absorption (see section 2.2.1) even for small NP sizes, the LFIEF of AuNPs is much less influenced by radiation effects [18].

Furthermore, for Au and Ag spheres additional multipolar resonances are progressively activated with increasing diameter<sup>[27]</sup>. Multipolar resonances appear at shorter wavelengths with respect to the dipolar LSPR peak of the corresponding metal<sup>[18]</sup>.

- **Shape effects:** Usually, the shift of the LSPR frequency is more affected by changing the shape of the particle, e.g. its aspect ratio, than simply changing its size. It has been shown that the LSPR frequency can be tuned from Vis to IR regions by using differently shaped nanostructures such as spheres, triangles, cubes, prisms, bipyramids, octahedrons, rods, shells and stars<sup>[33]</sup>. It has also been reported that the LFIEF is more pronounced at tips, corners or edges in comparison to flat surfaces which is referred to as the *lightning rod effect*<sup>[34]</sup>. Furthermore, the number of arising LSPR peaks per nanostructure scales with the number of modes excitable by polarized light and thus with the complexity of the structure<sup>[33]</sup>.
- **Gap effects:** If two (or more) NPs approach each other their individual plasmons start to couple. This results in a redistribution of LFIEFs in the vicinity of the NPs which is depicted in Figure 2.4 **b**. For a single NP the highest values for the LFIEF arise at the poles along the axis of the incident laser field<sup>[22]</sup>. Especially high LFIEFs are reached in the gap between two adjacent NPs which is referred to as the formation of a hot spot. The smaller the gap size the higher is the expected LFIEF (compare NP dimers in Figure 2.4 **b**)<sup>[22]</sup>. However, this effect is also accompanied by a more pronounced localization resulting in a rapid decrease of the LFIEF with increasing angle  $\theta$  (Figure 2.4 **b**, right dimer)<sup>[27]</sup>. Moreover, plasmon coupling causes the splitting of the LSPR band in longitudinal (low frequency) and transversal (high frequency) components (see section 2.2.3) which are not distinguishable in single spherical NPs<sup>[27]</sup>.

### 2.2.3. Coupling of LSPR

The plasmon hybridization model visualizes the mutual coupling between several plasmonic structures as an analogue consideration to molecular orbital coupling<sup>[35]</sup>. The model was initially designed by PRODAN *et al.* to describe the interactions of plasmons within nanoshells consisting of a dielectric core and a metal shell<sup>[36]</sup>. Afterwards it was adopted to explain interactions in numerous kinds of compositions of various complexity, such as dimers of nanorods<sup>[37,38]</sup>, nanostars<sup>[39]</sup>, Au-Ag-core-shell nanospheres<sup>[40]</sup> or Au-Ag-core-shell nanocubes<sup>[41]</sup>. Within the hybridization model the interactions of all elementary components are considered in order to obtain the resulting plasmon modes of a nanostructure<sup>[40]</sup>.

#### Plasmon coupling within a AuNP dimer

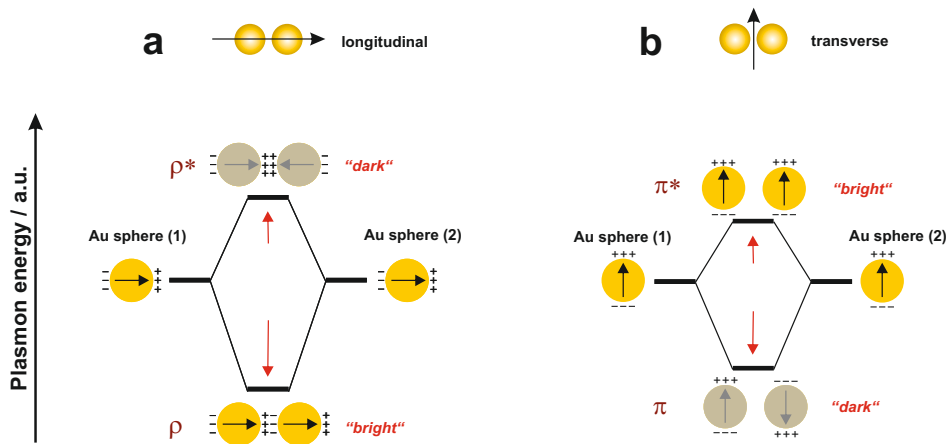
Considering a AuNP dimer consisting of two identical spheres, two extreme cases can be distinguished depending on the incoming light being: (a) polarized along the dimeric axis (longitudinal polarization, Figure 2.5 **a**) or (b) polarized perpendicular to the dimeric axis (transverse polarization, Figure 2.5 **b**).

For longitudinal polarization (Figure 2.5 **a**) the bonding mode ( $\rho$ ) and anti-bonding mode ( $\rho^*$ ) correspond to in-phase coupling ( $(\Psi_1 + \Psi_2)$ , symmetric dielectric fields) and out-of-phase coupling ( $(\Psi_1 - \Psi_2)$ , antisymmetric dielectric fields), respectively<sup>[42]</sup>. Since the dipoles are oppositely oriented for the  $\rho^*$  mode, resulting in a net dipole moment of 0, this mode is referred to as “dark”<sup>[43]</sup>. Consequently, only the  $\rho$  mode (“bright” mode) occurs for longitudinal polarization which appears red-shifted with respect to the plasmon mode of a single AuNP. For large distances  $d_{\text{gap}}$  between the two AuNPs the mutual interactions are weak resulting



in a symmetric splitting of  $\rho$  and  $\rho^*$  modes. This is due to coupling between plasmon modes with the same angular momentum  $l$ <sup>[43]</sup>. According to classical dipole interactions the extent of splitting scales with  $1/d_{\text{gap}}^3$ <sup>[43]</sup>. Furthermore, with decreasing distances  $d_{\text{gap}}$  the splitting between  $\rho$  and  $\rho^*$  modes appears progressively antisymmetric (indicated by the red arrows in Figure 2.5), which is caused by interactions between dipolar plasmons ( $l = 1$ ) and higher multiple plasmons ( $l > 1$ ). Thereby, the red-shift of the  $\rho$  mode is more pronounced than the blue-shift of the  $\rho^*$  mode<sup>[43]</sup>.

In the case of transverse polarization (Figure 2.5 b) the assignment of the modes is reversed, that is, the out-of-phase coupling giving rise to the bonding mode ( $\pi$ , “dark” mode) and the in-phase coupling to the anti-bonding mode ( $\pi^*$ , “bright” mode)<sup>[42]</sup>. Compared to longitudinal polarization the resulting LSPR shifts for transverse polarization are less pronounced due to weaker interactions<sup>[42]</sup>.



**Figure 2.5.:** Plasmon hybridization model for AuNP dimers depending on the polarization of the incoming light. (a) For longitudinal excitation the mode splitting is more pronounced resulting in a bright in-phase mode. (b) Transverse polarization leads to a bright out-of-phase mode. (Figures adapted and modified from ref.<sup>[42]</sup>.)

### Plasmon coupling within Au-Ag-core-shell NPs

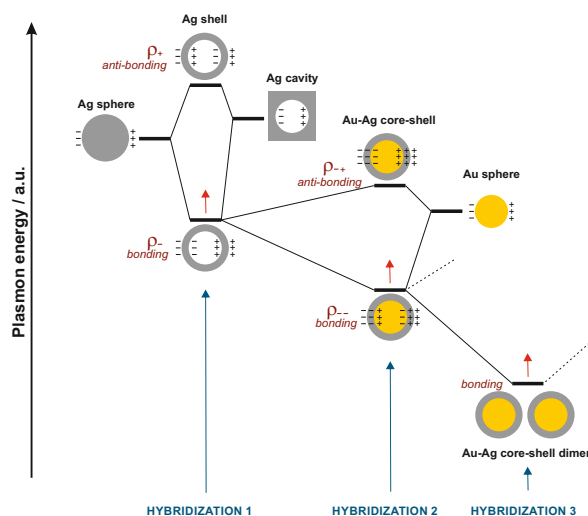
The plasmon hybridization model can also be applied for nanostructures of higher complexity, such as spherical AuNPs with a surrounding Ag shell (Au-Ag-core-shell NPs)<sup>[40]</sup>. In order to express the resulting plasmon modes the individual contributions have to be considered stepwise from the outer Ag shell to the inner Au core which is qualitatively depicted in the plasmon hybridization scheme in Figure 2.6.

As a starting point, the plasmonic interactions of the Ag shell with its surrounding is expressed in terms of plasmon coupling between a Ag sphere and a cavity surrounded by bulk Ag<sup>[44]</sup>. The interactions between sphere and cavity plasmons, and thus the correlated extent of splitting in bonding ( $\rho_-$ ) and anti-bonding ( $\rho_+$ ) mode, depend on the Ag shell thickness<sup>[36]</sup> (Figure 2.6, hybridization 1). Within a second step the Ag shell  $\rho_-$  mode couples with the Au sphere’s plasmon resulting in Au-Ag-core-shell bonding  $\rho_{--}$  and anti-bonding  $\rho_{-+}$  modes (Figure 2.6, hybridization 2)<sup>[40]</sup>. As a result, for a single Au-Ag-core-shell NP three linearly independent dipolar plasmon resonances are obtained, which are  $\rho_+$  (anti-bonding, Ag shell),  $\rho_{--}$  (bonding, Au-Ag-core-shell) and  $\rho_{-+}$  (anti-bonding, Au-Ag-core-shell), respectively<sup>[40]</sup>. With increasing Ag shell thickness the plasmon coupling between Ag sphere and cavity (Figure 2.6, hybridization 1) becomes less pronounced<sup>[36]</sup> resulting in a blue-shift of the  $\rho_-$  mode.

Consequently, the  $\rho_{--}$  mode of the Au-Ag-core-shell NP is also blue-shifted (indicated by the red arrows in Figure 2.6).

Since the complexity of the plasmon hybridization scheme would dramatically increase for the consideration of a Au-Ag-core-shell NP dimer, a third hybridization is only partially indicated in Figure 2.6 by assuming a mirror-inverted hybridization scheme for a second Au-Ag-core-shell NP. Several additional mode interactions would have to be considered such as coupling between the two Ag shells, the two Au cores and the two final Au-Ag-core-shell NPs. All these modes are highly sensitive to the ratio between Au core and Ag shell, to the gap size  $d_{\text{gap}}$  and to the polarization of the incident light<sup>[40,43]</sup>. Furthermore, with increasing complexity of plasmonic structures consisting of Au and Ag, inter-band absorption by the Au component gain further importance which has been demonstrated for asymmetric Au-Ag heterodimers<sup>[42]</sup>.

Nevertheless, the two aforementioned examples demonstrate possibilities to obtain plasmonic structures with tailored optical properties.



**Figure 2.6.:** Partial plasmon hybridization model for a Au-Ag-core-shell NP dimer. The mutual plasmon coupling is stepwise described by considering three plasmon hybridization steps starting from the outer Ag shell to the inner Au core. (Figure partially adapted with modifications and further extensions from ref.<sup>[40]</sup>.)

## 2.3. Surface-enhanced Raman scattering (SERS)

The two previously discussed approaches of Raman scattering (section 2.1) and Plasmonics (section 2.2) are merged in the concept of surface-enhanced Raman scattering (SERS) which will be the topic of the present section.

### 2.3.1. Enhancement mechanisms

#### Electromagnetic enhancement

As discussed in section 2.1 within the Raman process light is inelastically scattered by instantaneous absorption of one photon and re-emission of a second photon. The weak nature of Raman signals can be enhanced by placing the analyte molecule(s) in close vicinity to a metal surface. If the LSPR frequency  $\omega_{\text{LSPR}}$  of the metal is excited, the molecule(s) are affected by the LFIEF<sup>[27]</sup>. Since in the Raman process, excitation and emission are connected to each

other, both, the absorbed as well as the scattered light are enhanced by the LFIEF at their corresponding frequencies  $\omega_L$  and  $\omega_S$ <sup>[18]</sup>. The resulting enhancement factor EF at a specific point  $z$  is therefore given by equation 2.18:

$$\text{EF} \approx \text{LFIEF}(z, \omega_L) \cdot \text{LFIEF}(z, \omega_S) \quad (2.18)$$

Since the differences between the LFIEF at  $\omega_L$  and  $\omega_S$  can often be neglected, the simplified equation 2.19 results, which is known as the  $|\vec{E}|^4$ -approximation for SERS<sup>[27]</sup>. By analogy with equation 2.17 in section 2.2.2  $\vec{E}(z, \omega_L)$  and  $\vec{E}_0(z, \omega_L)$  describe the electromagnetic field at point  $z$  in absence and presence of a metal surface.

$$\text{EF} \approx \text{LFIEF}^2(z, \omega_L) = \frac{|\vec{E}(z, \omega_L)|^4}{|\vec{E}_0(z, \omega_L)|^4} \quad (2.19)$$

Although further simplifications (e.g. neglect of polarization within the incident and scattered light) have been applied to obtain equation 2.19, the  $|\vec{E}|^4$ -approximation can be widely used to estimate the EF within a SERS experiment<sup>[27]</sup>. Since this approximation holds for  $\omega_L \gg \omega_S$  or  $\omega_L \approx \omega_L - \omega_S$ , it is especially suitable for excitation in the blue or green spectral region<sup>[18]</sup>.

The resulting overall SERS intensity can be estimated by the relation given in equation 2.20<sup>[24]</sup>:

$$I_{\text{SERS}} = N_{\text{SERS}} \cdot I_L(\omega_L) \cdot |\text{LFIEF}(\omega_L)| \cdot |\text{LFIEF}(\omega_S)| \cdot \sigma_{\text{R,ads}}^2 \quad (2.20)$$

where  $N_{\text{SERS}}$  is the number of molecules involved in the SERS experiment,  $I_L(\omega_L)$  is the laser intensity and  $\sigma_{\text{R,ads}}$  is the Raman cross section of molecules directly adsorbed on the metal surface. The latter is a result of chemical enhancement processes which are discussed in the subsequent section.

It has to be mentioned that the SERS intensity  $I_{\text{SERS}}$  is highly distance-dependent. In the case of a metal sphere the distance ( $r + d_{\text{mol.-met.}}$ ) between the molecule and the center of the metal sphere has to be considered (where  $r$  is the radius of the sphere and  $d_{\text{mol.-met.}}$  is the distance between the molecule and the metal surface). The corresponding SERS intensity scales with  $(r + d_{\text{mol.-met.}})^{-12}$  since the corresponding electric field strength exhibits a  $(r + d_{\text{mol.-met.}})^{-3}$ -dependence<sup>[19]</sup>.

### Chemical enhancement

The term chemical enhancement, which is still controversially discussed, covers a wide range of effects that do not have any plasmonic origin, but are a consequence of altered electronic properties of molecules adsorbed on a metal surface<sup>[27]</sup>. Since the chemical enhancement only affects molecules which are in direct contact to the metal surface it is also often referred to as the *first layer effect*.

Basically, the electronic properties of the molecules are influenced by the presence of the metal. Depending on the extent of contact different contributions to the overall chemical enhancement may occur, which are usually difficult to disentangle. On the one hand, already slight interactions may lead to the appearance of new energy levels within the molecule, which may represent new resonant excitation channels for the incident laser light<sup>[19]</sup>. On the other hand, upon the formation of a molecule-metal-complex, charge transfer (CT) processes may be enabled. This results in an altered polarizability of the adsorbed molecules, which is directly related to a different Raman cross section  $\sigma_{\text{R,ads}}$  in comparison to the one hold by free molecules  $\sigma_{\text{R,free}}$ <sup>[18,19]</sup>. Thus, the detected SERS intensity is directly influenced (see equation 2.20). Again, new resonance processes may be enabled.

### 2.3.2. SERS enhancement factors

In analogy to the LFIEF discussed in section 2.2.2., the overall signal enhancement obtained in a SERS experiment is usually quantified in terms of an enhancement factor  $EF_{\text{SERS}}$ . Depending on the experimental setup and the definition of the scientific problem several definitions of  $EF_{\text{SERS}}$  have been discussed<sup>[45]</sup>. For the following discussions it is only referred to the most general definition (equation 2.21)<sup>[46]</sup>:

$$EF_{\text{SERS}} = \frac{I_{\text{SERS}}/N_{\text{SERS}}}{I_{\text{Raman}}/N_{\text{Raman}}} \quad (2.21)$$

where  $I_{\text{SERS}}$  and  $N_{\text{SERS}}$  are the intensity and the number of contributing molecules within the SERS experiment, whereas  $I_{\text{Raman}}$  and  $N_{\text{Raman}}$  represent the same terms under analogue non-enhanced Raman conditions.

Both, electromagnetic and chemical enhancement mechanisms contribute to the overall SERS enhancement factor  $EF_{\text{SERS}}$ . However, electromagnetic enhancement accounts for EFs up to  $10^{11}$ <sup>[16]</sup> which significantly exceed EFs from chemical enhancement which are typically on the order of  $10$ – $100$ <sup>[24]</sup>.

In many cases the minimum enhancement factor necessary to detect a single molecule within a SERS experiment  $EF_{\text{sm-SERS}}^{\text{min}}$  is of special interest. Its value can be estimated by a rule-of-thumb (equation 2.22)<sup>[22]</sup>:

$$EF_{\text{sm-SERS}}^{\text{min}} \approx \frac{d\sigma_{\text{R}}/d\Omega}{10^{-19} \text{ cm}^2 \text{ sr}^{-1}} \quad (2.22)$$

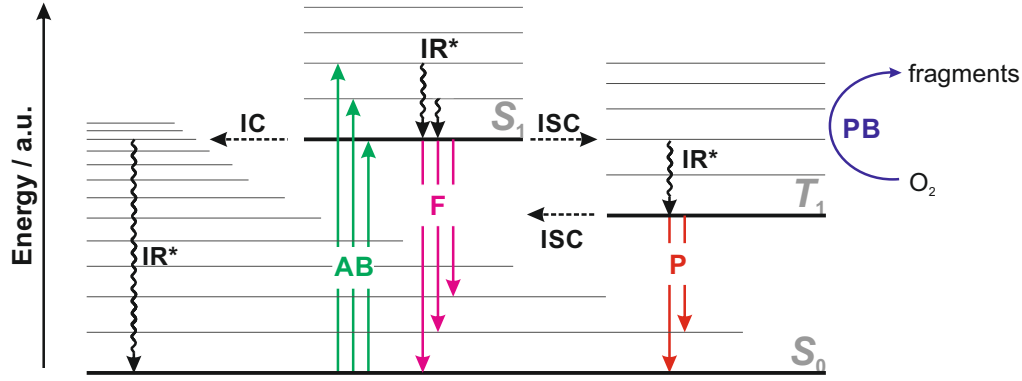
Thus, for the detection of single dye molecules with a relatively high differential Raman cross section in the range of  $10^{-27}$ – $10^{-28} \text{ cm}^2 \text{ sr}^{-1}$  an  $EF_{\text{sm-SERS}}^{\text{min}}$  of  $10^7$ – $10^8$  is required<sup>[19]</sup>. On the contrary, non-resonant molecules with significantly lower differential Raman cross sections ( $10^{-29}$ – $10^{-30} \text{ cm}^2 \text{ sr}^{-1}$ ) require an  $EF_{\text{sm-SERS}}^{\text{min}}$  on the order of  $10^9$ – $10^{11}$ <sup>[19]</sup>.

### 2.3.3. Competing effects in SERS

As in usual Raman spectroscopy, SERS experiments are in many cases accompanied by fluorescence and photobleaching upon resonant excitation. Both effects in turn are affected by the presence of a metal surface and briefly discussed in the following considerations. To illustrate the competition between the effects a simplified JABLONSKI diagram<sup>[47]</sup> is shown in Figure 2.7.

#### Surface-enhanced fluorescence (SEF)

Although both, Raman scattering and fluorescence, are two-photon processes the involved transitions are fundamentally different. First, as already discussed, within the Raman process light is inelastically scattered by instantaneous absorption and re-emission of two photons. Second, fluorescence is a stepwise process, which is initiated by the absorption (AB) of a photon, leading to the excitation of the molecule from the  $S_0$  state to a higher electronic state  $S_n$ <sup>[17]</sup> (Figure 2.7 with  $n = 1$  as an example). Subsequently, internal relaxation (IR\*) of the molecule to the lowest vibrational level of the  $S_1$  state occurs, which is the starting point for radiative (i.e. fluorescence (F)) and non-radiative deactivation processes with  $S_0$  as the final state<sup>[17]</sup>. Hereby, the non-radiative pathway includes internal conversion (IC) to a higher vibrational level of  $S_0$  and subsequent IR\*.

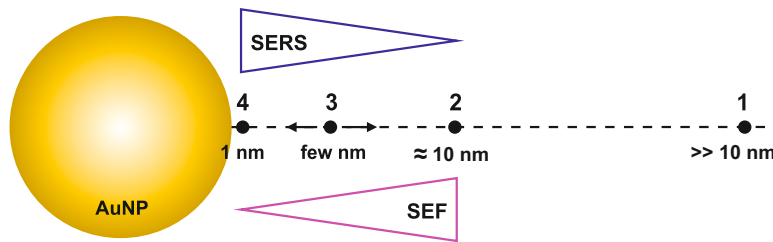


**Figure 2.7.: Simplified Jablonski diagram.** Illustration of the electronic states of a molecule and related radiative and non-radiative transitions. AB: absorption, F: fluorescence, P: phosphorescence, PB: photobleaching, IR\*: internal relaxation, IC: internal conversion, ISC: intersystem crossing,  $S_0$ : singlet ground electronic state,  $S_1$ : singlet first electronic state,  $T_1$ : first triplet state.

The fundamental differences in the origins of Raman scattering and fluorescence result in significant differences regarding their enhancement in close vicinity to a metal surface. The corresponding enhancement factor  $EF_F$  is given by equation 2.23 where  $\eta$  is the radiation efficiency (compare equation 2.18 for the analogue expression of  $EF_{SERS}$ )<sup>[27]</sup>.

$$EF_F \sim LFIEF(\omega_L) \cdot \eta \quad (2.23)$$

Depending on the distance between the fluorophore and the metal surface, the contributions of  $LFIEF(\omega_L)$  and  $\eta$  compete with each other, resulting in distance-dependent fluorescence enhancement ( $EF_F > 1$ ) and quenching ( $EF_F < 1$ ). The competition between SERS and surface-enhanced fluorescence (SEF) as a function of distance to a AuNP surface is depicted in Figure 2.8. In the case of spherical single AuNPs a maximum SEF has been observed for distances in the range of approximately 5–10 nm<sup>[48,49]</sup>. These values are in good accordance with a general consideration for metal surfaces from ref.<sup>[27]</sup>, which is the basis of the subsequent discussion.



**Figure 2.8.: SERS and SEF as a function of distance to the AuNP surface.** SERS is especially pronounced at very small distances whereas the regime for highest SEF intensities is located at approximately 10 nm distance. For distances much larger than 10 nm none of the two phenomena is affected by the AuNP surface. (Figure and discussion are based on considerations from ref.<sup>[27]</sup>.)

For distances much larger than 10 nm (point 1 in Figure 2.8) both effects, Raman scattering and fluorescence, are not influenced by the LFIEF. Due to the higher fluorescence cross sections  $\sigma_F$  fluorescence is exclusively detected. At approximately 10 nm (point 2 in Figure 2.8) the SEF regime is located, meaning that both, Raman scattering and fluorescence, are mildly enhanced but due to its higher efficiency only SEF is detected. With decreasing distance (few nm distance; point 3 in Figure 2.8) both local field intensities  $LFIEF(\omega_L)$  and  $LFIEF(\omega_S)$  start to increase. Since the Raman effect is defined by both (see equation 2.18) SERS is

progressively observed. On the other hand, although the LFIEF( $\omega_L$ ) leads to a fluorescence enhancement, the same is at the same time quenched due to growing influence of the condition  $\eta \ll 1$ . In total, the fluorescence is therefore partially quenched. For extremely small distances between the fluorophor and the metal surface ( $\approx 1$  nm; point 4 in Figure 2.8) the fluorescence is more efficiently quenched since non-radiative deactivation processes outweigh the radiative pathways. Consequently, at very small distances SERS predominates. Nevertheless, it has to be mentioned that for resonant excitation a remaining fluorescence may be detected which is called the SERS continuum whose origin is still controversially discussed<sup>[50]</sup>.

### Photobleaching

The term photobleaching summarizes several photochemical reactions resulting in irreversible damage of fluorophors and the related loss of their fluorescence capability<sup>[51]</sup>. A fluorophor is especially sensitive to photobleaching reactions within its long-lived triplet state  $T_1$  (see Figure 2.7), since the time frame for possible reactions is significantly prolonged in comparison to the  $S_1$  state (related lifetimes:  $S_1 \approx$  ns;  $T_1 \approx$  ms-s)<sup>[17,51]</sup>. As shown in Figure 2.7 the first excited triplet state is populated upon intersystem crossing (ISC) from the lowest vibrational level of the  $S_0$  state to an excited vibrational level of the  $T_1$  state<sup>[17]</sup>. Since this transition requires an inversion of the spin multiplicity, it is usually forbidden and only observed under sufficiently intense spin-orbit coupling<sup>[51]</sup>. Among other origins the probability of ISC is increased upon collisions with substances that can participate in an electron exchange mechanism (e.g.  $O_2$ )<sup>[51]</sup>.

The photobleaching quantum yield  $\Phi_{pb}$  quantifies the photostability of a fluorophor considering the photobleaching rate constant  $k_{pb}$  [ $s^{-1}$ ] divided by the sum of the rate constants for all possible deactivation processes ( $k_r, k_{nr}$  : rate constants for radiative and non-radiative processes [ $s^{-1}$ ])<sup>[52]</sup>.

$$\Phi_{pb} = \frac{k_{pb}}{k_r + k_{nr} + k_{pb}} \quad (2.24)$$

$\Phi_{pb}$  describes the probability of photobleaching per excitation cycle<sup>[51]</sup>. Regarding different chemical classes, carbocyanine and rhodamine derivatives are among the most photostable dyes with approximately  $2 \times 10^5$  (Cyanine 5 (Cy5)) or even more than  $10^6$  (Rhodamine 6G (R6G)) possible excitation cycles before photobleaching occurs<sup>[51]</sup>.

By analogy to equation 2.24 the radiative quantum yield  $\Phi_r$  is obtained (equation 2.25) and the resulting number of emitted photons  $n_{ph}$  per excitation cycle is given by equation 2.26<sup>[52]</sup>.

$$\Phi_r = \frac{k_r}{k_r + k_{nr} + k_{pb}} \quad (2.25)$$

$$n_{ph} = \frac{\Phi_r}{\Phi_{pb}} = \frac{k_r}{k_{pb}} \quad (2.26)$$

In order to increase the number  $n_{ph}$  of emitted photons per excitation cycle, several strategies to decrease  $k_{pb}$  or to increase  $k_r$  have been developed. In this context, chemical strategies such as triplet quenchers (e.g. mercaptoethylamine (MEA)<sup>[53]</sup>) and oxygen scavengers<sup>[54]</sup> including Reducing and Oxidizing Systems (ROXS)<sup>[55]</sup>, mainly aim at the decrease of  $k_{pb}$ , whereas physical approaches (e.g. exploiting the PURCELL effect<sup>[56]</sup> in order to increase the photonic mode density) point at the increase of  $k_r$ .

It has also been demonstrated that coupling of a single dye to a AuNP in the near field (8.5 nm distance from the AuNP surface) increases the number  $n_{ph}$  of emitted photons before photobleaching<sup>[52]</sup>. Hereby,  $n_{ph}$  was found to scale with the size of the AuNP from 20 nm to 80 nm.

### 2.3.4. Single-molecule-SERS (sm-SERS)

The detection of a single molecule (sm) is subject of extensive research since versatile information can be uncovered that is not accessible in ensemble measurements<sup>[46]</sup>. In contrast to sm-fluorescence experiments, sm-SERS measurements can provide extensive information about vibrational modes and thus about the chemical fingerprint of a molecule.

Based on the previous considerations it is obvious that the detection of a single molecule within a SERS experiment is especially challenging since two fundamental requirements have to be fulfilled:

- As shown in sections 2.2.2 and 2.3.1 the SERS substrate has to provide a hot spot with a sufficiently high EF to render single molecule detection possible (see equation 2.22).
- Since the EF rapidly drops within a few nm, the relevant analyte molecule has to be placed in the hot spot with high accuracy.

With the pioneering reports about sm-SERS in 1997<sup>[6,7]</sup>, different approaches have been developed that are briefly discussed with regard to their limitations.

#### Ultralow concentration approach

In 1997, the KNEIPP group<sup>[7]</sup> and the NIE group<sup>[6]</sup> independently reported the first detection of single molecules via SERS using an ultralow concentration approach. This approach is based on using aqueous colloidal solutions consisting of metal particles together with an ultralow analyte concentration. Additionally, the scattering volume is chosen to be small enough to contain on average one single analyte molecule per SERS measurement.

However, this approach does not consider that the detected signals only arise from a small fraction of molecules that are located within a hot spot<sup>[22]</sup>. The resulting sparse statistics were subject of long-lasting discussions regarding the evidence of real single molecule events<sup>[22]</sup>.

#### Bi-analyte approach

The bi-analyte SERS technique (BiASERS) is a statistical approach which was introduced in 2006 by LE RU *et al.*<sup>[8]</sup>. Basically, two distinguishable SERS analyte molecules are used in concentrations approximately 100 times larger than in the ultralow-concentration approach. Ultimately, increased concentrations are used in order to improve the reliability of the resulting statistics. From a bi-analyte experiment four different types of SERS spectra are detected originating from: (1) only analyte 1; (2) only analyte 2; (3) a mixture of both analytes; (4) none of the analytes<sup>[8,46]</sup>. By studying the relative intensities of both analytes statistically using a principle component analysis, single-molecule events can be identified in the background of other signals<sup>[22]</sup>. Furthermore, by normalizing the data to a reference the EF can be obtained<sup>[45]</sup>.

The bi-analyte approach was further improved by using isotopically substituted analytes<sup>[57–59]</sup>. In this way, analytes with the same surface chemistries can be probed and still distinguished by their different Raman signals.

#### Nanoengineered self-assembly

Although SERS from single molecules has been demonstrated in various applications, the two previous approaches mainly suffer from uncontrolled formation of hot spots and unknown concentration of analyte molecules within the enhancing sites. With increasing progress in the field of nanoscience, new approaches have been developed in order to generate hot spots by

controlled arrangement of metal NPs. In this process, especially the formation of NP dimers has been subject of extensive research. Therefore, bifunctional linkers as well as linkers with selective recognition ability have been studied<sup>[60]</sup>. As non-biological linkers mainly dithiol-<sup>[61-63]</sup> and diamine-functionalized<sup>[9]</sup> molecules have been investigated. Furthermore, biological linkers such as antibodies and antigens, proteins and DNA strands have been used to connect metal NPs.

Based on this approach two studies aimed at the detection of a single molecule via SERS. On the one hand, VLČKOVÁ *et al.* linked two 100 nm AgNPs using on average one molecule of 4-4'-diaminoazobenzene<sup>[9]</sup>. On the other hand, LIM *et al.* developed heterodimers of Au-Ag-core-shell nanodumbbells (GSND) linked by DNA hybridization between two single-stranded DNA (ssDNA) coating strands modified with one Cy3 molecule<sup>[10]</sup>. However, the main drawback of both examples is the lack of universal application. Since the analyte molecule is incorporated within the linker molecule a subsequent functionalization in order to detect a wide range of different analytes is excluded.

## 2.4. DNA nanotechnology

### 2.4.1. Deoxyribonucleic acid (DNA)

Already in 1869 MIESCHER identified and isolated deoxyribonucleic acid (DNA) using leucocytes from pus<sup>[64]</sup>. However, the first strong indication of DNA being the carrier of the genetic information was found only years later in 1944 by AVERY<sup>[65]</sup>. Going on from this, in 1953 WATSON and CRICK identified the characteristic double helix structure of DNA as well as the underlying construction principle, which is based on specific base pairing between the involved nucleobases<sup>[66]</sup>.

Basically, DNA is a polymer consisting of several monomeric nucleotides (nt) each including three covalently linked building blocks: (1) an aromatic nucleobase, (2) the five-carbon sugar deoxyribose and (3) a phosphate group<sup>[67]</sup>. The deoxyribose unit and the nucleobase are connected via the 1'-carbon atom of the sugar<sup>[68]</sup>. At the same time, sugars of adjacent nucleotides form a 5'→3'-phosphodiester bond between the 5'-carbon atom of the first nucleotide and the 3'-carbon atom of the second nucleotide<sup>[69]</sup>. This results in the characteristic polymeric structure of ssDNA with a negatively charged backbone and a 5'- and 3'-end (Figure 2.9 a). The involved nucleobases are classified in purine bases (adenine (A) and guanine (G)) and pyrimidine bases (thymine (T) and cytosine (C)) according to their basic chemical structure<sup>[68]</sup>. Among the four bases, two complementary pairs (A-T and G-C) exist, which can specifically bind via hydrogen bonds (Figure 2.9 b).

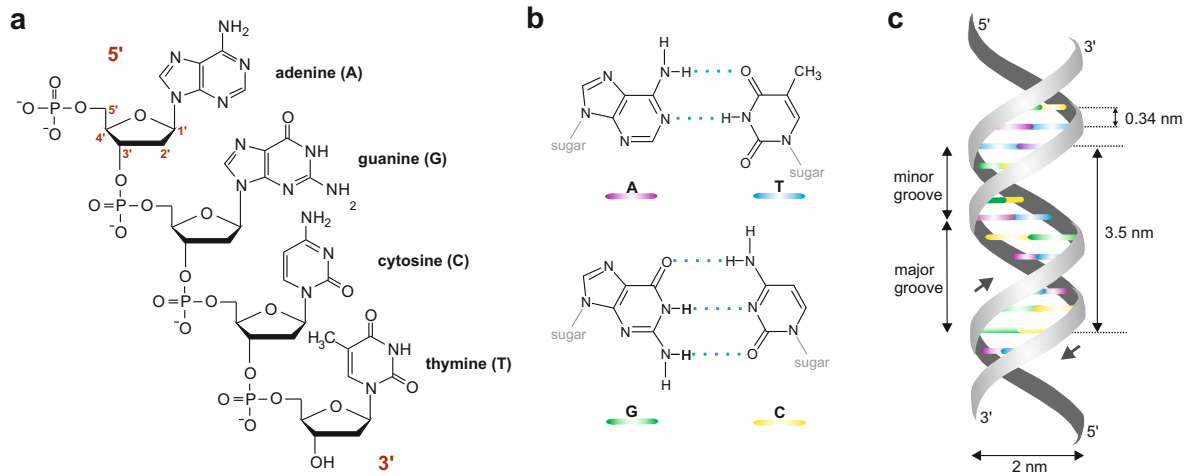
Furthermore, double-stranded DNA (dsDNA) is formed via hybridization between two single DNA strands while meeting the requirements of complementary base pairing. The two hybridizing strands are antiparallel, that is, their 3'- and 5'-ends are opposed to each other<sup>[69]</sup>. As a result, a double helix strand is obtained, which is roughly 2 nm in width with a helical periodicity of 10.5 nucleobases or 3.5 nm for a full turn<sup>[70]</sup> (Figure 2.9 c). Moreover, the antisymmetric nature of a double helix is characterized by so-called minor and major grooves with sizes of 7.5 Å and 8.5 Å, respectively<sup>[69]</sup>.

Although the specificity of DNA hybridization is provided by hydrogen bonds, the stability of a DNA double helix is mainly determined by  $\pi$ - $\pi$  stacking interactions between adjacent base pairs, with G-C pairs yielding higher stabilization free energy than A-T pairs<sup>[68,71]</sup>. Upon DNA hybridization the rigidity is significantly increased which is reflected in persistence lengths of approximately 1 nm for ssDNA and approximately 50 nm for dsDNA<sup>[70]</sup>.

It has to be mentioned that the previous details are valid for the canonical DNA structure



(B-type conformation, right-handed) which is the most frequently occurring in nature<sup>[68]</sup>. Furthermore, DNA can exist in A-type and Z-type conformations, G-quadruplexes or i-motifs<sup>[68]</sup>.



**Figure 2.9.: Building blocks of DNA and DNA double helix.** (a) Structural formula of the four existing nucleotides within a DNA strand. Each nucleotide consists of a phosphate group, the sugar deoxyribose and one out of four nucleobases (adenine (A), guanine (G), cytosine (C), thymine (T)). Several nucleotides are connected via phosphodiester bonds resulting in a DNA single strand with a negatively charged backbone. (b) Specific base pairing between complementary bases including two (A–T) or three (G–C) hydrogen bonds (blue dotted lines). (c) DNA double helix and related dimensions.

### 2.4.2. DNA as building block for materials

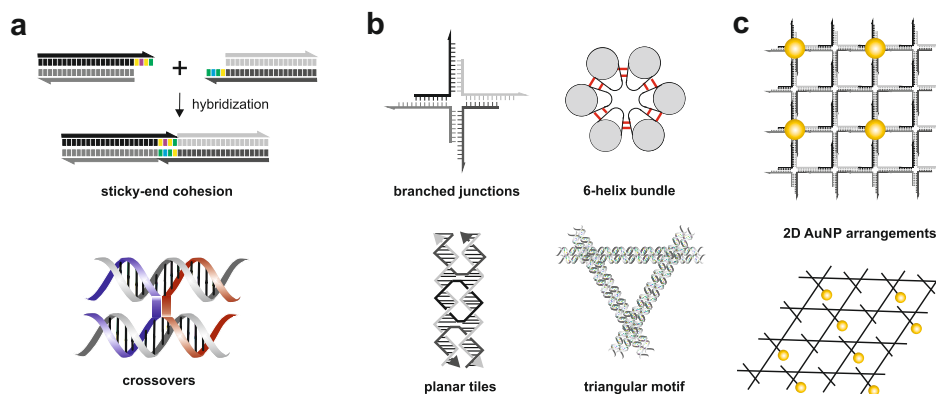
Using DNA as building block for materials is a classical bottom-up approach. The necessary foundation for DNA nanotechnology was laid in the early 1980s with the development of a phosphoramidite-based methodology by CARUTHERS allowing for the synthesis of artificial DNA sequences<sup>[72]</sup>. At the same time SEEMAN came up with the idea of using DNA constructs in order to facilitate protein crystallography<sup>[73]</sup>. For several years versatile artificial structures have been created using the tile-based approach introduced by SEEMAN<sup>[73]</sup>. However, with the groundbreaking development of the DNA origami technique in 2006<sup>[11]</sup>, the field of DNA nanotechnology was rapidly guided in a new direction.

#### Tile-based DNA nanotechnology

Basically, the tile-based approach to DNA nanotechnology relies on creating small DNA structures (so-called *tiles*) and connecting them in order to fabricate 3D structures or 2D lattices. To this end, two fundamental construction principles are applied (Figure 2.10 a):

- **Sticky-end cohesion:** Sticky-end cohesion is a concept originally applied in the field of genetic engineering<sup>[74]</sup>. It was then adopted for DNA nanotechnology in order to realize end-to-end connections between DNA double helices (Figure 2.10 a, top). On this occasion, each attending double helix consists of two DNA single strands with different lengths, which leads to an overhang of unpaired nucleotides. Upon hybridization between the two complementary sticky-ends the double helices are connected<sup>[75]</sup>.
- **Crossover junctions:** Crossovers are used in order to link double helices side-by-side (Figure 2.10 a, bottom). This type of junction is introduced by reciprocal exchange

between two double helices, that is, one single strand leaves its initial helix (Figure 2.10 a, blue strand) and crosses over to the adjacent second helix<sup>[76]</sup>. The same applies for a single strand from the second helix (Figure 2.10 a, red strand). Depending on their relative polarities (direction of 3'- and 5'-end) of the two helices different crossovers are obtained<sup>[76]</sup>. Furthermore, the spacing between successive crossover junctions determines the gap between parallel helices and thus the rigidity of the whole construct (see section “DNA origami” for further details)<sup>[11]</sup>.



**Figure 2.10.: Tile-based DNA nanotechnology.** (a) Sticky-end cohesion and crossover junctions are the underlying construction principles used in the tile-based approach. (b) Differently shaped types of tiles: branched junctions, 6-helix bundles, planar tiles as well as triangular motifs. (c) Nanoarrays based on tiles in order to obtain 2D arrangements of AuNPs. (Figure “planar tiles” adapted and modified from ref.<sup>[75]</sup>; Figures in c based on ref.<sup>[77,78]</sup>.)

Based on the previously mentioned construction principles versatile DNA-tiles are obtained which can be categorized in three classes<sup>[79]</sup> (see Figure 2.10 b for schematic illustration):

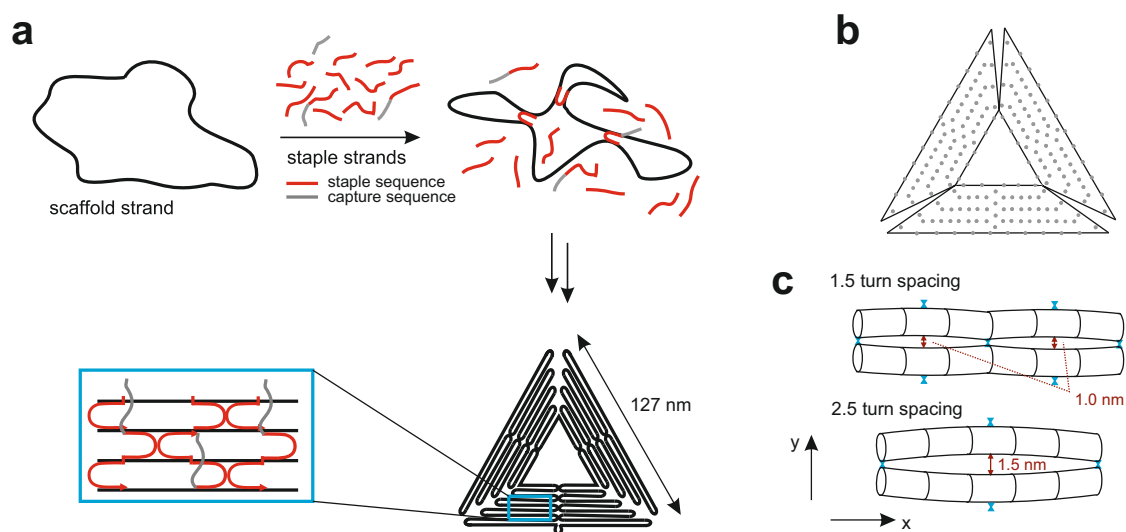
- **Branched junctions:** This type of DNA-tile was initially introduced by SEEMAN in his pioneering work about artificially constructed molecular structures using four-arm branched junctions as an analogue to naturally occurring HOLLIDAY junctions<sup>[73]</sup>. Basically, this type of tile is based on several DNA arms (e.g. 3-arms, 4-arms, 8-arms, 12-arms) all meeting at one central point<sup>[76]</sup>.
- **Planar tiles:** Planar tiles are constructed by merging several parallel double helices via crossover junctions. The resulting rigidity can be tuned by the number of introduced crossovers, resulting in versatile tiles such as double-crossover motifs (DX), three-domain motifs (TX) or paranemic crossover motifs<sup>[76]</sup>. A special case is the 3D-DX triangle motif based on three DX motifs connected in an over-and-under pattern of each edge<sup>[80]</sup>.
- **6-helix bundles:** 6-helix bundles also originate from the connection of double helices by means of crossovers. However, the positions of the introduced multiple crossover junctions are chosen to result in non-coplanar arrangements<sup>[81]</sup>.

Ultimately, several small DNA tiles can be connected to each other in order to obtain larger constructs such as 2D lattices or 3D structures. In this way, versatile hollow structures such as cubes<sup>[82]</sup>, tetrahedrons, dodecahedrons and “bucky balls”<sup>[83]</sup> as well as 2D<sup>[84,85]</sup> and 3D<sup>[86]</sup> DNA crystals have been realized. Furthermore, lattices have been shown to be suitable for the arrangement of proteins<sup>[87,88]</sup> or AuNPs<sup>[77,78]</sup>. Two exemplary nanoarrays of AuNPs are shown in Figure 2.10 c.

Although versatile DNA structures have been realized by using the tile-based approach, the design of complex structures is challenging for several reasons. On the one hand, to obtain stable DNA branched junctions a minimum of DNA sequence symmetry within the involved arms is required<sup>[76]</sup>. Otherwise the resulting structure might undergo misfoldings or branch migration with the latter one causing the instability of the naturally occurring HOLLIDAY junction<sup>[68]</sup>. On the other hand, the size of the resulting structures depends strongly on the used stoichiometry since arrays of DNA tiles are extended as long as sticky-ends exist<sup>[89]</sup>. Therefore, tile-based DNA nanotechnology is more suitable for the design of small and simple structures.

### DNA origami

Before 2006 some foreshadowing work has been reported already guiding in the direction of DNA origami. First, the word “RNA origami” was already mentioned in 1994 by WILLIAMSON in the context of 3D structures<sup>[90]</sup>. Additionally, the first scaffold assembly was used in DNA-based computing by LABEAN *et al.*<sup>[91]</sup>. A year later, YAN *et al.* synthesized the first barcode-patterned nanoarrays by using a scaffold strand and shorter strands but without any control over size and shape<sup>[92]</sup>. Finally, SHIH *et al.* successfully folded a 1.7 kb ssDNA into an octahedron which is often referred to as the first example of a 3D DNA origami structure<sup>[93]</sup>. In 2006 ROTHEMUND presented the revolutionary DNA origami strategy to overcome the drawbacks associated with the tile-based method<sup>[11]</sup>. The basic principle of this technique is exemplarily presented for a DNA origami triangle in Figure 2.11 a.



**Figure 2.11.: DNA origami technique.** (a) A 7249 nt-long circular scaffold strand (black strand) is folded into a triangular shape by adding 208 short staple strands (red strands). By extending the sequence of a staple strand, capture sequences (grey parts of red strands) for subsequent functionalization of the DNA origami template can be introduced. (b) Resulting pegboard with about 200 individually addressable anchor points (grey dots). (c) Packing density of parallel double helices (white cylinders) in dependence of the spacing between successive crossover junctions (labelled in blue). (Figure c adapted and modified from ref.<sup>[11]</sup>.)

In ROTHEMUND’s approach one circular 7249 nt-long ssDNA strand serves as scaffold (Figure 2.11 a, black strand) which can be folded into desired shapes and patterns by adding a set of approximately 200 suitable short ssDNA staple strands (approximately 32 nt, Figure 2.11 a, red strands). Since every single staple strand is complementary to exactly two domains within the scaffold, the circular strand is progressively folded into the desired shape. Depend-

ing on the sequences of the staple strands differently shaped nanostructures of approximately 100 nm in size can be created (in his original publication ROTHEMUND presented rectangles, squares, stars, triangles with sharp edges, triangles with rectangular domains as well as smiley faces<sup>[11]</sup>).

By extending a staple strand either at its 3'-end or its 5'-end by additional nucleotides a ssDNA sequence is introduced which remains unpaired upon DNA hybridization and thus can act as capture strand for functional units (Figure 2.11 a, grey parts). Since every staple strand can be modified individually, the resulting DNA origami template ultimately represents a pegboard with more than 200 addressable pixels (Figure 2.11 b). In this way, versatile entities such as AuNPs<sup>[94]</sup>, telomeric DNA<sup>[95]</sup> or fluorophors<sup>[96]</sup> can be placed on the DNA origami template at predefined positions.

It has to be mentioned that parallel double helices are not necessarily closely packed due to electrostatic repulsion between their negatively charged phosphate backbones<sup>[11]</sup>. In order to screen the negative charges a sufficiently high amount of positive counter ions (in most cases  $Mg^{2+}$ ) is added within the folding process<sup>[11]</sup>. However, a remaining repulsion leads to a small gap between adjacent helices whose size is defined by the spacing between crossover junctions and the distance to the crossovers (Figure 2.11 c). For crossovers separated by 1.5 turns (usually used) a gap of up to approximately 1 nm arises, which is enlarged to 1.5 nm in the case of 2.5 turn spacing<sup>[11]</sup>. Thus, the minimum distance between functional entities bound to a DNA origami substrate is determined by (i) the distance between two helices (in y-direction) and (ii) the distance between adjacent base pairs (3.5 nm for a full turn; in x-direction). It has to be mentioned that the distances are slightly smaller under dry conditions.

In order to obtain an arbitrary DNA origami shape, ROTHEMUND described several steps that are necessary<sup>[11]</sup>. First, the shape of the desired structures is drawn with the corresponding dimensions. This shape is then filled with parallel cylinders with diameters equal to the diameter of a DNA double helix and with lengths being an integral multiple of helical full turns. In order to establish planarity, crossover junctions between adjacent helices are introduced at 1.5 turn spacing. Second, a scaffold strand is folded in the raster passing every single cylinder. With this step, further crossover junctions (scaffold crossovers) are introduced. Third, a computer program creates a set of suitable short staple strands and defines periodic crossover junctions (1.5 turn spacing). In the last two steps the program calculates the twist of the scaffold and reduces the strain by optimizing the positions of scaffold crossovers. Furthermore, where possible, adjacent staple strands are fused together to reduce the total number of staples.

A lot of efforts have been made regarding the formation of three-dimensional structures consisting of DNA, since they are highly promising in the fields of drug delivery, protein regulation, catalysis or biomolecule crystallography<sup>[79]</sup>. The first 3D structures obtained by ROTHEMUND's DNA origami technique were presented by DOUGLAS *et al.*<sup>[97]</sup>, followed by twisted and curved 3D structures<sup>[98]</sup> as well as hollow structures<sup>[99]</sup>. Basically, there are different strategies to obtain 3D structures. On the one hand, planar 2D DNA origami structures might be folded and connected at the edges in order to obtain prisms with different numbers of sides<sup>[100]</sup>, icosahedrons<sup>[97]</sup> or even a box with an controllable lid<sup>[101]</sup>. On the other hand, 3D structures can be obtained by folding a layer of parallel double helices by means of several crossover junctions resulting in rigid structures consisting of multiple DNA origami layers<sup>[97]</sup>. Curved 3D structures have been shown to be available by winding the scaffold strand in terms of concentric rings with different numbers of crossover junctions which allows for adjusting the circumference of each ring<sup>[99]</sup>.

The genome of the bacteriophage M13mp18 is by far the most frequently used scaffold for DNA origami related research, since it is well-studied and only exhibits a minimal secondary structure including a hairpin stem-loop of 73 nt<sup>[70]</sup>. However, several scaling-up strategies have been developed in order to obtain objects that are not limited by the length of the M13mp18 strand. One of the alternative routes to larger structures relies on connecting several individual DNA origami by means of sticky-end cohesion<sup>[102]</sup> or edge-to-edge base stacking<sup>[103]</sup>. In contrast, longer scaffold strands have been used such as a 26 kb ssDNA fragment obtained from long-range polymerase chain reaction (PCR) amplification<sup>[104]</sup> or a  $\lambda$ /M13 hybrid scaffold resulting in a 51 kbp DNA origami<sup>[105]</sup>. Moreover, DNA origami structures have been obtained from a dsDNA scaffold<sup>[106]</sup> as well as from a mini-scaffold (2404 bases)<sup>[107]</sup>.

Another interesting field is the development of dynamic DNA nanodevices and nanomachines in order to confer a certain function on DNA structures. Although small switchable devices have already been realized before DNA origami existed<sup>[108–110]</sup>, the advent of the DNA origami technique significantly facilitated the development of dynamic nanostructures. As a result, several reconfigurable systems have been developed such as a DNA Möbius strip<sup>[111]</sup>, DNA pliers that can open and close<sup>[112]</sup>, simple DNA origami templates that stepwise reconfigure into complex, quasifractal patterns<sup>[113]</sup> or even reconfigurable plasmonic systems<sup>[114]</sup>. Moreover, DNA origami substrates have been used to create predefined tracks that can be passed by DNA walkers covering distances of about 100 nm, e.g. a DNA spider with several legs<sup>[115]</sup>, a nanorobot collecting AuNPs as cargo on its way<sup>[116]</sup> or a ssDNA motor<sup>[117]</sup>. The long-term vision of developing “DNA walkers” is to mimic the movement of naturally occurring motor proteins<sup>[118]</sup>.

The growing complexity of DNA nanostructures requires further development of existing software programs. Besides basic software (e.g. GIDEON and SARSE) more sophisticated tools such as caDNAno<sup>[119]</sup> and canDo<sup>[120]</sup> have been evolved allowing for the design of 2D and 3D structures as well as for the prediction of properties such as flexibility and final shape.

### 2.4.3. Arrangement of AuNPs on DNA origami

#### Functionalization of AuNPs with DNA

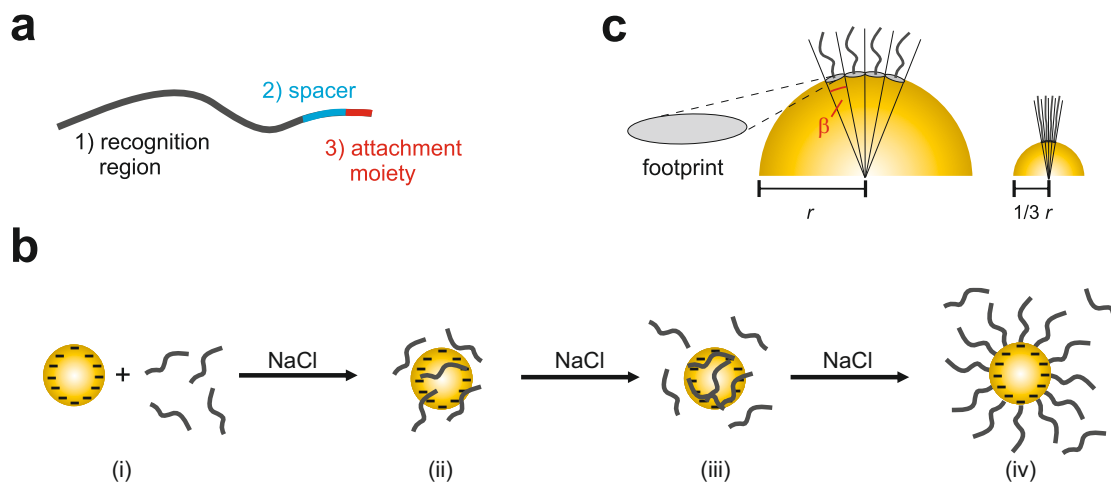
In 1996 the MIRKIN group and the ALIVISATOS group independently presented novel strategies in order to functionalize AuNPs by alkylthiol-modified DNA and to assemble them via DNA hybridization<sup>[121,122]</sup>. Since then these water-soluble conjugates attracted a lot of attention in various research fields<sup>[123]</sup>.

A few years later, the first assemblies of DNA-coated AuNPs on 2D DNA arrays have been reported by KIEHL and coworkers<sup>[124,125]</sup>. This concept was then extended to DNA origami substrates by DING *et al.* who assembled six different AuNPs on a triangular DNA origami within one row<sup>[94]</sup>.

Basically, the DNA coating strands consist of three different units: 1) an attachment moiety which is usually a propyl- or hexylthiol group, 2) a spacer region composed of nucleobases or synthetic groups such as polyethylene glycol (PEG) and 3) a recognition region which represents the active part for subsequent hybridization and consists of DNA or analogue polymers such as ribonucleic acid (RNA), locked nucleic acid (LNA) or peptide nucleic acid (PNA) (see Figure 2.12 a)<sup>[123]</sup>.

In principle, the DNA coating procedure relies on relatively strong Au-S interactions in comparison to Au-citrate interactions resulting in an exchange of citrate ions by thiol-modified

DNA strands<sup>[123]</sup>. Since both, the AuNP surface and the DNA strands are negatively charged the adsorption of DNA is hampered by long-range electrostatic repulsion which is characterized by a high salt-dependent Debye-length ( $\lambda_D$ )<sup>[126]</sup>. The adsorption can exclusively occur when the interactions between AuNP surface and DNA strands are dominated by short-range attraction which is related to a decrease of  $\lambda_D$ <sup>[126]</sup>. Practically, this is achieved either by adding salt (in most cases sodium chloride (NaCl)) or by reducing the pH<sup>[126,127]</sup>.



**Figure 2.12.: Functionalization of AuNPs with ssDNA.** (a) The three units of a DNA coating strand: a recognition area, a spacer region and an attachment moiety. (b) The DNA density is stepwise increased by the “salt aging” procedure. (c) Dependence of the surface coverage on the radius of curvature of the AuNP. For larger particle sizes with a radius  $r$  the deflection angle  $\beta$  between adsorbed DNA strands is increased resulting in larger footprints and thus in a lower surface coverage. (Figure b and c adapted and modified from ref.<sup>[127]</sup> and ref.<sup>[128]</sup>, respectively.)

In the case of salt addition the adsorption process is affected in three different ways<sup>[129]</sup>. First, the repulsion between AuNP surface and DNA strands is decreased resulting in faster adsorption. Second, the mutual repulsion between the several individual DNA strands is also reduced which leads to an increase of the final surface coverage. Third, the repulsion between different AuNPs is diminished with the result of increased aggregation tendency. In order to achieve a well-balanced compromise between the adsorption of DNA strands and the aggregation of AuNPs, a so-called “salt aging” procedure was established relying on the stepwise addition of salt to achieve a progressive increase of the DNA density at the AuNP surface (Figure 2.12 b)<sup>[130,131]</sup>. With every salt addition (from (i) to (iv)) the density of DNA and thus the stability of the AuNPs is slightly increased which is sufficient to stand the next addition of salt. It has to be mentioned that within the salt aging process the conformation of adsorbed DNA strands is changed from initially parallel ((ii) and (iii)) to successively upright (iv)<sup>[123]</sup> (Figure 2.12 b).

The standard salt aging procedure is practicable up to AuNP sizes of approximately 50 nm<sup>[127]</sup>. For larger particles one can evade to the low pH method introduced by ZHANG *et al.*<sup>[127]</sup>. Hereby, the reduced charge repulsion is achieved by protonating A and C bases as well as partially protonating the citrate units<sup>[127]</sup>.

Basically, the stability of the resulting DNA-capped AuNPs is defined by the DNA density which in turn is affected by the size and shape of the AuNPs, the chemical attachment moiety, the spacer sequence as well as the length of the DNA coating sequence<sup>[123]</sup>. Furthermore, it was shown, that high salt concentrations, low pH values as well as sonication and heating result in higher surface coverages<sup>[127,131,132]</sup>.

First of all, the surface coverage is influenced by the size of the AuNP. This is quantified in terms of a deflection angle  $\beta$  between adjacent DNA strands and the related footprint which is a measure of the average area occupied by a oligonucleotide<sup>[128]</sup> (Figure 2.12 c). Basically, with increasing AuNP size the radius of curvature is decreased resulting in larger deflection angles and more expanded footprints. As a result, the surface coverage is decreased with increasing AuNP size<sup>[128]</sup>.

Upon DNA adsorption exclusion areas at the AuNP surface are created that are no longer accessible for further DNA adsorption<sup>[126]</sup>. With increasing length of a DNA strand its flexibility is also increased which progressively enables hairpin coiling<sup>[133]</sup>. Thereby the hydrodynamic size as well as the electrostatic repulsion of a DNA strand is increased<sup>[126]</sup>. As a consequence, longer DNA strands cause larger exclusion areas at the AuNP surface.

Additionally, the spacer regions within the DNA strands significantly influence the stability of DNA-coated AuNPs. The four nucleobases reveal differently pronounced affinities to Au with T having the lowest and A the highest affinity<sup>[134]</sup>. Therefore, T-rich DNA sequences are more stretched on the AuNP surface in comparison to A-rich sequences. Thus T-rich DNA sequences are more densely packed leading to higher loading capacities<sup>[131]</sup>.

## 2.5. Graphene

In 2010 GEIM and NOVOSELOV were honoured with the Nobel Prize in Physics “for groundbreaking experiments regarding the two-dimensional material graphene”<sup>[135,136]</sup>. Graphene is a one-atom thick 2D material in which sp<sup>2</sup>-hybridized carbon atoms are arranged in a honeycomb lattice<sup>[137]</sup>. Initially, graphene was obtained by micromechanical cleavage of highly-oriented pyrolytic graphite (HOPG) using scotch tape<sup>[138]</sup>. Afterwards several other production methods such as chemical vapour deposition (CVD), graphene growth on silicon carbide (SiC), liquid-phase exfoliation and molecular beam epitaxy have been developed leading to graphene lattices that significantly differ in size and quality<sup>[139]</sup>. Since its discovery, graphene has attracted much interest in countless research fields due to the unique combination of its electronic, mechanical and optical properties.

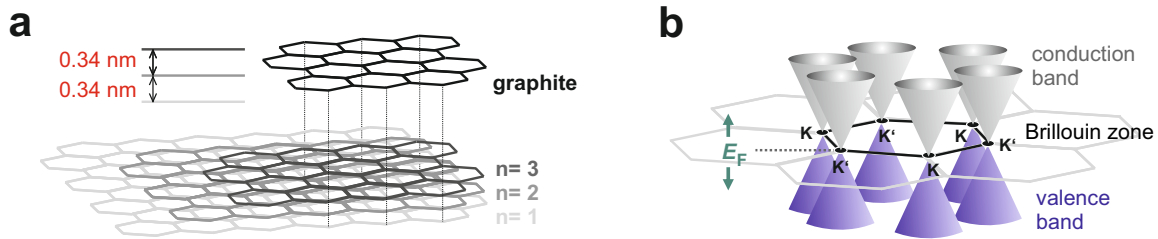
### 2.5.1. Electronic, optical and mechanical properties

Depending on the number  $n$  of layers graphene can exist in many different modifications, ranging from single-layer graphene (SLG,  $n = 1$ ) over bilayer graphene (BLG,  $n = 2$ ), trilayer graphene (TLG,  $n = 3$ ) and few-layer graphene (FLG,  $n > 3$ ) to graphite (Fig. 2.13 a). Thereby, adjacent layers are separated by 0.34 nm<sup>[137]</sup> and can be stacked congruently (AA stacking) or shifted to each other (AB stacking, ABC stacking)<sup>[140]</sup>. Within one layer the carbon atoms are connected by three in-plane  $\sigma$  bonds, whereas  $\pi$  orbitals perpendicular to the plane enable interactions between different layers<sup>[140]</sup>.

SLG exhibits a unique electronic structure which is characterized by a hexagonal BRILLOUIN zone with six conical DIRAC points (K and K' points) in which conduction and valence bands meet each other<sup>[140]</sup> (Figure 2.13 b). Consequently, SLG is a zero band gap semiconductor whose FERMI level  $E_F$  is located at the DIRAC point without an external field<sup>[137,140]</sup>. However, when a gate bias is applied,  $E_F$  is shifted above or below the DIRAC point, resulting in free carriers, that is,  $e^-$  for n-type doping and  $h^+$  for p-type doping, respectively<sup>[141]</sup> (indicated by the green arrows in Figure 2.13 b). The same effect of doping can be obtained by charged impurities, chemical functional groups or contact to a metal surface<sup>[142–144]</sup>.

For BLG the gapless band structure is changed to parabolic bands touching at the K and

$K'$  points<sup>[140]</sup>. With increasing number of layers the gapless structure is maintained and graphene becomes successively metallic<sup>[140]</sup>.



**Figure 2.13.: Graphene lattice and electronic band structure of SLG.** (a) AA stacking of several graphene layers resulting in SLG ( $n = 1$ ), BLG ( $n = 2$ ), TLG ( $n = 3$ ) up to graphite. (b) Electronic band structure in SLG represented by DIRAC cones (grey cones: conduction band; blue cones: valence band) which meet at the  $K$  and  $K'$  points of the hexagonal BRILLOUIN zone. In pristine graphene the FERMI level  $E_F$  is located at the  $K$  point.

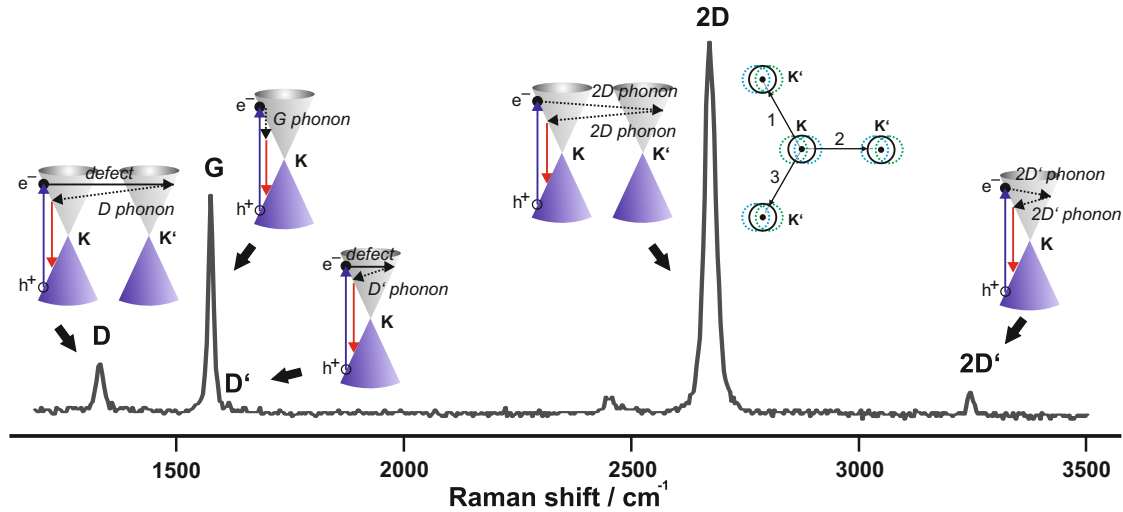
As a consequence of its inner framework and its electronic band structure graphene exhibits several outstanding properties making it currently to the most intensely studied material<sup>[143]</sup>. First, it is the strongest 2D material ever measured revealing a YOUNG'S modulus of 1 TPa and an intrinsic strength of 130 GPa<sup>[145]</sup>. Furthermore, graphene can reversibly stand tensile strain up to 25%<sup>[145]</sup>. Second, extreme high electron mobilities on the order of  $2 \times 10^5 \text{ cm}^2 \text{ V}^{-1} \text{ s}^{-1}$  have been measured in graphene<sup>[146]</sup>. Third, graphene shows an optical transmittance of 90% with an absorption of approximately 2.3% per layer<sup>[147,148]</sup>. Fourth, it reveals a very high thermal conductivity above  $3000 \text{ W K}^{-1}$ <sup>[149]</sup>. Last, graphene is completely impermeable to any kind of gases<sup>[150]</sup> and can be easily chemically functionalized<sup>[151,152]</sup>.

### 2.5.2. Raman scattering of graphene

Raman scattering is a very convenient method in order to study the electronic and structural properties of graphene. A Raman spectrum reveals versatile information about the number of graphene layers, the presence of defects and edges, the degree of doping and strain as well as chemical modifications<sup>[153,154]</sup>. The main features in a typical Raman spectrum of SLG, that is, the D, G,  $D'$ , 2D and  $2D'$  bands, are depicted in Figure 2.14.

All Raman features in Figure 2.14 originate from the same elementary events, that is, the absorption of a photon (blue arrows), emission of a second photon (red arrows) and scattering of an electron (black arrows). Although those events are depicted separately in Figure 2.14, all processes take place instantaneously. Basically, one can distinguish between first-order and second-order Raman scattering processes depending on the number of scattering events taking place<sup>[141]</sup>. Here, the involved electrons can be scattered in two different ways: (i) elastically by defects within the graphene lattice (horizontal black arrows in Figure 2.14) and (ii) inelastically by interactions with phonons<sup>[141]</sup> (black dashed arrows in Figure 2.14). The G band at approximately  $1580 \text{ cm}^{-1}$  is the only feature arising from a first-order scattering process including only one doubly degenerate phonon mode<sup>[141]</sup>. The D band at  $1339 \text{ cm}^{-1}$  and the  $D'$  band at  $1620 \text{ cm}^{-1}$  on the other hand are second-order Raman scattering processes in which the electron is scattered twice: elastically by a defect and inelastically by a phonon<sup>[141]</sup>. Therefore, both bands require the presence of a defect and are thus indicators for disorder within the lattice. The main difference between both features is that the D band originates from a scattering process between two adjacent DIRAC cones (= intervalley process), whereas for the  $D'$  band the electron is scattered within one DIRAC cone (= intravalley process)<sup>[157,158]</sup>.





**Figure 2.14.:** Scattering processes and resulting Raman bands in SLG. A typical Raman spectrum of SLG is shown with the most characteristic Raman peaks (D, G, D', 2D and 2D' bands). The involved processes for each individual band are illustrated, including absorption of a photon (blue arrows), emission of a second photon (red arrows), elastic scattering of an electron by a defect (horizontal black arrows) and inelastic scattering of an electron by a phonon (black dashed arrows). Additionally, in the case of the 2D band, the three possible scattering paths with the nearest neighbours of a DIRAC cone are depicted, illustrating the strain induced splitting of the 2D band. (Figure based on ref. [141,155,156].)

Furthermore, the two overtones of the D and the D' bands, termed 2D and 2D' bands, are detected at approximately  $2671 \text{ cm}^{-1}$  and  $3245 \text{ cm}^{-1}$ , respectively. Since both overtones involve two phonons with opposite wave vectors giving rise to momentum conservation, no defects are required for their activation [155]. Again, 2D and 2D' bands differ in terms of their underlying intervalley and intravalley nature.

As depicted in Figure 2.14, the 2D band stems from an interaction between two DIRAC cones at point K and K', respectively. In principle, all three adjacent DIRAC cones (at point K') are potential scattering partners giving rise to three possible scattering paths (1, 2 or 3 in the top view next to the 2D band in Figure 2.14) [156]. If uniaxial strain is applied to the graphene lattice the BRILLOUIN zone is deformed resulting in displacements of the DIRAC cones relative to their original positions (the blue and green circles represent the displaced cones in zigzag and armchair samples) [156]. These perturbations within the scattering paths are directly reflected in a theoretically predicted splitting of the 2D band in three components. However, the third peak appears only weakly [156].



# 3

## Materials and methods

### 3.1. List of chemicals and DNA strands

The used chemicals and modified DNA strands are summarized in Tables 3.1 and 3.2. For a complete list of all non-modified staple strands see Table A.1 in the Appendix.

**Table 3.1.:** List of chemicals.

substance	source of supply	purity
acetone	Sigma-Aldrich <sup>1</sup>	≥ 99.5%
Bis( <i>p</i> -sulfonatophenyl)phenylphosphine (BSPP) dehydrate dipotassium salt	Sigma-Aldrich <sup>1</sup>	97.0%
DL-dithiothreitol (DTT)	Sigma-Aldrich <sup>1</sup>	≥ 98.0%
ethanol (EtOH)	Sigma-Aldrich <sup>1</sup>	≥ 99.8%
gold nanoparticles (AuNPs) (citrate stabilized)	BBI solutions <sup>3</sup>	-
HQ silver enhancement kit	Nanoprobes <sup>2</sup>	-
LI silver enhancement kit	Nanoprobes <sup>2</sup>	-
magnesium chloride (MgCl <sub>2</sub> )	Sigma-Aldrich <sup>1</sup>	≥ 98.0%
methanol (MeOH)	ROTH <sup>4</sup>	≥ 99.5%
methyl isobutyl ketone (MIBK)	Sigma-Adrich <sup>1</sup>	≥ 98.5%
2-propanol	Sigma-Aldrich <sup>1</sup>	≥ 99.5%
sodium chloride (NaCl)	Sigma-Aldrich <sup>1</sup>	-
sodium dodecyl sulfate (SDS)	Sigma-Aldrich <sup>1</sup>	≥ 98.5%
Tris-acetate-EDTA (TAE) buffer	Sigma-Aldrich <sup>1</sup>	-

<sup>1</sup> Sigma-Aldrich Chemie GmbH, Steinheim, Germany

<sup>2</sup> Nanoprobes, Inc., New York, USA

<sup>3</sup> BBI solutions, Cardiff, UK

<sup>4</sup> Carl Roth GmbH & Co. KG, Karlsruhe, Germany

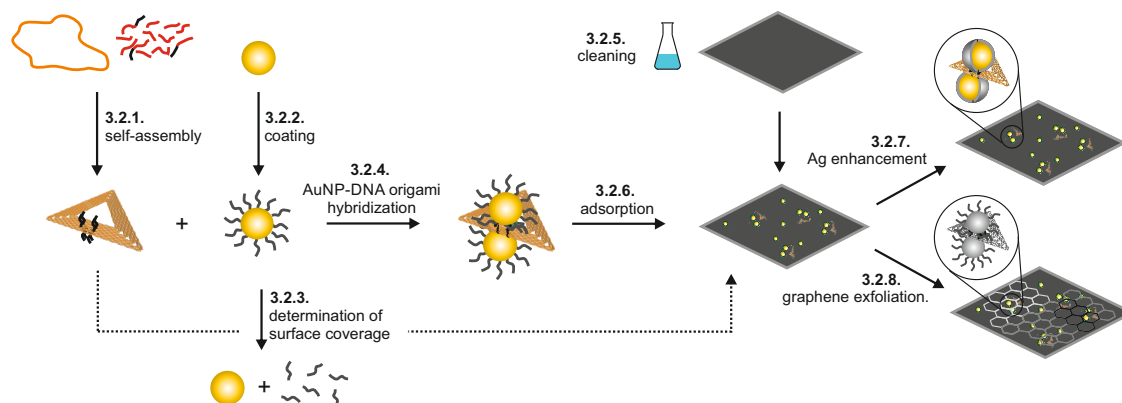
**Table 3.2.:** List of DNA strands.<sup>1</sup>

DNA sequence (5' → 3')	source of supply	purity
scaffold strand		
M13mp18 (supplied in 10 mM Tris-HCl (pH 8.0 @ 25°C), 1 mM EDTA)	New England Biolabs <sup>2</sup>	-
staple strands		
non-modified staple strands (see Table A.1)	IDT <sup>3</sup>	desalted
└ (t-6s7f) -(AAT) <sub>8</sub> T <sub>4</sub>	metabion <sup>4</sup>	HPLC
└ (t-5s6e) -(AAT) <sub>8</sub> T <sub>4</sub>	metabion <sup>4</sup>	HPLC
└ (t-4s7f) -(AAT) <sub>8</sub> T <sub>4</sub>	metabion <sup>4</sup>	HPLC
└ (t-1s6i) -(AAT) <sub>8</sub> T <sub>4</sub>	metabion <sup>4</sup>	HPLC
└ (t1s6i) -(AAT) <sub>8</sub> T <sub>4</sub>	metabion <sup>4</sup>	HPLC
└ (t1s8i) -(AAT) <sub>8</sub> T <sub>4</sub>	metabion <sup>4</sup>	HPLC
└ (t1s6i) -(AAA) <sub>8</sub> T <sub>4</sub>	metabion <sup>4</sup>	HPLC
└ (t1s8i) -(AAA) <sub>8</sub> T <sub>4</sub>	metabion <sup>4</sup>	HPLC
└ (t2s5f) -(AAA) <sub>8</sub> T <sub>4</sub>	metabion <sup>4</sup>	HPLC
└ (t2s7f) -(AAA) <sub>8</sub> T <sub>4</sub>	metabion <sup>4</sup>	HPLC
└ (t5s6e) -(AAA) <sub>8</sub> T <sub>4</sub>	metabion <sup>4</sup>	HPLC
└ (t5s8g) -(AAA) <sub>8</sub> T <sub>4</sub>	metabion <sup>4</sup>	HPLC
└ (t7s8g) -(AAA) <sub>8</sub> T <sub>4</sub>	metabion <sup>4</sup>	HPLC
└ (t-1s6e) -(AAA) <sub>8</sub> T <sub>4</sub>	metabion <sup>4</sup>	HPLC
└ (t-1s8g) -(AAA) <sub>8</sub> T <sub>4</sub>	metabion <sup>4</sup>	HPLC
└ (t-2s5f) -(AAA) <sub>8</sub> T <sub>4</sub>	metabion <sup>4</sup>	HPLC
└ (t-2s7f) -(AAA) <sub>8</sub> T <sub>4</sub>	metabion <sup>4</sup>	HPLC
└ (t-3s6e) -(AAA) <sub>8</sub> T <sub>4</sub>	metabion <sup>4</sup>	HPLC
└ (t-3s8g) -(AAA) <sub>8</sub> T <sub>4</sub>	metabion <sup>4</sup>	HPLC
└ (t-5s8g) -(AAA) <sub>8</sub> T <sub>4</sub>	metabion <sup>4</sup>	HPLC
<b>TAMRA</b> -(t-3s6e)┐	metabion <sup>4</sup>	HPLC
<b>TAMRA</b> -(t-2s7f)┐	metabion <sup>4</sup>	HPLC
<b>TAMRA</b> -(t-1s6e)┐	metabion <sup>4</sup>	HPLC
└ (t1s6i) - <b>TAMRA</b>	metabion <sup>4</sup>	HPLC
<b>Cy3</b> -(t-1s6i)┐	metabion <sup>4</sup>	HPLC
AuNP coating strands		
(ATT) <sub>3</sub> T <sub>4</sub> -SH	metabion <sup>4</sup>	HPLC
(ATT) <sub>8</sub> T <sub>4</sub> -SH	metabion <sup>4</sup>	HPLC
(TTT) <sub>4</sub> T-SH	metabion <sup>4</sup>	HPLC
(ATT) <sub>8</sub> T <sub>3</sub> ( <b>TAMRA</b> )-SH	metabion <sup>4</sup>	HPLC
(TTT) <sub>4</sub> T( <b>Cy3</b> )-SH	metabion <sup>4</sup>	HPLC
(TTT) <sub>4</sub> T( <b>TAMRA</b> )-SH	metabion <sup>4</sup>	HPLC
( <b>TAMRA</b> )-(TTT) <sub>4</sub> T-SH	metabion <sup>4</sup>	HPLC

<sup>1</sup> └ and ┐ represent the anchor points to the DNA origami triangle<sup>2</sup> New England Biolabs GmbH, Frankfurt am Main, Germany<sup>3</sup> IDT Integrated DNA Technologies, Leuven, Belgium<sup>4</sup> metabion, Steinkirchen, Germany

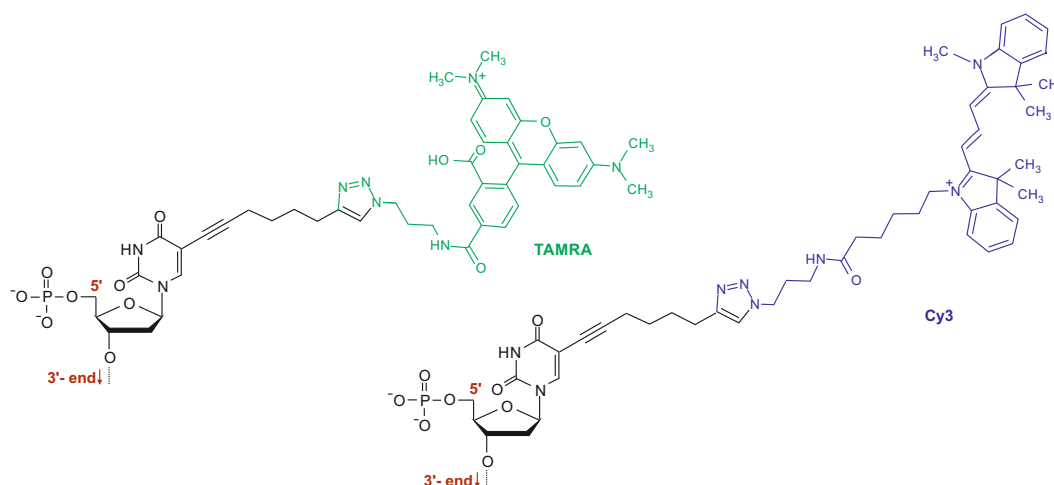
## 3.2. Sample preparation

All steps of the sample preparation are illustrated in Figure 3.1.



**Figure 3.1.: General overview of sample preparation steps.** For each step the corresponding section for detailed information is stated. The dashed arrow indicates the alternative DNA hybridization route at the surface of a silicon (Si) wafer (see section 3.2.4).

As Raman reporter molecules the well-established dyes carboxytetramethylrhodamine (TAMRA) and cyanine 3 (Cy3) were used. In Figure 3.2 the molecular structures are shown as well as the positions of covalent connection to ssDNA.



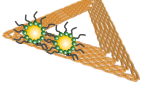
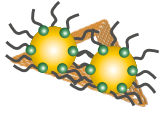
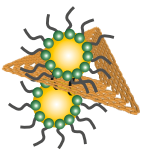
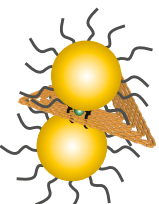
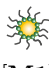
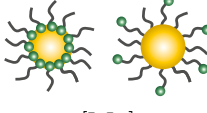
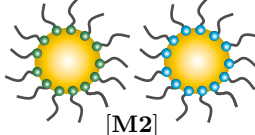
**Figure 3.2.: Molecular structures of Raman reporter molecules.** TAMRA and Cy3 are covalently attached to an alkyne-terminated DNA base. The dye functionalities have been introduced by the manufacturer (metabion) via click chemistry using C8-alkyne-dU and a dye-azide (TAMRA-azide (green) or Cy3-azide (blue)) as precursors (see Figure A.1 in the Appendix for molecular structures of the precursors).

### 3.2.1. Synthesis of DNA origami substrates

The triangular DNA origami substrates are based on the original design published by ROTHEMUND<sup>[11]</sup> (see Figure 3.3). Basically, the scaffold strand and staple strands were mixed in a molar ratio of 1:30 by adding 5  $\mu\text{L}$  of the genome of bacteriophage M13mp18 ( $c_{\text{initial}} = 250 \mu\text{g mL}^{-1}$ ;  $c_{\text{final}} = 5 \text{ nM}$ , New England Biolabs) to 40  $\mu\text{L}$  of a staple strand solution



**Table 3.3.: Overview of DNA origami designs.** All investigated systems are shown together with the related manuscript (**M1**, **M2** or **M4**). The braces include capture sequences binding the same AuNP.

Design [Manuscript]	Origami captures	dye(s)	diameter	AuNPs coating	gap
 [M1]	5'-(AAT) <sub>8</sub> T <sub>4</sub> -3' { t-5s6e t-6s7f t-4s7f t-1s6i t1s6i t1s8i	-	15 nm	5'-(ATT) <sub>8</sub> T <sub>3</sub> X-SH-3' <b>X = TAMRA</b>	≈ 10 nm <sup>1</sup>
 [M2]	5'-(AAA) <sub>8</sub> T <sub>4</sub> -3' { t-3s6e t-3s8g t-5s8g t5s6e t5s8g t7s8g	-	40 nm	5'-(TTT) <sub>4</sub> TX-SH-3' / 5'-(TTT) <sub>4</sub> T-SH-3' <b>X = TAMRA</b>	≈ 14 nm <sup>1</sup>
 [M4]	5'-(AAA) <sub>8</sub> T <sub>4</sub> -3' { t-1s6e t1s6i t-1s8g t1s8i t-2s5f t-2s7f t2s5f t2s7f	-	40 nm	5'-(TTT) <sub>4</sub> TX-SH-3' <b>X = TAMRA</b>	≈ 7 nm <sup>2</sup>
 [M2]	5'-(AAA) <sub>8</sub> T <sub>4</sub> -3' { t-1s6e t1s6i t-1s8g t1s8i t-2s5f t-2s7f t2s5f t2s7f	<b>TAMRA</b> t1s6i (3')  or <b>Cy3</b> t-1s6i (5')	60 nm	5'-(TTT) <sub>4</sub> T-SH-3'	≈ 7 nm <sup>2</sup>
 [M1]	-	-	15 nm	5'-(ATT) <sub>8</sub> T <sub>3</sub> X-SH-3' <b>X = TAMRA</b>	-
 [M4]	-	-	40 nm	5'-(TTT) <sub>4</sub> TX-SH-3' or 5'-X(TTT) <sub>4</sub> T-SH-3' / 5'-(TTT) <sub>4</sub> T-SH-3' <b>X = TAMRA</b>	-
 [M2]	-	-	60 nm	5'-(TTT) <sub>4</sub> TX-SH-3' <b>X = TAMRA or Cy3</b>	-

<sup>1</sup> estimated from the distance between adjacent DNA base pairs.

<sup>2</sup> estimated from a 2.5 nm thick DNA coating per AuNP<sup>[159]</sup> and a 2.0 nm thick DNA origami template.

### 3.2.2. Coating of AuNPs with ssDNA

Initially, AuNPs were coated by DNA using a one-step salt addition method. Up to a AuNP diameter  $d$  of approximately 15 nm (depending on the DNA sequence) this method is working well. However, with increasing  $d$  a salt aging method (for  $d \approx 15-40$  nm) or a low pH method (for  $d \approx 40-80$  nm) turned out to be necessary in order to obtain stable DNA-coated AuNPs.

#### One-step salt addition

The following preparation of DNA-coated AuNPs is similar to the protocol of DING *et al.*<sup>[94]</sup>. Initially, 5 mg of Bis(p-sulfonatophenyl)phenylphosphine dehydrate dipotassium salt (BSPP) were added to 15 mL of citrate-stabilized AuNPs (for  $d = 5$  nm or 15 nm), covered with aluminium foil and stirred for 24 h. Then, NaCl was added to the solution in several steps until the color of the solution changed from red to purple. Subsequently, the solution was centrifuged at 500  $g$  for 35 min, the supernatant was discarded and the AuNPs were re-suspended in 0.3 mL of 2.5 mM BSPP solution, resulting in another change of color back to red. Then, 0.5 mL MeOH were added leading to a third change of color to black. Again, the solution was centrifuged at 500  $g$  for 35 min, the supernatant was removed and the AuNPs were re-suspended in 0.2 mL of 2.5 mM BSPP solution.

Subsequently, phosphinated AuNPs (25  $\mu\text{L}$ ) were mixed with a 200-fold excess of thiol-modified ssDNA (22  $\mu\text{L}$ ; 100  $\mu\text{M}$ ; sequences are listed in Table 3.3) in 0.5x TAE containing 50 mM of NaCl. Here, the concentration of NaCl was adjusted by adding 0.5  $\mu\text{L}$  of 5 M NaCl solution in one step. The mixture was stirred for at least 80 h at room temperature. Excess DNA strands were removed by spin filtering (50  $\mu\text{L}$  AuNP solution + 100  $\mu\text{L}$  (first run) and 200  $\mu\text{L}$  (second run) of 1x TAE with 10 mM  $\text{MgCl}_2$ ) using Amicon Ultra-0.5 filters (100 kDa MWCO, Millipore) at 3830  $g$  for 10 min.

#### Salt aging method

The salt aging method also requires the above mentioned phosphination steps. Here, for the DNA coating process phosphinated AuNPs ( $d = 40$  nm, 13  $\mu\text{L}$ ) were mixed with a 64000-fold excess of thiol-modified ssDNA (32  $\mu\text{L}$ ; 100  $\mu\text{M}$ ; sequences are listed in Table 3.3). Furthermore, 2.9  $\mu\text{L}$  of 10x TAE were added and the mixture was allowed to stir overnight. Over a period of approximately 7 days, small amounts of a 2 M NaCl solution (0.5–2.0  $\mu\text{L}$  steps;  $V_{\text{NaCl, final}} = 10.5$   $\mu\text{L}$ ;  $c_{\text{NaCl, final}} = 360$  mM) were added in order to prevent the AuNPs from precipitation. After each salt addition, the mixture was sonicated (Bandelin Sonorex Super RK 255 H) for 20 s and subsequently stirred until the next step of salt aging. Excess DNA strands were removed by spin filtering (approximately 50–60  $\mu\text{L}$  AuNP solution + 100  $\mu\text{L}$  of 1x TAE with 10 mM  $\text{MgCl}_2$ ) using Amicon Ultra-0.5 filters (100 kDa MWCO, Millipore) at 3830  $g$  for 10 min. The subsequent washing process with 200  $\mu\text{L}$  of 1x TAE with 10 mM  $\text{MgCl}_2$  at 3830  $g$  for 10 min was performed 4 times. After the last filtration step no signals from excess DNA strands were detected via UV-Vis spectroscopy anymore.

#### Low pH method

As an alternative coating procedure the low pH method was used which is based on the protocol of ZHANG *et al.*<sup>[129]</sup> with slight modifications.

At first, 0.4 mL of citrate-capped AuNPs were concentrated by centrifugation at 1000  $g$  for 10 min. Then, the supernatant was gently removed and 4  $\mu\text{L}$  of 0.2% SDS solution were added to 20  $\mu\text{L}$  of the concentrated AuNPs (1–2 nM). Subsequently, 1.8  $\mu\text{L}$  of the ssDNA



coating strands (sequences are listed in Table 3.3; 100  $\mu\text{M}$ ) were added. The mixture was covered with aluminium foil and allowed to stir for at least 30 min. Subsequently, 8  $\mu\text{L}$  of 50 mM citrate buffer (pH 3, containing three equivalents  $\text{Na}^+$  for each citrate molecule) were added stepwise (1–2  $\mu\text{L}$  per step) over a period of 2 h in order to prevent the AuNPs from aggregation upon addition of the buffer in one single step. Next, 6.4  $\mu\text{L}$  of Milli-Q-water were added and the mixture was stirred for at least 60 min. Then, 5  $\mu\text{L}$  of 2.5 M NaCl solution were added in small steps of 0.5–1.0  $\mu\text{L}$  within 2 h ( $c_{\text{NaCl, final}} = 322 \text{ mM}$ ), again, to prevent AuNP aggregation. Afterwards the mixture was allowed to stir overnight. The AuNP solution was centrifuged at 1500  $g$  for 7 min and the supernatant was discarded. In order to remove excess coating strands the mixture was washed 5 times by adding 200  $\mu\text{L}$  of 1x TAE with 10 mM  $\text{MgCl}_2$  and 0.02% SDS, followed by centrifuging at 1500  $g$  for 7 min and discarding the supernatant.

### 3.2.3. Determination of DNA surface coverage on AuNPs

The DNA surface coverage on AuNPs was determined based on a method published by HURST *et al.*<sup>[132]</sup> which can only be applied to dye-modified DNA sequences. Initially, the concentration of DNA-coated AuNPs was determined by UV-Vis spectroscopy (see section 3.3.3). In order to remove all DNA-coating strands from the AuNP surface 10  $\mu\text{L}$  of the AuNP solution were incubated overnight with 10  $\mu\text{L}$  of 1 M dithiothreitol (DTT) in 1x TAE with 10 mM  $\text{MgCl}_2$  [2x dilution]. Subsequently, the gold precipitate was removed by centrifugation at 5000  $g$  for 4 min. Then 17  $\mu\text{L}$  of the supernatant were mixed with 493  $\mu\text{L}$  of 1x TAE with 10 mM  $\text{MgCl}_2$  [30x dilution] and the fluorescence of the mixture containing the dye-modified DNA was measured in triplicate (see section 3.3.4). Then, the fluorescence intensity was compared to a calibration curve which was prepared by mixing the volumes listed in Table 3.4. The concentrations of corresponding stock solutions were  $c_{\text{dye-DNA}} = 100 \text{ nM}$  (dye: TAMRA or Cy3) and  $c_{\text{DTT}} = 1 \text{ M}$ . As buffer 1x TAE with 10 mM  $\text{MgCl}_2$  was used.

**Table 3.4.:** Preparation of a calibration curve in order to determine the DNA surface coverage on AuNPs. Concentrations of stock solutions:  $c_{\text{dye}} = 100 \text{ nM}$  (dye: TAMRA or Cy3);  $c_{\text{DTT}} = 1 \text{ M}$ . Each mixture was filled to 200  $\mu\text{L}$  with 1x TAE with 10 mM  $\text{MgCl}_2$ .

$c_{\text{dye-DNA}} / \text{nM}$	0	1	2	4	8	12	20	30	40
$V_{\text{dye-DNA}} / \mu\text{L}$	0	2	4	8	16	24	40	60	80
$V_{\text{DTT}} / \mu\text{L}$	3.33	3.33	3.33	3.33	3.33	3.33	3.33	3.33	3.33
$V_{\text{TAE}} / \mu\text{L}$	196.7	194.7	192.7	188.7	180.7	172.7	156.7	136.7	116.7

### 3.2.4. AuNP-DNA origami hybridization

Basically, the hybridization between DNA capture strands within the DNA origami substrates and the DNA coating strands on the surface of AuNPs can take place either in solution or on the surface of a Si wafer. The latter method was used for AuNPs with  $d = 5 \text{ nm}$ . With increasing size the binding yield significantly decreased which is most probably due to less pronounced diffusion. Consequently, for all other AuNP sizes the hybridization was performed in solution.

For AuNP-DNA origami hybridization on the surface, DNA origami substrates (2  $\mu\text{L}$ ;  $c \approx 20 \text{ nM}$ ) were adsorbed on a Si wafer following the steps mentioned in sections 3.2.5 and 3.2.6. Directly after drying with compressed air, a 20  $\mu\text{L}$  drop of the 5 nm AuNPs ( $c = 50\text{--}100 \text{ nM}$ ) was placed on the Si surface. After an incubation time of 20 min at room temperature excess

AuNPs were removed from the surface by dipping the Si wafer for 10 min in Milli-Q-water. Finally, the Si wafer was dried with a stream of compressed air.

For AuNP-DNA origami hybridization in solution a total synthesis scale of 10  $\mu\text{L}$  was used by preparing a mixture of DNA origami substrates and DNA-coated AuNPs in a ratio of 1:1. Subsequently, 2  $\mu\text{L}$  of 1x TAE buffer with 50 mM  $\text{MgCl}_2$  were added yielding a final concentration of 10 mM  $\text{MgCl}_2$ . Then, using a Primus advanced 25 thermocycler (Peqlab) a pre-defined temperature program was applied to the mixture keeping the solution first at 45  $^\circ\text{C}$  for 41 min followed by cooling it down to a final temperature of 25  $^\circ\text{C}$  in steps of 2  $^\circ\text{C}$  within 20 min (total time: 71 min).

#### 3.2.5. Pre-treatment of Si substrates

After delivery, all Si wafers were covered by sticky stape (Nitto Denko ELP BT150ECM) in order to prevent the adsorption of impurities. The basic sample preparation was performed using p-type Si wafers ((100), CrysTec). However, if subsequent graphene exfoliation was performed a different type of Si wafers with 290 nm thick thermal oxide ( $\text{SiO}_2/\text{Si}$ ) (IDB TECHNOLOGIES LTD) was used in order to enable the visualization of graphene flakes by optical microscopy<sup>[160]</sup>.

Prior to use Si samples were cut into pieces (approximately  $1\text{ cm}^2 \times \text{cm}^2$ ) using a diamond knife and the edges were thoroughly cleaned from uprising Si powder using non-sterile cotton tipped applicators (Solon Care) soaked with acetone (pure). For basic sample preparation the substrates were rinsed with 4 mL EtOH (pure), with 4 mL Milli-Q-water and finally dried with compressed air. Afterwards the surfaces of the Si wafers were treated either with a UV lamp ( $\lambda = 254\text{ nm}$ , Vilber Lourmat) for 10–15 min or with an ozone cleaner (Diener electronic, ZEPTO) for 10 min. For mechanical exfoliation of graphene particularly clean Si surfaces are required. Therefore, subsequent to cleaning with acetone the  $\text{SiO}_2/\text{Si}$  wafers were heated to 250  $^\circ\text{C}$  for 10 min using a heating plate, then allowed to cool down to room temperature and finally treated with the ozone cleaner for 10 min.

#### 3.2.6. Adsorption of DNA origami substrates or DNA origami-AuNP hybrids

Immediately after cleaning a 0.4–1.0  $\mu\text{L}$  drop of the pristine DNA origami solution or the DNA-AuNP solution was applied on a Si wafer followed by the addition of approximately 40  $\mu\text{L}$  of 10x TAE with 100 mM  $\text{MgCl}_2$ . By changing the volume of added buffer the resulting surface coverage was adjusted. During an incubation time of 45–60 min the Si samples were stored in a box partly filled with water in order to increase the humidity and thus to prevent the drop from drying. Subsequently, the substrates were rinsed with 4 mL of 1:1 Milli-Q-water/EtOH (pure) and dried with compressed air.

#### 3.2.7. Electroless silver deposition

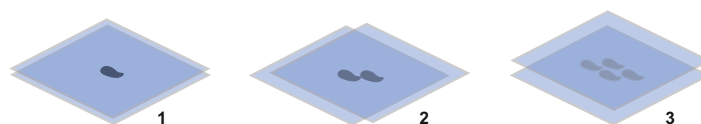
Two commercially available Ag enhancement kits (LI silver, HQ silver; Nanoprobes) were used at room temperature and darkened light conditions as recommended by the manufacturer. The Ag enhancement solutions were freshly prepared prior to use by carefully mixing the individual components of each kit in equal parts, that is, three components for HQ silver (initiator, activator and mediator) and two components for LI silver (initiator and enhancer). Immediately after mixing, a 20  $\mu\text{L}$  drop of the mixture was applied to the DNA-AuNP hybrids adsorbed on a Si wafer. The deposition time was set to 60 s (HQ silver) or 3 min (LI silver) and afterwards the Si wafers were rinsed and quickly dipped in Milli-Q-water and finally dried

with compressed air.

The main difference between both Ag enhancement kits is the mediator component in the HQ solution which serves as a thickening agent to retard the deposition rate.

### 3.2.8. Mechanical exfoliation of graphene

Graphene deposition was performed via micromechanical cleavage<sup>[138]</sup>. Therefore, a flake of Kish graphite (Naturgraphite GmbH) was repeatedly cleaved between two sheets of sticky tape (Nitto Denko ELP BT150ECM). Basically, micromechanical cleavage yields high-quality graphene up to flake dimensions on the order of mm. However, it was found that larger flakes do not properly adsorb on NP structures. Therefore, the thickness, density and size of cleaved flakes were adjusted by shifted overlapping of the two tapes for each cleaving step (see Figure 3.4). The as-prepared tape was then carefully rolled on top of the SiO<sub>2</sub>/Si wafers with the adsorbed structures to be encapsulated. The tape-covered wafers were then stored in a glass with MIBK at room temperature for the time necessary to remove the tape by its own (approximately 3 h). Immediately after removal of the tape the wafers were washed two times with MIBK, then once by 2-propanol and finally dried with a stream of compressed air. At this stage, usually no SLG flakes are adsorbed. Therefore, the flakes were carefully cleaved one more time by using another sticky tape. It has to be mentioned that the velocity of peeling the tape off is of highest importance for the resulting quality and size of the flakes since rapid peeling leads to intensified ripping.



**Figure 3.4.:** Tape preparation for mechanical exfoliation of graphene. The initial flake of graphite is repeatedly cleaved by shifted overlapping of the two tapes.

### 3.2.9. Introducing a marker

Prior to analysis by AFM and SERS imaging a slight scratch was introduced to the surface of a Si wafer using a diamond knife. The scratch serves as macroscopic marker visible in both images and thus enables the superposition of the data.

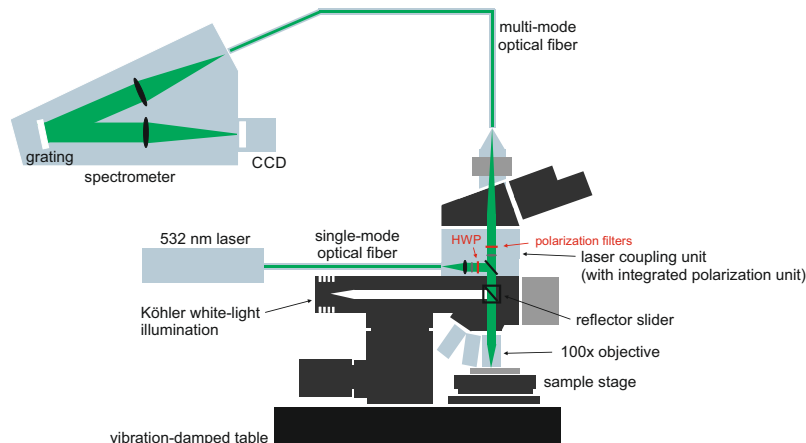
This treatment was not necessary in the case of samples covered by graphene since the flakes themselves serve as indicator for superposition.

## 3.3. Methods

### 3.3.1. SERS imaging

SERS images and single spectra were recorded using a confocal Raman microscope (WITec alpha300) equipped with an upright optical microscope. The corresponding laser beam path is depicted in Fig. 3.5. The incident laser light ( $\lambda_{\text{exc}} = 532 \text{ nm}$ ) was first coupled into a single-mode optical fiber, followed by coupling into the microscope by a laser coupling unit with integrated polarization unit. Here, the laser light passed a collimating lens, filters and a beam splitter. Additionally, in the case of polarization-dependent measurements, a half-wave plate (HWP) was inserted. Subsequently, the laser light was passed through a reflector slider with Köhler illumination and focused through a 100x objective (Olympus MPlanFL N, NA = 0.9) to a diffraction-limited spot ( $1.3 \mu\text{m}^2$  spot size) on the Si sample. The back-scattered light was then passed through a notch filter in order to suppress the RAYLEIGH

scattering intensity. For polarization-dependent measurements the polarization planes for laser excitation and detection were adjusted by polarization filters. Subsequently, the light was coupled into a multi-mode optical fiber (core diameter: 50  $\mu\text{m}$ ) and finally reached the spectrometer (UHTS 300). Within the spectrometer the light was directed onto a grating (either 600  $\text{g mm}^{-1}$  or 1800  $\text{g mm}^{-1}$ ) by a collimating lens and afterwards focused by another focusing lens on the charge-coupled device (CCD) camera (DV401-BV with 1024  $\times$  127 pixel, 26  $\mu\text{m} \times$  26  $\mu\text{m}$  pixel size and an image area of 26.6 mm  $\times$  3.3 mm).



**Figure 3.5.:** Laser beam path within the confocal Raman microscope. The optical components within the microscope are colored in light blue. Components related to polarization adjustment are highlighted in red (HWP: half wave plate). (Figure adapted and modified from ref. <sup>[161]</sup>.)

The applied laser power was measured using a laser power meter (FieldMaxII-TO, Coherent) connected to a semiconductor sensor (OP-2 VIS, Coherent) before each measurement. To this end, the sensor head was positioned in between the scan stage and the selected objective with a predefined distance.

In Table 3.5 the applied parameters for individual measurements are summarized.

**Table 3.5.:** Parameters for SERS measurements.

[Manuscript] Fig.	laser power [ $\mu\text{W}$ ]	mode	integration time [s]	accumu- lations	scan size [ $\mu\text{m}^2$ ]	grating [ $\text{g mm}^{-1}$ ]
<b>[M1]</b>						
Fig. 2	900–1000	image	2	-	15 $\times$ 15	600
Fig. 3	400–500	image	10	-	15 $\times$ 15	600
Fig. 4	400–500	image	10	-	15 $\times$ 15	600
<b>[M2]</b>						
Fig. 3	900–1000	image	2	-	25 $\times$ 25	600
Fig. 4	900–1000	image	2	-	30 $\times$ 30	600
Fig. 5	400–500	image	10	-	28 $\times$ 28	600
<b>[M4]</b>						
Fig. 2	80	image	10	-	24 $\times$ 24	600
Fig. 3 a	900–1000	image	2	-	30 $\times$ 30	600
Fig. 3 b (a–c; A–C)	80	image	10	-	24 $\times$ 24	600
Fig. 4	25	single spectra	10	1	-	600
Fig. 5	25	single spectra	10	1	-	600
<b>[M6]</b>						
Fig. 6 (overview)	13000	single spectra	10	3	-	600
Fig. 6 (inset)	13000	single spectra	10	3	-	1800

### 3.3.2. Atomic force microscopy (AFM) imaging

AFM imaging was performed with a Nanosurf FlexAFM connected to a C3000 controller (Nanosurf) using two different scan heads either for large-area imaging (maximum scan range: 100  $\mu\text{m}$ ; resolution: 1.525 nm (xy), 0.152 nm (z)) or for higher resolution (maximum scan range: 10  $\mu\text{m}$ ; resolution: 0.152 nm (xy), 0.046 nm (z)).

All measurements were performed in tapping mode using Tap150Al-G cantilevers (Budget Sensors) with a force constant of 5  $\text{N m}^{-1}$ , a resonance frequency of approximately 150 kHz and a tip radius of  $< 10$  nm. AFM images were recorded using 512 data points/line, a set-point between 50–75% and a scan speed between 0.3–0.9 s/line. P-Gain (proportional gain) and I-Gain (integral gain) were in the range of 500–1000.

After imaging, the data was visualized and analyzed using the software Gwyddion 2.34 (free-ware). The data was prepared by plane leveling, basic line correction, eliminating stripes and strokes, removing a polynomial background (if necessary), setting the minimum value to zero and finally adjusting the color range.

### 3.3.3. UV-Vis absorption measurements

UV-Vis absorption measurements of DNA origami substrates and AuNPs were carried out using a Nanodrop 2000 (Thermo Scientific) covering wavelength ranges of 220–350 nm (DNA origami) or 190–840 nm (AuNPs), respectively. As blank the corresponding filtration solution (see above) was used: (i) for DNA origami substrates: 1x TAE with 10 mM  $\text{MgCl}_2$ , (ii) for AuNPs (one-step addition / salt aging): 1x TAE with 10 mM  $\text{MgCl}_2$  and (iii) for AuNPs (low pH method): 1x TAE with 10 mM  $\text{MgCl}_2$  and 0.02% SDS.

The corresponding molar decadic extinction coefficients  $\varepsilon(\lambda)$  for individual AuNP diameters were calculated using equation 3.1 suggested by LIU *et al.*<sup>[162]</sup>.

$$\ln\varepsilon(\lambda) = K \cdot \ln d + C \quad (3.1)$$

where  $d$  [nm] is the diameter of the AuNP,  $K = 3.32111$  and  $C = 10.80505$ . For the relevant AuNP sizes equation 3.1 yields:

$$\varepsilon(\lambda)_{5 \text{ nm}} = 1.03 \times 10^7 \text{ M cm}^{-1} \quad (3.2)$$

$$\varepsilon(\lambda)_{15 \text{ nm}} = 3.96 \times 10^8 \text{ M cm}^{-1} \quad (3.3)$$

$$\varepsilon(\lambda)_{40 \text{ nm}} = 1.03 \times 10^{10} \text{ M cm}^{-1} \quad (3.4)$$

$$\varepsilon(\lambda)_{60 \text{ nm}} = 3.96 \times 10^{10} \text{ M cm}^{-1} \quad (3.5)$$

Using the calculated values for  $\varepsilon(\lambda)$ , the corresponding concentrations were determined based on LAMBERT-BEER's law (equation 3.6), where  $E(\lambda)$  is the extinction,  $c$  [ $\text{mol L}^{-1}$ ] is the concentration and  $b$  [mm] is the thickness of the absorbing substance ( $b = 1$  mm in the case of the Nanodrop 2000).

$$E(\lambda) = \varepsilon(\lambda) \cdot c \cdot b \quad (3.6)$$

In order to determine the concentration of the DNA origami substrates the nucleic acid data for the M13mp18 strand provided by the manufacturer was used (7249 nt; 1  $\mu\text{g}$  of M13mp18  $\hat{=}$  0.21 pmol  $\hat{=}$   $1.3 \times 10^{11}$  molecules;  $M = 4.762 \times 10^6 \text{ g mol}^{-1}$ )<sup>[163]</sup>.

### 3.3.4. Fluorescence measurements

Fluorescence measurements were performed in microliter quartz cuvettes (High precision cell, Hellma Analytics) using a FluoroMax-P (Horiba Jobin Yvon). For all measurements an integration time of 0.2 s was used and the slit size was set to 5.0 nm. The fluorescence of TAMRA-modified DNA was measured using an excitation wavelength of  $\lambda_{\text{exc}} = 535$  nm and recording the emission from 550–750 nm. In the case of Cy3-modified DNA the excitation wavelength was set to  $\lambda_{\text{exc}} = 500$  nm and the emission was collected from 520–700 nm.

### 3.3.5. Scanning electron microscope (SEM) imaging

For SEM imaging a Quanta250 (FEI) with an EVERHART-THORNLEY detector (ETD) in secondary electron (SE) mode was used working under high vacuum conditions. The accelerating voltage and the spot size were set to 30 kV and 2.0 nm.

# 4

## Discussion

### 4.1. Main manuscripts

SERS is a powerful tool to obtain rich chemical information about analyte molecules at trace levels. Although single molecules have first been spectroscopically detected by fluorescence based methods<sup>[164–166]</sup>, SERS is superior regarding the amount of accessible structural information. However, usual SERS measurements are based on enhancing the Raman signal of a certain analyte by coprecipitation with a metal salt. In this way, randomly distributed hot spots over the whole solution are created that can differ in terms of the corresponding EF by several order of magnitudes. Since differently pronounced hot spots contribute to the overall SERS intensity to various extents, the detected SERS signal of such a colloidal solution is eventually a sum of an unknown analyte concentration.

Although the detection of single-molecule events has been demonstrated based on the ultralow concentration approach<sup>[6,7]</sup> and the bi-analyte approach<sup>[8,57–59]</sup>, both methods do not allow for the controlled formation of hot spots and a predefined analyte concentration within the same.

With the uprising field of nanotechnology new doors were opened to design plasmonic structures either by top-down or by bottom-up techniques. However, with top-down strategies, such as the widely used electron beam lithography (EBL)<sup>[167]</sup>, three-dimensional plasmonic structures are difficult to obtain and this method is not cost-effective regarding mass-production<sup>[168]</sup>. Therefore, new bottom-up approaches relying on the self-assembly of smaller building blocks into larger constructs were developed. In this context, DNA-based nanotechnology attracted particularly high interest since it provides outstanding programmability and intrinsic biocompatibility at the same time.

Since the electromagnetic field enhancement can reach particularly high values within the gap between adjacent AuNPs<sup>[4,5]</sup>, a lot of effort has been made in the design of dimeric AuNP structures connected by DNA strands. Especially SUH and co-workers carried out extensive research in this field<sup>[10,169–171]</sup>. In their developed approach two AuNPs are coated with two types of DNA strands, that is, a protective sequence and a target sequence carrying a Cy3 modification<sup>[10]</sup>. The stoichiometry is adjusted to make sure that exactly one Cy3 dye is located in the gap between the two AuNPs upon DNA hybridization. Subsequently a Ag enhancement solution is applied in order to decrease the gap size resulting in Au-Ag-core-shell nanodumbbells that provide EFs on the order of  $10^{12}$ .

However, since the analyte molecule is part of the DNA hybridization process, this approach leaves no possibility for the subsequent functionalization of the SERS substrate. This drawback can be overcome by using DNA origami substrates as a platform for SERS.

The first assembly of AuNPs on DNA origami substrates was introduced in 2008 by SHARMA *et al.* who attached either one or two AuNPs to rectangular DNA origami substrates reaching yields higher than 90%<sup>[172]</sup>. Two years later, DING *et al.* assembled six AuNPs with different sizes (15 nm, 10 nm, 5 nm) in a row on a DNA origami triangle<sup>[94]</sup>. In this way, a potential plasmonic nanolens was created with gap sizes < 10 nm. Since then, numerous DNA origami-AuNP hybrids with versatile architectures have been designed covering a broad field of applications. On the one hand, AuNP arrangements on DNA origami substrates are predefined structures for fundamental studies on plasmon coupling<sup>[173,174]</sup>. On the other hand, DNA origami-AuNPs hybrids have been used to study fluorescence enhancement<sup>[175]</sup> and quenching effects<sup>[96]</sup> or to build plasmonic waveguides<sup>[176]</sup>. Moreover, chiral assemblies of AuNPs on DNA origami have been reported to exhibit plasmonic circular dichroism responses<sup>[177–179]</sup>.


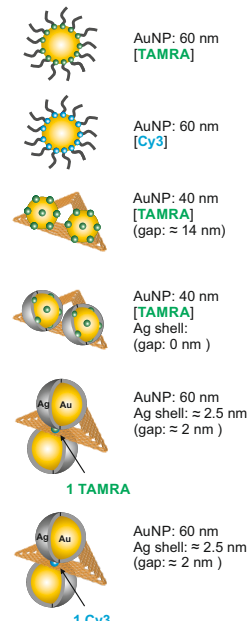
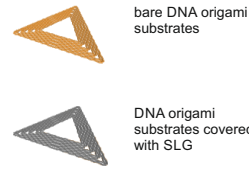
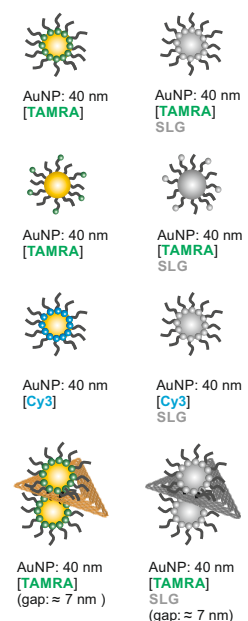
Although several applications have already been demonstrated using AuNP-DNA origami hybrid structures, up to this point none of the work aimed at using such structures in the context of SERS. Therefore, the present study aims at the development of a versatile DNA origami-based platform that is suitable for the detection of analyte molecules – down to a single-molecule level – by means of SERS. To this end, dimers of AuNPs are assembled on triangular DNA origami substrates. By changing the sizes of the AuNPs as well as the interparticle distances the hot spot is optimized in order to improve the field enhancement. Furthermore, graphene is introduced as a new building block resulting in enhanced structural stability of the DNA origami substrates as well as improved photostability of the incorporated dye molecules.

Throughout the whole thesis, information about different structures is collected by means of correlated AFM and SERS imaging allowing for the assignment of certain signals to defined structures. An overview of the four main manuscripts (**M1–M4**) related to the present thesis is given in Figure 4.1, showing the investigated structures and the central results (see chapter 6 for full manuscripts and correlated Supporting Information). Figure 4.1 should serve as a guide for the subsequent superordinate discussion of the main results.

In **M1**<sup>1</sup> the overall concept of using DNA origami substrates as a platform for SERS measurements is presented. It has to be mentioned that **M1** is the first publication dealing with this particular combination of techniques. Herein, initial proof-of-principle experiments are performed using 15 nm AuNPs coated with TAMRA-modified DNA. The TAMRA dyes are separated from the AuNP surface by a T<sub>4</sub>-DNA spacer sequence. It is shown that single 15 nm AuNPs only result in very weak TAMRA signals (see Figure 4.2 a (**A**) and [**M1**, Figure 2]). However, when two AuNPs are attached to one side of the DNA origami with a gap size of approximately 10 nm, the surface plasmon resonances of the individual AuNPs can couple resulting in intense TAMRA signals at 1215 cm<sup>-1</sup>, 1356 cm<sup>-1</sup>, 1509 cm<sup>-1</sup>, 1534 cm<sup>-1</sup> and 1647 cm<sup>-1</sup> (Figure 4.2 a (**B**) and [**M1**, Figure 2]). Although both particles are completely covered by TAMRA molecules, only a small fraction of the dyes – namely those which are directly located in the hot spot – contribute to a large extent to the SERS signal. However, in this arrangement the number of dye molecules can only be estimated from geometrical considerations.

<sup>1</sup> [**M1**] J. Prinz, B. Schreiber, L. Olejko, J. Oertel, J. Rackwitz, A. Keller, I. Bald, “DNA Origami Substrates for Highly Sensitive Surface-Enhanced Raman Scattering”, *J. Phys. Chem. Lett.* **4**, 4140–4145 (2013).



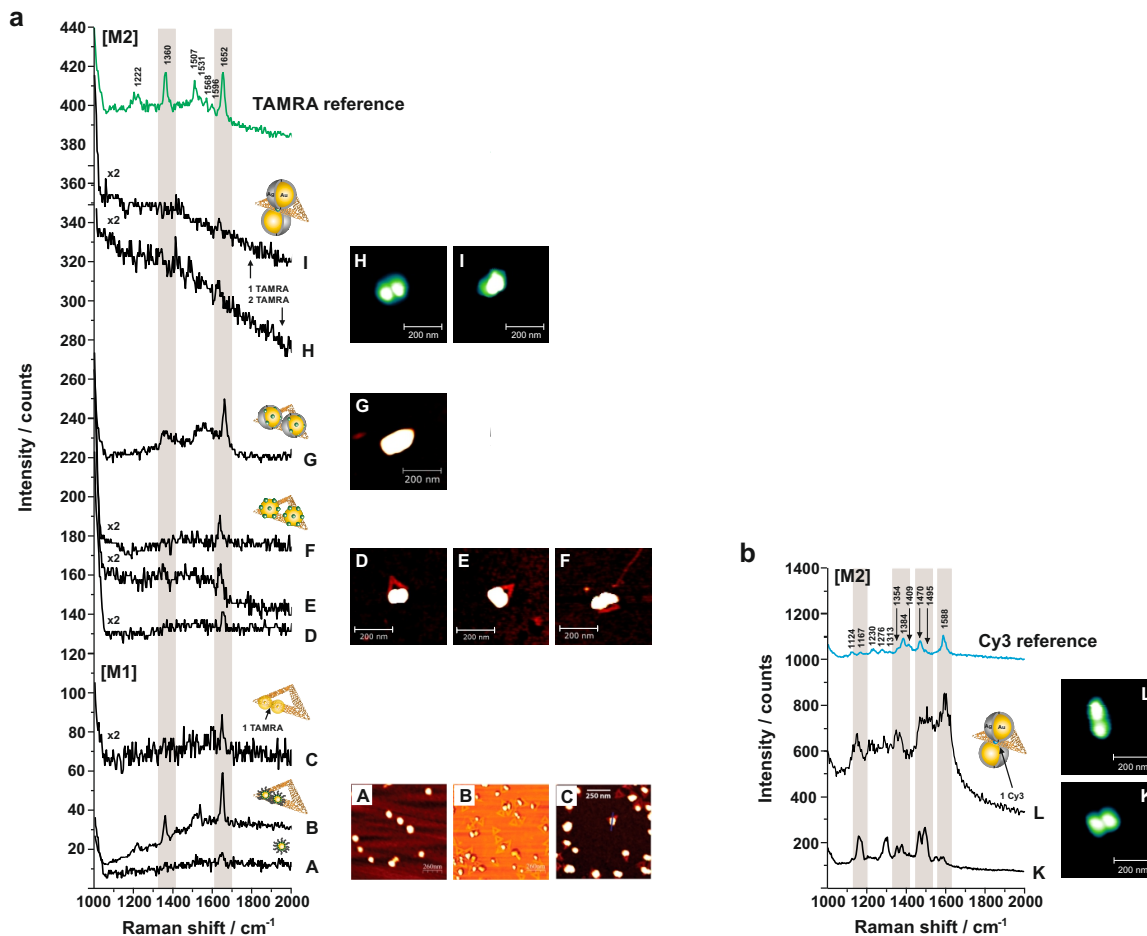
M1 Proof-of-principle	M2 Single-molecule detection	M3 Graphene encapsulation	M4 Hybrid structures: DNA origami / AuNP dimer / graphene
			
<p><b>Main results</b></p> <ul style="list-style-type: none"> <li>- first demonstration of DNA origami-based SERS experiments</li> <li>- few-molecule detection</li> </ul>	<p><b>Main results</b></p> <ul style="list-style-type: none"> <li>- detection of single molecules</li> <li>- EF: <math>\approx 10^{10}</math></li> </ul>	<p><b>Main results</b></p> <ul style="list-style-type: none"> <li>- enhanced structural stability of DNA origami substrates due to graphene encapsulation</li> </ul>	<p><b>Main results</b></p> <ul style="list-style-type: none"> <li>- reduced fluorescence background</li> <li>- strain induced effects in graphene</li> <li>- improved photostability of TAMRA</li> </ul>

**Figure 4.1.: Overview of the four main manuscripts M1–M4.** All investigated structures are depicted along with the corresponding main results. In some structures the DNA coating strands are not shown for better clarity.

This circumstance can be avoided by incorporating the dye molecules in the DNA origami instead of binding them to the AuNP surface. Therefore, three TAMRA molecules are incorporated to the DNA origami in form of dye-modified staple strands. Additionally, two 5 nm AuNPs are attached to the DNA origami at a nominal distance of 25 nm, thereby surrounding the TAMRA dyes. In order to determine the optimal distance between the two particles, a Au enhancement solution is applied leading to a controlled growth of the AuNPs by electroless Au deposition. This is a method usually used as a staining technique for microscopy applications in order to improve the detection sensitivity. As a result, the remaining gap size is adjusted from approximately 13 nm down to 1 nm. Further growth of the Au shell finally leads to a fusion of both AuNPs. In this respect, it is found that the most intense TAMRA signals are obtained for AuNP diameters of 25 nm, that is, the two AuNPs are almost touching. This finding is in good agreement with the supporting discrete dipole approximation (DDA) simulations ([M1, Figure 3]) as well as with previously reported high field enhancements for 1 nm gap sizes<sup>[180]</sup>.

This finding is further exploited for experiments demonstrating the applicability at the single-molecule level. To this end, one single TAMRA molecule is placed in the gap between two 5 nm AuNPs at a nominal distance of 25 nm and the size of the AuNPs is increased by approximately 20 nm according to the findings for three TAMRA molecules. SERS measurements of this structure reveal that the most characteristic TAMRA band at  $1647\text{ cm}^{-1}$  is still detectable. In particular, it is shown that within the laser spot (approximately  $1.3\text{ }\mu\text{m}^2$  spot

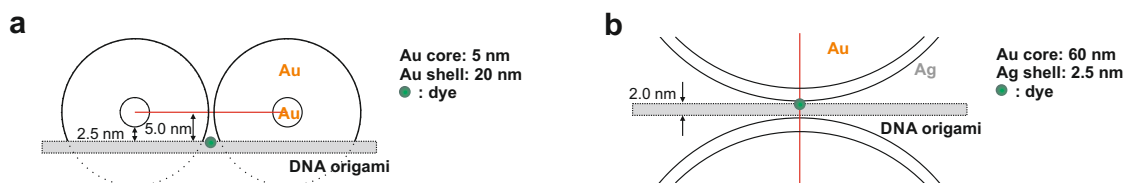
size), 17 individual TAMRA-modified DNA origami substrates give a detectable SERS signal that is just above the LOD (Figure 4.2 a (C) and [M1, Figure 4]).



**Figure 4.2.:** Overview of the correlated SERS and AFM data from M1 and M2. (a) Detection of TAMRA molecules using different DNA origami-AuNP hybrid structures. Several optimization steps finally lead to single-molecule sensitivity (structure **I**). (b) Detection of single Cy3 molecules using the optimized structure. SERS spectra in **a** and **b** are vertically shifted.

It has to be mentioned that the position of the TAMRA molecule bound to the DNA origami templates is not optimized at this stage. Since the dye molecules are located approximately 5 nm below the axis between the two NPs, and thus not directly in the hot spot, the dyes do not benefit from the maximum field enhancement (see geometrical considerations in Figure 4.3 a). The maximum EF for two 25 nm AuNPs with a gap size of approximately 1 nm is expected to be on the order of  $10^6$  (for  $\lambda_{\text{exc}} = 532 \text{ nm}$ <sup>[18]</sup>). Due to the small gap size the hot spot should be highly localized resulting in a significantly lower field enhancement at the dye position. The resonant excitation of the TAMRA dyes leads to an additional contribution to the overall field enhancement since the Raman cross section is increased by a factor of at least  $10^4$  under this condition<sup>[18]</sup>. Consequently, considering both contributions, the highest expectable EF at the dye position hardly reaches the range where single dye molecules become detectable ( $\text{EF}_{\text{sm-SERS}}^{\text{min}} \approx 10^7\text{--}10^8$ ; see equation 2.22). Since the AuNP diameters vary by several nm (see [M1, Figure S5]), the gap size for individual structures is also expected to differ to the same extent. For these reasons, it is highly probable that only a few of the structures (or at least one structure) located in the laser spot result in a detectable SERS

signal. This in turn confirms the possibility to reach single-molecule sensitivity with the here applied structures if the hot spot is sufficiently optimized.



**Figure 4.3.: Geometrical considerations for different DNA origami-AuNPs arrangements.** In both cases the DNA origami template is not shown in full length. Since the dye molecule is either located at the 3'-end or the 5'-end of a staple strand it is slightly protruding from the DNA origami template. (a) Two 5 nm AuNPs with a 20 nm thick Au shell are attached to one side of the DNA origami substrate (the dotted lines imply that a spherical growth of the Au shell is not possible since the structures are adsorbed on Si wafers). This design is initially used in **M1**. Assuming a 2.5 nm thick DNA coating surrounding the AuNPs, the hot spot is located approximately 5.0 nm above the DNA origami template. Consequently, a single dye molecule incorporated in the DNA origami template is not correctly aligned to profit from the highest field enhancement. (b) By attaching the two AuNPs to different sides of the DNA origami template, it is ensured that the single dye molecule is positioned in the axis between the particles (red line) and thus within the hot spot (design presented in **M2** with two 60 nm AuNPs and a Ag shell of approximately 2.5 nm).

The high relevance and timeliness of the approach introduced in **M1** is reflected by several similar reports that were published shortly afterwards<sup>[159,181,182]</sup>.

First, THACKER *et al.* assembled two 40 nm AuNPs on a multi-layer DNA origami platform with two predefined grooves. In this way, sub-5 nm gap sizes were created. SERS measurements of single dimeric structures were performed by rinsing them with a R6G solution. The resulting SERS signal was estimated to arise from approximately five R6G molecules and the corresponding EFs were calculated to be in the range of  $10^5$ – $10^7$ .

Second, PILO-PAIS *et al.* attached four 5 nm AuNPs at the corners of a rectangular DNA origami substrate. Subsequently, the size of the AuNPs was increased to approximately 50 nm by using a Ag enhancement solution resulting in estimated gap sizes of 3 nm. To perform SERS measurements the four-particle assemblies were incubated in a 4-aminobenzenethiol (4-ABT) solution resulting in covalent attachment of the Raman reporter molecules to the metal surface. By combining the SERS signals of the four-particle assemblies with the signal arising when only one particle is attached to the DNA origami template, an EF of  $\approx 100$  per NP was estimated.

Third, KÜHLER *et al.* attached two 40 nm AuNPs to different sides of a three-layered DNA origami block leading to an estimated gap size of 6 nm under dry conditions. As Raman reporter molecule SYBR Gold was used which binds to the minor grooves within dsDNA. It was estimated that 25 SYBR Gold molecules are located within the hot spot. The EFs were calculated by finite-difference time-domain (FDTD) calculations yielding a maximum value of  $2 \times 10^6$  in the center of the hot spot and an averaged value of  $1.4 \times 10^5$  over the whole hot spot area.

The main difference between these three reports and the approach introduced in **M1** is the way the Raman reporter molecules are incorporated within the DNA origami-AuNP assemblies. In all three cases the number of analyte molecules contributing to a certain SERS signal is based on geometrical considerations similar to the one for TAMRA-coated AuNPs in **M1** ([**M1**, Figure 2]). However, the DNA origami technique allows for the positioning of a known number of analyte molecules at predefined positions by incorporating them directly in the DNA origami template. This strategy is followed in **M1** (Figure 4.2 a (C)) and [**M1**, Figures 3, 4]) and further applied for the detection of single molecules by SERS.

The experiments published in **M1** are initial qualitative results with the priority of presenting the proof-of-principle. However, the detection of single molecules by SERS requires higher field enhancements as well as a precise placement of the analyte molecule within the hot spot. Therefore, in **M2**<sup>2</sup> several optimization steps are presented. First of all, larger TAMRA-coated AuNPs with a diameter of 40 nm are used in order to increase the signal enhancement. They are arranged into dimers at one side of the DNA origami substrate with a maximum gap size of 14 nm ([**M2**, Figure 1 a]). Single-structure correlations reveal that the most characteristic TAMRA peak at  $1652\text{ cm}^{-1}$  is detectable for this particular design (Figure 4.2 a (D–E) and [**M2**, Figure 3]). The spectral position of this peak is shifted by  $5\text{ cm}^{-1}$  with respect to the results shown in **M1**, which is attributed to altered dye-modified DNA coating sequences.

The same structures are used in order to test the effect of a Ag shell surrounding the AuNP. From a plasmonic point of view, AgNPs exhibit several advantages towards AuNPs, since the SERS performance of Ag within the visible range of the electromagnetic spectrum is superior to that of Au (see section 2.2). However, AgNPs are more difficult to synthesize and they suffer from rapid oxidation under ambient conditions which leads to difficulties regarding DNA functionalization<sup>[183–185]</sup>. Therefore, only a few reports deal with DNA origami substrates functionalized with AgNPs<sup>[186–188]</sup>. In **M2**, a compromise is used by first attaching AuNPs to a DNA origami template and afterwards surrounding them with a Ag shell. This method is widely used in order to enhance the visualization in immunoelectron microscopy techniques<sup>[189]</sup>. Furthermore, it was applied by others, e.g. for scanometric DNA array detection<sup>[190]</sup> or to fuse small metal seeds on DNA origami templates<sup>[191]</sup>. By varying the Au core diameter and Ag shell thickness, this method allows for tuning the optical properties of the core-shell NPs<sup>[192]</sup> which makes it a predestined technique for SERS<sup>[10,192,193]</sup>.

In **M2** SERS signals of individual structures before and after the Ag enhancement process are compared. It is clearly shown that the SERS signal of individual structures are increased upon the Ag enhancement process (Figure 4.2 a (G) and [**M2**, Figure 4]). However, the origin of the field enhancement is difficult to reveal since in this arrangement the TAMRA molecules are incorporated between the Au core and the Ag shell. Furthermore, in some cases strong bands from the DNA coating arise upon Ag enhancement ([**M2**, Figure S4 and Table S1]).

The increased field enhancement upon electroless Ag deposition is further exploited in single-molecule experiments. Since the LFIEF is highly sensitive to the interparticle gap, reaching immense values at approximately 1 nm distance, a new design was developed in which the two AuNPs are attached to opposite sides of the DNA origami triangle ([**M2**, Figure 1 b]). This design exhibits several improvements. First, the gap between the AuNPs is halved with regard to the previously used arrangement, resulting in a distance of approximately 7 nm (assuming 2 nm thickness of the DNA origami and 2.5 nm thickness of the DNA coating per AuNP). Second, by incorporating a single dye to the DNA origami substrate, it is ensured that the Raman reporter molecule is located directly in the axis between the two particles and thus in the hot spot (see Figure 4.3 b). However, due to the altered arrangement the DNA origami template can not flatly adsorb on the Si wafer and is thus no longer visible in the AFM images (for AuNPs sizes  $\geq 60\text{ nm}$ ). In order to reduce the flexibility of the attached AuNPs a fourth capture strand per AuNP is introduced. Additionally, larger AuNPs with a diameter of 60 nm are used. In this context, it is necessary to change the coating strategy, since the previously applied salt aging method fails for AuNPs larger than 40 nm (see section 3.2.2). Again, the AuNPs sizes are increased by electroless Ag deposition, resulting in

<sup>2</sup> [**M2**] J. Prinz, C. Heck, L. Ellerik, V. Merk, I. Bald, “DNA origami based Au-Ag-core-shell nanoparticle dimers with single-molecule SERS sensitivity”, *Nanoscale* **8**, 5612–5620 (2016).

Au-Ag-core-shell dimers with Ag shell diameters of approximately 2.5 nm and a remaining gap size of 2 nm. Particular attention is paid to the incubation time of the Ag enhancement solution in order to prevent the fusion of the two particles. Accompanied FDTD simulations reveal that keeping all parameters the same but further increase the Au core size to 80 nm would lead to a decrease of the LFIEF at the dye position ([M2, Supporting Figure S7]). Therefore, subsequent experiments are performed by using 60 nm AuNPs.

In the case of TAMRA as Raman reporter molecule the most prominent TAMRA band at  $1652\text{ cm}^{-1}$  is detectable for two molecules and only one single dye molecule placed in the hot spot. However, in both cases the signal intensity hardly exceeds the S/N ratio (Figure 4.2 a (H, I) and [M2, Figure 5 a]). By using Cy3 as an alternative dye much higher signal intensities for the characteristic Raman bands at  $1167\text{ cm}^{-1}$ ,  $1354\text{ cm}^{-1}$ ,  $1384\text{ cm}^{-1}$ ,  $1470\text{ cm}^{-1}$ ,  $1495\text{ cm}^{-1}$  and  $1588\text{ cm}^{-1}$  are observed (Figure 4.2 b (K, L) and [M2, Figure 5 b]). The different behaviour of TAMRA and Cy3 is hereby assigned to different Raman cross sections of the two dyes within the hot spot.

In order to quantify the field enhancement in terms of an estimated EF, a reference system is necessary. However, due to the appearance of an intense fluorescence background at  $\lambda_{\text{exc}} = 532\text{ nm}$ , normal Raman spectra of TAMRA and Cy3 cannot be recorded. Therefore, single 60 nm that are coated with dye-modified ssDNA (either TAMRA or Cy3) serve as reference system with a known EF of approximately  $9 \times 10^5$ <sup>[194]</sup>. To this end, the average number of dye-modified DNA per AuNP is determined by fluorescence spectroscopy using the protocol of HURST *et al.*<sup>[132]</sup>. It is found that the surface coverage with TAMRA-modified DNA exceeds the one for the analogue Cy3-modified DNA by approximately 22%. This is most probably caused by a higher sterical demand of the Cy3 modification leading to a larger exclusion area on the AuNP surface (see molecular structures of both dyes in section 3.2 (Figure 3.2)). Additionally, for each dye, SERS signals of 15 single 60 nm particles are recorded and averaged. It has to be mentioned that in both cases a wide distribution of SERS signal intensities is observed (see Figure A.2). This observation will be explored in more detail in the context of graphene encapsulated AuNPs in M4. From the strongest averaged SERS bands ( $1652\text{ cm}^{-1}$  for TAMRA;  $1470\text{ cm}^{-1}$  and  $1588\text{ cm}^{-1}$  for Cy3) EFs on the order of  $10^8$  for TAMRA and  $10^9$ – $10^{10}$  for Cy3 are estimated which are in good agreement with the supporting FDTD simulations and sufficiently high to detect single molecules.

All previously discussed SERS spectra in M1 and M2 result from the detection of an unpolarized scattering signal. However, especially in the case of single molecules, polarization-dependent measurements would be of great interest since they should provide extensive information about the conformation of the molecule within the hot spot. To this end, in practice, a series of SERS measurements using different polarization angles is required. However, up to this stage, under the here applied conditions, series measurements significantly suffer from photobleaching (see Figure A.3). As soon as photobleaching occurs, a change in the SERS signal intensities can no further be assigned to a polarization-induced effect. Therefore, a strategy to overcome the drawback of photobleaching is a crucial step towards polarization-dependent measurements.

In view of the above, the impact of graphene to the developed SERS substrates is studied. Since the discovery of graphene by NOVOSELOV *et al.* in 2004<sup>[138]</sup> this ultrathin material attracted a lot of interest due to its unique combination of optical, mechanical and electrical properties. Several reports deal with the combination of graphene and AuNPs for several applications, such as biosensing, bioimaging or drug delivery<sup>[195]</sup>.

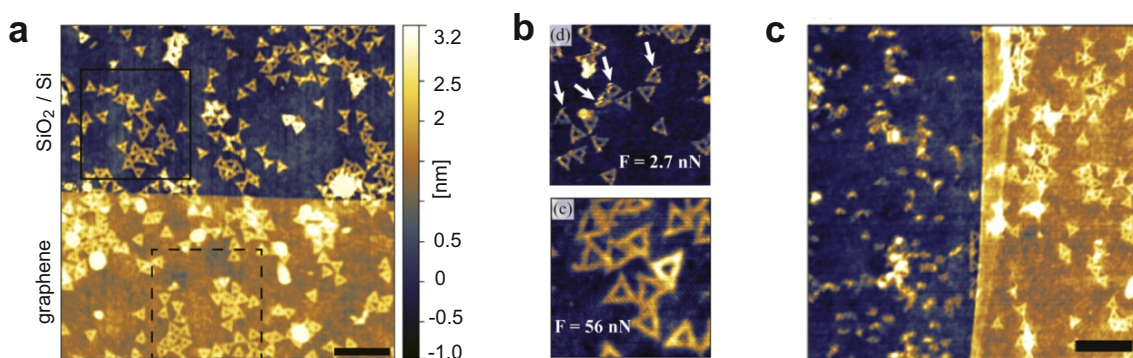
Recently, graphene was demonstrated to suppress the photobleaching of dye molecules in close vicinity. In 2014 LIU *et al.* investigated metal NPs (Cu, Ag and Au) that were encapsu-

lated by FLG<sup>[12]</sup>. The probe molecules (cobalt phthalocyanine (CoPc)) were immobilized by a Langmuir-Blodgett technique and the detected SERS signals from graphene encapsulated AuNPs were stable over a period of 160 s. The suppression of the photobleaching was attributed to a decreased catalytic activity of the metal surface and  $\pi$ - $\pi$  interactions between the graphene shell and the CoPc molecules.

Almost at the same time, a similar observation was made by ZHAO *et al.* who used a Ag surface covered with SLG<sup>[13]</sup>. R6G was immobilized either on top or in between these two components. In both cases the photostability was significantly improved in comparison to R6G molecules on a bare Ag surface. This was verified by detecting a SERS signal over a period of 8 min.

Combining DNA origami with graphene is quiet innovative since, up to this date, is has only been subject of discussion in the report of YUN *et al.*<sup>[196]</sup>. Herein, nanopatterns of DNA origami on chemically modified graphene oxide are presented. In contrast to the publication of YUN *et al.*, the work presented in the following is based on pristine graphene that is exfoliated on top of functionalized or bare DNA origami substrates.

In **M3**<sup>3</sup> it is shown that the structural stability of bare DNA origami substrates is significantly enhanced upon graphene encapsulation. The covering sheet of SLG replicates the shape of the DNA origami triangles – even the inner holes – very well which is confirmed by AFM imaging (Figure 4.4 **a** and [**M3**, Figure 2]). The replication ability of graphene has also been demonstrated by others in the context of ds plasmid DNA<sup>[197]</sup> and 2D double-crossover lattices<sup>[198]</sup>. Furthermore, in **M3** the maximum force that is required to damage the DNA origami substrates is determined by AFM manipulation in contact mode. It is shown that the force threshold for graphene encapsulated DNA origami is over one order of magnitude higher in comparison to non-protected ones (Figure 4.4 **b** and [**M3**, Figures 4, 5]). In addition, the behaviour towards deionized water is tested, demonstrating that graphene encapsulated DNA origami structures remain intact for at least 30 min, whereas non-protected substrates are already damaged on a time scale below 1 min (Figure 4.4 **c** and [**M3**, Figure 8]).

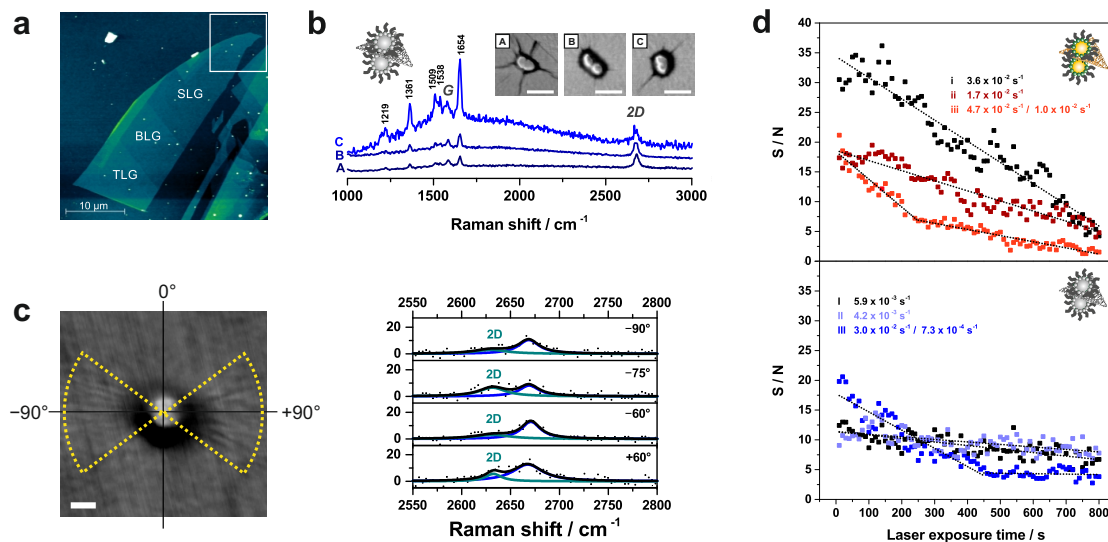


**Figure 4.4.:** AFM images from **M3**. (a) DNA origami triangles adsorbed on SiO<sub>2</sub>/Si. The lower part of the DNA origami substrates is covered by SLG. Scale bar: 500 nm. (b) Non-covered DNA origami substrates exhibit a force threshold of  $\approx 2.5$  nN (top), whereas encapsulated substrates stay intact up to an applied force of  $\approx 56$  nN (bottom). Scan areas:  $1 \times 1 \mu\text{m}^2$  (top),  $500 \times 500 \text{nm}^2$  (bottom). (c) Comparison of non-protected (left) and graphene covered DNA origami substrates after 30 min of incubation in deionized water. Scale bar: 500 nm.

<sup>3</sup> [**M3**] A. Matković, B. Vasić, J. Pešić, J. Prinz, I. Bald, A. Milosavljević, R. Gajić, “Enhanced structural stability of DNA origami nanostructures by graphene encapsulation”, *New J. Phys.* **18**, 025016 (2016).

Besides the influence of graphene on the developed SERS substrates, which will be discussed hereafter, the enhanced structural stability of DNA origami substrates upon graphene encapsulation might be advantageous for using these structures in bottom-up fabrication methods<sup>[199]</sup>.

Finally, in **M4**<sup>4</sup> all building blocks presented so far, are merged within a novel kind of hybrid material. To this end, a DNA origami substrate is first functionalized with a dye-modified 40 nm AuNP dimer and subsequently covered with a single layer of graphene (Figure 4.5 **a** and [**M4**, Figure 1]). In this way, the unique properties of each individual building block are efficiently merged.



**Figure 4.5.: Summarized results from M4.** (a) AFM image of a large graphene flake covering underlying AuNPs. (b) Correlated SERS and (phase) AFM data for three individual AuDG hybrid structures. Scale bars: 200 nm. (c) Polarization-dependent SERS measurements of one representative AuDG hybrid. The folds within the SLG lattice, which are visible in the phase AFM image (left), can be correlated to strain-induced features in the SERS spectra (right). Scale bar: 100 nm. (d) Photobleaching rates of individual AuNP dimers and AuDG hybrids obtained from the temporal evolution of the TAMRA band at  $1654\text{ cm}^{-1}$  upon prolonged laser exposure.

In order to test the competing influence of the AuNPs and graphene on incorporated TAMRA molecules, SERS signals from covered and non-covered single 40 nm AuNPs are initially compared. To this end, two different positions of the TAMRA molecules within the hybrid structures are carefully investigated ([**M4**, Figure 2]). Depending on the internal position of the TAMRA modification within the AuNP coating strands, two cases are distinguished: (i) the TAMRA molecules are located close to the AuNP surface and (ii) the TAMRA molecules are separated from the AuNP surface by a DNA spacer of 13 bases. It is shown that the TAMRA fluorescence background visible in the SERS spectra is efficiently quenched when the dyes are positioned in close proximity to the AuNP surface ([**M4**, Figure 2 **a,b**]). This is in good agreement with a previously published distance-dependent fluorescence quenching<sup>[96]</sup>. Additionally, when the two different types of AuNPs are covered by graphene, the involved dye molecules are sandwiched in between the AuNP surface and the graphene layer. In this arrangement it is shown that the interplay between the individual building blocks is highly

<sup>4</sup> [**M4**] J. Prinz, A. Matković, J. Pešić, R. Gajić, I. Bald, “Hybrid Structures for Surface-Enhanced Raman Scattering: DNA Origami/Gold Nanoparticle Dimer/Graphene”, *Small* **12**, 5458–5467 (2016).

dependent on the relative positions of dye molecules within the hybrid structure ([M4, Figure 2 b,d]). For dye molecules close to the graphene layer (but further away from the AuNP surface) the fluorescence of the TAMRA dyes is only quenched if the interaction between graphene and dye molecules is strong enough ([M4, Figure 2 d]). For the opposite case, that is, the TAMRA dyes are in close vicinity to the AuNP surface (but further away from the graphene layer) the TAMRA fluorescence is efficiently quenched for all AuNPs resulting in a clean baseline and a decreased S/N ratio ([M4, Figure 2 b]). Since the TAMRA molecules are not directly in contact with the covering layer of graphene, the underlying mechanism of fluorescence quenching is postulated to be based either on an energy transfer from excited TAMRA molecules to SLG or on a DNA-mediated charge transfer process from the AuNP to SLG. Both possibilities are schematically depicted in Figure 4.6.



**Figure 4.6.:** Postulated mechanisms for the fluorescence quenching within graphene covered AuNPs. (a) Energy transfer from excited dye molecules to SLG. (b) Charge transfer from the AuNP to SLG mediated by the DNA coating in between.

Furthermore, in agreement with the observation in M2 for dye-coated 60 nm AuNPs (see Figure A.2), non-covered dye-coated 40 nm AuNPs exhibit a wide distribution of SERS signal intensities ([M4, Figure 2 a,c]). On the contrary, the distribution of TAMRA signals for graphene encapsulated AuNPs is significantly narrower. The same effect is found for 40 nm AuNPs that are coated with Cy3-modified DNA (Cy3 located close to the AuNP surface) ([M4, Figure S2]). In this context, the higher reproducibility of SERS signals is assigned to a more stable environment of the dye molecules upon graphene protection.

Based on the findings for single AuNPs, dimeric structures are synthesized using 40 nm AuNPs with TAMRA close to the AuNP surface. SERS spectra of individual AuNP dimers and DNA origami-AuNP dimer-graphene (AuDG) hybrid structures are compared revealing the characteristic TAMRA bands at  $1219\text{ cm}^{-1}$ ,  $1361\text{ cm}^{-1}$ ,  $1509\text{ cm}^{-1}$ ,  $1538\text{ cm}^{-1}$ ,  $1570\text{ cm}^{-1}$  and  $1654\text{ cm}^{-1}$  in all cases. Again, the most intense band at  $1654\text{ cm}^{-1}$  is slightly shifted with respect to the results in M1 and M2 which is attributed to altered interactions between the AuNP surface and the dye molecules upon graphene encapsulation. Additionally, for the graphene covered AuDG hybrids the characteristic graphene features at  $1586\text{ cm}^{-1}$  (G band) and  $2670\text{ cm}^{-1}$  (2D band) are visible with the G band interfering with the TAMRA band at  $1570\text{ cm}^{-1}$  (Figure 4.5 b and [M4, Figure 3]).

In 2010, graphene itself was found to provide Raman enhancement – an effect that is termed *graphene-enhanced Raman scattering* (GERS)<sup>[200]</sup> – resulting in EFs ranging from less than 10 to approximately 100<sup>[200,201]</sup>. In contrast to the electromagnetic enhancement caused by metal substrates, GERS is based on a charge transfer process and is therefore only significant if the distance between the analyte molecules and graphene is less than 1 nm<sup>[202]</sup>. However, in all measurements related to M4 no indication for an additional enhancement caused by graphene is found. For the sake of completeness it has to be mentioned that the surface plasmon resonance of graphene is located in the range of THz<sup>[203]</sup> and accordingly does not support the electromagnetic mechanism under the here applied conditions.

As previously mentioned for the single AuNPs, the extent of contact between the graphene layer and the underlying structure significantly influences the detected SERS signal. In order to get a better understanding of the mutual interaction between AuNPs and graphene,



polarization-dependent SERS measurements of single AuDG hybrids are performed. In this context, Raman scattering can provide extensive information about uniaxial strain applied to graphene which is indicated by shifting and splitting of the G band<sup>[204,205]</sup> and the 2D band<sup>[156]</sup>. Upon graphene encapsulation the underlying structure also induces local strain within graphene. The corresponding polarization-dependent SERS experiments (Figure 4.5 **c** and [M4, Figure 4]) reveal that the 2D band is splitted in two components for certain polarization angles which are directly correlated to the direction of folds visible in the corresponding AFM image. Although the laser spot size (approximately  $1.3 \mu\text{m}^2$ ) is much larger than the strained area, the recorded SERS spectra exhibit contributions from both areas. From the amount of the 2D band splitting it is estimated that the underlying structure induces a uniaxial strain component of 1–2% within SLG.

Ultimately, a clear polarization dependence of the TAMRA signals is observed, offering new insights about the dye molecules within the hot spot. These information are only accessible due to a significantly improved photostability of the TAMRA molecules upon graphene encapsulation. This effect is quantified by determination of photobleaching rates for three AuNP dimers and three AuDG hybrids upon prolonged laser exposure of 800 s. It is found that the photobleaching rate is reduced by approximately one order of magnitude upon graphene encapsulation (Figure 4.5 **d** and [M4, Figure 5]). Again, the extent of contact between the AuNPs and the graphene layer determines the efficiency of photobleaching reduction. Furthermore, two contributions to the overall photobleaching rate can be identified: (i) heating effects due to the laser exposure and (ii) reactions with ambient oxygen. On the one hand, the latter contribution can be excluded for AuDG hybrids since SLG is impermeable to any kind of gases<sup>[150]</sup>. On the other hand, the photobleaching effect is especially pronounced in the hot spot due to plasmonic heating<sup>[206,207]</sup>. Since SLG is known to be an excellent heat conductor<sup>[149]</sup>, the arising heat can be dissipated by graphene if the extent of contact with the underlying AuNPs is sufficiently high.

## 4.2. Side projects

In addition to the manuscripts discussed in section 4.1, the present thesis also includes results from side projects which are either related to DNA origami substrates, SERS or a combination of both.

In **M5**<sup>5</sup> DNA origami substrates are used to determine absolute cross sections for UV photon-induced DNA strand breakage. To this end, two target DNA sequences (TT(ATA)<sub>3</sub>TT and TT(CTC)<sub>3</sub>TT) with a biotin marker on the 5'-end are bound to a triangular DNA origami template at predefined positions. Upon vacuum UV irradiation with energies around the ionization threshold of the involved nucleobases (6.50, 7.29, 8.44 and 8.94 eV), DNA strand breaks occur which either proceed via the DNA backbone or via fragmentation of the nucleobases. Subsequent to irradiation the strand breaks are identified by treating the DNA origami substrates with a solution of streptavidin, which binds to the biotin markers of intact target DNA sequences. In this way, intact strands can be visualized by means of AFM imaging. Ultimately, DNA origami substrates are demonstrated to be a reliable technique to determine absolute cross sections for DNA strand breakage.

In **M6**<sup>6</sup> the metallization of phospholipid nanodiscs (NDs) is investigated. These systems are

<sup>5</sup> [M5] S. Vogel, J. Rackwitz, R. Schürman, J. Prinz, A. R. Milosavljević, M. Réfrégiers, A. Giuliani, I. Bald, “Using DNA Origami Nanostructures to Determine Absolute Cross Sections for UV Photon-Induced DNA Strand Breakage”, *J. Phys. Chem. Lett.* **6**, 4589–4593 (2015).

<sup>6</sup> [M6] J. Oertel, A. Keller, J. Prinz, B. Schreiber, R. Hübner, J. Kerbusch, I. Bald, K. Fahmy, “Anisotropic metal growth on phospholipid nanodiscs via lipid bilayer expansion”, *Sci. Rep.* **6**, 26718 (2016).

highly promising to study the structure of membrane proteins, since they can provide a native-like environment. NDs are assembled from the membrane scaffold protein variant MSP1D1 and negatively charged DMPG (1,2-dimyristoyl-*sn*-glycero-3-phospho-1'-*rac*-glycerol) lipids. Subsequently, the NDs are functionalized with positively charged amine-coated AuNPs (diameter 1.4 nm). Upon electroless gold deposition metallized AuNDs are obtained, which are extensively characterized by versatile techniques including SERS measurements. The corresponding SERS spectra exhibit several characteristic peaks in the spectral regions from 800–1500  $\text{cm}^{-1}$  and from 2800–3000  $\text{cm}^{-1}$  arising from the phospholipids. Since these peaks do not occur in the spectra of non-metallized NDs this investigation demonstrates the SERS-activity of metallized AuNDs.

In **M7**<sup>7</sup> again, SERS substrates based on DNA origami templates are subject of research. However, in contrast to the main manuscripts discussed in 4.1, **M7** deals with the assembly of three differently sized AuNPs (10 nm, 20 nm and 60 nm) in order to obtain so-called gold nanolenses (AuNLs). In particular, the AuNPs are assembled in three different spatial arrangements either on one side or on different sides of the DNA origami substrate. The SERS performance of each AuNL design is studied at the single-structure level and the SERS signals are correlated to AFM, SEM and dark-field-microscopy of the individual structures. When only the 10 nm AuNP is coated with TAMRA-modified DNA it is found that the highest SERS signals arise from the design with the 20 nm, the 10 nm and the 60 nm AuNPs arranged in one row (design 20-10-60) on the same side of the DNA origami substrate. For the 20-10-60-AuNL with the most intense SERS signal an EF of  $1.4 \times 10^6$  is estimated which is, however, expected to be underestimated for reasons that are discussed in **M7**. The 20-10-60 design is further investigated by selectively labelling the 20 nm AuNP and the 60 nm AuNP with TAMRA. It is demonstrated that the area of highest field enhancement is located in the gap between the 10 nm and the 20 nm AuNP.

---

<sup>7</sup> [**M7**] C. Heck, J. Prinz, A. Dathe, V. Merk, O. Stranik, W. Fritzsche, J. Kneipp, I. Bald, “Gold nanolenses self-assembled by DNA origami”, *submitted manuscript*.

# 5

## Summary and outlook

In the previous chapters the development of a novel SERS substrate was presented, which is based on a DNA origami triangle functionalized with a AuNP dimer. The structures were synthesized via DNA hybridization between capture strands protruding from the DNA origami substrate and coating strands on the AuNP surface. All structures were investigated by correlated AFM and SERS imaging in order to assign the chemical information to a certain structure.

Initially, the potential of using DNA origami substrates for SERS applications was qualitatively verified on a few-molecule level. By optimizing the hot spot between the two AuNPs in multiple respects, the LOD could be significantly lowered, finally reaching single-molecule sensitivity. In this context, the optimization steps were related to the size and the metal of the NPs, to their interparticle gap size as well as to the position of the Raman reporter molecule (TAMRA or Cy3). Finally, the optimized structures, that is, a Au-Ag-core-shell NP dimer (Au core: 60 nm; Ag shell: 2.5 nm; gap size: 2 nm) attached to a DNA origami template, were found to exhibit EFs up to  $10^{10}$  which is sufficiently high to detect single dye molecules.

The SERS substrates were further improved by introducing a single layer of graphene. Besides the positive effect of SLG on the structural stability of DNA origami substrates, it turned out to be a highly beneficial additive to the initially explored SERS substrates. In particular, SLG can efficiently suppress the photobleaching of the investigated TAMRA molecules since it is impermeable to ambient oxygen and dissipates heat arising from the plasmonic nanostructure. Furthermore, novel insights concerning the interplay within AuNP-graphene hybrid structures were obtained.

In the overall context, the developed SERS substrate was extensively characterized in terms of its potentials and limitations. Ultimately, based on the obtained insights, the novel SERS substrates are highly promising systems for future analytical and bioapplications.

Throughout the whole thesis dyes were used as Raman reporter molecules in order to benefit from the additional resonant contribution to the EF. To obtain the same signal intensity for non-resonant molecules, the resonant contribution to the EF ( $\approx 10^5$ ) has to be compensated by the number of analyte molecules contributing to the overall signal. Thus, approximately  $10^5$  non-resonant molecules measured in a bulk sample would result in the same SERS signal intensity, corresponding to a LOD in the range of  $10^{-18}$  M. Although different SERS-based approaches were demonstrated to reach LODs in the femto-<sup>[208]</sup> or attomolar<sup>[209]</sup> range, the

main advantage of the DNA origami based substrates is the universal usability. In particular, the same basic system can be applied for the detection of a wide range of substances by simply adjusting the receptor molecule for an individual analyte. In this context, the system may also be extended to multiplexing experiments of several different analytes.

In order to use the developed SERS substrates to study the structure of biologically relevant molecules, such as DNA, aptamers or proteins, several points have to be considered. First of all, it has to be ensured that the field enhancement is sufficiently high for a gap size that is large enough for the corresponding biomolecule. To this end, the DNA origami design has to be altered with regard to a more accessible anchor point. Furthermore, it has to be noted that increasing the gap size has two main effects: (i) a reduced maximum EF within the hot spot and (ii) a less pronounced localization of the overall hot spot area. The resulting “mild” enhancement over a larger volume might be beneficial in terms of more evenly distributed SERS signals arising from individual structures. Furthermore, plasmonically induced heating effects should be less pronounced, thereby meeting the requirements of inherently delicate biomolecules. In this context, SERS measurements in solution are inevitable in order to mimic a more realistic environment and to ensure that the biomolecules are correctly aligned within the hot spot. Although the overall SERS signal obtained by such ensemble measurements is a sum of numerous individual molecules, structural information as well as insights in dynamic processes, such as protein folding or DNA strand breakage, might become accessible.

To detect a SERS signal from a single biomolecule additional effort has to be done to adjust the hot spot for the needs of the individual biomolecule. One challenge is the significantly lower Raman cross section of a biomolecule in comparison to a dye molecule due to non-resonant excitation. Accordingly, this amount has to be compensated by a higher LFIEF at the analyte position. The exact matching of the LSPR of the plasmonic nanostructure with the laser excitation line was not a primary interest in the present thesis. Consequently, by precisely tuning the LSPR of a core-shell NP dimer towards the laser excitation line, an even more efficient SERS process should result. In view of future biological applications, Ag-Au-core-shell NPs might be advantageous over the opposite core-shell system since the biocompatibility of a AuNP is maintained.

The novel approach of merging DNA origami substrates, AuNPs and graphene within one hybrid structure might also be advantageous in the field of cell-target applications. Both, AuNPs and DNA origami substrates are compatible with cellular uptake due to their sizes<sup>[195,210]</sup>. In the last few years, it was already demonstrated that graphene-AuNP hybrid structures are interesting systems for bioimaging, photothermal therapy or drug delivery<sup>[195]</sup>. For instance, it has been verified that AuNPs wrapped by graphene-oxide can serve as efficient drug carrier systems allowing for an even distribution of the anticancer agent doxorubicin inside cancer cells<sup>[195]</sup>. In another study, DNA origami substrates have been loaded by the same chemotherapy drug via intercalation and subsequently internalized by tumor cells<sup>[211]</sup>. This approach has been demonstrated to efficiently circumvent doxorubicin resistance.

In this respect, hybrid structures consisting of a DNA origami substrate, AuNPs and graphene might be beneficial drug carrier systems, since they could provide biocompatibility merged with interesting optical, thermal and mechanical properties.

The aforementioned examples elucidate the high diversity of nanotechnology, ranging from fundamental analytical applications to improved health care and the development of new materials. A high proportion of the future research in this field will – more or less obviously – affect our daily lives.

# 6

## Manuscripts

### Main manuscripts

- [M1] J. Prinz, B. Schreiber, L. Olejko, J. Oertel, J. Rackwitz, A. Keller, I. Bald, “DNA Origami Substrates for Highly Sensitive Surface-Enhanced Raman Scattering”, *J. Phys. Chem. Lett.* **4**, 4140–4145 (2013).
- [M2] J. Prinz, C. Heck, L. Ellerik, V. Merk, I. Bald, “DNA origami based Au-Ag-core-shell nanoparticle dimers with single-molecule SERS sensitivity”, *Nanoscale* **8**, 5612–5620 (2016).
- [M3] A. Matković, B. Vasić, J. Pešić, J. Prinz, I. Bald, A. R. Milosavljević, R. Gajić, “Enhanced structural stability of DNA origami nanostructures by graphene encapsulation”, *New J. Phys.* **18**, 025016 (2016).
- [M4] J. Prinz, A. Matković, J. Pešić, R. Gajić, I. Bald, “Hybrid Structures for Surface-Enhanced Raman Scattering: DNA Origami/Gold Nanoparticle Dimer/Graphene”, *Small* **12**, 5458–5467 (2016).

### Manuscripts related to side projects

- [M5] S. Vogel, J. Rackwitz, R. Schürman, J. Prinz, A. R. Milosavljević, M. Réfrégiers, A. Giuliani, I. Bald, “Using DNA Origami Nanostructures to Determine Absolute Cross Sections for UV Photon-Induced DNA Strand Breakage”, *J. Phys. Chem. Lett.* **6**, 4589–4593 (2015).
- [M6] J. Oertel, A. Keller, J. Prinz, B. Schreiber, R. Hübner, J. Kerbusch, I. Bald, K. Fahmy, “Anisotropic metal growth on phospholipid nanodiscs via lipid bilayer expansion”, *Sci. Rep.* **6**, 26718 (2016).
- [M7] C. Heck, J. Prinz, A. Dathe, V. Merk, O. Stranik, W. Fritzsche, J. Kneipp, I. Bald, “Gold nanolenses self-assembled by DNA origami”, *submitted manuscript*.

## Author contributions to the manuscripts

[M1] J. Prinz *et al.*, *J. Phys. Chem. Lett.* **4**, 4140–4145 (2013).

The DNA origami-AuNP hybrid structures were partially synthesized by the author. Additionally, the author performed the main part of the SERS and AFM measurements and in this context optimized the correlation between SERS and AFM data. Furthermore, the author contributed to the data analysis and assisted with the writing of the manuscript.

[M2] J. Prinz *et al.*, *Nanoscale* **8**, 5612–5620 (2016).

The author carried out the complete sample preparation. Furthermore, the author performed all SERS, AFM, SEM and fluorescence measurements and analyzed the corresponding data. The manuscript was written by the author with the assistance of I. Bald.

[M3] A. Matković *et al.*, *New J. Phys.* **18**, 025016 (2016).

Together with A. Matković and J. Pešić the author prepared the DNA origami substrates, immobilized them on Si wafers and finally performed the mechanical exfoliation of graphene.

[M4] J. Prinz *et al.*, *Small* **12**, 5458–5467 (2016).

All sample preparation steps were performed by the author. In this context, the author was previously instructed on the synthesis steps for graphene exfoliation by A. Matković and J. Pešić at the Center of Solid State Physics at the Institute of Physics in Belgrade, Serbia. Furthermore, the author performed all SERS and AFM measurements. The data analysis was done by the author with support by I. Bald and A. Matković. The manuscript was written by the author with the assistance of I. Bald.

[M5] S. Vogel *et al.*, *J. Phys. Chem. Lett.* **6**, 4589–4593 (2015).

The author contributed to the DNA origami sample preparation and the irradiation experiments with VUV light at the DISCO beamline of the SOLEIL synchrotron facility (France).

[M6] J. Oertel *et al.*, *Sci. Rep.* **6**, 26718 (2016).

The author recorded the SERS spectra and discussed the SERS data with the co-authors.

[M7] C. Heck *et al.*, *submitted manuscript*.

The author contributed to the development of the synthesis steps and the correlated AFM and SERS imaging.

## 6.1. Proof-of-principle

### “DNA Origami Substrates for Highly Sensitive Surface-Enhanced Raman Scattering”

*J. Phys. Chem. Lett.* **4**, 4140–4145 (2013).

- Main text: pp. 61–66
- Supporting Information (SI): pp. 67–70





## DNA Origami Substrates for Highly Sensitive Surface-Enhanced Raman Scattering

Julia Prinz,<sup>‡</sup> Benjamin Schreiber,<sup>†,#</sup> Lydia Olejko,<sup>‡</sup> Jana Oertel,<sup>‡</sup> Jenny Rackwitz,<sup>‡</sup> Adrian Keller,<sup>\*,†</sup> and Ilko Bald<sup>\*,‡,§</sup>

<sup>‡</sup>Institute of Chemistry – Physical Chemistry, University of Potsdam, Potsdam, Germany

<sup>†</sup>Institute of Ion Beam Physics and Materials Research and <sup>‡</sup>Institute of Resource Ecology, Helmholtz-Zentrum Dresden-Rossendorf, Dresden, Germany

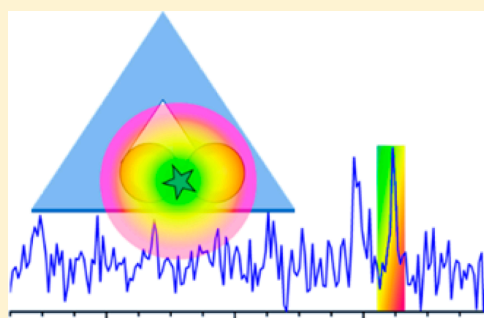
<sup>#</sup>Technische Universität Dresden, Dresden, Germany

<sup>§</sup>BAM Federal Institute of Materials Research and Testing, Berlin, Germany

### Supporting Information

**ABSTRACT:** DNA nanotechnology holds great promise for the fabrication of novel plasmonic nanostructures and the potential to carry out single-molecule measurements using optical spectroscopy. Here, we demonstrate for the first time that DNA origami nanostructures can be exploited as substrates for surface-enhanced Raman scattering (SERS). Gold nanoparticles (AuNPs) have been arranged into dimers to create intense Raman scattering hot spots in the interparticle gaps. AuNPs (15 nm) covered with TAMRA-modified DNA have been placed at a nominal distance of 25 nm to demonstrate the formation of Raman hot spots. To control the plasmonic coupling between the nanoparticles and thus the field enhancement in the hot spot, the size of AuNPs has been varied from 5 to 28 nm by electroless Au deposition. By the precise positioning of a specific number of TAMRA molecules in these hot spots, SERS with the highest sensitivity down to the few-molecule level is obtained.

**SECTION:** Physical Processes in Nanomaterials and Nanostructures



Surface-enhanced Raman scattering (SERS)<sup>1</sup> provides both single-molecule sensitivity<sup>2–5</sup> and rich chemical information and thus enables the multiplexed detection of analyte molecules at trace levels.<sup>6</sup> DNA-based plasmonic nanostructures such as nanogap particles and nanodumbbells were shown to be very efficient SERS substrates with extremely high enhancement factors for Raman scattering.<sup>7–9</sup> However, a versatile SERS substrate requires not only a controlled arrangement of nanoparticles but also specific anchor points for analyte molecules to enable quantitative analyte detection. The fabrication of substrates for highly sensitive and quantitative SERS represents the greatest challenge in current SERS research as it requires (i) a precise arrangement of metal nanoparticles to optimize the Raman scattering from the SERS hot spot, (ii) sophisticated surface functionalization for the immobilization of analytes in the hot spot, and (iii) accurate control of analyte concentration in the SERS hot spots. In this work, we thus demonstrate SERS from gold nanoparticle (AuNP) dimers immobilized on DNA origami substrates with a specific number of analyte molecules positioned in the hot spots in between the AuNPs.

DNA origami nanostructures<sup>10</sup> are versatile substrates for arranging metal nanoparticles into two- and three-dimensional arrays.<sup>11–13</sup> Due to the tunable plasmonic coupling between the

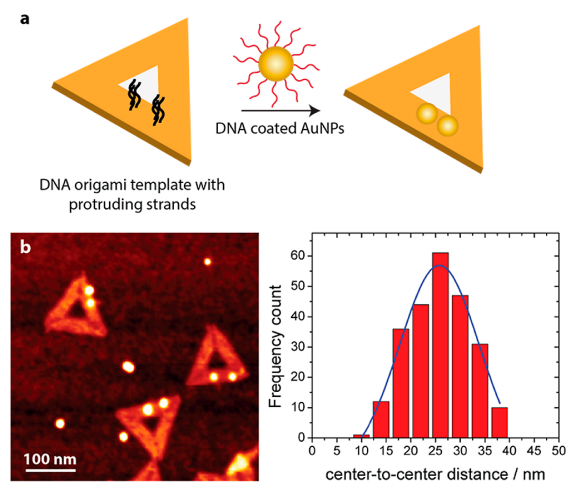
nanoparticles, assemblies with tailored optical properties can be synthesized in this way.<sup>13</sup> DNA origami nanostructures furthermore enable the spatially controlled positioning of single analyte molecules with nanometer precision, which has recently been exploited in fluorescence enhancement studies.<sup>14,15</sup> The use of DNA origami nanostructures as scaffolds to arrange AuNPs thus allows for the engineering of SERS hot spots by control of the interparticle gap and precise quantification and positioning of molecules in these gaps.

The DNA–AuNP hybrids presented here are based on triangular DNA origami nanostructures, which are formed by hybridization of the single-stranded (ss) M13mp18 viral DNA scaffold with a suitable set of 208 short staple strands.<sup>10</sup> Selected staple strands can be individually modified for instance for the binding of analyte molecules, or they can be simply extended to provide protruding ss anchoring sites for the hybridization with DNA-coated AuNPs. To bind the AuNPs, three adjacent staple strands for each AuNP are extended with a capture sequence (see the Experimental Methods section for details). The AuNPs are coated with thiol-modified ssDNA,

**Received:** September 26, 2013

**Accepted:** November 19, 2013

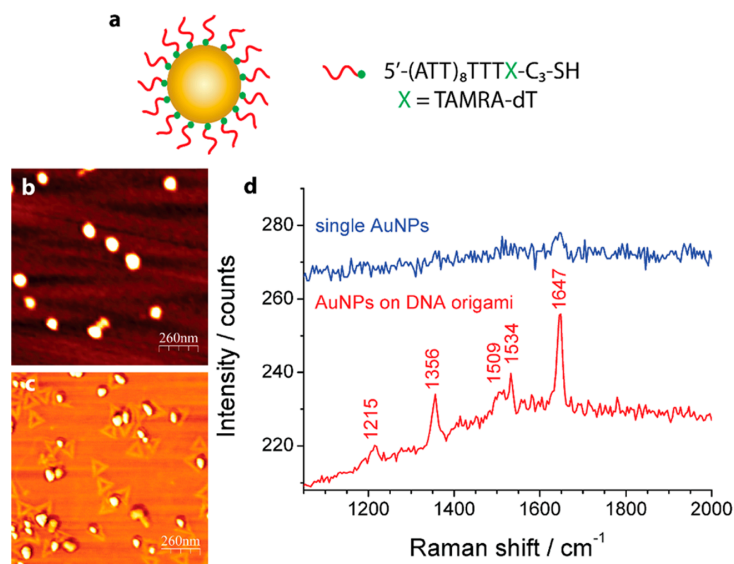
complementary to the capture sequences located on the DNA origami structure (Figure 1).<sup>12</sup> By hybridization, two AuNPs



**Figure 1.** Immobilization of AuNPs on DNA origami triangles. (a) Scheme illustrating the attachment of two DNA-coated AuNPs to the DNA origami substrate by DNA hybridization. (b) Atomic force microscopy (AFM) image of triangular DNA origami structures carrying two 5 nm AuNPs at a nominal distance of 25 nm. The histogram shows the experimentally determined distribution of the center-to-center distance between the two AuNPs, which is based on AFM images (see the Supporting Information). The bin size was 4 nm.

are bound at predefined positions to one DNA origami triangle to form a dimer. Due to the coupling of the surface plasmon resonances of the individual AuNPs, a Raman hot spot is formed in the interparticle gap. Figure 1 shows triangular DNA origami structures with two 5 nm AuNPs placed at a nominal distance of 25 nm. The interparticle distance of a total of 242 individual AuNP–DNA origami assemblies was measured by AFM (see Supporting Information Figure S1 for a larger AFM image). In agreement with the nominal value, the resulting distribution in Figure 1b reveals an average interparticle distance of 25.8 nm with a fwhm of 18.9 nm.

To demonstrate the SERS detection of specific target molecules by means of the hybrid AuNP–DNA origami structures, we used carboxytetramethylrhodamine (TAMRA) as a Raman reporter molecule. In initial experiments, we coated 15 nm AuNPs with thiol-modified ssDNA, carrying a TAMRA modification at the 5'-side of the thiol group (Figure 2a). Figure 2b shows an AFM image of disperse DNA/TAMRA-modified AuNPs adsorbed to an oxidized Si wafer. The corresponding SERS spectrum shown in Figure 2d was collected by confocal Raman microscopy using a 532 nm laser for Raman excitation. Previous studies revealed only a rather weak electric field enhancement in the vicinity of single AuNPs upon excitation of the surface plasmon resonance, resulting in an enhancement factor of  $10\text{--}10^3$  depending on the size of the AuNPs.<sup>16</sup> Consequently, the blue SERS spectrum in Figure 2d shows only a very weak TAMRA-characteristic signal at around  $1650\text{ cm}^{-1}$ . However, the Raman signal becomes considerably stronger when the AuNPs are bound to DNA origami nanostructures at a distance of 25 nm to form AuNP dimers (see the red spectrum in Figure 2d). An AFM image of

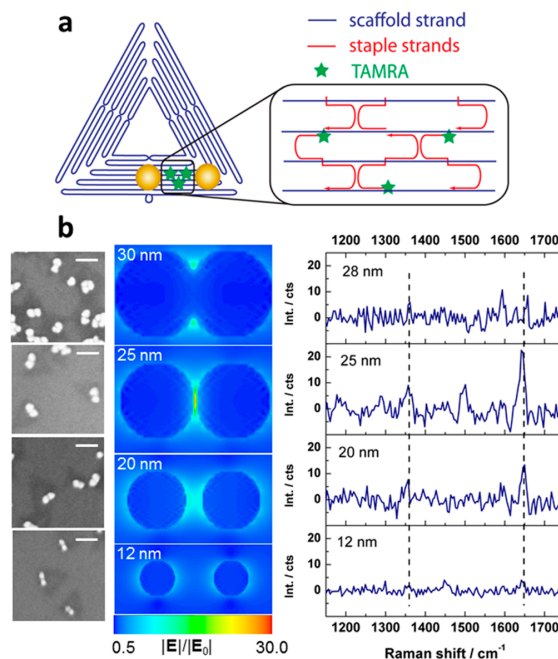


**Figure 2.** SERS measurements using TAMRA-coated AuNPs. (a) Illustration of AuNPs functionalized with DNA via a thiol group. The ssDNA is additionally modified with the fluorescent dye TAMRA (green) at the position indicated with X. (b,c) AFM images of 15 nm TAMRA–DNA-coated AuNPs (b) dispersed on a Si/SiO<sub>2</sub> substrate and (c) arranged on DNA origami substrates. (d) SERS spectra obtained from the samples shown in (b) and (c). For dispersed and isolated AuNPs, only a weak SERS signal is detected at around  $1650\text{ cm}^{-1}$ . The SERS spectrum of the DNA origami-bound AuNPs on the other hand shows bands at  $1647$ ,  $1534$ ,  $1509$ ,  $1356$ , and  $1215\text{ cm}^{-1}$ , which correspond to the characteristic SERS signals of TAMRA. The comparatively strong SERS signal is due to the DNA origami-directed formation of hot spots between the two AuNPs. The blue spectrum is shifted vertically by 65 counts. On average, the concentration of AuNPs in the DNA origami samples (red spectrum) is about 2.6 times higher than that of the single AuNP sample (blue spectrum).

TAMRA–AuNP–DNA origami substrates is shown in Figure 2c. The visible Raman bands at 1647, 1534, 1509, 1356, and 1215  $\text{cm}^{-1}$  are all characteristic SERS bands for TAMRA.<sup>17,18</sup> Due to the close proximity of the AuNPs on the DNA origami substrates, the surface plasmon resonances of the individual AuNPs can couple to form localized hot spots with particularly high electric field enhancement, which results in a correspondingly strong Raman signal. To exclude a Raman enhancement due to image charges on Si,<sup>19</sup> different substrates have been used for DNA origami adsorption, and no differences were found in the SERS intensity (Figure S4, Supporting Information).

However, it is not clear how many TAMRA molecules are located in the hot spots and contribute to the SERS signal. The red Raman spectrum shown in Figure 2d originates mainly from the TAMRA molecules located within the hot spots between the two AuNPs. To estimate the total number of molecules contributing to the SERS signal, we consider the laser focus area of 1.3  $\mu\text{m}^2$ . On the basis of our AFM images, we can assume that on average about 12 well-assembled DNA origami structures are located in the laser focus area and that each 15 nm AuNP is covered by a maximum of 200 oligonucleotides,<sup>20</sup> about 10% of which are actually located in the hot spots. Accordingly, the total number of molecules contributing to the signal is on the order of  $10^2$ – $10^3$ .

However, with the DNA origami technique, it is possible to exactly control the number of dye molecules in the hot spot. To this end, we modified three staple strands in the DNA origami substrate with TAMRA at the 5'-end such that the three TAMRA molecules were placed in between the AuNPs, that is, in the hot spot (Figure 3a). In this arrangement, the AuNPs were coated with DNA without TAMRA modification, that is, there are exactly three TAMRA molecules immobilized on each DNA origami triangle. Because the number of analyte molecules is considerably lower compared to the arrangement shown in Figure 2, the hot spots have to be further optimized in order to yield stronger electric field enhancement. When using 15 nm AuNPs at a distance of 25 nm, the gap size of 10 nm is too large to enable few-molecule detection. However, if larger AuNPs (e.g., 20 nm) are used, the yield of well-assembled AuNP dimers will be rather small due to steric hindrance. Therefore, we first immobilized two 5 nm AuNPs on the DNA origami substrates and increased their size by electroless Au deposition to optimize the gap size. By varying the incubation time, it was possible to exactly control the size of AuNPs on the DNA origami substrate and thus their interparticle gap (see Figure S5, Supporting Information). The diameters of the AuNPs have been extracted from their heights in AFM topography images, which were determined to be 12, 20, 25, and 28 nm. Subsequently, the samples have been analyzed by scanning electron microscopy (SEM) and Raman spectroscopy (Figure 3b). In addition to the SEM images and the SERS spectra obtained from the differently sized AuNPs, Figure 3b shows near-field simulations of the electric field enhancement in the vicinity of AuNPs in the discrete dipole approximation (DDA).<sup>21,22</sup> At a diameter of 20 nm, the surface plasmon resonances can couple, and a localized hot spot appears. The field enhancement is strongest at a diameter of 25 nm when the two AuNPs are almost in direct contact. At larger diameters, the two AuNPs are fused together and rather behave like rough nanorods, as indicated by the appearance of a strong second plasmon resonance in the absorbance spectra shown in Figure S6 (Supporting Information). This results in a weaker field



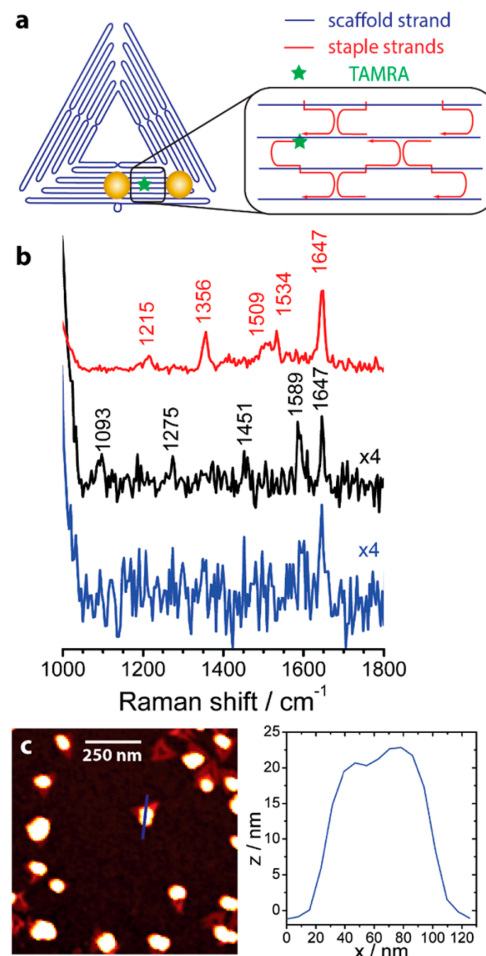
**Figure 3.** AuNPs arranged into dimers on DNA origami substrates with three single TAMRA molecules positioned in the resulting hot spots. (a) Scheme of the DNA origami substrate carrying three single TAMRA molecules between two AuNPs. In contrast to the system shown in Figure 2, no TAMRA is attached to the AuNPs. (b) Scanning electron micrographs of DNA origami–AuNP hybrid structures having AuNP diameters ranging from 12 to 28 nm (left, scale bar is 100 nm), the DDA simulations of the normalized electric field intensity  $|E|/|E_0|$  in the vicinity of the AuNP dimers (center), and corresponding SERS spectra (right). The spectral positions indicated by the dashed lines are located at 1357 and 1647  $\text{cm}^{-1}$ , respectively. The size of the AuNPs was controlled by electroless deposition of preattached 5 nm AuNPs. By variation of the deposition time, the size of the AuNPs can be precisely tuned. In the SERS spectra, the characteristic band of TAMRA at around 1650  $\text{cm}^{-1}$  appears at a AuNP diameter of 20 nm, in agreement with the appearance of a localized hot spot in the DDA simulations. The intensity of both the hot spot and the corresponding SERS spectra reaches a maximum at a AuNP diameter of 25 nm. At about a 28 nm AuNP diameter, however, the TAMRA signal decreases considerably due to the fusing of the two AuNPs and consequently weaker and more localized hot spots, as is confirmed by the DDA simulations shown on the left.

enhancement localized around the ring in the center. The corresponding SERS spectra in Figure 3b confirm the results of the simulations (see also Figure S7 (Supporting Information) for comparison of the measured SERS intensity with the intensity of the electric field in the hot spot according to the simulations). The strongest bands in the SERS spectrum of TAMRA (located at around 1650 and 1350  $\text{cm}^{-1}$ , the spectral positions are indicated by dashed vertical lines) are clearly visible for 20 nm particle size and become even more pronounced for 25 nm AuNPs. Additional signals result from the DNA surrounding the AuNPs. At larger AuNP diameter (28 nm), the TAMRA signal decreases considerably due to the weaker and more localized field enhancement when no gap between the AuNPs is present.

These experiments demonstrate that detection of three TAMRA molecules per DNA origami structure is possible with SERS using optimized AuNP dimers. In order to explore the possibility of single-molecule detection, a single TAMRA molecule was placed in the hot spot of AuNPs with 25 nm diameter. The schematic of the SERS substrate, recorded SERS spectra, and an AFM image are shown in Figure 4. The red SERS spectrum is the same as that in Figure 2 (with the fluorescent background removed) and is shown as a reference. The black spectrum represents an average of several spots on the surface, whereas the blue spectrum was obtained from a single spot. Both spectra (black and blue) exhibit a weak band at  $1647\text{ cm}^{-1}$  that corresponds to the most intense Raman band of TAMRA and thus originates from the single TAMRA molecules in the hot spots. The signal-to-noise ratio ( $S/N = (I_{\text{signal}} - I_{\text{baseline}})/\sigma_{\text{noise}}$ , with  $I$  being the signal intensity and  $\sigma$  the standard deviation) for this band is 5.8 (black spectrum) and 4.7 (blue spectrum), which is just above the detection limit of  $S/N = 3$ . Figure 4c shows an AFM image of the spot from which the blue SERS spectrum was recorded indicating that the Raman signal is due to a maximum of 17 DNA origami structures, that is, 17 independent single TAMRA molecules. The height profile shown in Figure 4c indicates that the AuNPs have an optimal diameter of 23–25 nm. This demonstrates the possibility to reach few-molecule sensitivity with optimized DNA origami-based SERS substrates. The additional Raman bands observed in the black spectrum in Figure 4b are due to the A/T-containing DNA sequences surrounding the AuNPs. The most pronounced DNA signal is detected at  $1589\text{ cm}^{-1}$ , which is due to the C–N stretching vibration of the A ring.<sup>23</sup> The signal at  $1275\text{ cm}^{-1}$  can also be assigned to the A ring, and the signal at  $1093\text{ cm}^{-1}$  is due to the  $\text{PO}_2$  stretching vibration within the DNA backbone.<sup>24</sup> The weak band at  $1451\text{ cm}^{-1}$  can be assigned to third-order Raman scattering from the Si/SiO<sub>2</sub> substrate. Control experiments using AuNP dimers on DNA origami substrates without TAMRA modification did not show any signal at around  $1650\text{ cm}^{-1}$  (Figure S8, Supporting Information).

In summary, we have demonstrated SERS from AuNP assemblies on DNA origami substrates. By exploiting the local addressability of the DNA origami nanostructures, AuNPs were arranged into dimers with tunable particle spacing in order to create localized and well-defined hot spots between the particles. We have shown that the electromagnetic field enhancement in the hot spots can be strong enough to excite specific and detectable Raman modes in fluorophores located in the hot spots. By optimizing the particle size and thus the gap size between the particles to obtain highest field enhancements, we were able to identify specific Raman bands of single TAMRA molecules attached to the DNA origami substrates.

Due to the high spatial control provided by the DNA origami technique, the hot spots can be further optimized, for instance, by realizing more complex nanoparticle arrays such as trimers of AuNPs.<sup>25</sup> Furthermore, our DNA origami-based SERS substrates can be developed into nanoscale SERS sensor chips by incorporating capture sites for target biomolecules into the hot spots. This can, for instance, be achieved by positioning a single aptamer in the hot spot that can bind to a single target protein.<sup>26</sup> Because the SERS technique provides rich chemical information, the combination of several target-specific DNA origami nanosensors may thus enable the multiplexed detection<sup>6</sup> of a variety of different analyte molecules at a single-molecule level.



**Figure 4.** SERS measurements using DNA origami-directed AuNP dimers with a single TAMRA molecule placed in the hot spot. (a) Illustration showing the functionalization of the DNA origami substrate with a single TAMRA molecule in the center between two AuNPs. (b) SERS spectra of TAMRA–DNA-coated 15 nm AuNPs arranged on DNA origami substrates (red) and DNA origami structures modified with a single TAMRA molecule placed in the hot spot between two 25 nm AuNPs (the black spectrum is an average of several spots, and the blue spectrum was obtained from a single spot). In the blue and black SERS spectra, the TAMRA signal at  $1647\text{ cm}^{-1}$  is still detectable. The other signals at 1589, 1275, and  $1093\text{ cm}^{-1}$  are ascribed to the DNA surrounding the AuNPs, whereas the weak band at  $1451\text{ cm}^{-1}$  is due to the Si/SiO<sub>2</sub> substrate. (c) AFM image of the same spot from which the blue SERS spectrum was obtained. Accordingly, a maximum of 17 isolated TAMRA molecules contribute to the Raman signal in the blue spectrum. On the right, the height profile of a AuNP dimer indicated by a blue line in the AFM image is shown.

## ■ EXPERIMENTAL METHODS

Triangular DNA origami were synthesized as previously described<sup>27</sup> from the M13mp18 viral scaffold (New England Biolabs) using the original design by Rothemund.<sup>10</sup> For the binding of the AuNPs, three staple strands per AuNP (t-6s27f, t-5s26e, t-4s27f, and t-1s6i, t1s6i, t1s8i in Rothemund's original notation) were extended on their 5'-end by the capture

sequence 5'-(AAT)<sub>8</sub>T<sub>4</sub>-3'. For the introduction of the three TAMRA molecules, three staple strands located between the capture sites (t-3s6e, t-2s7f, and t-1s6e) were modified to carry a 5' TAMRA modification. For the DNA origami with only one TAMRA modification, only the modified staple strand t-1s6e was used. All staple strands were purchased from Metabion.

DNA-coated AuNPs were prepared similar to the protocol of Ding et al.<sup>12</sup> Phosphinated AuNPs were coated with DNA in 0.5 × TAE with 50 mM NaCl (both from Sigma Aldrich) by adding a 200-fold excess of 3' disulfide-modified oligonucleotides of the sequence 5'-(ATT)<sub>3</sub>T<sub>4</sub>-3' (for 5 nm AuNPs) or 5'-(ATT)<sub>8</sub>T<sub>4</sub>-3' (for 15 nm AuNPs) (Metabion). The resulting solution was left at room temperature for at least 80 h. Unbound oligos were removed by spin filtering the AuNP solution (50 μL + 200 μL of 1 × TAE with 10 mM MgCl<sub>2</sub>, Sigma Aldrich) using Amicon Ultra-0.5 filters (100 kDa MWCO, Millipore) for 10 min at 2400 g, followed by washing with 300 μL of 1 × TAE-MgCl<sub>2</sub>. For TAMRA-modified 15 nm AuNPs, oligonucleotides of the sequence 5'-(ATT)<sub>8</sub>T<sub>3</sub>X-SS-3', with X = TAMRA, have been used (Metabion).

A 2 μL aliquot of the DNA origami sample (concentration ≈ 20 nM) was incubated for 1 h in 48 μL of 10 × TAE with 200 mM MgCl<sub>2</sub> on epi-polished Si(100) substrates with native oxide (1 × 1 cm<sup>2</sup>, cleaned in an O<sub>2</sub> plasma). The substrates were then washed with 10–15 mL of 1:1 H<sub>2</sub>O/ethanol and dried in a stream of N<sub>2</sub>.

For hybridization of the adsorbed DNA origami with 5 nm AuNPs, 20 μL of the AuNP solution (50–100 nM) was then deposited on the substrate and incubated for 20 min at 21 °C. Excess AuNPs were removed by dipping the substrate for 10 s into Milli-Q water followed by drying in a stream of N<sub>2</sub>.

The hybridization of DNA-modified 15 nm AuNPs to the DNA origami structures was performed in solution by incubation of an equimolar mixture (concentration of AuNPs and DNA origami ≈ 50 nM) for 7 h at 30 °C. Subsequently, the DNA origami structures were deposited on Si(100) substrates, as described above. The DNA-modified 15 nm AuNPs without a DNA origami substrate were deposited on Si(100) in the same way.

Electroless deposition was performed at 21 °C using GoldEnhance LM/Blot from Nanoprobes. The four solutions were mixed as suggested by the manufacturer and diluted 1:1 in 1 × TAE-MgCl<sub>2</sub> buffer before applying 20 μL of the resulting solution to the Si substrates with the adsorbed AuNP-decorated DNA origami. The deposition time was varied between 30 and 100 s before washing the sample with 1 mL of Milli-Q water. The size of the AuNPs was determined as a function of deposition time from AFM images, and a constant growth rate of 2.5 Å/s was obtained (see Figure S5, Supporting Information). AFM imaging was performed in air using a Bruker MultiMode 8 (Figures 1, 4, S1, and S5 (Supporting Information)) and a Nanosurf FlexAFM (Figures 2 and S2 (Supporting Information)) scanning probe microscope operated in tapping mode.

SERS spectra have been recorded using a confocal Raman microscope (WITec 300α) equipped with an upright optical microscope. For Raman excitation, laser light at 532 nm was used that was coupled into a single-mode optical fiber and focused through a 100× objective (Olympus MPlanFL N, NA = 0.9) to a diffraction-limited spot of about 1.3 μm<sup>2</sup>. The laser power was set between 0.4 and 1 mW, and the integration time was either 2 s (for TAMRA coated AuNPs, Figure 2) or 10 s (for TAMRA bound to DNA origami structures; Figures 3 and

4). The coverage of DNA origami structures was chosen such that about 10 DNA origami structures were located in the laser focus area. The Raman spectra presented in Figures 2 (red) and 4 (red and black) are averages from different spots. The other displayed Raman spectra were collected from a single spot and correlated with AFM images using the following procedure: (i) introduction of a macroscopic marker, namely, a scratch in the Si samples, (ii) scanning of approximately the same 15 × 15 μm<sup>2</sup> area close to the marker by AFM (1024 × 1024 pixels) and confocal Raman microscopy (30 × 30 pixels), (iii) identification of pronounced surface features in both images that allow for an overlay of the images, and (iv) assignment of individual Raman spectra to surface topography recorded by AFM.

## ■ ASSOCIATED CONTENT

### Supporting Information

Extended methods, characterization of DNA origami–AuNP hybrids by AFM (Figure S1), AFM image and Raman spectra of AuNPs covered with TAMRA-modified DNA (Figures S2 and S3), SERS spectra on different substrates (Figure S4), AuNP growth rate (Figure S5), simulated absorbance spectra (Figure S6), comparison of SERS intensity and electric field intensity (Figure S7), and SERS spectrum of the control sample (Figure S8). This material is available free of charge via the Internet at <http://pubs.acs.org>.

## ■ AUTHOR INFORMATION

### Corresponding Authors

\*E-mail: [a.keller@hzdr.de](mailto:a.keller@hzdr.de).

\*E-mail: [bald@uni-potsdam.de](mailto:bald@uni-potsdam.de).

### Notes

The authors declare no competing financial interest.

## ■ ACKNOWLEDGMENTS

We thank S. Benemann and Dr. R. Bienert at the BAM for recording SEM images and S. Facsko for discussions. This research was supported by a Marie Curie FP7 Integration Grant within the 7th European Union Framework Programme, by the Deutsche Forschungsgemeinschaft (DFG), the University of Potsdam, and the Alexander von Humboldt Foundation.

## ■ REFERENCES

- (1) Willets, K. A.; Van Duyne, R. P. Localized Surface Plasmon Resonance Spectroscopy and Sensing. *Annu. Rev. Phys. Chem.* **2007**, *58*, 267–297.
- (2) Kneipp, K.; Wang, Y.; Kneipp, H.; Perelman, L. T.; Itzkan, I.; Dasari, R.; Feld, M. S. Single Molecule Detection Using Surface-Enhanced Raman Scattering (SERS). *Phys. Rev. Lett.* **1997**, *78*, 1667–1670.
- (3) Kneipp, J.; Kneipp, H.; Kneipp, K. SERS — A Single-Molecule and Nanoscale Tool for Bioanalytics. *Chem. Soc. Rev.* **2008**, *37*, 1052–1060.
- (4) Le Ru, E. C.; Etchegoin, P. G. Single-Molecule Surface-Enhanced Raman Spectroscopy. *Annu. Rev. Phys. Chem.* **2012**, *63*, 65–87.
- (5) Lee, H. M.; Jin, S. M.; Kim, H. M.; Suh, Y. D. Single-Molecule Surface-Enhanced Raman Spectroscopy: A Perspective on the Current Status. *Phys. Chem. Chem. Phys.* **2013**, *14*, 5276–5287.
- (6) Cao, Y. W. C.; Jin, R. C.; Mirkin, C. A. Nanoparticles with Raman Spectroscopic Fingerprints for DNA and RNA Detection. *Science* **2002**, *297*, 1536–1540.
- (7) Graham, D.; Thompson, D. G.; Smith, W. E.; Faulds, K. Control of Enhanced Raman Scattering Using a DNA-Based Assembly Process of Dye-Coded Nanoparticles. *Nat. Nanotechnol.* **2008**, *3*, 548–551.

- (8) Lim, D.-K.; Jeon, K.-S.; Hwang, J.-H.; Kim, H.; Kwon, S.; Suh, Y. D.; Nam, J.-M. Highly Uniform and Reproducible Surface-Enhanced Raman Scattering from DNA-Tailorable Nanoparticles with 1-nm Interior Gap. *Nat. Nanotechnol.* **2011**, *6*, 452–460.
- (9) Lim, D.-K.; Jeon, K.-S.; Kim, H. M.; Nam, J.-M.; Suh, Y. D. Nanogap-Engineerable Raman-Active Nanodumbbells for Single-Molecule Detection. *Nat. Mater.* **2010**, *9*, 60–67.
- (10) Rothemund, P. W. K. Folding DNA to Create Nanoscale Shapes and Patterns. *Nature* **2006**, *440*, 297–302.
- (11) Pal, S.; Deng, Z. T.; Ding, B. Q.; Yan, H.; Liu, Y. DNA-Origami-Directed Self-Assembly of Discrete Silver-Nanoparticle Architectures. *Angew. Chem., Int. Ed.* **2010**, *49*, 2700–2704.
- (12) Ding, B. Q.; Deng, Z. T.; Yan, H.; Cabrini, S.; Zuckermann, R. N.; Bokor, J. Gold Nanoparticle Self-Similar Chain Structure Organized by DNA Origami. *J. Am. Chem. Soc.* **2010**, *132*, 3248.
- (13) Kuzyk, A.; Schreiber, R.; Fan, Z. Y.; Pardatscher, G.; Roller, E. M.; Hogege, A.; Simmel, F. C.; Govorov, A. O.; Liedl, T. DNA-Based Self-Assembly of Chiral Plasmonic Nanostructures with Tailored Optical Response. *Nature* **2012**, *483*, 311–314.
- (14) Acuna, G. P.; Moller, F. M.; Holzmeister, P.; Beater, S.; Lalkens, B.; Tinnefeld, P. Fluorescence Enhancement at Docking Sites of DNA-Directed Self-Assembled Nanoantennas. *Science* **2012**, *338*, 506–510.
- (15) Pal, S.; Dutta, P.; Wang, H. N.; Deng, Z. T.; Zou, S. L.; Yan, H.; Liu, Y. Quantum Efficiency Modification of Organic Fluorophores Using Gold Nanoparticles on DNA Origami Scaffolds. *J. Phys. Chem. C* **2013**, *117*, 12735–12744.
- (16) Joseph, V.; Matschulat, A.; Polte, J.; Rolf, S.; Emmerling, F.; Kneipp, J. SERS Enhancement of Gold Nanospheres of Defined Size. *J. Raman Spectrosc.* **2011**, *42*, 1736–1742.
- (17) Park, T.; Lee, S.; Seong, G. H.; Choo, J.; Lee, E. K.; Kim, Y. S.; Ji, W. H.; Hwang, S. Y.; Gweon, D. G. Highly Sensitive Signal Detection of Duplex Dye-Labelled DNA Oligonucleotides in a Pdms Microfluidic Chip: Confocal Surface-Enhanced Raman Spectroscopic Study. *Lab Chip* **2005**, *5*, 437–442.
- (18) Stokes, R. J.; Macaskill, A.; Lundahl, P. J.; Smith, W. E.; Faulds, K.; Graham, D. Quantitative Enhanced Raman Scattering of Labeled DNA from Gold and Silver Nanoparticles. *Small* **2007**, *3*, 1593–1601.
- (19) Mock, J. J.; Hill, R. T.; Degiron, A.; Zauscher, S.; Chilkoti, A.; Smith, D. R. Distance-Dependent Plasmon Resonant Coupling between a Gold Nanoparticle and Gold Film. *Nano Lett.* **2008**, *8*, 2245–2252.
- (20) Cutler, J. I.; Auyeung, E.; Mirkin, C. A. Spherical Nucleic Acids. *J. Am. Chem. Soc.* **2012**, *134*, 1376–1391.
- (21) Draine, B. T.; Flatau, P. J. Discrete-Dipole Approximation for Scattering Calculations. *J. Opt. Soc. Am. A* **1994**, *11*, 1491–1499.
- (22) Flatau, P. J.; Draine, B. T. Fast Near Field Calculations in the Discrete Dipole Approximation for Regular Rectilinear Grids. *Opt. Express* **2012**, *20*, 1247–1252.
- (23) Jang, N. H. The Coordination Chemistry of DNA Nucleosides on Gold Nanoparticles as a Probe by SERS. *Bull. Korean Chem. Soc.* **2002**, *23*, 1790–1800.
- (24) Treffer, R.; Lin, X.; Bailo, E.; Deckert-Gaudig, T.; Deckert, V. Distinction of Nucleobases — A Tip-Enhanced Raman Approach. *Beilstein J. Nanotechnol.* **2011**, *2*, 628–637.
- (25) Wustholz, K. L.; Henry, A. I.; McMahon, J. M.; Freeman, R. G.; Valley, N.; Piotti, M. E.; Natan, M. J.; Schatz, G. C.; Van Duyne, R. P. Structure–Activity Relationships in Gold Nanoparticle Dimers and Trimers for Surface-Enhanced Raman Spectroscopy. *J. Am. Chem. Soc.* **2010**, *132*, 10903–10910.
- (26) Rinker, S.; Ke, Y.; Liu, Y.; Chhabra, R.; Yan, H. Self-Assembled DNA Nanostructures for Distance-Dependent Multivalent Ligand–Protein Binding. *Nat. Nanotechnol.* **2008**, *3*, 418–422.
- (27) Keller, A.; Bald, I.; Rotaru, A.; Cauet, E.; Gothelf, K. V.; Besenbacher, F. Probing Electron-Induced Bond Cleavage at the Single-Molecule Level Using DNA Origami Templates. *ACS Nano* **2012**, *6*, 4392–4399.

## Supporting Information

### “DNA Origami Substrates for Highly Sensitive Surface-Enhanced Raman Scattering”

#### 1. Methods

##### *Preparation of DNA-coated AuNPs*

DNA-coated AuNPs were prepared similar to the protocol of Ding *et al.* [1] First, 2 mg of Bis(psulfonatophenyl) phenylphosphine dihydrate dipotassium salt (BSPP, Sigma Aldrich) were added to 15 mL of the colloidal gold solution (5 nm and 15 nm diameter, citrate-stabilized, BBIInternational), covered with an aluminium foil and stirred slowly for 24 hours. NaCl was then slowly added to the solution until the color changed from red to purple, at which point the solution was centrifuged for 30 min at 500 *g*. The supernatant was gently removed and 0.3 mL of 2.5 mM BSPP solution was added to re-suspend the particles, indicated by another color change from black purple to dark red. After addition of 0.5 mL methanol the solution was centrifuged another 30 min at 500 *g*. After removal of the supernatant, the particles were re-suspended in 0.2 mL of 2.5 mM BSPP solution. The AuNPs were coated with DNA in 0.5x TAE with 50 mM NaCl (both from Sigma Aldrich) by adding a 200-fold excess of 3' disulfide-modified oligonucleotides of the sequence 5'-(ATT)<sub>3</sub>T<sub>4</sub>-3' (for 5 nm AuNPs), or 5'-(ATT)<sub>8</sub>T<sub>4</sub>-3' (for 15 nm AuNPs), respectively (Metabion). The resulting solution was left at room temperature for at least 80 hours. Unbound oligos were removed by spin filtering the AuNP solution (50  $\mu$ L + 200  $\mu$ L of 1x TAE with 10 mM MgCl<sub>2</sub>, Sigma Aldrich) using Amicon Ultra-0.5 filters (100 kDa MWCO, Millipore) for 10 min at 2400 *g*, followed by washing with 300  $\mu$ L of 1x TAE-MgCl<sub>2</sub>. For TAMRA-modified 15 nm AuNPs, oligonucleotides of the sequence 5'-(ATT)<sub>8</sub>T<sub>3</sub>X-SS-3' with X = TAMRA have been used (Metabion).

##### *AFM imaging*

AFM imaging was performed in air using a Bruker MultiMode 8 (Figure 1, 4, S1, and S5) and a Nanosurf FlexAFM (Figure 2 and S2) scanning probe microscope operated in tapping mode. Soft tapping cantilevers Tap150Al-G from BudgetSensors with a force constant of nominally 5 N/m and a tip radius of < 10 nm have been used. The AFM images were obtained from samples deposited on Si(100) (Figure 1, Figure 2b, and Figure 4) or mica (Figure 2c).

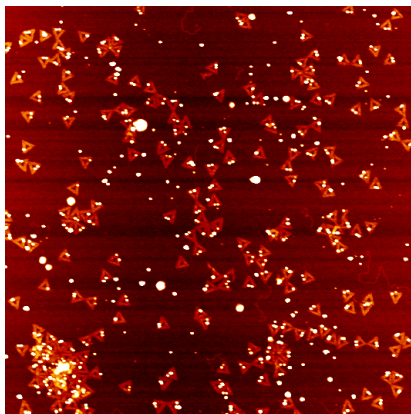
##### *DDA simulations*

DDA simulations have been performed using DDSCAT 7.2. [2,3] The number of dipoles was kept rather constant for all simulations at about 28,000. The refractive index of the environment was adjusted to 1.24 in order to reproduce the position of the plasmon resonance of the DNA-coated AuNPs (520 nm) obtained from absorption measurements. The near-field images (Figure 3) were obtained at an excitation wavelength of 532 nm with the polarization being parallel to the dimer axis.

##### *SEM imaging*

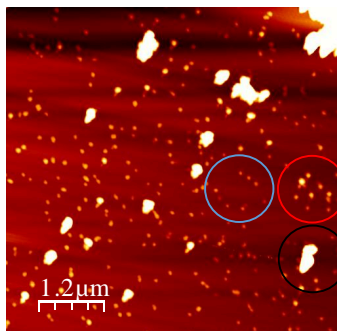
SEM imaging was performed on a Zeiss Gemini Supra 40 instrument using 3 kV acceleration voltage.

## 2. Characterization of DNA origami - AuNP hybrids by AFM

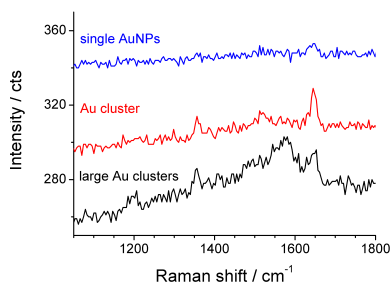


**Figure S1:** AFM image of a DNA origami sample functionalized with two 5 nm AuNPs. The image was used to characterize the center-to-center distance of AuNPs.

## 3. AFM image and Raman spectra of AuNPs covered with TAMRA modified DNA



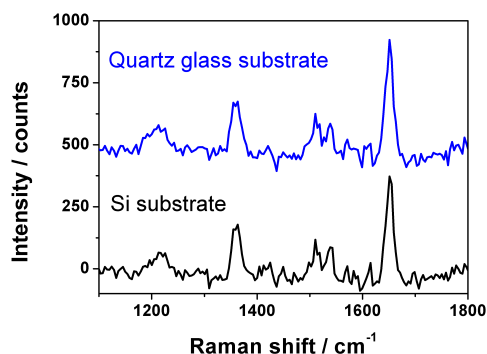
**Figure S2:** AFM image of AuNPs covered with TAMRA modified DNA deposited on a Si surface. Single isolated AuNPs are visible, but also clusters of different size. On the top-right corner the end of the scratch in the Si substrate is visible that is used to correlate AFM and confocal Raman microscopy images. Correlated confocal Raman microscopy allows for an assignment of Raman spectra to the isolated AuNPs and clusters. The indicated positions correspond to the Raman spectra shown in Figure S3.



**Figure S3:** Raman spectra obtained from the positions indicated in the AFM image shown in Figure S2. Single AuNPs show only a very weak signal originating from the strongest band from TAMRA. The AuNP clusters show a significant fluorescence background and TAMRA specific Raman bands. For larger clusters stronger signals from the surrounding DNA are obtained. The blue spectrum is shifted vertically by 140 cts and the red spectrum is shifted vertically by 80 cts.

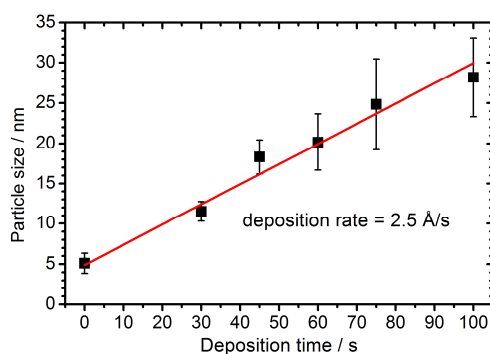


#### 4. SERS spectra on different substrates



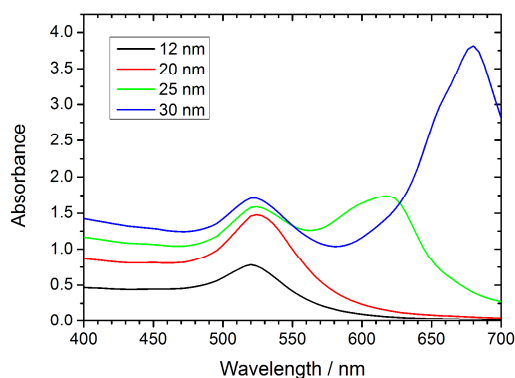
**Figure S4:** SERS spectra of 15 nm AuNP dimers covered with TAMRA modified DNA and immobilized on DNA origami triangles, which are adsorbed on two different substrates, quartz glass and Si. Due to the strong signal on the quartz glass substrate an enhancement ascribed to image charges present on Si can be excluded. Both spectra are baseline corrected and represent the sum of ten single spectra.

#### 5. AuNP growth rate



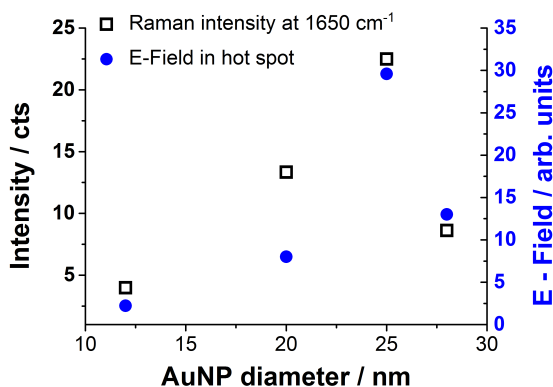
**Figure S5:** AuNP size as a function of deposition time as determined by AFM.

#### 6. Simulated absorbance spectra



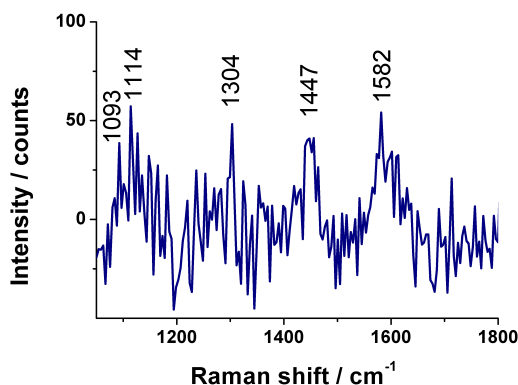
**Figure S6:** Simulated absorbance spectra of AuNP dimers with 25 nm distance in dependence of particle diameter. The spectra have been averaged over polarizations being parallel and perpendicular to the dimer axis. Note that no significant red shift of the plasmon resonance at 520 nm is observed with increasing AuNP diameter.

## 7. Comparison of SERS intensity and electric field intensity



**Figure S7:** SERS signal intensity of the 1650 cm<sup>-1</sup> band and electrical field intensity according to DDA simulations (see Figure 3) plotted against AuNP diameter.

## 8. SERS spectrum of control sample (pure DNA)



**Figure S8:** SERS spectra of a control sample of DNA origami structures carrying two AuNPs but no TAMRA modification were recorded (integration time 10 s). Most spectra do not show any detectable SERS signal, but in some spectra SERS signals are detected that are due to the DNA surrounding the AuNPs. A typical SERS spectrum with DNA background signals is shown here.

## 9. References

- [1] B. Q. Ding, Z. T. Deng, H. Yan, S. Cabrini, R. N. Zuckermann, J. Bokor, “Gold Nanoparticle Self-Similar Chain Structure Organized by DNA Origami”, *J. Am. Chem. Soc.* **132**, 3248–3249 (2010).
- [2] P. J. Flatau, B. T. Draine, “Fast Near Field Calculations in the Discrete Dipole Approximation for Regular Rectilinear Grids”, *Opt. Express* **20**, 1247–1252 (2012).
- [3] B. T. Draine, P. J. Flatau, “User Guide to the Discrete Dipole Approximation Code DDSCAT 7.2”, <http://arxiv.org/abs/1202.3424v3>, (2012).

## 6.2. Single-molecule-SERS

**“DNA origami based Au-Ag-core-shell nanoparticle dimers  
with single-molecule SERS sensitivity”**

*Nanoscale* **8**, 5612–5620 (2016).

- Main text: pp. 73–81
- Electronic Supplementary Information (ESI): pp. 82–89



Cite this: *Nanoscale*, 2016, 8, 5612

## DNA origami based Au–Ag-core–shell nanoparticle dimers with single-molecule SERS sensitivity†

J. Prinz,<sup>a</sup> C. Heck,<sup>a,b,c</sup> L. Ellerik,<sup>a</sup> V. Merk<sup>c</sup> and I. Bald<sup>\*a,b</sup>

DNA origami nanostructures are a versatile tool to arrange metal nanostructures and other chemical entities with nanometer precision. In this way gold nanoparticle dimers with defined distance can be constructed, which can be exploited as novel substrates for surface enhanced Raman scattering (SERS). We have optimized the size, composition and arrangement of Au/Ag nanoparticles to create intense SERS hot spots, with Raman enhancement up to  $10^{10}$ , which is sufficient to detect single molecules by Raman scattering. This is demonstrated using single dye molecules (TAMRA and Cy3) placed into the center of the nanoparticle dimers. In conjunction with the DNA origami nanostructures novel SERS substrates are created, which can in the future be applied to the SERS analysis of more complex biomolecular targets, whose position and conformation within the SERS hot spot can be precisely controlled.

Received 6th December 2015,

Accepted 11th February 2016

DOI: 10.1039/c5nr08674d

www.rsc.org/nanoscale

### Introduction

The DNA origami technique introduced by Paul Rothemund in 2006<sup>1</sup> is a versatile tool that allows for the programmable folding of DNA in various shapes and patterns. Since then, the technique has extensively been applied in order to create for instance three-dimensional structures such as 3D curved structures<sup>2</sup> or structures with switchable conformations based on DNA regulation.<sup>3</sup> Recently, a new approach for the formation of higher-order 3D objects *via* shape recognition and without base pairing has been demonstrated.<sup>4</sup> Since DNA origami templates can be easily modified in numerous ways this technique is frequently used in the field of analytical science. Several DNA origami based studies use atomic force microscopy (AFM) for analytical applications *e.g.* for the detection of inorganic or organic targets,<sup>5</sup> to analyze enzymatic DNA repair activity<sup>6</sup> or to study DNA strand breaks.<sup>7,8</sup> Furthermore, optical methods such as fluorescence spectroscopy are widely used for the ana-

lysis of DNA origami templates *e.g.* to perform super-resolution imaging<sup>9</sup> or to study G-quadruplex folding.<sup>10</sup>

One of the main advantages of DNA origami templates is the possibility of arranging functional units, *e.g.* gold nanoparticles (AuNPs), with nm precision, which makes it a predestined technique for the study of plasmonic effects<sup>11,12</sup> and surface-enhanced spectroscopies.

Surface-enhanced spectroscopies are based on the enhancement of the electromagnetic field close to metal nanoparticles (NPs) upon excitation of their surface plasmon resonance. This can result in enhanced optical signals such as fluorescence and Raman scattering. Particularly high field enhancement can be generated in the gap between adjacent NPs due to a coupling of the individual surface plasmon resonances.<sup>13,14</sup> Thus, to benefit from highest field enhancements it is required to control the position of the AuNPs with respect to the analyte molecules.

Depending on the distance to the plasmonic nanostructure a fluorescent dye can be subject to fluorescence quenching<sup>15</sup> or fluorescence enhancement.<sup>16</sup> At close distance to the NP surface analyte molecules can also be detected by surface-enhanced Raman scattering (SERS).<sup>17–20</sup> SERS is a particularly interesting technique since the Raman signal can be enhanced by many orders of magnitude, which renders the detection of single molecules possible.<sup>21,22</sup>

Apart from using ultralow analyte concentrations different approaches aiming at the detection of SERS from single molecules have been developed. On the one hand, the bi-analyte method has been introduced by Le Ru *et al.*,<sup>23</sup> which is based on the measurement of a mixture of two substances with dis-

<sup>a</sup>Institute of Chemistry, University of Potsdam, Karl-Liebknecht-Str. 24-25, 14469 Potsdam, Germany. E-mail: bald@uni-potsdam.de

<sup>b</sup>BAM Federal Institute for Materials Research and Testing, Richard-Willstätter Str. 11, 12489 Berlin, Germany

<sup>c</sup>Department of Chemistry + SALSA, Humboldt-Universität zu Berlin, Brook-Taylor-Str. 2, 12489 Berlin, Germany

† Electronic supplementary information (ESI) available: Additional information about materials and methods, designs of DNA origami templates, height profiles, additional SERS spectra, assignment of DNA bands, SEM images, additional AFM images, FDTD simulations, additional reference spectra for Cy3 and detailed description of EF estimation, simulated absorption and scattering spectra. See DOI: 10.1039/c5nr08674d

tinguishable SERS spectra. Subsequently, single-molecule events have to be asserted by a statistical analysis. The bi-analyte method has been improved by isotopic labelling of dyes resulting in spectral shifts of certain SERS peaks.<sup>24</sup> On the other hand, dimers of Au–Ag-core-shell NPs with tailored gap size have been used for single-molecule SERS. Suh *et al.* presented gap-tailored Au–Ag core-shell nanodumbbells providing enhancement factors (EFs) of the order  $10^{12}$  as well as gold nanobridged nanogap particles generating EF values between  $10^8$ – $10^9$  for about 90% of the enhancing sites.<sup>25,26</sup> In both cases the gap sizes were in the range of 1 nm and the EFs were high enough for the detection of single Cy3 dyes.

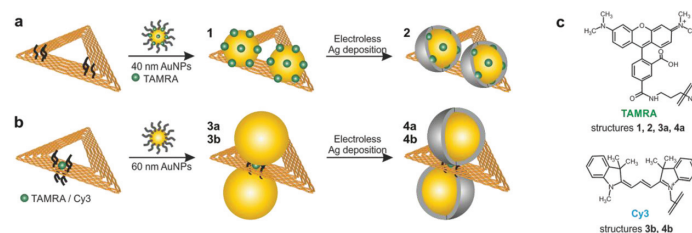
The use of DNA origami structures as scaffolds for SERS active nanostructures is particularly attractive due to their versatility with respect to further functionalization. Additionally, the DNA origami technique represents a bottom-up approach, which allows for the production of a large number of plasmonic nanostructures at once. Such processes are much more cost-effective than widely used top-down lithography methods.<sup>27</sup> Here, we present DNA–AuNP hybrids that are optimized in various respects in order to increase the SERS sensitivity to a single-molecule level. To the best of our knowledge, this is the first study that combines the DNA origami technique with SERS to detect single molecules. Furthermore, we have estimated EFs for selected nanostructures through direct correlation of AFM and Raman images.

Here, we present structures based on triangular DNA origami substrates that are functionalized with AuNP dimers. The DNA origami substrates are folded during a hybridization process between the M13mp18 ssDNA scaffold strand and 208 suitable ssDNA staple strands.<sup>1</sup> By modification of certain staple strands with a capture sequence that protrudes from the DNA triangle anchor points for AuNPs are introduced (see Experimental section for details). Fig. 1 illustrates the attachment process of AuNP dimers to the DNA origami template. Two different strategies (Fig. 1a and b) are pursued that differ in terms of the positions of AuNPs as well as analyte molecules (carboxytetramethylrhodamine (TAMRA), cyanine 3 (Cy3);

molecular structures shown in Fig. 1c). In both strategies the attachment process is realized *via* DNA hybridization between the ssDNA capture sequences ( $5'-(AAA)_8T_4-3'$ ) and the ssDNA coating strands ( $5'-(TTT)_4T-SH-3'$ ) covering the AuNPs. In strategy (a) two 40 nm AuNPs are attached to one side of the DNA origami template by three anchor points per particle resulting in structure 1. In that case the AuNPs are covered with a TAMRA-modified sequence ( $5'-(TTT)_4TX-SH-3'$ ; X = TAMRA) and a non-TAMRA-modified thiolated DNA strand used as a spacer to reduce the TAMRA concentration on the AuNP surface. In contrast, in strategy (b) one single analyte molecule (TAMRA or Cy3) is incorporated into the DNA origami template by modification of one staple strand. In the following step two 60 nm AuNPs are attached to different sides of the DNA origami template by four anchor points per particle resulting in structure 3a (TAMRA) or 3b (Cy3). The different DNA–AuNP hybrids (structures 1, 3a, 3b) are further modified by electroless silver deposition yielding DNA–Au–Ag-core-shell hybrids (structures 2, 4a, 4b). For subsequent Raman and AFM studies the hybrid structures are adsorbed on Si substrates.

Single-particle SERS measurements are performed by correlation of AFM images and Raman maps as illustrated in Fig. 2. For SERS experiments a confocal Raman microscope and a 532 nm excitation laser is used resulting in resonant excitation of TAMRA or Cy3. AFM (Fig. 2, blue frame) and SERS images (Fig. 2, red frame) are superimposed by means of a marker on the Si surface. This approach allows for a direct assignment of SERS signals to specific DNA–AuNP hybrid structures. In this way the effect of NP structure modification on the SERS enhancement is revealed.

In Fig. 3 correlated AFM images and SERS spectra for single DNA origami substrates functionalized with a 40 nm AuNP dimer covered with TAMRA-modified DNA (structure 1) are shown. The maximum gap size of approximately 14 nm between the two individual particles is estimated by considering the number of DNA bases located in the DNA origami between the two center positions of the particles (see Fig. S1 in the ESI† for details). Within the remaining structural flexibility



**Fig. 1** Formation of AuNP dimers using DNA origami substrates. The attachment process is realized by DNA hybridization between ssDNA capture strands protruding from the substrate and the complementary ssDNA coating of the AuNPs. (a) Two 40 nm AuNPs coated with the dye-modified sequence  $5'-(TTT)_4TX-SH-3'$  (X = TAMRA) are attached to one side of the DNA origami template resulting in structure 1 with an estimated gap size of 14 nm. Subsequent silver enhancement leads to Au–Ag-core-shell NPs with a decreased gap size (structure 2). (b) For single-molecule measurements one dye molecule (either TAMRA or Cy3) is incorporated into the DNA origami template. The attachment of two 60 nm AuNPs to different sides of the DNA origami ensures the position of the dye to be exactly in the hot spot (structures 3a, 3b). Subsequent addition of a silver layer results in structures 4a or 4b. (c) Raman reporter molecules used in the present study with the covalent connection between dye and ssDNA marked in both molecular structures. Structures 1, 2, 3a and 4a are functionalized with TAMRA whereas structures 3b and 4b contain a Cy3 modification.

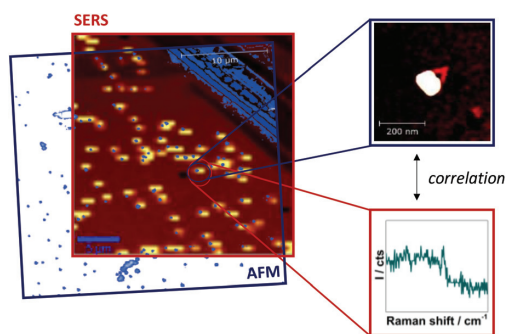


Fig. 2 Illustration of correlated AFM and SERS imaging. AFM and SERS images are superimposed using a scratch on the Si as a marker in order to correlate structural and chemical information. In this way SERS signals can clearly be assigned to defined structures (the laser spot diameter is approximately 1.3  $\mu\text{m}$ ). For better visualization the large scan-size AFM image is shown in transparent colors.

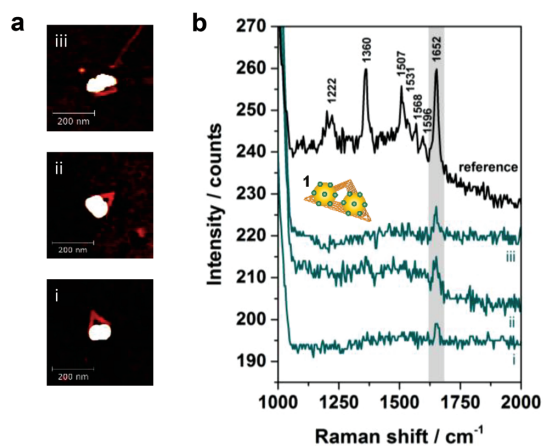
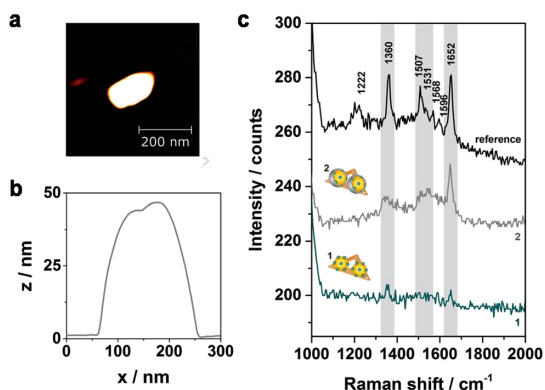


Fig. 3 Single nanostructure correlations of 40 nm AuNP dimers covered with TAMRA-modified ssDNA (structure 1). (a) AFM images of three individual DNA-AuNP hybrids. (b) SERS spectra of the nanostructures i–iii showing the most prominent TAMRA peak at 1652  $\text{cm}^{-1}$  (cyan spectra). For comparison a reference spectrum containing characteristic TAMRA bands at 1222, 1360, 1507, 1531, 1568, 1596 and 1652  $\text{cm}^{-1}$  is shown (black spectrum). The number of TAMRA molecules contributing to each of the spectra i–iii is estimated to be approximately 40. SERS experiments were performed with laser excitation at 532 nm, laser power of 900–1000  $\mu\text{W}$  and 2 s integration time.

of the AuNPs connected to the DNA origami platforms the AuNPs might approach each other slightly during the drying process due to a temporarily increased salt concentration. Thus, the minimal gap size is determined by the DNA coating which is assumed to be 2.5 nm per AuNP. In Fig. 3a AFM images of three individual and well-defined DNA-AuNP hybrids (i, ii, iii) are presented (height profiles shown in Fig. S2 (ESI<sup>†</sup>)). The corresponding SERS spectra are shown in

Fig. 3b (cyan spectra). In all three cases the most prominent TAMRA band at 1652  $\text{cm}^{-1}$  has been detected with an intensity of approximately 5–10 cts (highlighted in grey). For comparison a reference spectrum obtained from single 60 nm AuNPs covered with TAMRA-modified DNA is shown, which contains the characteristic TAMRA bands at 1222, 1360, 1507, 1531, 1568, 1596 and 1652  $\text{cm}^{-1}$  (black spectrum). Since single 40 nm AuNPs covered with TAMRA are found to give extremely weak SERS signals (see Fig. S3 (ESI<sup>†</sup>)) under the presently applied conditions we conclude that the detected signal for structures i–iii mainly arises from TAMRA molecules located in the hot spot formed in-between the two particles. To estimate the number of TAMRA molecules that contribute to each of the three SERS spectra we assume that one 40 nm AuNP is covered with 430 oligonucleotides.<sup>28</sup> Furthermore, half of the DNA coating strands are modified with a TAMRA molecule and we assume about 10% of all coating strands being located in the hot spot. Therefore, a maximum of approximately 40 TAMRA molecules contribute to each SERS spectrum (i–iii) presented in Fig. 3b. It should be emphasized that among all correlated hybrids with structure 1 only those revealing the strongest SERS signals are presented. Thus, the dimers i–iii are expected to have smaller gap sizes than 14 nm.

To further improve the Raman signal enhancement an additional Ag layer is grown on the AuNPs which is expected to result in an increase of the electromagnetic field enhancement for two reasons: (a) Ag exhibits a better enhancement performance in the visible range of the electromagnetic spectrum,<sup>29</sup> (b) the gap size between the two NPs is reduced upon the silver shell growth. In order to compare the effect of the silver shell, SERS and AFM data of selected nanostructures have been collected before and after the silver enhancement process (Fig. 4). In Fig. 4a an AFM image of one representative hybrid structure with silver shell is shown. The DNA origami triangle is most probably hidden beneath the Au-Ag core-shell structure in the AFM image. Since the vertical resolution in AFM images is higher than the lateral resolution by a factor of up to 100 the shell thickness can be determined from the height difference in the associated cross sections. The height profile shown in Fig. 4b indicates a thickness of the silver shell of approximately 10 nm in vertical direction (see height profiles of analogue dimers without silver shell in Fig. S2 (ESI<sup>†</sup>) for comparison). In Fig. 4c the corresponding SERS spectra are shown demonstrating an overall increase of the SERS intensity after electroless silver deposition (grey spectrum). In addition to the bands at 1360  $\text{cm}^{-1}$  and 1652  $\text{cm}^{-1}$  two other characteristic spectral features for TAMRA at 1507  $\text{cm}^{-1}$  and 1531  $\text{cm}^{-1}$  become visible (highlighted in grey). Principally, the effect of photobleaching is observed upon consecutive laser exposures under the here applied conditions. Therefore, the detected SERS signals after silver deposition are expected to result even from a smaller number of TAMRA molecules compared to the initial measurement. Although this experiment demonstrates an increase of the SERS intensity upon silver enhancement the origin of the SERS signals in structure 2 is difficult to reveal since the dye molecules are completely embedded in the silver



**Fig. 4** Comparison of correlated AFM images and SERS spectra before and after the silver enhancement process. (a) AFM image of one selected DNA-AuNP hybrid with silver shell (structure 2) after 3 min of incubation (LI silver). (b) The height profile of the dimer shown in (a) indicates the growth of the silver shell. (c) Corresponding SERS spectra of the dimer shown in (a) before (cyan spectrum, 1) and after (grey spectrum, 2) electroless silver deposition. Spectrum 1 exhibits only the two most characteristic TAMRA bands at  $1360\text{ cm}^{-1}$  and  $1652\text{ cm}^{-1}$  (highlighted in grey). In comparison to spectrum 1 the overall SERS intensity in spectrum 2 is increased due to the silver shell. Furthermore, two additional spectral features at  $1507\text{ cm}^{-1}$  and  $1531\text{ cm}^{-1}$  arising from the TAMRA dyes become detectable for the core-shell system. SERS experiments were performed with laser excitation at  $532\text{ nm}$ , laser power of  $900\text{--}1000\text{ }\mu\text{W}$  and  $2\text{ s}$  integration time.

shell. This may lead to charge transfer processes between Ag and the TAMRA molecules resulting in possible contributions from chemical enhancement. Moreover, with regard to the silver shell thickness of approximately  $10\text{ nm}$  also DNA strands from the AuNP coating as well as from the DNA origami template might be embedded in the silver shell. Although the Raman cross section for TAMRA is considerably higher than the Raman cross sections for DNA for some hybrids clear SERS bands arising from the DNA can be detected (see Fig. S4 and Table S1 (ESI<sup>†</sup>) for an example). This observation is ascribed to two effects: on the one hand, the number of individual DNA bases incorporated in the silver shell is significantly higher in comparison to the number of TAMRA molecules. On the other hand, the two AuNPs are fused together upon silver shell growth resulting in a rod-like plasmonic particle. This can also be seen in scanning electron microscopy (SEM) images shown in Fig. S5a.† Since metal rods are known to provide the maximum electromagnetic enhancement at the particle tips<sup>30</sup> new hot spots are created that provide better SERS enhancement for the DNA located at the end of the tips than for the embedded TAMRA molecules. Consequently, core-shell systems with reduced silver shell thicknesses are necessary in order to reduce the amount of embedded DNA in the shell as well as to avoid the relocation of hot spots. To improve the control of the shell size another silver enhancement kit (HQ silver, Nanoprobes) was used for subsequent experiments since it is characterized by a thickening agent to retard the deposition rate.

To explore the suitability of DNA origami based SERS substrates for the detection of single molecules the design was optimized taking the following aspects into account (structures 3 and 4; strategy shown in Fig. 1b): first, placing the single dye molecule with high accuracy in the hot spot is a crucial condition since the EF decreases strongly within distances of a few nm away from the NP surface.<sup>31</sup> This condition is fulfilled by attaching the two individual AuNPs to opposite sides of the DNA origami and placing the dye molecule into the axis in between the AuNPs. Moreover, in this arrangement the initial gap size is reduced to  $7\text{ nm}$  (assuming  $2\text{ nm}$  thickness for the DNA origami template and  $2 \times 2.5\text{ nm}$  thickness for the DNA coating surrounding the AuNPs). Second, finite-difference time-domain (FDTD) calculations revealed that Au-Ag-core-shell NP dimers ( $2.5\text{ nm}$  Ag shell and  $2\text{ nm}$  gap size) with  $60\text{ nm}$  Au cores show a superior electromagnetic field enhancement compared to  $40\text{ nm}$  or  $80\text{ nm}$  Au cores (see Fig. 5c and S7 (ESI<sup>†</sup>)). Consequently, the initial size of the AuNPs was increased to  $60\text{ nm}$  and a thin Ag coating was added, which further reduces the gap (see Fig. S5b and S5c†). Third, an additional (-fourth) anchor point per AuNP was introduced to the DNA origami template in order to reduce the flexibility of the AuNP attachment position.

In Fig. 5a correlated Raman spectra and AFM images for structure 4a (TAMRA as analyte molecule) are presented. Initially, an experiment with two TAMRA molecules placed into the gap has been performed (dimer i). In the corresponding AFM image the triangular DNA origami is no longer visible which is valid for all hybrids with structure 3 or 4. This is due to the fact that the AuNP dimers are immobilized on the Si surface, while the DNA triangle can no longer lie flatly on the surface resulting in a twisted arrangement of the hybrid structures (see AFM image of a corresponding dimeric structure with two  $40\text{ nm}$  AuNPs in Fig. S6†). The corresponding SERS spectrum for dimer i (light cyan spectrum) exhibits a weak band at  $1652\text{ cm}^{-1}$  (highlighted in grey) which originates from a maximum of both TAMRA molecules located in the hot spot. Furthermore, the same peak was detected for only one TAMRA molecule incorporated in the DNA origami substrate (dimer ii). Additionally, a second weak band that is assigned to TAMRA is visible at  $1507\text{ cm}^{-1}$  (also highlighted in grey). These experiments demonstrate that the detection of TAMRA at a single-molecule level is possible using the optimized hybrid structure 4a. However, the use of TAMRA suffers from very low SERS intensities (with signal-to-noise ratios of  $3.6\text{--}6.3$  for the strongest TAMRA signals) and the fact that the detection is mainly based on the presence of a single peak at  $1652\text{ cm}^{-1}$ .

In order to confirm the single-molecule detection of the analyte molecule the same experiment was repeated with one Cy3 molecule incorporated into the DNA-Au-Ag hybrid structure instead of TAMRA (structure 4b, Fig. 5b). The comparison of both single-molecule SERS spectra reveals that most spectral peak positions coincide for dimer iii and iv. All these bands at  $1167$ ,  $1354$ ,  $1384$ ,  $1470$ ,  $1495$  and  $1588\text{ cm}^{-1}$  (highlighted in grey) are also visible in the reference (black spectrum) and



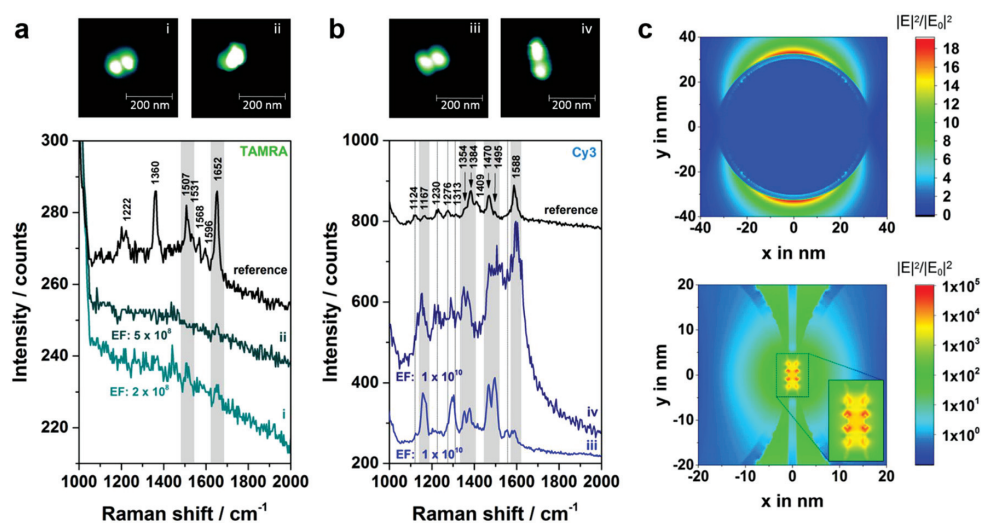


Fig. 5 Experiments at the single-molecule level. (a) Correlated AFM and Raman study for structure 4a with two (dimer i) or only one (dimer ii) TAMRA molecule incorporated. In both cases peaks arising from TAMRA have been detected (highlighted in grey). (b) Analogue experiment to (a) by using a single Cy3 as analyte molecule (structure 4b). Several Cy3 bands are visible in the SERS spectra of both dimers iii and iv (highlighted in grey). Additionally, the dotted lines mark spectral positions of Cy3 which can either be detected for dimer iii or dimer iv. SERS experiments were performed with laser excitation at 532 nm, laser power of 400–500  $\mu\text{W}$  and 10 s integration time. (c) FDTD calculations showing the distribution of the electromagnetic field enhancement that can be expected for a single 60 nm AuNP (top) as well as for a dimer consisting of two 60 nm AuNPs with a 2.5 nm silver shell (below). The dimer is separated by the 2 nm thick DNA origami template that is arranged concentrically in the simulation. For excitation a 532 nm laser line is assumed.

thus can be assigned to Cy3. Some spectral features matching the reference spectrum are only present either in the SERS spectrum of dimer iii or in the one for dimer iv (marked with dashed lines). In the case of dimer iii (light blue spectrum) an additional band at  $1124 \text{ cm}^{-1}$  as well as overlapping bands in the range between  $1270\text{--}1310 \text{ cm}^{-1}$  have been detected, which arise also from the Cy3 molecule. The band at  $1553 \text{ cm}^{-1}$  is only visible as a shoulder in the reference spectrum. Another reference spectrum for Cy3, which confirms the presence of that band can be found in the ESI (Fig. S8<sup>†</sup>). In contrast, the SERS spectrum for dimer iv (dark blue spectrum) reveals a spectral feature at  $1230 \text{ cm}^{-1}$  arising from Cy3 that is only very weakly present in the spectrum of dimer iii. The observed differences between the recorded spectra (absence or presence of certain bands as well as intensity ratios) are ascribed to slight conformational variations in every individual structure. On the one hand, the position of the dye relative to the axis of the dimer is certainly different for every hybrid structure, which might lead to preferential enhancement of specific bands. On the other hand, the size ratio between Au core and Ag shell slightly differs which has been reported to have an effect on the plasmon coupling.<sup>32</sup> The high background in the SERS spectrum of dimer iv (Fig. 5b, dark blue line) which is visible for some nanostructures is most likely caused by some residues from the Ag enhancement solution. In summary, the experiment shows that using Cy3 as analyte molecule gives a clear evidence of single-molecule SERS for two reasons: (a) the

intensity of the SERS bands is considerably higher than for TAMRA, (b) the detection of a single Cy3 molecule is based on at least six bands (detected for both dimers iii and iv).

In order to find out whether single-molecule SERS sensitivity can be expected for the structures 4a and 4b EFs have been estimated, which are generally based on a comparison of the SERS signal with that of the same molecule in normal Raman conditions.<sup>31</sup> Recording a normal Raman spectrum of TAMRA and Cy3 at 532 nm is hampered by a strong fluorescence background. Thus, the characterization of a reference system with known EF is necessary. Since SERS spectra of a single 60 nm AuNP covered with dye containing DNA (sequence:  $5'-(\text{TTT})_4\text{TX-SH-3}'$ ; X = TAMRA or Cy3) show clear bands with an acceptable signal-to-noise ratio this system was chosen to serve as a reference, whose EF was reported previously.<sup>33</sup> First, the number of dye molecules per NP has been determined using a fluorescence based approach following the protocol of Hurst *et al.*<sup>34</sup> Second, the average SERS intensity for a single AuNP has been determined by correlating AFM and SERS data for approximately 15 TAMRA and 15 Cy3 labeled NPs. In the case of TAMRA the intensities of the band at  $1652 \text{ cm}^{-1}$  have been averaged whereas for Cy3 the bands at  $1470 \text{ cm}^{-1}$  and at  $1588 \text{ cm}^{-1}$  serve as references. Third, the EF for a single 60 nm AuNP was assumed to be  $9 \times 10^5$  according to Hong and Li.<sup>33</sup> Relating the EF from the literature to the reference system and in turn to all individual hybrids shown in Fig. 5 reveals an estimated EF for every single dimer i–iv

**Table 1** Experimentally obtained data from SERS and fluorescence measurements used for the estimation of EFs

TAMRA				
System	$I$ (1652 $\text{cm}^{-1}$ )/cts	Nr. TAMRA/system	$I$ (1652 $\text{cm}^{-1}$ )/cts (per TAMRA)	EF
60 nm AuNP [TAMRA] (reference)	28	4805 $\pm$ 556	5.83 $\times 10^{-3}$	9 $\times 10^5$ <sup>a</sup>
Dimer i	3	2	1.5	2 $\times 10^8$
Dimer ii	3	1	3.0	5 $\times 10^8$
Cy3				
System	$I$ (1470 $\text{cm}^{-1}$ )/cts	Nr. Cy3/system	$I$ (1470 $\text{cm}^{-1}$ )/cts (per Cy3)	EF
60 nm AuNP [Cy3] (reference)	30	3745 $\pm$ 672	8.01 $\times 10^{-3}$	9 $\times 10^5$ <sup>a</sup>
Dimer iii	119	1	119	1 $\times 10^{10}$
Dimer iv	130	1	130	1 $\times 10^{10}$
System	$I$ (1588 $\text{cm}^{-1}$ )/cts	Nr. Cy3/system	$I$ (1588 $\text{cm}^{-1}$ )/cts (per Cy3)	EF
60 nm AuNP [Cy3] (reference)	40	3745 $\pm$ 672	1.07 $\times 10^{-2}$	9 $\times 10^5$ <sup>a</sup>
Dimer iii	30	1	30	3 $\times 10^9$
Dimer iv	65	1	60	5 $\times 10^9$

<sup>a</sup> Reference EFs adopted from ref. 33.

(see Fig. S9 and S10 (ESI<sup>†</sup>) for detailed information). All relevant values used for the EF estimation are summarized in Table 1. It turned out, that the EFs for the Cy3 containing systems (dimer iii and iv) are of the order of  $10^{10}$ , that is one order of magnitude higher than the EFs for the systems with TAMRA (dimer i and ii). This can be explained by a higher Raman cross section of Cy3 in comparison to TAMRA within the hot spot.

In order to confirm the experimentally estimated EFs FDTD simulations for a single 60 nm AuNP (Fig. 5c, top) as well as for a 60 nm AuNP dimer (2.5 nm Ag shell, gap size 2 nm) (Fig. 5c, below) have been performed assuming excitation with 532 nm. In the case of the dimer the area with EFs in the range of  $10^7$  or higher is expanded over approximately 5 nm in  $y$  direction reaching a maximal EF of  $10^{10}$ . Thus, the localization of a single dye molecule incorporated into the DNA origami structure within the hot spot is highly probable. Moreover, the experimentally estimated EFs coincide with the simulated ones. However, the EFs revealed by FDTD simulations are only based on the electromagnetic enhancement and do not consider additional effects such as the contribution due to resonant excitation of the analyte which can result in an increase of the intensity up to 5 orders of magnitude.<sup>35</sup> On the other hand, the simulation is based on the excitation with light polarized along the dimer axis. Since in the experiment non-polarized light was used the simulation overestimates this contribution. Additionally, the experimentally estimated EFs are based on the EF from ref. 33 which has been determined using a 647 nm laser for excitation. Since the EF is directly correlated to the excitation wavelength the listed values only represent a first approximation. However, it should be noted that for 532 nm excitation the electromagnetic field enhancement is higher (see FDTD simulations in Fig. S11 (ESI<sup>†</sup>) for 647 nm excitation) resulting in a total EF of a single 60 nm AuNP that is about 10 times higher. Fig. S12<sup>†</sup> shows the simulated absorption and scattering spectra of the Au-Ag core-shell

nanostructures, which exhibit maximum cross sections at 549 nm and 561 nm, respectively, corresponding roughly to the excitation laser used in the current experiment (532 nm).

## Experimental section

### Synthesis of DNA origami structures

Triangular DNA origami structures (design published by Rothmund<sup>1</sup>) were synthesized as previously described<sup>36</sup> using the M13mp18 virus strand (New England Biolabs) as scaffold. For AuNP attachment either three (structures **1** and **2**) or four (structures **3a** (**4a**), **3b** (**4b**)) staple strands per AuNP were extended at the 5'-end by the capture sequence 5'-(AAA)<sub>8</sub>T<sub>4</sub>-3'. The positions of the capture strands were t-3s6e, t-3s8g, t-5s8g (according to the nomenclature used by Rothmund) and t5s6e, t5s8g, t7s8g (for structures **1** and **2**) or t-1s6e, t1s6i, t-1s8g, t1s8i and t-2s5f, t-2s7f, t2s5f, t2s7f (for structures **3a** (**4a**), **3b** (**4b**)). For incorporation of one single TAMRA molecule in the DNA origami design (structure **3a** (**4a**)) a modified capture strand t1s6i carrying a TAMRA functionality at the 3'-end was used. For the DNA origami with one Cy3 molecule (structure **3b** (**4b**)) the staple strand t-1s6i with a Cy3 modification at the 5'-end was incorporated. Except of all extended or dye-modified sequences (ordered from metabion) all ssDNA staple strands were purchased from Integrated DNA Technologies. The annealing process from 80 °C to 8 °C was realized using a Primus 25 advanced thermal cycler (Peqlab). In order to remove excess staple strands the resulting DNA origami solution (approx. 35  $\mu\text{L}$  volume) was spin filtered two times at 3830  $g$  for 10 min using Amicon Ultra-0.5 filters (100 kDa MWCO, Millipore). In the first run 200  $\mu\text{L}$  (in the second run 300  $\mu\text{L}$ ) of 1 $\times$  TAE with 10 mM  $\text{MgCl}_2$  were added to the DNA origami solution. The final concentration of the DNA origami structures was determined *via* UV-Vis absorption

spectroscopy (NanoDrop 2000, Thermo Scientific) to be in the range of 25–60 nM.

#### DNA-coating of AuNPs

Citrate-capped AuNPs with a size of 40 nm or 60 nm were purchased from BBI Solutions. 40 nm AuNPs were modified similar to the protocol of Ding *et al.*<sup>37</sup> whereas 60 nm AuNPs were coated following the protocol of Zhang *et al.*<sup>38</sup> with slight modifications concerning concentrations, reaction times and the use of 0.02% sodium dodecyl sulfate (SDS, Sigma Aldrich) as an additional stabilizing agent (see the ESI† for complete coating procedures). Finally, the concentration of as-prepared AuNPs was quantified by measuring the absorbance at 527 nm (for 40 nm AuNPs) or 538 nm (for 60 nm AuNPs) (NanoDrop 2000, Thermo Scientific). Related molar extinction coefficients have been calculated to be  $1.03 \times 10^{10} \text{ M cm}^{-1}$  (40 nm AuNPs) or  $3.96 \times 10^{10} \text{ M cm}^{-1}$  (60 nm AuNPs) using the equation suggested by Liu *et al.*<sup>39</sup>

#### DNA hybridization

The hybridization process between ssDNA capture strands protruding from the DNA origami template and ssDNA coating strands located at the surface of the AuNPs was realized in solution with a synthesis scale of 10  $\mu\text{L}$ . Therefore, the DNA origami solution and the AuNP solution were mixed in a ratio of 1 : 1 (approx. 0.4 nM). Additionally, 1 $\times$  TAE buffer was added and the final concentration of  $\text{MgCl}_2$  was set to 10 mM. Using the Thermocycler a temperature program was applied to the mixture keeping the solution at 45  $^\circ\text{C}$  for 41 min and afterwards cooling down to 25  $^\circ\text{C}$  in steps of 2  $^\circ\text{C}$  within 20 min.

#### Preparation of Si substrates

Si samples (p-type, (100), CrysTec) were cut into pieces ( $1 \times 1 \text{ cm}^2$  in size), then rinsed with 4 mL ethanol (pure, Sigma Aldrich) and with 4 mL Milli-Q-water and finally dried in a stream of compressed air. Next, the Si samples were put under a UV lamp ( $\lambda = 254 \text{ nm}$ ; Vilber Lourmat) for 10 min to increase the hydrophilicity of the surface. A 0.4–1.0  $\mu\text{L}$  drop of the DNA–AuNP solution was applied on a Si sample followed by the addition of 40  $\mu\text{L}$  of 10 $\times$  TAE with 100 mM  $\text{MgCl}_2$ . During the incubation time of 60 min Si samples were stored in a box with high humidity in order to prevent the drop from drying. Finally, the substrates were rinsed with 4 mL of 1 : 1 Milli-Q-water/ethanol (pure) and dried with compressed air.

#### Electroless silver deposition

For electroless silver deposition commercial enhancement kits from Nanoprobes were used (LI Silver (structure 2) and HQ silver (structures 4a, 4b)). As recommended by the manufacturer the enhancement processes were performed at room temperature and under darkened light conditions. The either two (LI silver) or three (HQ silver) solutions were mixed carefully in ratios of 1 : 1 or 1 : 1 : 1 and subsequently 20  $\mu\text{L}$  of the mixture were applied to the DNA–AuNP hybrids adsorbed on Si wafers. After 3 min (LI silver) or 60 s (HQ silver) of deposition time the wafers were rinsed and quickly dipped in Milli-

Q-water and dried with compressed air. For single-molecule SERS measurements HQ silver was used since it is characterized by a thickening agent to retard the deposition rate and thus to increase the control over the shell size.

#### Superposition of AFM and SERS images

In order to enable the superposition of recorded AFM and SERS images a small part of the Si wafer was marked with a slight scratch using a diamond knife. Subsequent AFM and SERS experiments were performed by mapping an area of  $20 \times 20 \mu\text{m}^2$  including a part of the scratch.

#### AFM imaging

AFM imaging was performed using a Nanosurf FlexAFM with two compatible scan heads either for large-area imaging up to  $100 \mu\text{m}^2$  (Fig. 2) or for higher resolution (Fig. 2–5). In both cases Tap150Al-G cantilevers (Budget Sensors) with a force constant of  $5 \text{ N m}^{-1}$  operating in tapping mode have been used. For AFM data visualization and analysis the software Gwyddion 2.34 (freeware) was used.

#### Raman imaging

SERS imaging was performed with a confocal Raman microscope (WITec alpha300) equipped with an upright optical microscope. For excitation a 532 nm laser was used that was coupled into a single-mode optical fiber and focused through a 100 $\times$  objective (Olympus MPlanFL N, NA = 0.9) to a diffraction-limited spot ( $1.3 \mu\text{m}^2$ ) on the Si sample. Due to the size of the laser spot only NP structures without any other potential SERS active NPs in the vicinity of 0.65  $\mu\text{m}$  radius have been analyzed. The laser power and the integration time were set to 900–1000  $\mu\text{W}$  and 2 s for dye-covered AuNPs (structures 1, 2) or to 400–500  $\mu\text{W}$  and 10 s in the case of single-molecule measurements (structures 4a, 4b). The grating of the spectrograph was set to  $600 \text{ g mm}^{-1}$ . For better visualization SERS spectra are vertically shifted in all diagrams presenting more than one spectrum.

#### Determination of AuNPs surface coverage

The surface coverage of the AuNPs with dye-modified DNA was determined following the protocol of Hurst *et al.*<sup>34</sup> First, the concentration of AuNPs was quantified by UV-Vis absorption spectroscopy. In order to remove all DNA coating strands from the AuNP surface 10  $\mu\text{L}$  of the AuNPs stock solution were incubated overnight with 10  $\mu\text{L}$  of 1 M dithiothreitol (DTT, Sigma Aldrich) in 1 $\times$  TAE with 10 mM  $\text{MgCl}_2$  [2 $\times$  dilution]. The gold precipitate was removed by centrifugation at 5000g for 4 min. Subsequently, 17  $\mu\text{L}$  of the supernatant were mixed with 493  $\mu\text{L}$  of 1 $\times$  TAE with 10 mM  $\text{MgCl}_2$  [30 $\times$  dilution]. The fluorescence of the diluted supernatant containing the dye-modified DNA was measured in triplicate and compared to a calibration curve (see Fig. S10 of the ESI†). Fluorescence measurements were performed using a FluoroMax-P (Horiba Jobin Yvon). In the case of TAMRA the excitation wavelength was set to 535 nm and the emission was recorded from 550 nm to 750 nm. Cy3 was excited at 500 nm and the emis-

sion was collected from 520 nm to 700 nm. For both fluorophores an integration time of 0.2 s was used and the slit size was set to 5.0 nm.

#### FDTD simulations

FDTD simulations have been performed using Lumerical FDTD Solutions 8.6.3. The thicknesses of individual layers were modelled as follows: 2.0 nm DNA origami template, 2.5 nm ssDNA coating of the AuNPs, 2.5 nm silver shell and 2.0 nm SiO<sub>2</sub> substrate on a Si base. For all simulated nanostructures excitation with 532 nm was assumed. In the case of the dimeric structures the hybrids are illuminated with polarization along the axis of the dimer. All simulations are shown in equatorial plane of the particles. For the refractive indices the following values were used: 2.1 for DNA origami,<sup>18</sup> 1.7 for ssDNA coating,<sup>18</sup> Au and Ag (Johnson and Christy<sup>40</sup>), silicon and SiO<sub>2</sub> (Palik<sup>41</sup>), 1.0 for the surrounding medium. For the calculated absorption and scattering spectra (ESI, Fig. S12†) the Ag shell was modelled using the dielectric constant according to Weast.<sup>42</sup>

#### SEM imaging

SEM images have been recorded under high vacuum conditions with a Quanta250 (FEI) using an ETD detector in SE mode. The accelerating voltage was set to 30 kV and a spot size of 2.0 nm was used.

## Conclusion

In summary, we have demonstrated SERS from Au–Ag-core-shell NPs arranged on DNA origami substrates. A stepwise optimization strategy in terms of the AuNP size and their arrangement as well as the introduction of a silver shell has been presented in order to increase the SERS sensitivity provided by the hybrid structures. Finally, single molecules of TAMRA and Cy3 positioned in the hot spot have been successfully detected using the optimized Au–Ag-core-shell dimers. Moreover, the SERS sensitivity has been quantified by estimation of EFs for selected hybrid structures revealing values in the range between 10<sup>9</sup>–10<sup>10</sup> for Cy3, which is one order of magnitude higher in comparison to TAMRA. The experimentally estimated EFs were found to be in good agreement with theoretical values provided by FDTD simulations.

The novel SERS substrates presented here are highly promising for biosensing applications. For instance, single proteins or DNA strands can be placed in the hot spot with high local precision in order to investigate *e.g.* protein folding<sup>43</sup> or DNA strand break events. Furthermore, the plasmon resonance of the Au–Ag-core-shell NPs can be easily tuned by adjusting the size ratio between core and shell<sup>32</sup> which enables the creation of tailored nanostructures for individual applications. Extending the dimeric structures by an additional NP might result in even higher EFs, especially in the case of so called nanolenses consisting of three differently sized AuNPs with specific size ratios.<sup>44,45</sup> Consequently, single-molecules with much lower

Raman cross-sections might become detectable using DNA–NP hybrid structures in the future.

## Acknowledgements

This research was supported by the Deutsche Forschungsgemeinschaft (DFG), a Marie Curie FP7 Integration Grant within the 7th European Union Framework Programme, the European Regional Development Fund (EFRE), by the University of Potsdam and the Federal Institute of Materials Research (BAM). V.M. acknowledges funding by ERC Grant No. 259432 issued to Janina Kneipp (HU), who provided resources for FDTD simulations. SALSA (School of Analytical Sciences Adlershof, HU Berlin, IRIS Building, Unter den Linden 6, DE-10099 Berlin) is being financed by the DFG as part of the Excellence Initiative. We thank Dr D. Munzke (UP) for assistance with SEM imaging.

## Notes and references

- 1 P. W. K. Rothemund, *Nature*, 2006, **440**, 297–302.
- 2 D. Han, S. Pal, J. Nangreave, Z. Deng, Y. Liu and H. Yan, *Science*, 2011, **332**, 342–346.
- 3 A. Kuzyk, R. Schreiber, H. Zhang, A. O. Govorov, T. Liedl and N. Liu, *Nat. Mater.*, 2014, **13**, 862–866.
- 4 T. Gerling, K. F. Wagenbauer, A. M. Neuner and H. Dietz, *Science*, 2015, **347**, 1446–1452.
- 5 A. Kuzuya, Y. Sakai, T. Yamazaki, Y. Xu and M. Komiyama, *Nat. Commun.*, 2011, **2**, 449.
- 6 M. Tintoré, I. Gállego, B. Manning, R. Eritja and C. Fàbrega, *Angew. Chem., Int. Ed.*, 2013, **52**, 7747–7750.
- 7 A. Keller, J. Rackwitz, E. Cauët, J. Liévin, T. Körzdörfer, A. Rotaru, K. V. Gothelf, F. Besenbacher and I. Bald, *Sci. Rep.*, 2014, **4**, 7391.
- 8 S. Vogel, J. Rackwitz, R. Schürman, J. Prinz, A. R. Milosavljević, M. Réfrégiers, A. Giuliani and I. Bald, *J. Phys. Chem. Lett.*, 2015, **6**, 4589–4593.
- 9 J. J. Schmied, A. Gietl, P. Holzmeister, C. Forthmann, C. Steinhauer, T. Dammeyer and P. Tinnefeld, *Nat. Methods*, 2012, **9**, 1133–1134.
- 10 L. Olejko, P. J. Cywinski and I. Bald, *Angew. Chem., Int. Ed.*, 2015, **54**, 673–677.
- 11 X. Shen, A. Asenjo-Garcia, Q. Liu, Q. Jiang, G. de Abajo, F. Javier, N. Liu and B. Ding, *Nano Lett.*, 2013, **13**, 2128–2133.
- 12 C. Zhou, X. Duan and N. Liu, *Nat. Commun.*, 2015, **6**, 8102.
- 13 C. E. Talley, J. B. Jackson, C. Oubre, N. K. Grady, C. W. Hollars, S. M. Lane, T. R. Huser, P. Nordlander and N. J. Halas, *Nano Lett.*, 2005, **5**, 1569–1574.
- 14 K. L. Wustholz, A.-I. Henry, J. M. McMahon, R. G. Freeman, N. Valley, M. E. Piotti, M. J. Natan, G. C. Schatz and R. P. Van Duyne, *J. Am. Chem. Soc.*, 2010, **132**, 10903–10910.
- 15 G. P. Acuna, M. Bucher, I. H. Stein, C. Steinhauer, A. Kuzyk, P. Holzmeister, R. Schreiber, A. Moroz,

## Paper

## Nanoscale

- F. D. Stefani, T. Liedl, F. C. Simmel and P. Tinnefeld, *ACS Nano*, 2012, **6**, 3189–3195.
- 16 G. P. Acuna, F. M. Möller, P. Holzmeister, S. Beater, B. Lalkens and P. Tinnefeld, *Science*, 2012, **338**, 506–510.
- 17 J. Prinz, B. Schreiber, L. Olejko, J. Oertel, J. Rackwitz, A. Keller and I. Bald, *J. Phys. Chem. Lett.*, 2013, **4**, 4140–4145.
- 18 V. V. Thacker, L. O. Herrmann, D. O. Sigle, T. Zhang, T. Liedl, J. J. Baumberg and U. F. Keyser, *Nat. Commun.*, 2014, **5**.
- 19 M. Pilo-Pais, A. Watson, S. Demers, T. H. LaBean and G. Finkelstein, *Nano Lett.*, 2014, **14**, 2099–2104.
- 20 P. Kühler, E.-M. Roller, R. Schreiber, T. Liedl, T. Lohmüller and J. Feldmann, *Nano Lett.*, 2014, **14**, 2914–2919.
- 21 K. Kneipp, Y. Wang, H. Kneipp, L. T. Perelman, I. Itzkan, R. R. Dasari and M. S. Feld, *Phys. Rev. Lett.*, 1997, **78**, 1667–1670.
- 22 S. Nie and S. R. Emory, *Science*, 1997, **275**, 1102–1106.
- 23 Le Ru, E. C. M. Meyer and P. G. Etchegoin, *J. Phys. Chem. B*, 2006, **110**, 1944–1948.
- 24 J. A. Dieringer, R. B. Lettan, K. A. Scheidt and R. P. Van Duyne, *J. Am. Chem. Soc.*, 2007, **129**, 16249–16256.
- 25 D.-K. Lim, K.-S. Jeon, J.-H. Hwang, H. Kim, S. Kwon, Y. D. Suh and J.-M. Nam, *Nat. Nanotechnol.*, 2011, **6**, 452–460.
- 26 D.-K. Lim, K.-S. Jeon, H. M. Kim, J.-M. Nam and Y. D. Suh, *Nat. Mater.*, 2010, **9**, 60–67.
- 27 J. Chao, Y. Lin, H. Liu, L. Wang and C. Fan, *Mater. Today*, 2015, **18**, 326–335.
- 28 H. D. Hill, J. E. Millstone, M. J. Banholzer and C. A. Mirkin, *ACS Nano*, 2009, **3**, 418–424.
- 29 R. J. Stokes, A. Macaskill, P. J. Lundahl, W. E. Smith, K. Faulds and D. Graham, *Small*, 2007, **3**, 1593–1601.
- 30 E. Hao and G. C. Schatz, *J. Chem. Phys.*, 2004, **120**, 357–366.
- 31 Le Ru, C. Eric and P. G. Etchegoin, *Annu. Rev. Phys. Chem.*, 2012, **63**, 65–87.
- 32 B. Aswathy, G. Sony and K. G. Gopchandran, *Plasmonics*, 2014, **9**, 1323–1331.
- 33 S. Hong and X. Li, *J. Nanomater.*, 2013, **2013**, 790323.
- 34 S. J. Hurst, A. K. Lytton-Jean and C. A. Mirkin, *Anal. Chem.*, 2006, **78**, 8313–8318.
- 35 R. A. Álvarez-Puebla, *J. Phys. Chem. Lett.*, 2012, **3**, 857–866.
- 36 A. Keller, I. Bald, A. Rotaru, E. Cauët, K. V. Gothelf and F. Besenbacher, *ACS Nano*, 2012, **6**, 4392–4399.
- 37 B. Ding, Z. Deng, H. Yan, S. Cabrini, R. N. Zuckermann and J. Bokor, *J. Am. Chem. Soc.*, 2010, **132**, 3248–3249.
- 38 X. Zhang, T. Gouriye, K. Göeken, M. R. Servos, R. Gill and J. Liu, *J. Phys. Chem. C*, 2013, **117**, 15677–15684.
- 39 X. Liu, M. Atwater, J. Wang and Q. Huo, Supramolecular Chemistry Applied to Interfaces Selected papers presented at the 2006 Florida Annual Meeting and Exhibition of the American Chemical Society, and at the Western Regional Meeting of the American Chemical Society, 2007, vol. 58, pp. 3–7.
- 40 P. B. Johnson and R. W. Christy, *Phys. Rev. B: Solid State*, 1972, **6**, 4370–4379.
- 41 E. D. Palik, *Handbook of Optical Constants of Solids*, Academic Press, 1997.
- 42 R. C. Weast, *CRC Handbook of Chemistry & Physics*, CRC Press, 1988.
- 43 K. Singhal and A. K. Kalkan, *J. Am. Chem. Soc.*, 2010, **132**, 429–431.
- 44 J. Kneipp, X. Li, M. Sherwood, U. Panne, H. Kneipp, M. I. Stockman and K. Kneipp, *Anal. Chem.*, 2008, **80**, 4247–4251.
- 45 K. Li, M. I. Stockman and D. J. Bergman, *Phys. Rev. Lett.*, 2003, **91**, 227402.

**Electronic Supplementary Information (ESI)****“DNA origami based Au-Ag-core-shell nanoparticle dimers with single-molecule SERS sensitivity”****1. Coating procedure of AuNPs***Salt aging method*

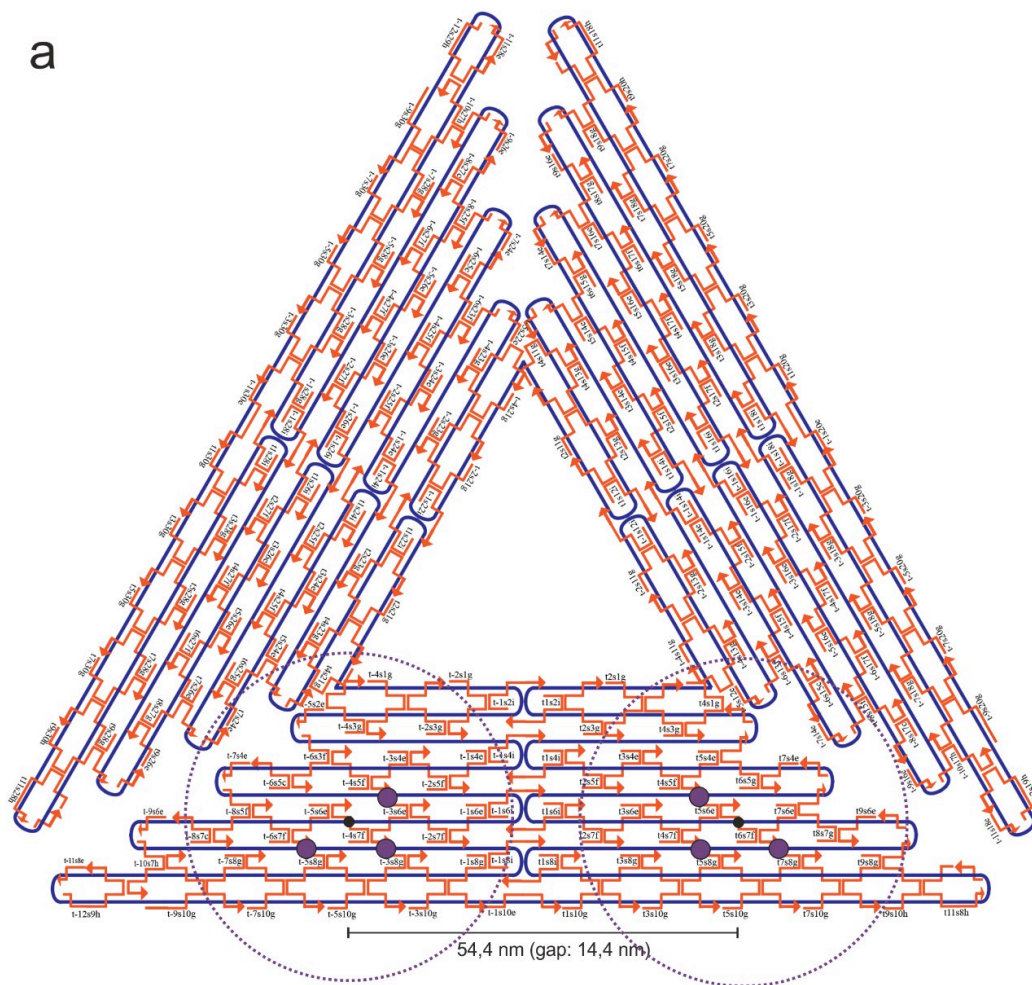
First, 5 mg of Bis(p-sulfonatophenyl)phenylphosphine dehydrate dipotassium salt (BSPP, Sigma Aldrich) were added to 15 mL of 40 nm citrate-stabilized AuNPs, covered with aluminium foil and stirred for 24 h. Next, NaCl was added to the solution until a change of color from red to purple was visible. The solution was centrifuged at 500 *g* for 35 min, the supernatant was discarded and 0.3 mL of 2.5 mM BSPP solution were added. The re-suspension of the AuNPs was indicated by a change of color back to red. Subsequently, 0.5 mL methanol (Sigma Aldrich) were added resulting in a third change of color to black. The solution was centrifuged at 500 *g* for 35 min, the supernatant was removed and AuNPs were re-suspended in 0.2 mL 2.5 mM BSPP solution. For the DNA coating process a 64000-fold excess of disulfide-modified DNA strands over AuNPs was used 13  $\mu\text{L}$  of phosphinated AuNPs were mixed with 11.5  $\mu\text{L}$  TAMRA-containing ssDNA (5'-(TTT)<sub>4</sub>TX-SH-3' ; X = TAMRA; 100  $\mu\text{M}$ ) and 11.5  $\mu\text{L}$  of the analogue ssDNA strand without TAMRA (5'-(TTT)<sub>4</sub>T-SH-3'; 100  $\mu\text{M}$ ). Furthermore, 2.9  $\mu\text{L}$  of 10x TAE was added and the mixture was allowed to stir overnight. The following salt aging process was realized over a long period of 7 days in order to prevent the AuNPs from precipitation. During that time volumes between 0.5–2.0  $\mu\text{L}$  of a 2 M NaCl solution were stepwise added to the AuNP solution resulting in a final NaCl concentration of 360 mM. After each step, the mixture was sonicated for 20 s and stirred until the next salt addition. Excess DNA strands were removed by spin filtering (58.4  $\mu\text{L}$  of AuNP solution + 200  $\mu\text{L}$  of 1x TAE with 10 mM MgCl<sub>2</sub>) using Amicon Ultra-0.5 filters (100 kDa MWCO, Millipore) at 3830 *g* for 10 min. The following washing process with 200  $\mu\text{L}$  of 1x TAE with 10 mM MgCl<sub>2</sub> at 3830 *g* for 10 min was performed 4 times. After the last washing step no signals arising from unbound DNA strands were detected via UV-Vis spectroscopy anymore.

*pH method*

First, the stock solution of 60 nm AuNPs was concentrated by centrifuging 0.4 mL of citrate-stabilized AuNPs at 1000 *g* for 10 min. The supernatant was gently removed and 4  $\mu\text{L}$  of 0.2% SDS were added to 20  $\mu\text{L}$  of the concentrated AuNPs (1–2 nM). Next, 1.8  $\mu\text{L}$  of the ssDNA coating strands (sequence 5'-(TTT)<sub>4</sub>T-SH-3'; 100  $\mu\text{M}$ ) was added. The mixture was covered with aluminium foil and stirred for at least 30 min. Then, 8  $\mu\text{L}$  of 50 mM citrate buffer (pH 3) were added in steps of 1–2  $\mu\text{L}$  over a period of 2 h. After addition of 6.4  $\mu\text{L}$  of Milli-Q-water the mixture was stirred for at least 60 min. A total volume of 5  $\mu\text{L}$  NaCl solution (2.5 M) was added in steps of 1  $\mu\text{L}$  within 2 h and afterwards the mixture was allowed to stir overnight. The AuNPs solution was centrifuged at 1500 *g* for 7 min and the supernatant was discarded. In order to remove unbound coating strands the mixture was washed 5 times by adding 200  $\mu\text{L}$  of 1x TAE with 0.02% SDS and 10 mM MgCl<sub>2</sub>, spinning at 1500 *g* for 7 min and discarding the supernatant.

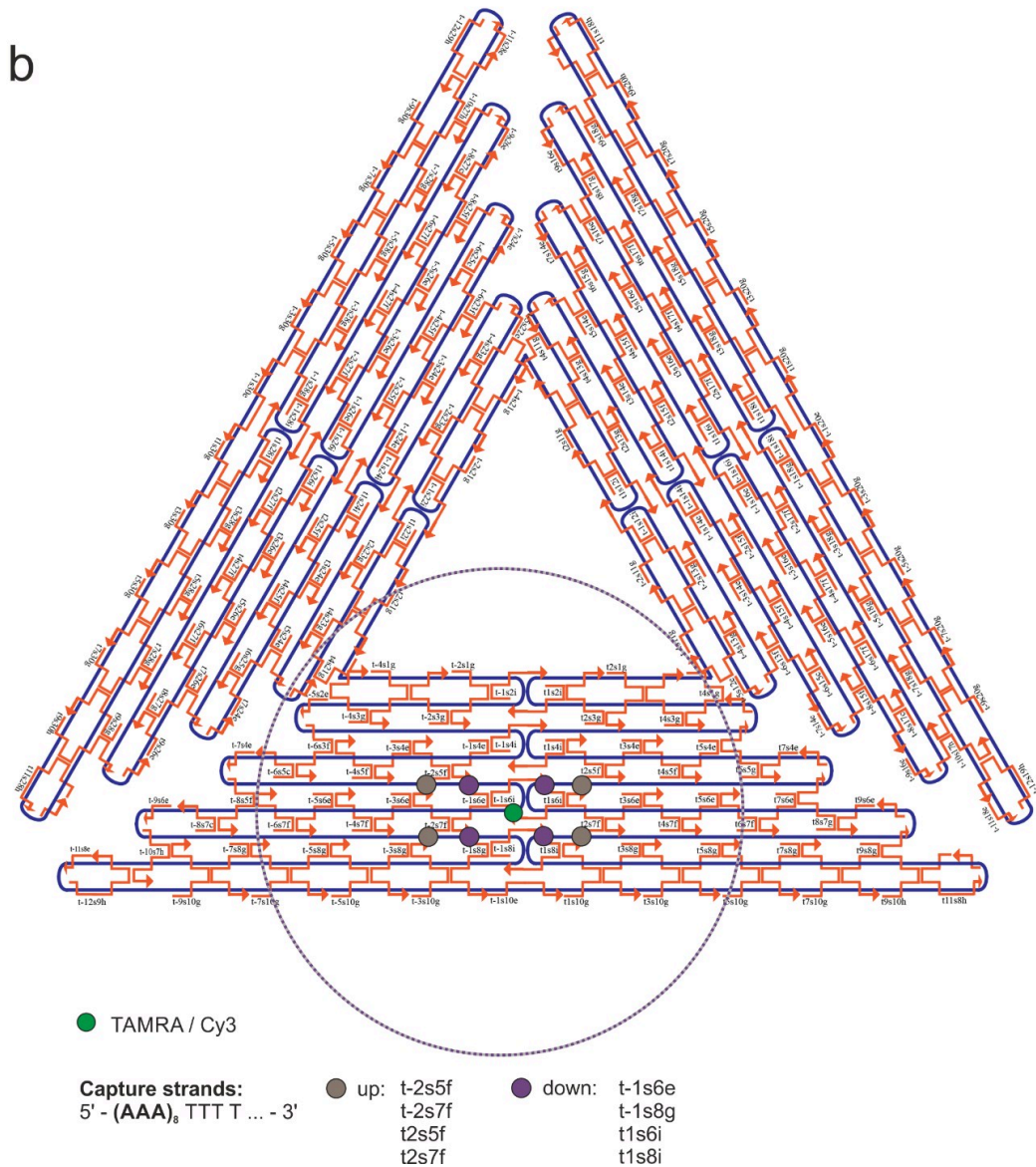
## 2. Designs of the DNA origami triangles

a



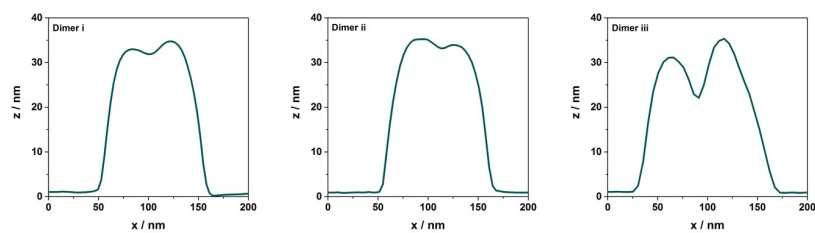
Capture strands:  
5' - (AAA)<sub>8</sub> TTT T ... - 3'

● down: t-3s6e    t5s6e  
          t-3s8g    t5s8g  
          t-5s8g    t7s8g



**Figure S1:** Designs of DNA origami triangles (according to the nomenclature used by Rothemund [1]). The first design (a) was used for the attachment of two 40 nm AuNPs to one side of the DNA origami template (strategy a in Figure 1), the second design (b) for the attachment of two 60 nm AuNPs to different sides (strategy b Figure 1). The positions of capture strands are marked in grey and violet; the position for the dye molecule is marked in green.

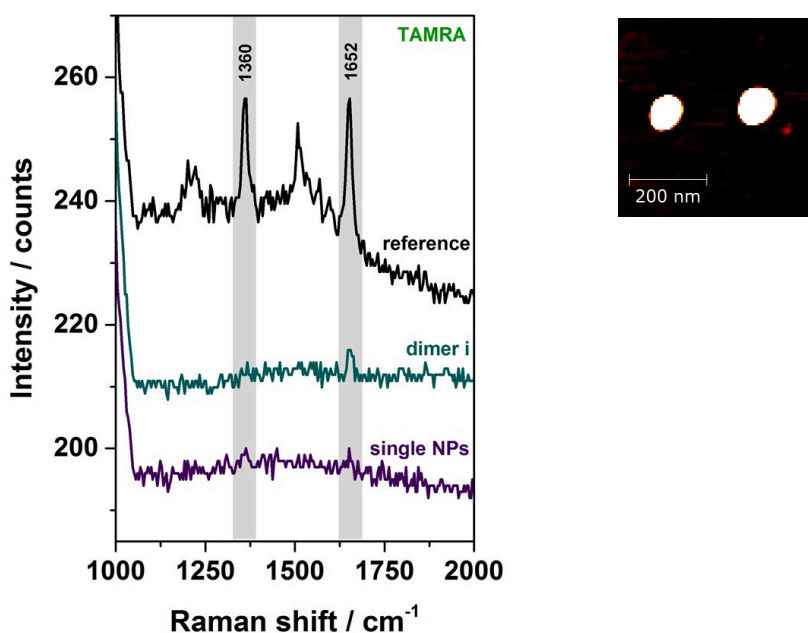
### 3. Height profiles for dimers



**Figure S2:** Height profiles for dimers i, ii and iii shown in Figure 3 (structure 1).

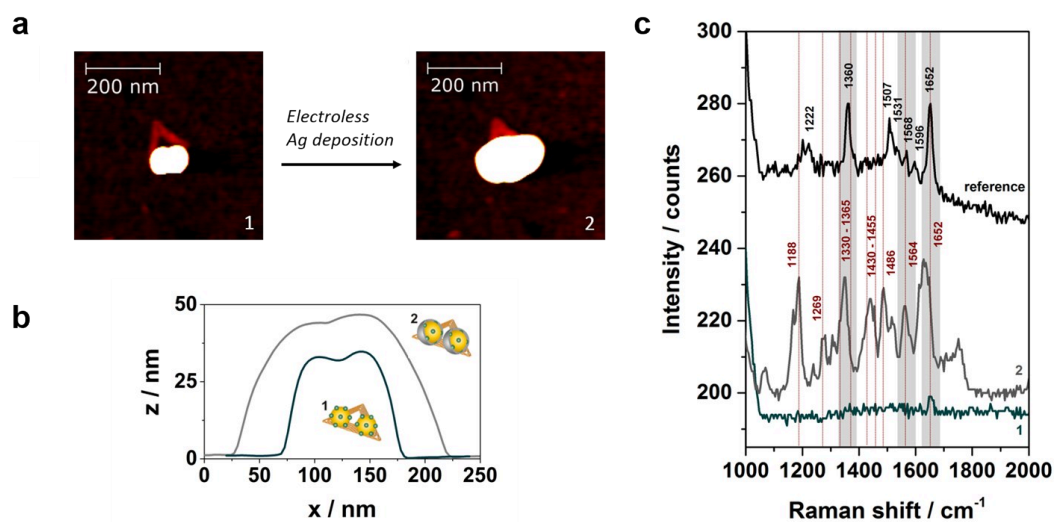


## 4. SERS spectrum for single 40 nm AuNPs covered with TAMRA-modified DNA



**Figure S3:** Comparison of SERS spectra for a dimeric structure (structure **1**, dimer **i**) and two single 40 nm AuNPs (corresponding AFM image shown on the right) covered with TAMRA-modified DNA. Single AuNPs only give negligibly weak SERS signals at 1360 and 1652 cm<sup>-1</sup>.

## 5. Assignment of additional DNA bands

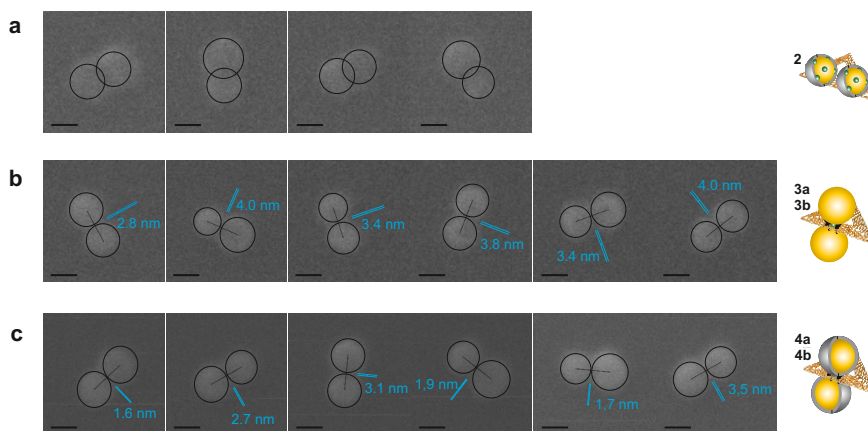


**Figure S4:** Example of a hybrid structure revealing DNA bands in the SERS spectrum upon electroless silver deposition. (a) AFM images of the selected DNA-AuNP hybrid without (structure **1**) and with (structure **2**) silver shell after 3 min of incubation (LI silver). (b) The height profiles of the two dimers shown in a) indicate the growth of the silver shell. (c) Corresponding SERS spectra of the dimers shown in a) before (cyan spectrum, **1**) and after (grey spectrum, **2**) electroless silver deposition. Spectral positions of TAMRA are highlighted in grey whereas bands arising from DNA are indicated by red dotted lines. In the corresponding Table S1 the assignment of all bands to certain DNA bases is summarized.

**Table S1:** Assignment of DNA bands visible in the SERS spectrum of Figure S4 (red dotted lines).

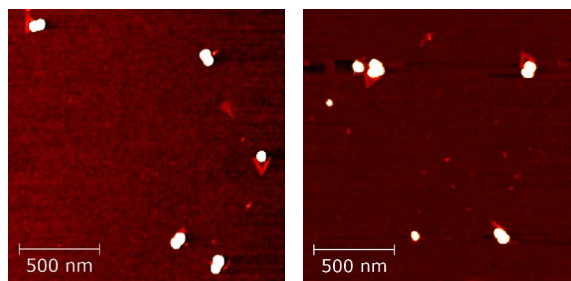
Raman shift / $\text{cm}^{-1}$	DNA base	
1188	T [2]	T = thymine
1269	T, A [2]	A = adenine
1330 – 1365	T, A, G, C [2]	G = guanine
1430 – 1455	T, A, G [2]	C = cytosine
1486	A [3]	
1564	T [2]	
1652	T [2]	

## 6. SEM images



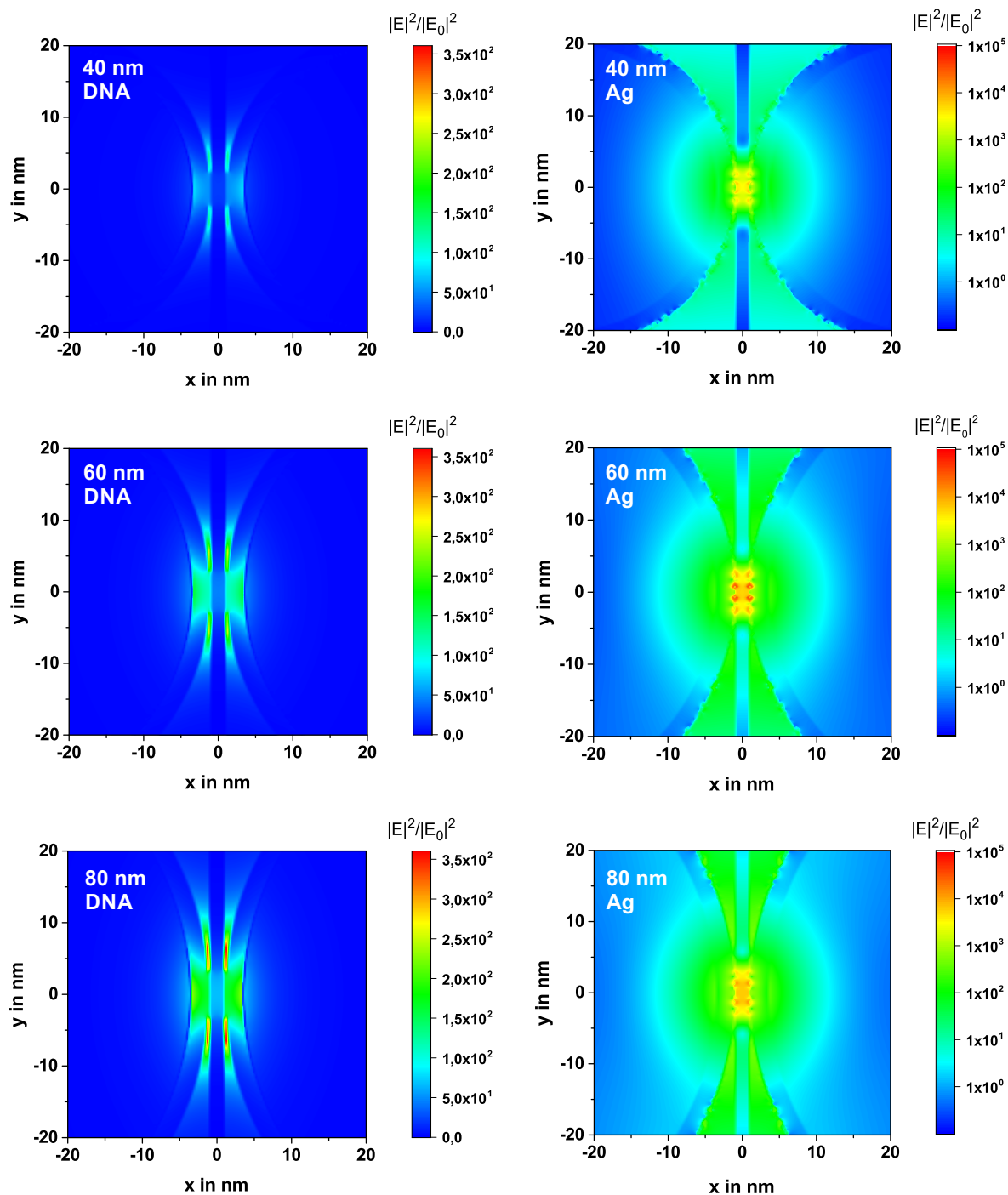
**Figure S5:** Scanning electron microscopy (SEM) images of representative DNA-origami-AuNP-hybrids with different structures. (a) SEM images of hybrids functionalized with two 40 nm AuNPs on one side of the DNA origami (structure **2**) confirm that the two individual AuNPs are fused together upon electroless silver deposition resulting in gapless structures. (b,c) For hybrids of structure **3a(3b)** an average gap size of 3.6 nm has been determined. Due to the silver enhancement process the analogue Au-Ag-core-shell-hybrids **4a(4b)** reveal a reduced average gap size of 2.4 nm. Scale bars = 50 nm.

## 7. AFM images of DNA origami substrates with two 40 nm AuNPs on different sides



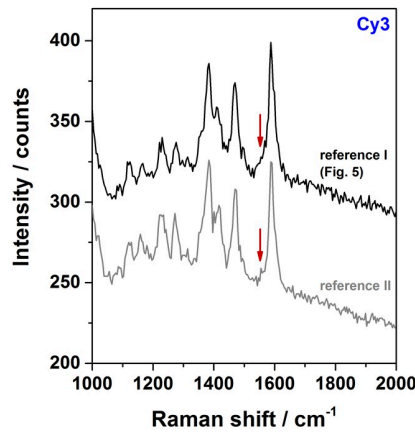
**Figure S6:** AFM images of DNA origami triangles functionalized with two 40 nm AuNPs on different sides before (left) and after the silver enhancement process (right). In both cases the DNA origami substrates are clearly visible which is not the case for the analogue structures functionalized with two 60 nm AuNPs (see Figure 5 for comparison).

## 8. FDTD simulations



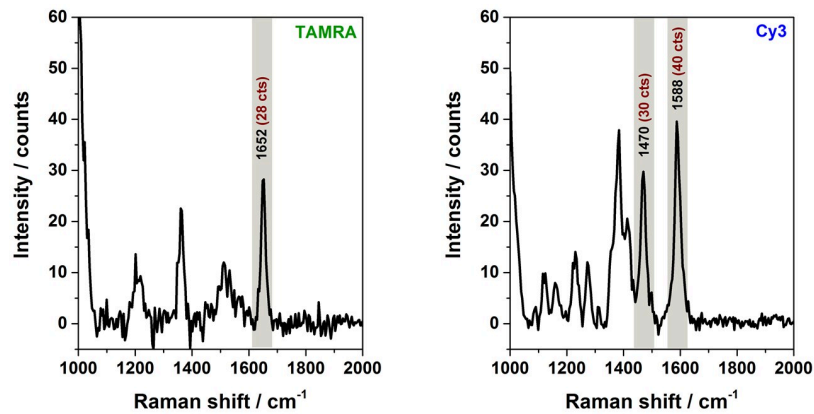
**Figure S7:** FDTD simulations for 40 nm (first row), 60 nm (second row) and 80 nm AuNP dimers (third row) attached to different sides of the DNA origami template ((Figure 1b), structures **3,4**). All dimers are separated by the DNA origami template (2.0 nm thickness) which is arranged concentrically in the simulations. For the simulations a 2.5 nm DNA coating (bare Au cores; left column) or a 2.5 nm Ag shell (Au-Ag-core-shell NPs; right column) is assumed. For all individual Au core sizes a significant increase of the electromagnetic field enhancement is observed upon electroless silver deposition. Comparing all simulations reveals that highest electromagnetic field enhancements can be expected for 60 nm AuNP dimers covered with a silver shell (second row, right column).

## 9. Reference spectra for Cy3

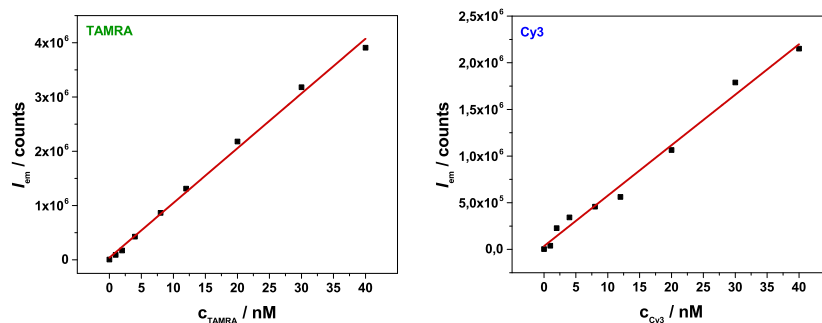


**Figure S8:** Two different SERS spectra serving as a reference for Cy3. The peak at  $1553\text{ cm}^{-1}$  (red arrow) which is only visible as a shoulder for reference I (black spectrum) is clearly detected for reference II (grey spectrum).

## 10. Data for EF estimation

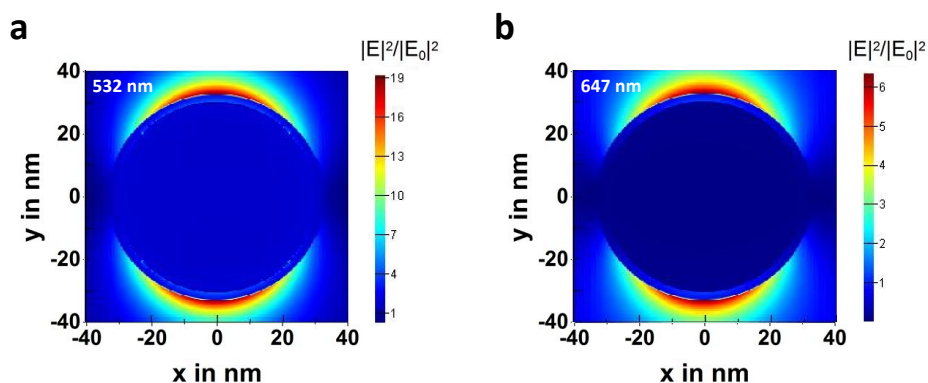


**Figure S9:** Background corrected average SERS spectra of approximately 15 single 60 nm AuNPs covered with dye-modified ssDNA ( $5'-(\text{TTT})_4\text{TX-SH-3}'$ ; X = TAMRA (left), X = Cy3 (right)). SERS experiments were performed using the same parameters as for the dimers in Figure 5. The SERS intensity of the highlighted bands were used for the experimental estimation of EFs (see Table 1).



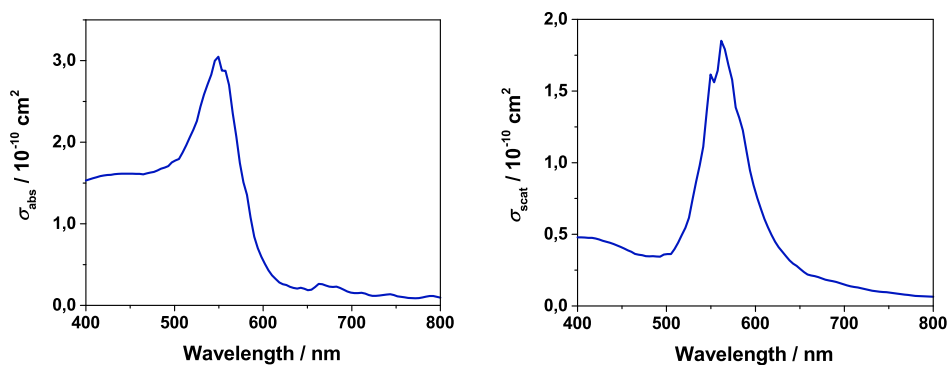
**Figure S10:** Calibration curves to determine the number of dye-modified DNA strands ( $5'-(\text{TTT})_4\text{TX-SH-3}'$ ) per 60 nm AuNP for X = TAMRA (left) and X = Cy3 (right) in order to estimate EFs for selected structures (see Table 1). The method was adopted from Hurst *et al.* [4].

## 11. Comparison of FDTD simulations for different excitation wavelengths



**Figure S11:** Comparison of FDTD calculations for a single 60 nm AuNP using a 532 nm (a) or a 647 nm (b) laser for excitation. The maximum electromagnetic field that can be expected is approximately 10 times higher for excitation with 532 nm.

## 12. Calculated absorption and scattering spectra



**Figure S12:** Calculated absorption (left) and scattering (right) spectra for dimeric Au-Ag-core-shell-structures (60 nm Au core, 2.5 nm silver shell) separated by a gap of 2.0 nm. Calculations reveal a maximum absorption cross-section at 549 nm and a maximum scattering cross-section at 561 nm.

## References

- [1] P. W. K. Rothmund, “Folding DNA to create nanoscale shapes and patterns”, *Nature* **440**, 297–302 (2006).
- [2] C. Otto, T. J. J. van den Tweel, F. F. M. de Mul, J. Greve, “Surface-enhanced Raman spectroscopy of DNA bases”, *J. Raman Spectrosc.* **17**, 289–298 (1986).
- [3] V. V. Thacker, L. O. Herrmann, D. O. Sigle, T. Zhang, T. Liedl, J. J. Baumberg, U. F. Keyser, “DNA origami based assembly of gold nanoparticle dimers for surface-enhanced Raman scattering”, *Nat. Commun.* **5**, 3448 (2014).
- [4] S. J. Hurst, A. K. R. Lytton-Jean, C. A. Mirkin, “Maximizing DNA Loading on a Range of Gold Nanoparticle Sizes”, *Anal. Chem.* **78**, 8313–8318 (2006).



### 6.3. Enhanced structural stability due to graphene

**“Enhanced structural stability of DNA origami nanostructures by graphene encapsulation”**

*New J. Phys.* **18**, 025016 (2016).

- Main text: pp. 93–101





## New Journal of Physics

The open access journal at the forefront of physics

Deutsche Physikalische Gesellschaft  DPG  
IOP Institute of Physics

Published in partnership with: Deutsche Physikalische Gesellschaft and the Institute of Physics



### PAPER

# Enhanced structural stability of DNA origami nanostructures by graphene encapsulation

#### OPEN ACCESS

#### RECEIVED

30 November 2015

#### REVISED

9 January 2016

#### ACCEPTED FOR PUBLICATION

26 January 2016

#### PUBLISHED

15 February 2016

Original content from this work may be used under the terms of the [Creative Commons Attribution 3.0 licence](#).

Any further distribution of this work must maintain attribution to the author(s) and the title of the work, journal citation and DOI.



Aleksandar Matković<sup>1,5</sup>, Borislav Vasić<sup>1</sup>, Jelena Pešić<sup>1</sup>, Julia Prinz<sup>2</sup>, Ilko Bald<sup>2,3</sup>, Aleksandar R Milosavljević<sup>4,6</sup> and Radoš Gajić<sup>1</sup>

<sup>1</sup> Center for Solid State Physics and New Materials, Institute of Physics, University of Belgrade, Pregrevica 118, 11080 Belgrade, Serbia

<sup>2</sup> Institute of Chemistry—Physical Chemistry, University of Potsdam, Potsdam, Germany

<sup>3</sup> BAM Federal Institute for Materials Research and Testing, Richard-Willstätter Str. 11, D-12489 Berlin, Germany

<sup>4</sup> Laboratory for Atomic Collision Processes, Institute of Physics, University of Belgrade, Pregrevica 118, 11080 Belgrade, Serbia

<sup>5</sup> Present address: Institute of Physics, Montanuniversität Leoben, Franz Josef Straße 18, A-8700 Leoben, Austria.

<sup>6</sup> Present address: Radiation Laboratory, University of Notre Dame, Notre Dame, IN 46556, USA.

E-mail: [bvasic@ipb.ac.rs](mailto:bvasic@ipb.ac.rs)

**Keywords:** graphene, DNA origami nanostructures, atomic force microscopy

### Abstract

We demonstrate that a single-layer graphene replicates the shape of DNA origami nanostructures very well. It can be employed as a protective layer for the enhancement of structural stability of DNA origami nanostructures. Using the AFM based manipulation, we show that the normal force required to damage graphene encapsulated DNA origami nanostructures is over an order of magnitude greater than for the unprotected ones. In addition, we show that graphene encapsulation offers protection to the DNA origami nanostructures against prolonged exposure to deionized water, and multiple immersions. Through these results we demonstrate that graphene encapsulated DNA origami nanostructures are strong enough to sustain various solution phase processing, lithography and transfer steps, thus extending the limits of DNA-mediated bottom-up fabrication.

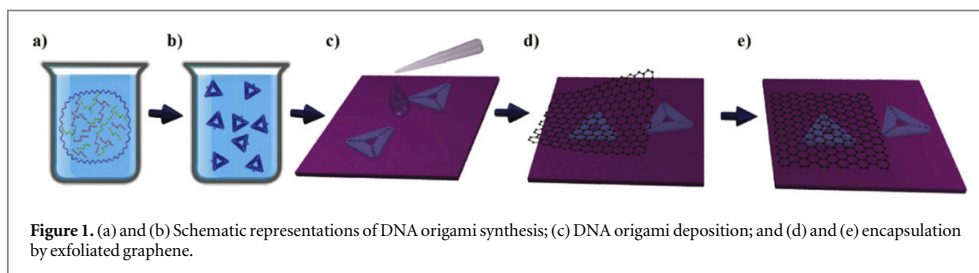
## 1. Introduction

Artificial deoxyribonucleic acid (DNA) macromolecules offer highly controllable bottom-up fabrication of various nanostructures. Since the first demonstration of DNA folding and the wide variety of structures and patterns that can be created at nanoscale [1], many 2D and 3D DNA origami nanostructures were fabricated using this method [2–4]. These structures often serve as substrates [5], offering a solution-based self-assembly with nanometer precision geometries. DNA nanostructures have been used as scaffolds for assembly of metallic nanoparticles [6–8], for routing polymers [9], surface-enhanced Raman scattering [10], as positive and negative masks for DNA nano-lithography [11–14], and even graphene patterning [15].

However, the delicate nature of DNA origami nanostructures constrains their applicability in bottom-up fabrication [16]. In particular any mechanical wear or solution phase processing could damage these nanostructures [7, 17, 18]. Thus enhancing the structural stability of DNA origami nanostructures is crucial for expanding the field of bottom-up nanofabrication.

On the other hand, graphene, a single atomic layer of crystal graphite, with its peerless mechanical properties can offer a solution to this issue. Young's modulus of graphene is about five times greater than of the bulk steel [19, 20], while at the same time graphene can be folded by 180° over less than one nanometer in length, without breaking its in-plane bonds. The crystal lattice of graphene (and graphite) is so densely packed that it is impermeable to any gases, even H<sub>2</sub> [21]. Also, graphene has low friction coefficient [22], and has been employed as a protective coating for friction reduction [23–27], wear protection [28, 29] and as corrosion barriers [30].

Recently, graphene has been employed to encapsulate objects such as single yeast cells [31], bacteria [32], water molecules [33–42], fluorescent films [43], single-stranded DNA and DNA nanostructures [44, 45]. It was demonstrated that graphene replicates the topography of the DNA molecules [44, 45]. Also, the directed



deposition of DNA rectangles onto lithography patterned strips of nitrogen-doped reduced graphene oxide was demonstrated [46].

In this study we focus on enhancing the structural stability of DNA origami nanostructures by graphene encapsulation. For this purpose triangular DNA origami nanostructures are deposited onto silicon substrates and encapsulated by single layer exfoliated graphene. The morphology of DNA origami nanostructures is very well transferred to the graphene, having even the inner triangle clearly resolved by atomic force microscopy (AFM). The samples are tested for their structural stability using AFM based manipulation and aqueous solution exposure. The forces required to damage bare and graphene encapsulated nanostructures are compared, and the effects of cumulative damage introduced by successive manipulations are investigated. In addition, stability of graphene encapsulated DNA origami nanostructures is tested against prolonged exposure to deionized water (DI H<sub>2</sub>O).

## 2. Materials and methods

### 2.1. DNA origami synthesis

Triangular DNA origami nanostructures were synthesized according to a modified version of Rothmund's method (schematically represented in figures 1(a) and (b)) [1]. Therefore, the M13mp18 virus strand (5 nM, New England Biolabs) serving as scaffold and 208 short staple strands (Integrated DNA Technologies) were mixed in a molar ratio of 1:30 in 1 × TAE (Sigma Aldrich) with 10 mM MgCl<sub>2</sub> (total volume 100 μl). The mixture was annealed by gradually decreasing the temperature from 80 °C to 8 °C within 1 h 48 min using a Primus 25 advanced thermal cycler (Peqlab). Excess staple strands were removed by spin filtering the resulting DNA origami solution two times at 3830 g for 10 min using Amicon Ultra-0.5 filters (100 kDa MWCO, Millipore) after the addition of 200 μl (first run) or 300 μl (second run) of 1 × TAE with 10 mM MgCl<sub>2</sub>.

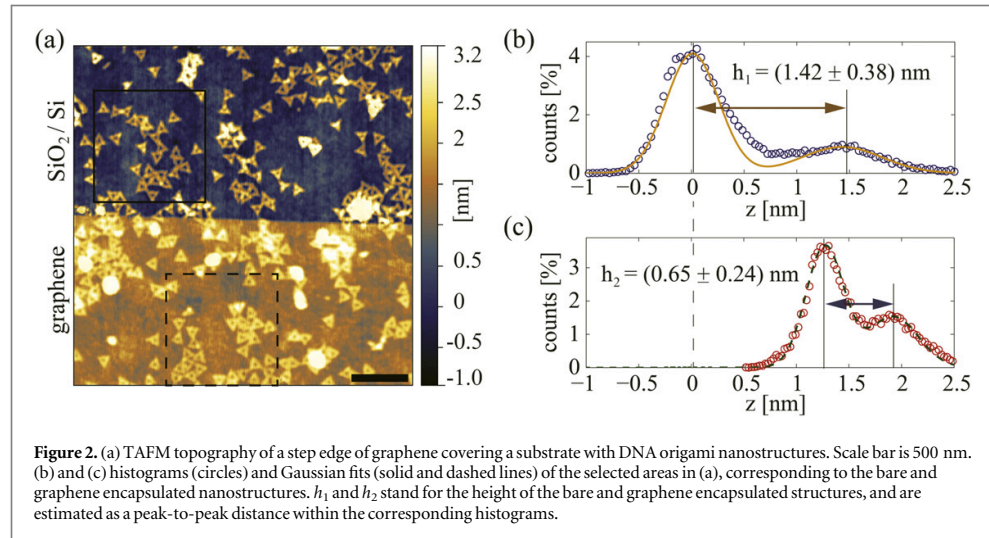
### 2.2. DNA origami deposition

After preparation, triangular DNA origami nanostructures were deposited onto  $\sim 1 \times 1$  cm<sup>2</sup> silicon substrates covered with 80 nm thick dry thermal oxide (SiO<sub>2</sub>/Si). Due to the interference of the light within the oxide layer, optical contrast of the graphene is enhanced and enables good visibility of graphene using optical microscopy, which is essential for the identification [47].

Before the deposition of DNA origami nanostructures, the substrates were cleaned and prepared by 5 min treatment in Novascan's ozone cleaner. Subsequently, drops of 0.5 μl of DNA origami solution were deposited on each substrate and covered with 10 μl of 10 × TAE with 10 mM of MgCl<sub>2</sub>. After one hour of incubation period in the water-saturated environment, the samples were rinsed in 1:1 water-ethanol solution to clean excess of material and dried with an argon gun (flow  $\sim 10$  l min<sup>-1</sup>). As a result DNA origami nanostructures covered the entire substrates with an averaged density of twenty triangular nanostructures per square micrometer. The DNA origami deposition is schematically represented in figure 1(c).

### 2.3. Graphene exfoliation

Graphene was deposited using the procedure known as micromechanical cleavage [48], yielding high-quality layers of graphene but limited in lateral size (on the order of tens of micrometers in diameter). Kish graphite (Naturgraphite GmbH) was used as starting material. Graphite flakes were cleaved using sticky tape (Nitto Denko ELP BT150ECM) and deposited on the substrates with DNA origami nanostructures. In order to avoid damaging DNA origami nanostructures, the entire micromechanical exfoliation was carried out at room temperature. After the deposition of graphene on top of the DNA origami nanostructures, individual flakes were detected using optical microscopy and single atomic layer samples were chosen by the optical contrast, and confirmed by the AFM. Schematic representation of the encapsulation by graphene is shown in figures 1(d) and (e).



#### 2.4. AFM measurements

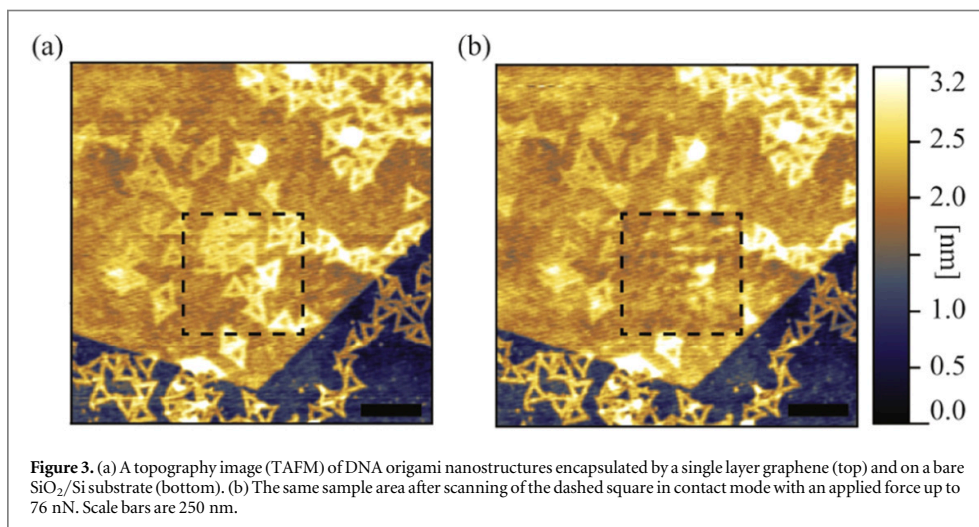
AFM experiments were carried out on the NT-MDT's NTEGRA Prima system. Imaging before and after AFM manipulation was performed in tapping mode (TAFM), using NSG01 probes from NT-MDT (typical force constant  $5.1 \text{ N m}^{-1}$ ). AFM manipulation was done in contact mode, using NT-MDT's CSG01 probes (typical force constant  $0.03 \text{ N m}^{-1}$ ). All measurements were done at ambient conditions. Initial imaging of the samples was done in TAFM mode. In this mode, the vibrating AFM tip is free from a torsion, so it does not push DNA origami nanostructures laterally leaving them practically intact.

AFM manipulation of graphene has been done using both static [49, 50] and dynamic plowing [51]. Here, AFM manipulation experiments were done in the following way. After selected sample areas were found and visualized using TAFM mode, AFM manipulations were carried out in contact mode, by scanning a selected sample area. Every image was recorded at constant normal force (constant set point). Manipulation on the graphene encapsulated DNA origami nanostructures was carried out using TAFM (NGS01, force constant  $5.1 \text{ N m}^{-1}$ ). However, imaging of bare DNA nanostructures was not possible in contact mode with these hard cantilevers. For this reason the manipulation of bare nanostructures was done using soft CSG01 probes (with two order of magnitude lower force constant).

AFM topography images of the samples were processed in an open source software Gwyddion. For each image first a mean plane was subtracted, followed by line corrections in the scanning direction, and finally a three point plane leveling is applied and the mean height is set to zero value. In the cases of graphene/substrate step edges, the three points were chosen on the bare substrate.

### 3. Results and discussion

A typical TAFM topography image of a step edge of graphene, with  $(1.26 \pm 0.21) \text{ nm}$  height, covering a substrate with DNA origami nanostructures is shown in figure 2(a). In order to estimate the structural damage, both the height and the shapes of the triangular DNA origami nanostructures were considered. The shapes were straightforwardly assessed from the topography images. The height of the structures was determined using a peak-to-peak difference from the selected area histograms, as shown in figures 2(b) and (c). Each histogram peak was fitted by a single Gaussian line. The uncertainty of the measured height was estimated as a half width at half maximum of the histogram peak that corresponds to either bare or graphene encapsulated DNA origami nanostructures. As a result, an average height of the bare triangular DNA origami nanostructures was found to be  $(1.42 \pm 0.38) \text{ nm}$ , while the graphene encapsulated ones were  $(0.65 \pm 0.24) \text{ nm}$  high. The observed difference is due to non-perfect replication of DNA origami by graphene. Some parts of graphene covering DNA nanostructures do not lie perfectly on  $\text{SiO}_2$  substrate. These parts of graphene are slightly lifted above the substrate and make the effective height of the graphene covered DNA nanostructures smaller. This effect is even more pronounced for high density of deposited DNA origami nanostructures since graphene does not fall perfectly on  $\text{SiO}_2$  substrate between adjacent DNA nanostructures.



### 3.1. AFM manipulation

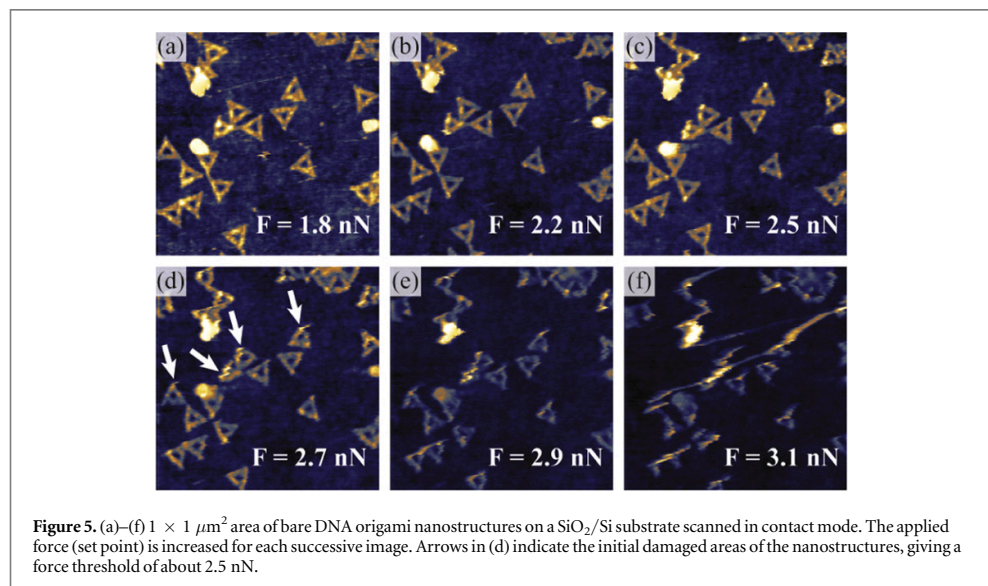
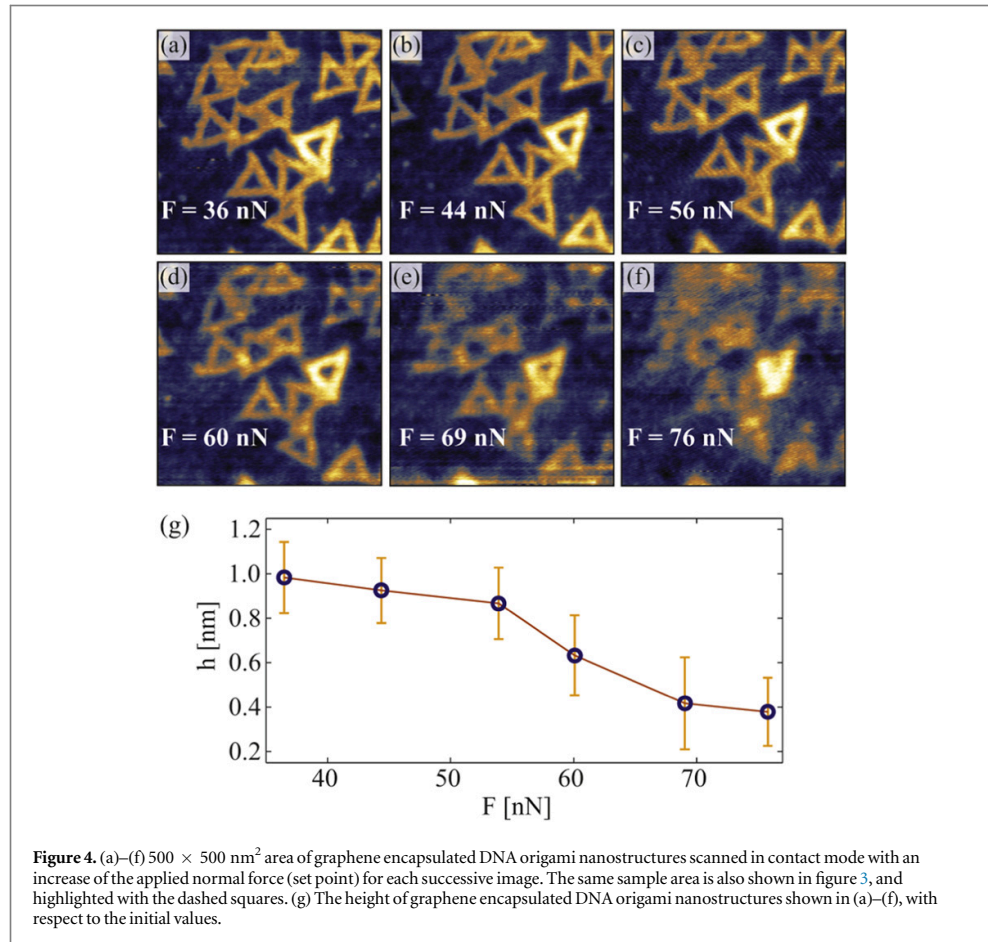
Imaging of DNA nanostructures in the contact mode is challenging [44]. Therefore, so far their mechanical properties and stability have been measured using peak force tapping mode with precisely controlled force in pico Newton range [52]. Here AFM manipulation in contact mode was applied in order to determine the forces required to damage both bare and graphene encapsulated DNA origami nanostructures. Figure 3 shows TAFM topography of DNA origami nanostructures before and after manipulation of a  $500 \times 500 \text{ nm}^2$  selected area, marked by the dashed square. The selected area was repeatedly scanned six times in contact mode. The applied normal force was increased for each successive scan ranging from 36 to 76 nN. The contact mode topography scans are shown in figures 4(a)–(f). The same probe (NGS01) was used both for the imaging of the sample in TAFM mode and for the manipulation in contact mode. The height of the encapsulated nanostructures was estimated for each contact mode scan using their corresponding histogram peak-to-peak distance. The results are presented in figure 4(g), showing encapsulated structure height as a function of the applied normal force. Both the height and the shape of the triangular origami nanostructures indicate that structural damage starts to occur when a normal force of about 60 nN is exerted.

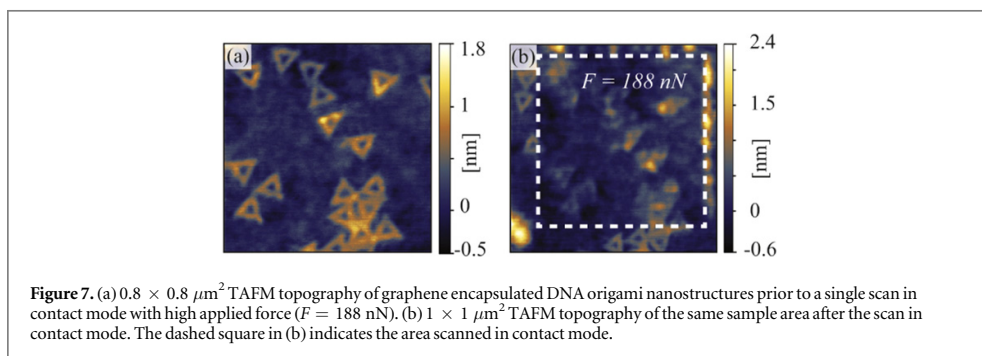
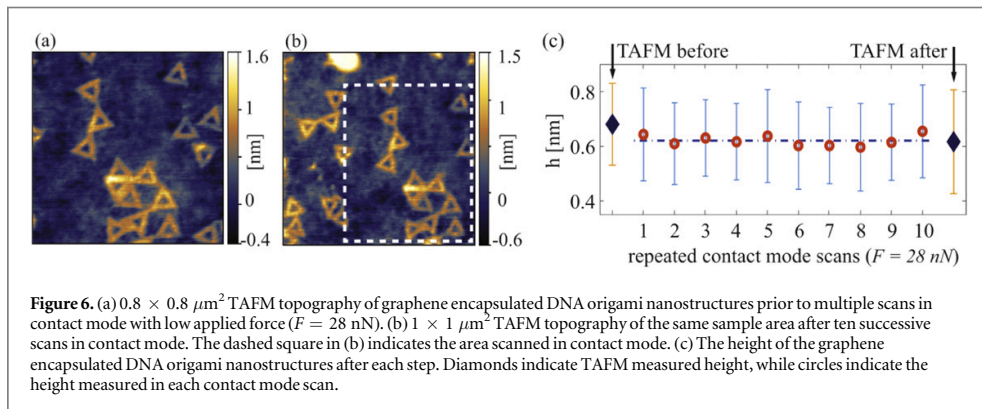
In order to estimate the amount of mechanical protection that graphene offers to DNA origami nanostructures, the same AFM manipulation experiments are carried out on the bare triangular DNA origami nanostructures (on SiO<sub>2</sub>/Si substrate). Here much smaller normal forces are required to damage the structures. Thus, a soft mode probes (CSG01) were used, with the typical force constant of  $0.03 \text{ N m}^{-1}$ . Figure 5 shows six subsequent scans in contact mode. Again, the normal force is increased for each scan, ranging from 1.8 to 3.1 nN. The triangular DNA origami nanostructures appeared unchanged up to the normal force of 2.5 nN.

The nature of the structural damage that is introduced by the AFM probe is different for the bare and graphene encapsulated DNA origami nanostructures. In the case of the encapsulated nanostructures graphene protects them from attaching to the tip of the AFM probe. As a result, the damaged structures appeared "smudged" and their height is reduced. On the other hand the bare nanostructures tend to attach to the tip and drift in the scanning direction. As a result the height of the bare structures that were not pushed and damaged by the AFM probe does not change significantly (figure 5(f)).

The arrows in figure 5(d) indicate the initial damage of the bare DNA origami nanostructures, that is introduced with the normal force of only 2.7 nN. Compared with the same tests carried out on the encapsulated structures (figure 4), the force required to damage the DNA origami nanostructures is over an order of magnitude greater for the ones encapsulated with graphene. The structural damage that can be introduced by AFM manipulation strongly depends on the adhesion of both the DNA nanostructures and the graphene layer to the substrate. For this reason it is not reliable to set the exact force threshold at which graphene offers wear protection to these structures.

Still the question remains whether the cumulative damage arises when the same graphene encapsulated structures are scanned multiple times. To test this the same graphene encapsulated area was scanned in contact mode ten times successively. The normal force was set to 28 nN for all scans. TAFM topography images of the same sample area before and after manipulation are respectively shown in figures 6(a) and (b). Figure 6(c) shows the height of the graphene encapsulated DNA origami nanostructures for each TAFM and contact mode scan.





The heights were obtained as a peak-to-peak distance from their corresponding topography images. The results show that there is no cumulative damage effect if the applied normal force is below the damage threshold ( $\sim 60 \text{ nN}$ ).

On the other hand, only a single contact mode scan with high enough force is sufficient to damage graphene encapsulated nanostructures. This is demonstrated in figure 7. Here, TAFM topography images are shown before and after the selected area was scanned in contact mode with the normal force set to  $188 \text{ nN}$ , well above the damage threshold.

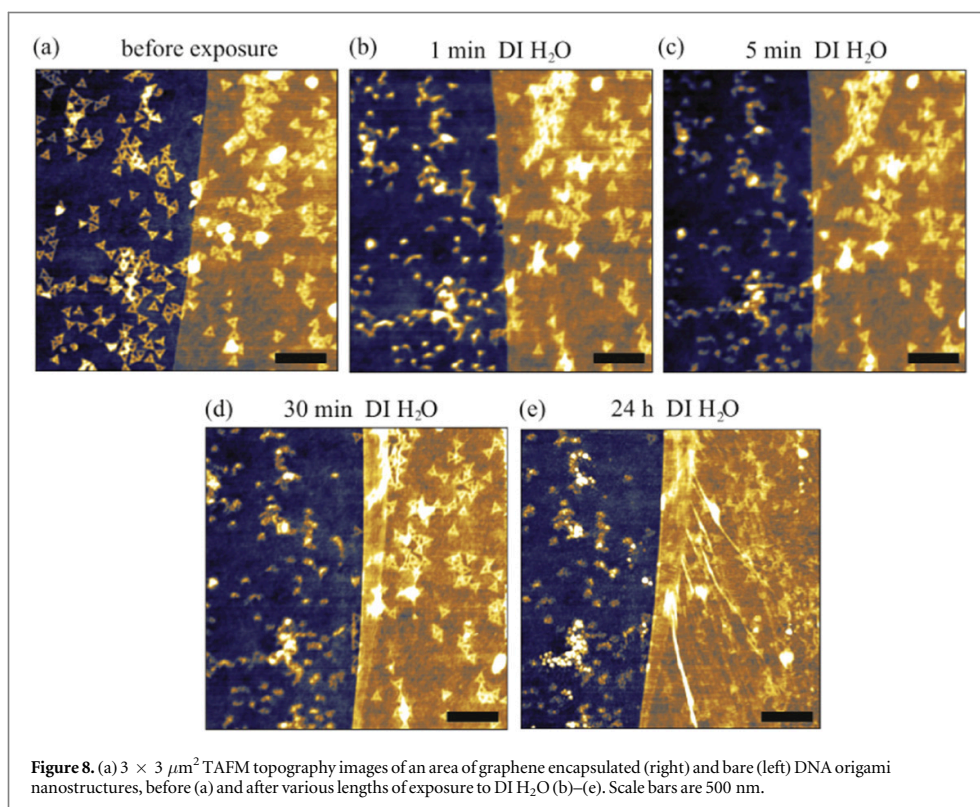
### 3.2. Deionized water exposure

In order to extend the use of DNA origami nanostructures as scaffolds in the bottom-up nanofabrication [16], these structures need to be strong enough to withstand the harsh conditions needed in many fabrication steps [18]. Commonly these steps include submersion into liquids. Either as the part of the solution phase processing or simple rinsing after a lithography step, DNA origami nanostructures need to withstand both short and prolonged liquid exposures.

In this study the exposure to deionized water was tested on both bare and graphene encapsulated structures. The exposure time was varied between 1 min and 24 h. The  $\text{SiO}_2/\text{Si}$  substrates covered with DNA origami nanostructures and partly encapsulated by graphene were submerged into 10 mL of  $\text{DI H}_2\text{O}$  (Millipore,  $18.2 \text{ M}\Omega \text{ cm}^{-1}$ ) and after the set exposure time quickly dried with an argon gun (flow  $\sim 10 \text{ l min}^{-1}$ ). Water exposure was done successively on each flake, e.g.: the flake was exposed to 1 min in  $\text{DI H}_2\text{O}$ , measured, then again exposed for 4 min more to give the total of 5 min exposure, and so on. This way properties that are unique for every sample, as adhesion of nanostructures and graphene to the substrate, did not figure in the test.

The selected sample areas were imaged using TAFM both prior and after  $\text{DI H}_2\text{O}$  exposure. Figure 8 shows TAFM topography images of triangular DNA origami nanostructures partly encapsulated by graphene before exposure (a) and after various lengths of exposure to  $\text{DI H}_2\text{O}$  (b)–(e).

The unprotected structures are significantly damaged even after only 1 min of  $\text{DI H}_2\text{O}$  exposure, and not lifted-off the substrate. Most likely the amount of residual  $\text{Mg}^{2+}$  ions on the substrate surface determines whether the structures are damaged or lifted-off the substrate [18].



**Figure 8.** (a)  $3 \times 3 \mu\text{m}^2$  TAFM topography images of an area of graphene encapsulated (right) and bare (left) DNA origami nanostructures, before (a) and after various lengths of exposure to DI H<sub>2</sub>O (b)–(e). Scale bars are 500 nm.

Graphene encapsulated DNA origami nanostructures appeared to be intact by the water exposure. Each individual triangular origami was preserved even after 30 min of DI H<sub>2</sub>O exposure. The height of the nanostructures was also unchanged. In the case of the sample shown in figures 8(a)–(d) the height of the encapsulated origami nanostructures was  $0.8(\pm 0.2)$  nm, after each exposure. In figure 8(d) the edge of graphene sample was folded, most likely during the drying step.

The only exception occurred after twenty four hours of exposure. In this case graphene started to wrinkle. Although some triangular DNA origami nanostructures are still visible underneath graphene (figure 8(f)), most of the nanostructures were damaged and their height estimation was not reliable.

The exact exposure time threshold will again depend on the adhesion to the substrate of both graphene and DNA origami nanostructures, and varies from sample to sample. Still, very short exposures do damage or lift-off bare DNA nanostructures [18]. On the other hand graphene encapsulation offers significant protection increasing the exposure times by at least two orders of magnitude.

#### 4. Conclusion

In summary, we have demonstrated that single layer exfoliated graphene can be used as a protective layer for DNA origami nanostructures. Through the AFM based manipulation we have shown that the normal force required to damage graphene encapsulated DNA origami nanostructures is over an order of magnitude greater than for the unprotected ones. The threshold for the normal force that induces structural damage to the graphene encapsulated DNA origami nanostructures was found to be about 60 nN. In addition, we have shown that graphene provides wear protection against multiple manipulations if the applied normal force is below the damage threshold.

Besides wear protection, graphene encapsulated DNA origami nanostructures were tested against prolonged exposure to deionized water, and multiple immersions. We show that graphene encapsulated nanostructures remain intact even after 30 min of the exposure to deionized water, while the bare structures are significantly damaged in the matter of seconds. The limits of graphene protection against deionized water exposure arise from wrinkling of the graphene layer itself.

We expect that other liquids will act in the similar manner as long as they do not damage graphene, and will only take different amount of time to damage bare DNA origami nanostructures. This extends the use of DNA origami scaffolds in many fabrication processes, as various lithography steps or wet transfer of 2D materials. Future studies could involve encapsulation by more than one layer of graphene and the use of other 2D materials, as hexagonal boron nitride, which could prove protection in harsh environments that graphene might not be suitable for.

### Acknowledgments

This work is supported by the Serbian MPNTR through Projects ON 171005, III 45018, IO 171020, 451-03-2802-IP/1/167, and by the DAAD bilateral project 451-03-01858/2013-09/1 between Republic of Serbia and Germany. BV acknowledges support from COST Action MP1303. IB acknowledges support from a Marie Curie FP7 Integration Grant within the 7th European Union Framework Programme, and by the Deutsche Forschungsgemeinschaft (DFG).

### References

- [1] Rothmund P W K 2006 Folding DNA to create nanoscale shapes and patterns *Nature* **440** 297–302
- [2] Han D, Pal S, Nangreave J, Deng Z, Liu Y and Yan H 2011 DNA origami with complex curvatures in three-dimensional space *Science* **332** 342–6
- [3] Ke Y, Ong L L, Shih W M and Yin P 2012 Three-dimensional structures self-assembled from DNA bricks *Science* **338** 1177–83
- [4] Wei B, Dai M and Yin P 2012 Complex shapes self-assembled from single-stranded DNA tiles *Nature* **485** 623–6
- [5] Bald I and Keller A 2014 Molecular processes studied at a single-molecule level using DNA origami nanostructures and atomic force microscopy *Molecules* **19** 13803–23
- [6] Li H, Park S H, Reif J H, LaBean T H and Yan H 2004 DNA-templated self-assembly of protein and nanoparticle linear arrays *J. Am. Chem. Soc.* **126** 418–9
- [7] Geng Y, Liu J, Pound E, Gyawali S, Harb J N and Woolley A T 2011 Rapid metallization of lambda DNA and DNA origami using a Pd seeding method *J. Mater. Chem.* **21** 12126–31
- [8] Schreiber R, Kempter S, Holler S, Schüller V, Schiffels D, Simmel S S, Nickels P C and Liedl T 2011 DNA origami-templated growth of arbitrarily shaped metal nanoparticles *Small* **7** 1795–9
- [9] Knudsen J B *et al* 2015 Routing of individual polymers in designed patterns *Nat. Nanotechnol.* **10** 892–8
- [10] Prinz J, Schreiber B, Olejko L, Oertel J, Rackwitz J, Keller A and Bald I 2013 DNA origami substrates for highly sensitive surface-enhanced Raman scattering *J. Phys. Chem. Lett.* **4** 4140–5
- [11] Becerril H A and Woolley A T 2007 DNA shadow nanolithography *Small* **3** 1534–8
- [12] Deng Z and Mao C 2004 Molecular lithography with DNA nanostructures *Angew. Chem. Int. Ed.* **43** 4068–70
- [13] Surwade S P, Zhao S and Liu H 2011 Molecular lithography through DNA-mediated etching and masking of SiO<sub>2</sub> *J. Am. Chem. Soc.* **133** 11868–71
- [14] Surwade S P, Zhou F, Wei B, Sun W, Powell A, O'Donnell C, Yin P and Liu H 2013 Nanoscale growth and patterning of inorganic oxides using DNA nanostructure templates *J. Am. Chem. Soc.* **135** 6778–81
- [15] Jin Z, Sun W, Ke Y, Shih C-J, Paulus G L C, Wang Q H, Mu B, Yin P and Strano M S 2013 Metallized DNA nanolithography for encoding and transferring spatial information for graphene patterning *Nat. Commun.* **4** 1663
- [16] Zhang G, Surwade S P, Zhou F and Liu H 2013 DNA nanostructure meets nanofabrication *Chem. Soc. Rev.* **42** 2488–96
- [17] Liu J, Geng Y, Pound E, Gyawali S, Ashton J R, Hickey J, Woolley A T and Harb J N 2011 Metallization of branched DNA origami for nanoelectronic circuit fabrication *ACS Nano* **5** 2240–7
- [18] Kim H, Surwade S P, Powell A, O'Donnell C and Liu H 2014 Stability of DNA origami nanostructure under diverse chemical environments *Chem. Mater.* **26** 5265–73
- [19] Lee C, Wei X, Kysar J W and Hone J 2008 Measurement of the elastic properties and intrinsic strength of monolayer graphene *Science* **321** 385–8
- [20] Lee G H *et al* 2013 High-strength chemical-vapor-deposited graphene and grain boundaries *Science* **340** 1073–6
- [21] Bunch J S, Verbridge S S, Alden J S, van der Zande A M, Parpia J M, Craighead H G and McEuen P L 2008 Impermeable atomic membranes from graphene sheets *Nano Lett.* **8** 2458–62
- [22] Kim K-S, Lee H-J, Lee C, Lee S-K, Jang H, Ahn J-H, Kim J-H and Lee H-J 2011 Chemical vapor deposition-grown graphene: the thinnest solid lubricant *ACS Nano* **5** 5107–14
- [23] Berman D, Erdemir A and Sumant A V 2014 Graphene: a new emerging lubricant *Mater. Today* **17** 31–42
- [24] Klemenz A, Pastewka L, Balakrishna S G, Caron A, Bennewitz R and Moseler M 2014 Atomic scale mechanisms of friction reduction and wear protection by graphene *Nano Lett.* **14** 7145–52
- [25] Filletter T, McChesney J L, Bostwick A, Rotenberg E, Emtsev K V, Seyller Th, Horn K and Bennewitz R 2009 Friction and dissipation in epitaxial graphene films *Phys. Rev. Lett.* **102** 086102
- [26] Lee C, Li Q, Kalb W, Liu X-Z, Berger H, Carpick R W and Hone J 2010 Frictional characteristics of atomically thin sheets *Science* **328** 76–80
- [27] Lee H, Lee N, Seo Y, Eom J and Lee S W 2009 Comparison of frictional forces on graphene and graphite *Nanotechnology* **20** 325701
- [28] Berma D, Erdemir A and Sumant A V 2013 Few layer graphene to reduce wear and friction on sliding steel surfaces *Carbon* **54** 454–9
- [29] Lin L Y, Kim D-E, Kim W-K and Jun S-C 2011 Friction and wear characteristics of multi-layer graphene films investigated by atomic force microscopy *Surf. Coat. Tech.* **205** 4864–9
- [30] Kirkland N T, Schiller T, Medhekar N and Birbilis N 2012 Exploring graphene as a corrosion protection barrier *Corros. Sci.* **56** 1–4
- [31] Kempaiah R, Salgado S, Chung W L and Maheshwari V 2011 Graphene as membrane for encapsulation of yeast cells: protective and electrically conducting *Chem. Commun.* **47** 11480–2



- [32] Mohanty N, Fahrenholtz M, Nagaraja A, Boyle D and Berry V 2011 Impermeable graphenic encasement of bacteria *Nano Lett.* **11** 1270–5
- [33] Xu K, Cao P and Heath J R 2010 Graphene visualizes the first water adlayers on mica at ambient conditions *Science* **329** 1188–91
- [34] Cao P, Xu K, Varghese J O and Heath J R 2011 The microscopic structure of adsorbed water on hydrophobic surfaces under ambient conditions *Nano Lett.* **11** 5581–6
- [35] Cao P, Xu K, Varghese J O, Xu K and Heath J R 2012 Visualizing local doping effects of individual water clusters on gold(111)-supported graphene *Nano Lett.* **12** 1459–63
- [36] Shim J, Lui C H, Ko T Y, Yu Y-J, Kim P, Heinz T F and Ryu S 2012 Water-gated charge doping of graphene induced by mica substrates *Nano Lett.* **12** 648–54
- [37] Severin N, Lange P, Sokolov I M and Rabe J P 2012 Reversible dewetting of a molecularly thin fluid water film in a soft graphene-mica slit pore *Nano Lett.* **12** 774–9
- [38] He K T, Wood J D, Doidge G P, Pop E and Lyding J W 2012 Scanning tunneling microscopy study and nanomanipulation of graphene-coated water on mica *Nano Lett.* **12** 2665–72
- [39] Komurasaki H, Tsukamoto T, Yamazaki K and Ogino T 2012 Layered structures of interfacial water and their effects on Raman spectra in graphene-on-sapphire systems *J. Phys. Chem. C* **116** 10084–9
- [40] Lee M J, Choi J S, Kim J-S, Byun I-S, Lee D H, Ryu S and Lee C 2012 Characteristics and effects of diffused water between graphene and a SiO<sub>2</sub> substrate *Nano Res.* **5** 710–7
- [41] Li Q, Song J, Besenbacher F and Dong M 2015 Two-dimensional material confined water *Acc. Chem. Res.* **48** 119–27
- [42] Song J, Li Q, Wang X, Li J, Zhang S, Kjems J, Besenbacher F and Dong M 2014 Evidence of Stranski–Krastanov growth at the initial stage of atmospheric water condensation *Nat. Commun.* **5** 4837
- [43] Lange P, Dorn M, Severin N, Vanden Bout D A and Rabe J P 2011 Single- and double-layer graphenes as ultrabarrriers for fluorescent polymer films *J. Phys. Chem. C* **115** 23057–61
- [44] Severin N, Dorn M, Kalachev A and Rabe J P 2011 Replication of single macromolecules with graphene *Nano Lett.* **11** 2436–9
- [45] Moon Y, Shin J, Seo S, Park J, Dugasani S R, Woo S H, Park T, Park S H and Ahn J R 2014 Nanoscale topographical replication of graphene architecture by artificial DNA nanostructures *Appl. Phys. Lett.* **104** 231904
- [46] Yun J M, Im K N, Kim J Y, Shin D O, Lee W J, Lee S H, Lieberman M and Kim S O 2012 DNA origami nanopatterning on chemically modified graphene *Angew. Chem.* **124** 936–9
- [47] Blake P, Hill E W, Castro Neto A H, Novoselov K S, Jiang D, Yang R, Booth T J and Geim A K 2007 Making graphene visible *Appl. Phys. Lett.* **91** 063124
- [48] Novoselov K S, Geim A K, Morozov S V, Jiang D, Zhang Y, Dubonos S V, Grigorieva I V and Firsov A A 2004 Electric field effect in atomically thin carbon films *Science* **306** 666–9
- [49] Giesbers A J M, Zeitler U, Neubeck S, Freitag F, Novoselov K S and Maan J C 2008 Nanolithography and manipulation of graphene using an atomic force microscope *Solid State Commun.* **147** 366–9
- [50] Eilers S and Rabe J P 2009 Manipulation of graphene within a scanning force microscope *Phys. Status Solidi B* **246** 2527–9
- [51] Vasić B, Kratzer M, Matković A, Nevošad A, Ralević U, Jovanović D, Ganser C, Teichert C and Gajić R 2013 Atomic force microscopy based manipulation of graphene using dynamic plowing lithography *Nanotechnology* **24** 015303
- [52] Song J, Zhang Z, Zhang S, Liu L, Li Q, Xie E, Gothelf K V, Besenbacher F and Dong M 2013 Isothermal hybridization kinetics of DNA assembly of two-dimensional DNA origami *Small* **9** 2954–9



## 6.4. DNA origami–AuNP dimer–graphene hybrid structures

### “Hybrid Structures for Surface-Enhanced Raman Scattering: DNA Origami/Gold Nanoparticle Dimer/Graphene”

*Small* **12**, 5458–5467 (2016).

- Main text: pp. 105–114
- Supporting Information (SI): pp. 115–116



## Hybrid Structures for Surface-Enhanced Raman Scattering: DNA Origami/Gold Nanoparticle Dimer/Graphene

Julia Prinz, Aleksandar Matković, Jelena Pešić, Radoš Gajić, and Ilko Bald\*

**A** combination of three innovative materials within one hybrid structure to explore the synergistic interaction of their individual properties is presented. The unique electronic, mechanical, and thermal properties of graphene are combined with the plasmonic properties of gold nanoparticle (AuNP) dimers, which are assembled using DNA origami nanostructures. This novel hybrid structure is characterized by means of correlated atomic force microscopy and surface-enhanced Raman scattering (SERS). It is demonstrated that strong interactions between graphene and AuNPs result in superior SERS performance of the hybrid structure compared to their individual components. This is particularly evident in efficient fluorescence quenching, reduced background, and a decrease of the photobleaching rate up to one order of magnitude. The versatility of DNA origami structures to serve as interface for complex and precise arrangements of nanoparticles and other functional entities provides the basis to further exploit the potential of the here presented DNA origami–AuNP dimer–graphene hybrid structures.

### 1. Introduction

With the introduction of the DNA origami technique by Paul Rothemund in 2006<sup>[1]</sup> a versatile tool for the folding of DNA into almost any desired shapes and patterns was created. Initially applied for the fabrication of 2D structures the technique was rapidly extended to construct 3D objects.<sup>[2]</sup>

J. Prinz, Prof. I. Bald  
Institute of Chemistry  
University of Potsdam  
Karl-Liebknecht-Str. 24-25, 14469 Potsdam, Germany  
E-mail: bald@uni-potsdam.de

Dr. A. Matković,<sup>[+]</sup> J. Pešić, Prof. R. Gajić  
Center for Solid State Physics and New Materials  
Institute of Physics  
University of Belgrade  
Pregrevica 118, 11080 Belgrade, Serbia

Prof. I. Bald  
BAM Federal Institute for Materials Research and Testing  
Richard-Willstätter Str. 11, 12489 Berlin, Germany

<sup>[+]</sup>Present address: Institute of Physics, Montanuniversität Leoben,  
Franz Josef Straße 18, A-8700 Leoben, Austria

DOI: 10.1002/sml.201601908



Due to the addressability of every single DNA staple strand being part of the self-assembly process, functional units, e.g., gold nanoparticles (AuNPs), can be attached to DNA origami templates with nm precision. Such hybrid structures have been used for the study of plasmonic effects<sup>[3–6]</sup> or surface-enhanced spectroscopies such as fluorescence enhancement<sup>[7]</sup> or quenching,<sup>[8]</sup> surface-enhanced Raman scattering (SERS),<sup>[9–12]</sup> and even for single-molecule SERS.<sup>[13]</sup>

The basis of surface-enhanced spectroscopy methods is a metal surface—in most cases a metal nanoparticle (NP)—which is brought in close vicinity to the analyte molecule(s). Caused by the excitation of the surface plasmon resonance the electromagnetic field surrounding the NP is enhanced resulting in an increase of the detected signal, that is, fluorescence or Raman scattering. Dimers of AuNPs turned out to be superior over single AuNPs regarding their performances in electromagnetic field enhancements due to hot spot formation.<sup>[14,15]</sup>

Graphene is a 2D material consisting of sp<sup>2</sup>-hybridized carbon atoms which are arranged in a honeycomb lattice. It exhibits a unique combination of electrical, mechanical, and optical properties including high electronic<sup>[16]</sup> and thermal conductivities,<sup>[17]</sup> impermeability to any gases,<sup>[18]</sup> as well as high optical transparency.<sup>[19]</sup> Although graphene flatly

adsorbs on various substrates, it has been shown to replicate the shape of underlying macromolecules such as double stranded plasmid DNA,<sup>[20]</sup> 1D five-helix ribbon structures and 2D double-crossover lattices,<sup>[21]</sup> as well as DNA origami structures<sup>[22]</sup> very well due to its flexible nature. Recently, it has been reported that the structural stability of triangular DNA origami substrates toward mechanical forces or prolonged exposure to deionized water can be enhanced by graphene encapsulation.<sup>[22]</sup>

Combining graphene and metal NPs within one hybrid structure is especially advantageous due to the resulting synergy of unique electrical, mechanical, and optical properties introduced by both initial materials. Especially within the fields of biomedicine<sup>[23,24]</sup> and biosensing<sup>[25,26]</sup> various types of hybrid materials based on graphene and NPs have been created. Principally, graphene-NP hybrid structures can be obtained either by decorating graphene sheets using metal NPs<sup>[27–29]</sup> or by wrapping<sup>[30,31]</sup> or covering<sup>[32,33]</sup> NPs with graphene. Furthermore, graphene has been reported to remarkably suppress the photobleaching of dye molecules during continuous laser exposure. In shell-isolated SERS experiments using metal nanoparticles encapsulated by few-layer graphene (FLG), the SERS signal intensity of cobalt phthalocyanine (CoP) has been shown to be constant over a time range of 160 s.<sup>[30]</sup> In another study, Zhao et al. presented R6G molecules being sandwiched between a Ag surface and a monolayer of graphene leading to enhanced photostability of the R6G molecules due to isolation from ambient oxygen.<sup>[34]</sup>

Here, we introduce a novel kind of multifunctional hybrid material in which the programmability of DNA origami structures, the optical properties of AuNPs, as well as the protective properties of graphene are efficiently merged. The synergistic properties of these hybrid structures are investigated with respect to their SERS performance, polarization

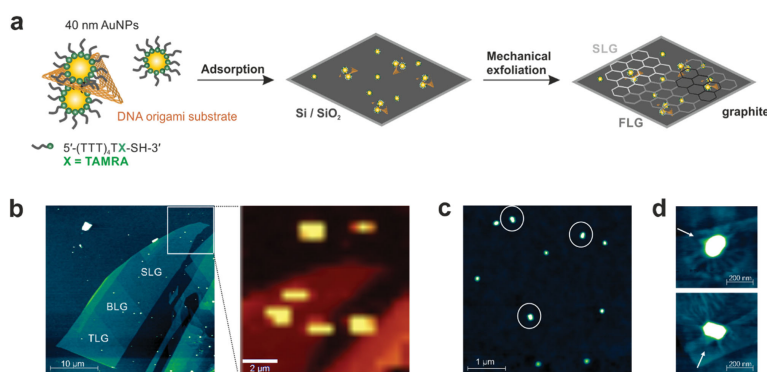
dependence of the SERS signal, and photostability of the dyes.

## 2. Results and Discussion

### 2.1. Synthesis of DNA Origami–AuNP Dimer–Graphene (AuDG) Hybrid Structures and Atomic Force Microscopy (AFM)–SERS Correlation

An overview of the two-step synthesis of the AuDG hybrid structures is depicted in **Figure 1a**. Initially, triangular DNA origami substrates are folded with a set of 208 staple strands using the genome of the bacteriophage M13mp18 as scaffold. Each DNA origami substrate contains four capture sequences for each AuNP ( $5'-(AAA)_8T_4-3'$ ) protruding from opposite sides of the DNA origami triangle. Furthermore, 40 nm AuNPs are coated with dye-modified ssDNA ( $5'-(TTT)_4TX-SH-3'$  or  $5'-X-(TTT)_4T-SH-3'$ ; X = carboxyethylrhodamine (TAMRA)). During a DNA hybridization process between the capture strands of the DNA origami substrates and the coating strands of the AuNPs the initial dimeric structures are created. Subsequently, the dimers are adsorbed on Si wafers covered with a layer of 290 nm thick dry thermal oxide (Si/SiO<sub>2</sub>), which enhances the optical contrast within graphene and therefore allows for its identification.<sup>[35]</sup> Since the mixture is not further purified after DNA hybridization AuNP dimers coexist with unbound AuNPs. In a second step graphene is deposited on top of the immobilized structures following the classical micromechanical exfoliation process<sup>[16]</sup> resulting in AuDG hybrid structures.

Subsequent correlation of AFM and SERS images allows for a direct assignment of SERS signals to defined structures which is illustrated in Figure 1b (left: AFM image; right: SERS image). Usually, in AFM images of AuDG



**Figure 1.** Scheme of sample preparation and correlated AFM-SERS imaging. a) AuNP dimers attached to DNA origami substrates coexisting with single 40 nm TAMRA-modified AuNPs are adsorbed on an Si/SiO<sub>2</sub> substrate. In a second step graphene is exfoliated on top of the aforementioned structures by mechanical exfoliation resulting in numerous variations of structures: AuNP dimers can be covered by single-layer graphene (SLG), bilayer graphene (BLG), trilayer graphene (TLG), few-layer graphene (FLG), or graphite. b) Large-size AFM image of one graphene flake exfoliated on top of AuNPs (left) as well as the corresponding Raman map of a selected area (right). c) AFM image of single AuNPs as well as AuNP dimers (marked with white circles) covered by SLG. d) High-resolution AFM images of AuDG hybrid structures with two 40 nm AuNPs attached to one side of the triangle in which a part of the DNA origami triangle is visible (white arrows). The folds of the SLG flake surrounding the hybrid structure are also clearly apparent.

## full papers

hybrid structures solely the AuNP dimers are visible (Figure 1c, white circles) due to the geometrical arrangement of the AuNPs with respect to the DNA origami substrate preventing the DNA origami from flat adsorption.<sup>[13]</sup> However, when the two AuNPs are attached to one side of the DNA origami substrate and when the structures are located in close proximity to the edge of the graphene flake the apex of the DNA origami triangle might become visible (Figure 1d, white arrows). Due to the larger gap size between the two AuNPs and the related reduced SERS signal this design of hybrid structure is not further investigated.

### 2.2. Dye-Modified Single AuNPs Covered by SLG

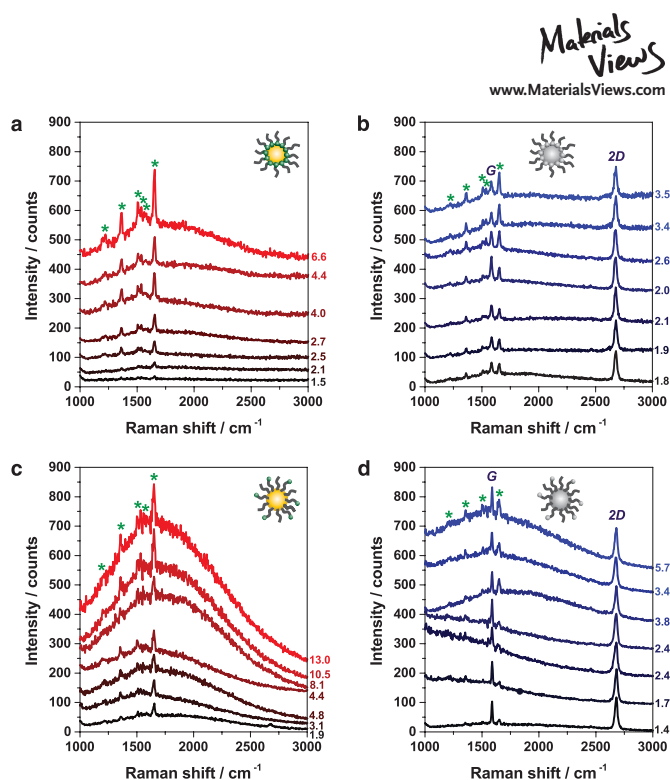
Basically, the TAMRA modification might be introduced at any position within the DNA coating strands of the AuNPs. Upon covering the structures with SLG some TAMRA molecules surrounding the AuNPs are sandwiched in between the Au surface and the graphene layer. Since both materials are known to influence the optical properties of dye molecules such as fluorescence<sup>[17,8,36]</sup> and Raman scattering<sup>[37,38]</sup> it is crucial to investigate the SERS performance of individual structures in dependence of the relative dye position. To disentangle additional effects due to hot spot formation within dimeric structures, also very basic SERS experiments on differently designed single 40 nm AuNPs are performed.

In the first case, the TAMRA dye is positioned in close vicinity to the AuNP surface using the 5'-(TTT)<sub>4</sub>TX-SH-3' (X = TAMRA) sequence as coating strands (Figure 2a). The same type of AuNPs is studied with SLG on top (Figure 2b). In the second case, the TAMRA dye is positioned further away from the AuNP surface by coating the particles with the 5'-X-(TTT)<sub>4</sub>T-SH-3' sequence and thereby introducing a DNA spacer of 13 bases between dye and Au surface. In order to reduce the concentration of TAMRA molecules per particle, coating strands without dye are introduced (Figure 2c). Again, the same type of AuNPs covered by SLG is studied (Figure 2d). In all cases SERS measurements on single AuNPs are accompanied by AFM measurements in order to confirm the origin of each signal. In every SERS series (Figure 2a–d) the characteristic TAMRA bands<sup>[13]</sup> are marked with a green star whereby the peaks at ≈1361 and 1654 cm<sup>-1</sup> are visible in all spectra and additional peaks at 1222, 1509, 1538, and 1570 cm<sup>-1</sup> only appear in some cases. For AuNPs coated by DNA with TAMRA at the 5'-end (Figure 2c,d) a slight red-shift of 4 cm<sup>-1</sup> for the two most prominent TAMRA bands is observed resulting in spectral

positions of 1357 and 1650 cm<sup>-1</sup>, which is attributed to distance-dependent interactions between the dye molecules and the gold surface. Upon graphene encapsulation no further shift of the spectral positions of the TAMRA bands is noticed.

Furthermore, in the two cases with SLG (Figure 2b,d) the two characteristic bands arising from graphene (G band (1586 cm<sup>-1</sup>) and 2D band (2680 cm<sup>-1</sup>)) are highlighted. Both bands are highly sensitive to doping<sup>[39–41]</sup> and strain<sup>[42–44]</sup> which can cause peak shifts of several cm<sup>-1</sup> even for pristine graphene without underlying AuNPs. Therefore, the slight variations in peak positions for the G and the 2D band which can be observed over the whole area of the graphene flake cannot be directly correlated to doping or strain caused by the AuNPs. For all SERS spectra of each series the noise within the spectral range of 1800–2200 cm<sup>-1</sup> is determined and stated next to each spectrum (in units of counts, Figure 2a–d).

Comparing the two cases without SLG (Figure 2a,c) it is obvious that the fluorescence background due to the resonant excitation of the TAMRA molecules ( $\lambda_{\text{cm}} = 582 \text{ nm} \hat{=} 1610 \text{ cm}^{-1}$ ) is more pronounced when the dyes are located at the 5'-end and thereby separated from



**Figure 2.** SERS spectra of differently functionalized AuNPs. Comparison of SERS spectra arising from several different single 40 nm AuNPs coated with TAMRA-modified ssDNA. a,b) In these cases the TAMRA dye is located close to the AuNP surface (5'-(TTT)<sub>4</sub>TX-SH-3' (X = TAMRA)), whereas c,d) in these cases dye and AuNP surface are separated by 13 DNA bases (5'-X-(TTT)<sub>4</sub>T-SH-3' (X = TAMRA)). Additionally, AuNPs in (b) and (d) are covered by SLG. The characteristic TAMRA bands (green stars) as well as the typical G and 2D bands of SLG are marked. Laser wavelength: 532 nm, laser power: 80 μW, integration time: 10 s. Recorded noise data are given in counts.

the AuNP surface (Figure 2c). This is in good agreement with the known distance dependence of fluorescence enhancement<sup>[7]</sup> and fluorescence quenching.<sup>[8]</sup> In both cases without graphene a broad distribution of SERS intensities can be observed which is attributed to slight variations in AuNP sizes, numbers of TAMRA molecules per particle, as well as different photobleaching rates for individual AuNPs. The absolute SERS intensities obtained from AuNPs coated by DNA with TAMRA at the 3'-end or 5'-end cannot directly be compared since in the latter case a mixture of dye-modified and non-modified sequences was used as coating strands. However, both the noise averaged over all spectra and the maximum noise among all spectra are higher in the case of TAMRA being at the 5'-end (average: 6.5 counts; maximum: 13.0 counts) (Figure 2c) compared to TAMRA at the 3'-end (average: 3.4 counts; maximum: 6.6 counts) (Figure 2a).

For both types of AuNPs (with TAMRA being close to the AuNP surface (Figure 2a) or further apart from it and thus closer to graphene (Figure 2c)) the appearance of the SERS spectra is dramatically influenced by graphene encapsulation (Figure 2b,d). In the case of TAMRA being at the 3'-end (Figure 2b) the fluorescence background appears to be efficiently quenched resulting in a cleaner baseline compared to the analogue non-covered AuNPs (Figure 2a). The function of graphene as a potential quencher of fluorescence from dye (R6G) molecules was first described by Xie et al.<sup>[36]</sup> and afterward also confirmed for the photoluminescence arising from a gold surface.<sup>[45]</sup> In the first case the quenching process was postulated to be caused by a resonance energy transfer from dyes to graphene enabled by considerable  $\pi$ - $\pi$  interactions.<sup>[36,46]</sup> However, within the here presented structures direct  $\pi$ - $\pi$  interactions between the TAMRA molecules and the graphene layer may not occur since both are separated by the DNA coating whose thickness is estimated to be 2.5 nm.<sup>[10]</sup> Nevertheless, a remarkable quenching of the fluorescence background is observed. Although the nature of this effect is not resolved here, two possible explanations might be considered. On the one hand, based on the distance between TAMRA molecules and graphene an energy transfer from excited dye molecules to SLG is conceivable. Typical energy transfer processes such as Förster resonance energy transfer (FRET) can be observed for distances between 1 and 10 nm<sup>[47]</sup> which is in good agreement with the here considered system. On the other hand, it cannot be excluded that a DNA-mediated charge transfer mechanism from the AuNPs to SLG is involved in the fluorescence quenching process similar to observations by Fritzsche and co-workers.<sup>[48,49]</sup> They found that the excitation of a silver nanoparticle can be transferred via a dsDNA nanowire over a distance of several micrometers resulting in photobleaching of intercalating dyes. In the case of the here presented structures, also a combination of both, energy transfer and charge transfer, is conceivable.

Compared to their non-covered analogues the values for the average noise and the maximum noise are reduced for both, TAMRA located at the 3'-end (average: 2.6 counts; maximum: 3.5 counts; Figure 2b) as well as at the 5'-end (average: 3.0 counts, maximum: 5.7 counts; Figure 2d). Furthermore, the distribution of SERS intensities arising from

the TAMRA signals is much narrower compared to the three other cases (Figure 2a,c,d).

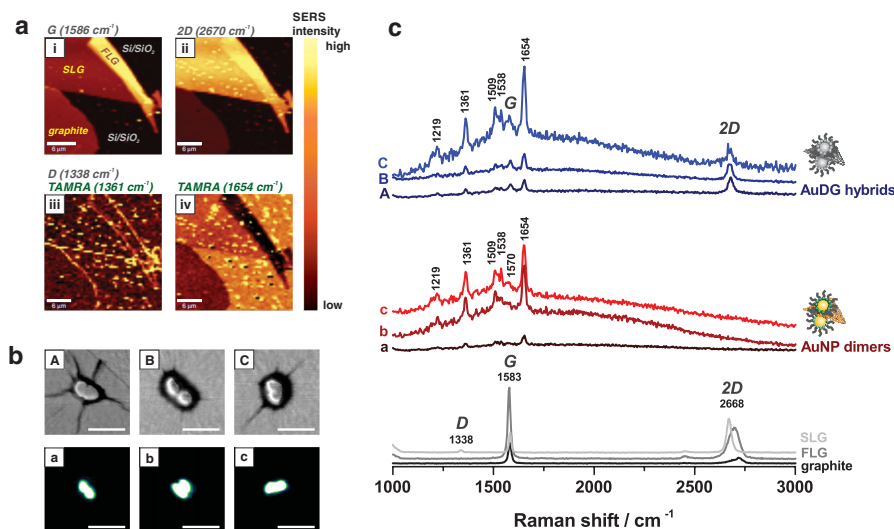
The aforementioned  $\pi$ - $\pi$  interactions responsible for an effective resonance energy transfer between dye molecules and graphene should be enabled if the TAMRA modification is located at the 5'-end of the AuNP coating strands. Interestingly, the SERS spectra arising from those types of structures seem to be categorized in two classes (Figure 2d). On the one hand, the three upper SERS spectra clearly display the characteristic fluorescence background of TAMRA with a maximum at  $\approx 1610$  cm<sup>-1</sup>. However, the different appearance of the backgrounds in the following three spectra can be assigned to the typical photoluminescence background characteristic for AuNPs with diameters less than 150 nm.<sup>[27]</sup> The occurring differences are most probably due to a different extent of contact between SLG and the underlying AuNPs. Although at least some of the TAMRA molecules get in direct contact to the SLG their fluorescence is not significantly quenched in the case of the upper three spectra. For the following three AuNPs the interactions between graphene and the TAMRA molecules are more pronounced resulting in efficient fluorescence quenching and a remaining background whose appearance is defined by the photoluminescence of the AuNPs. This type of luminescence in turn is not quenched due to an insufficient contact between the AuNPs and SLG. Phase AFM images of all AuNPs corresponding to the SERS spectra presented in Figure 2b are shown in Figure S1 (Supporting Information). Additionally, analogue measurements are performed using cyanine 3 (Cy3) as Raman reporter molecule instead of TAMRA (see Figure S2, Supporting Information).

In summary, these experiments show that the best reproducible TAMRA signals as well as the cleanest baselines are obtained under two conditions: (a) the TAMRA molecules have to be located in close proximity to the AuNP surface in order to experience efficient fluorescence quenching and (b) the dye-modified AuNPs have to be covered by SLG to benefit from an additional fluorescence quenching, a reduced noise level, as well as a narrow distribution of TAMRA signal intensities. As a consequence, the following discussions are based on AuDG hybrid structures containing AuNPs with TAMRA at the 3'-end.

### 2.3. Comparison of AuNP Dimers and AuDG Hybrid Structures

In the next step AuNP dimers attached to one DNA origami substrate are investigated. In Figure 3a typical Raman maps of a surface area covered by different types of graphene (SLG, FLG, and graphite) are presented. The four maps exhibit the SERS intensity distributions of the four most important bands arising from AuNP dimers/AuDG hybrid structures, that is, (i) the G band (1586 cm<sup>-1</sup>), (ii) the 2D band (2670 cm<sup>-1</sup>), (iii) the TAMRA band at 1361 cm<sup>-1</sup>, and (iv) the TAMRA band at 1654 cm<sup>-1</sup>. It has to be mentioned that the TAMRA band at 1361 cm<sup>-1</sup> can be spectrally overlapped by the D band of graphene at 1338 cm<sup>-1</sup>. For this reason Raman map (iii) exhibits the SERS intensity distribution of both peaks. Especially Raman map (iv) shows that there





**Figure 3.** AFM–SERS correlation of AuNP dimers and AuDG hybrid structures. a) Raman maps visualizing the SERS intensity distribution of the G band at  $1586\text{ cm}^{-1}$  (i), the 2D band at  $2670\text{ cm}^{-1}$  (ii), the D band at  $1338\text{ cm}^{-1}$  (spectral overlap with the TAMRA band at  $1361\text{ cm}^{-1}$ ) (iii), and the most characteristic TAMRA band at  $1654\text{ cm}^{-1}$  (iv). b) AFM images of three AuDG hybrid structures (first row; phase images) and three AuNP dimers (second row; topography images). Scale bars: 200 nm. c) Typical SERS spectra of SLG, FLG, and graphite (gray and black spectra). Extended SERS spectra including the  $2D'$  band at  $3245\text{ cm}^{-1}$  which has not been used for any analysis is shown in Figure S3 (Supporting Information). Additionally, SERS spectra of the AuNP dimers (red spectra) and the hybrid structures (blue spectra) originating from the structures shown in (b) are presented. Laser wavelength: 532 nm, laser power: 80  $\mu\text{W}$ , integration time: 10 s.

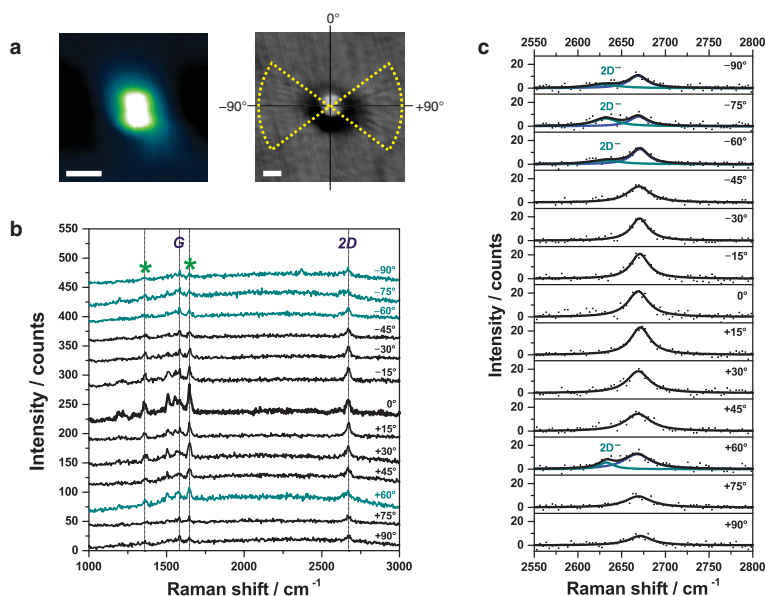
are three different types of AuNP dimers: some covered by SLG, some covered by FLG, and also non-covered structures. In Figure 3b phase AFM images of representative AuDG hybrid structures (A, B, C; first row) as well as topography AFM images of non-covered AuNP dimers (a, b, c; second row) are shown. In the case of the AuDG hybrid structures it is obvious that the graphene layer covering the hybrid structures is differently folded and therefore the extent of contact between AuNPs and SLG differs for each individual structure. For hybrid A several folds within the graphene layer can be observed as a result of AuNP replication. This is not the case for hybrid B, and for hybrid C only a few folds are visible. In Figure 3c correlated SERS spectra arising from the AuNP dimers (red spectra) and the AuDG hybrid structures (blue spectra) shown in the AFM images in Figure 3b are presented. Additionally, for comparison typical SERS spectra obtained from SLG, FLG, and graphite are shown in gray and black. A comparison of SERS spectra from AuNP dimers and AuDG hybrid structures reveals that in both cases the characteristic TAMRA bands<sup>[13]</sup> at 1219, 1361, 1509, 1538, 1570 (superimposed by the G band for hybrids; blue spectra), and  $1654\text{ cm}^{-1}$  can be detected which coincide with the recorded bands for the single AuNPs (Figure 2b,d). Furthermore, the SERS spectra of AuDG hybrid structures (blue spectra) also show the two most characteristic graphene bands at  $1586\text{ cm}^{-1}$  (G band) and at  $2670\text{ cm}^{-1}$  (2D band) whose spectral positions are in good agreement with the ones detected for SLG (light gray spectrum). For both types of structures (AuNP dimers/AuDG hybrids) the overall SERS intensity

differs for individual structures, which is caused by slight differences in AuNP and gap sizes.

#### 2.4. Polarization-Dependent SERS Measurements on AuDG Hybrid Structures

To test the extent of contact between SLG and underlying AuNP dimers which is related to induced strain within graphene, polarization-dependent SERS measurements are performed. In Figure 4 the obtained results for one representative AuDG hybrid are presented. Figure 4a shows two AFM images (left: topography; right: phase) of the investigated structure clearly exhibiting the folds within the covering SLG flake. In the right image the extension of folds is marked by yellow dashed lines and the position of the dimer axis ( $0^\circ$ ) relative to the angle of polarization is shown. SERS measurements are performed by using polarized laser light for excitation (parallel to the dimer axis;  $0^\circ$ ;  $\lambda = 532\text{ nm}$ ) and by changing the angle of the detection plane in steps of  $15^\circ$  for each measurement starting with  $+90^\circ$ . In Figure 4b the corresponding SERS spectra for different polarization angles are presented. Both, TAMRA signals (green stars) as well as SLG signals (G and 2D band) arising from the AuDG hybrid structure in Figure 4a are polarization-dependent.

On the one hand, highest intensities for the TAMRA signals are detected for the polarization angle parallel to the axis of the AuNP dimer due to the optimal geometry for plasmon coupling of the two individual AuNPs.<sup>[14]</sup> Moving



**Figure 4.** Polarization-dependent SERS measurements of one individual AuDG hybrid structure. a) AFM images (left: topography; right: phase) of one representative AuDG hybrid structure for which polarization-dependent SERS measurements are performed. Scale bars: 100 nm. b) SERS spectra obtained for different polarization angles in steps of 15°. The most characteristic bands for TAMRA (green stars) and SLG (G and 2D band) are highlighted. c) Lorentzian fit curves for the 2D band in dependence of the polarization angle. A splitting of the 2D band is observed for polarization angles of +60°, -60°, -75°, and -90°.

away from this optimal polarization angle for plasmon coupling toward  $-90^\circ/+90^\circ$  leads to a decrease of the TAMRA signal intensities. The remaining signal is due to the detection of scattered light, which is not or only to a small extent affected by plasmon coupling of the two individual AuNPs.

On the other hand, in the case of SLG a polarization-dependence of the 2D band at  $\approx 2670\text{ cm}^{-1}$  can be observed. This is clarified in Figure 4c where Lorentzian fit curves for the 2D band under different polarization angles are presented. Nine of the 13 different SERS spectra can be described by a single Lorentzian function with a maximum at around  $2670\text{ cm}^{-1}$  ( $+90^\circ$ ,  $+75^\circ$ ,  $+45^\circ$ ,  $+30^\circ$ ,  $+15^\circ$ ,  $0^\circ$ ,  $-15^\circ$ ,  $-30^\circ$ ,  $-45^\circ$ ). However, in the case of polarization angles of  $+60^\circ$ ,  $-60^\circ$ ,  $-75^\circ$ , and  $-90^\circ$  a second peak at  $\approx 2630\text{ cm}^{-1}$  arises resulting in fit curves consisting of two Lorentzian functions (blue and cyan bands in Figure 4c). From previous reports it is known that the G band<sup>[44,50]</sup> as well as the 2D band<sup>[43]</sup> in SLG can split in two components upon uniaxial strain. However, under the currently applied conditions the G band at  $1586\text{ cm}^{-1}$  is not clearly resolved due to low laser intensities and arising luminescence from the TAMRA dyes, especially for polarization along the axis of the dimer. Therefore, the following considerations concerning strain-induced observations are only based on the 2D band. Generally, splitting of the 2D band is induced by a change in symmetry of the graphene lattice upon uniaxial strain.<sup>[43]</sup> As a consequence, the Dirac cone—representing a scheme of the electronic dispersion—is displaced from its original position resulting in altered interactions with its three nearest neighbors. This

should result in the appearance of three contributions to the 2D band, however, the third peak is usually difficult to observe.<sup>[43]</sup>

In the case of the AuDG hybrid structure in Figure 4a a clear correlation between the direction of folds surrounding the underlying AuNP dimer (yellow dashed lines in Figure 4a, right) and the polarization-dependent SERS signal is observed. The relative orientation of the polarization angles for which a splitting of the 2D band appears (Figure 4c;  $+60^\circ$ ,  $-60^\circ$ ,  $-75^\circ$ , and  $-90^\circ$ ) to the AuNP dimer is in excellent agreement with the direction of folds and therefore with the direction of uniaxial strain.

It has to be mentioned that the laser spot size ( $\approx 1.3\text{ }\mu\text{m}$  in diameter) is much larger compared to the size of the AuDG hybrid structure. The detected SERS signals arising from SLG therefore contain information about several influences such as folding, doping,<sup>[39–41]</sup> or strain<sup>[42–44]</sup> summed up over the graphene area irradiated by the laser. Therefore, the main proportion of the band at  $2670\text{ cm}^{-1}$  is arising from the area of SLG which is surrounding the AuDG hybrid structure and therefore only weakly influenced by the induced strain. The  $2\text{D}^+$  mode which is expected to appear red-shifted upon uniaxial strain is most probably superimposed by the band at  $2670\text{ cm}^{-1}$ . Nevertheless, confirmed by the appearance of the  $2\text{D}^-$  band at  $2630\text{ cm}^{-1}$  the strain caused by the underlying AuNP dimer is obviously high enough to induce a mode splitting of the 2D band which is on the order of  $\approx 40\text{ cm}^{-1}$ . Based on results obtained by applying controlled strain to SLG<sup>[43]</sup> we estimate that the underlying structure in Figure 4a

induces an uniaxial strain component within the covering SLG of about 1%–2%.

## 2.5. Suppression of Photobleaching due to SLG

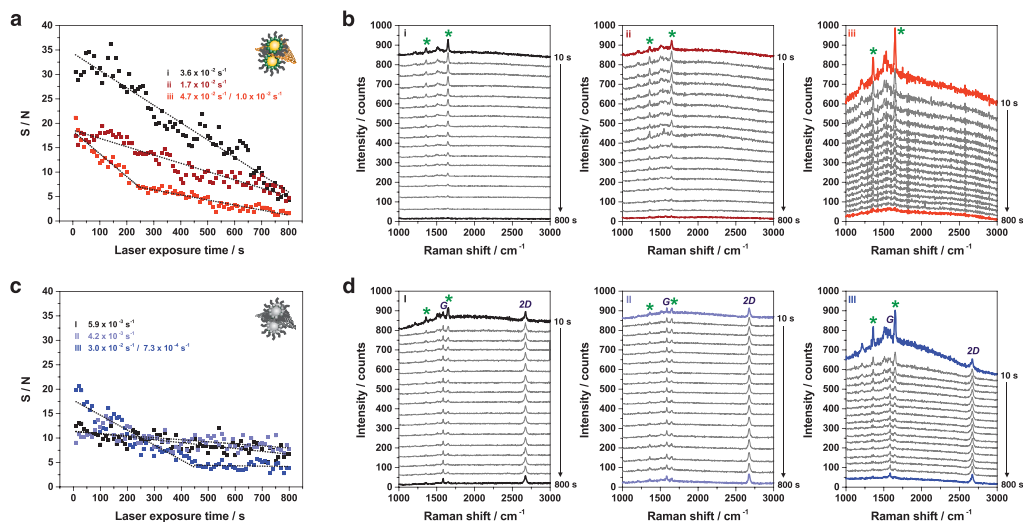
Photobleaching is an undesired side effect which often accompanies SERS measurements. It arises from irreversible decomposition of the analyte molecules caused by photochemical reactions.<sup>[51]</sup> Under the here applied conditions we expect heating effects<sup>[52]</sup> as well as reactions with ambient oxygen<sup>[53,54]</sup> to be the two main sources for damages of the dye molecules.

In order to investigate the potential of graphene in terms of suppressing the photobleaching of the TAMRA dyes SERS time series measurements under continuous laser exposure for 800 s are performed for individual AuNP dimers and AuDG hybrid structures (Figure 5). Therefore, SERS spectra are recorded in time intervals of 10 s and for every spectrum the signal-to-noise (S/N) ratio for the most intense TAMRA band at 1654 cm<sup>-1</sup> is calculated (the noise level is determined within the spectral range of 1800–2200 cm<sup>-1</sup> of each spectrum). As can be seen in Figure 5a the S/N ratio is continuously decreasing for all three AuNP dimers with increasing laser exposure time. Since the amount of the aforementioned processes resulting in damages of the TAMRA molecules differ for each individual structure different photobleaching rates are obtained for dimers i–iii (inset of Figure 5a). More precisely, for dimers i (black data) and ii (dark red data) photobleaching rates (with regards to the S/N ratios) of  $3.6 \times 10^{-2} \text{ s}^{-1}$  and  $1.7 \times 10^{-2} \text{ s}^{-1}$  are determined. On the contrary, the S/N ratio arising from dimer iii (light red

data) is decreasing following two different photobleaching rates:  $4.7 \times 10^{-2} \text{ s}^{-1}$  within the first 250 s of laser exposure and  $1.0 \times 10^{-2} \text{ s}^{-1}$  within the subsequent time interval. In Figure 5b the time evolution of the associated SERS spectra for the three investigated AuNP dimers are shown (the two most characteristic TAMRA bands are marked with a green star). The SERS spectra are presented in time intervals of 50 s starting with 10 s and ending with 800 s of laser exposure. Again, the first spectrum of each dimer recorded after 10 s of integration exhibits different overall SERS intensities, which is consistent with the aforementioned diversity for individual structures. In all three SERS time series measurements a significant photobleaching during laser exposure for 800 s can be observed. Interestingly, not only the SERS intensities of the TAMRA bands but also the noise level is reduced over time for all AuNP dimers, confirming the correlation between high SERS intensities and high noise levels (see Figure S4, Supporting Information for independent time evolutions of the signal and the noise level).

In contrast to the AuNP dimers a different photobleaching behavior is observed for the AuDG hybrid structures (Figure 5c,d). For hybrid I and II (Figure 5c, black and light blue data) the photobleaching rate of the S/N ratio is nearly identical ( $5.9 \times 10^{-3}$  and  $4.2 \times 10^{-3} \text{ s}^{-1}$ ). Thus, compared to the non-covered dimers (Figure 5a,b) the photobleaching rate is reduced by approximately one order of magnitude.

In the case of AuDG hybrid I (black data) the time evolution of the SERS signal (Figure S4c, Supporting Information) can be divided in two parts: (1) an initial rapid decrease of the TAMRA band at 1654 cm<sup>-1</sup> within the first 60 s of laser exposure and (2) in between the time interval of 60 and 800 s the decrease of signal intensity is significantly slowed down.



**Figure 5.** Photobleaching behavior of AuNP dimers and AuDG hybrid structures. Time series SERS measurements of a,b) individual non-covered AuNP dimers as well as of c,d) AuDG hybrid structures. SERS spectra are recorded in time intervals of 10 s using 532 nm laser excitation, a laser power of 25  $\mu\text{W}$ , and integration times of 10 s. The temporal evolution of the S/N ratio of the TAMRA band at 1654 cm<sup>-1</sup> is presented as a function of continuous laser exposure for three AuNP dimers (a) as well as for three AuDG hybrid structures (c). The corresponding SERS spectra recorded during 800 s of laser exposure are presented in steps of 50 s exposure time for AuNP dimers (b) and AuDG hybrid structures (d).

This behavior is attributed to different extents of interactions between the TAMRA molecules and the graphene layer. During the first 60 s of laser exposure the observed photobleaching is probably caused by those TAMRA dyes which are not or only weakly interacting with the SLG. Subsequently, the signal is more stable since the remaining intact TAMRA dyes efficiently interact with the SLG. On the contrary, after a slow decrease within the first 200 s the SERS signal of AuDG hybrid II (Figure S4c, Supporting Information, light blue data) stays constant until the end of the laser exposure confirming that SLG can provide extensive protection against photobleaching if the dye molecules interact strongly with the graphene layer. A damage of the SLG upon laser exposure can be excluded since no Raman modes characteristic for graphene damage such as D band ( $1338\text{ cm}^{-1}$ ), D' band ( $\approx 1620\text{ cm}^{-1}$ ),<sup>[55]</sup> or the combination band D+D' ( $\approx 2940\text{ cm}^{-1}$ )<sup>[55]</sup> are observed.

However, AuDG hybrid III (blue data in Figure 5c,d) also exhibits a time evolution of the TAMRA signal which can be divided in two different parts, similar to the non-covered dimer iii (light red data in Figure 5a,b). The initial time interval (0–450 s of laser exposure) is defined by a rapid decrease of the S/N ratio with a photobleaching rate of  $3.0 \times 10^{-2}\text{ s}^{-1}$  which is of the same order as for AuNP dimers. Subsequently, the rate is dramatically reduced to  $7.3 \times 10^{-4}\text{ s}^{-1}$  within the time interval between 450 and 800 s of laser exposure.

The fact that for some structures two successive photobleaching rates can be determined allows for the assumption that the observed decrease in SERS signal intensity is based on at least two different contributions. This is also confirmed by the time evolutions of the corresponding noise levels (Figure S4b,d, Supporting Information) and attributed to (a) heating effects caused by the laser exposure which should be especially pronounced within the hot spot<sup>[52,56]</sup> and (b) reactions with ambient oxygen. In the cases of AuNP dimers both should significantly contribute to the total photobleaching rate. However, for AuDG hybrid structures the SLG is expected to have an effect on both contributions for two reasons: (1) Since SLG has been demonstrated to be impermeable to any kind of gases<sup>[18]</sup> the reaction with ambient oxygen can be excluded as possible photobleaching mechanism. (2) Graphene is known to be an excellent heat conductor exhibiting values of  $\approx 5 \times 10^3\text{ W mK}^{-1}$ .<sup>[17]</sup> Thus, the plasmonically generated heat can be dissipated by the graphene.

The stronger the coupling of the surface plasmon resonances of the two individual AuNPs within a dimer the higher is the resulting electromagnetic field enhancement and thus the expected heating.<sup>[52]</sup> This postulation is in good agreement with the experimentally observed behavior for different structures. In the case of AuNP dimers (Figure 5a,b) the highest initial SERS signal has been recorded for dimer iii (light red data) which is attributed to a hot spot providing the highest field enhancements among the three investigated structures (i–iii). As a consequence, the initial photobleaching is more significant compared to the other two AuNP dimers (black and red data) due to higher heat induced damage.

A similar behavior is observed for AuDG hybrid structure III (Figure 5c,d; Figure S4c,d, Supporting Information; blue data). In this case the contact between SLG and the underlying AuNPs is probably not strong enough to enable efficient heat conduction. On the contrary, AuDG hybrid II exhibits a relatively low initial SERS signal correlated with a low noise level which both remain constant over the whole period of 800 s (Figure 5c,d; Figure S4c,d, Supporting Information; light blue data). This is caused by a less pronounced electromagnetic field enhancement within the hot spot resulting in lower heating effects.

### 3. Conclusion

In summary, the synthesis of novel AuDG hybrid structures is reported and their optical properties with regard to SERS are carefully characterized. We find that AuNPs and graphene have a competing influence on the appearance of the fluorescence background obtained by sandwiched dye molecules. Moreover, a deeper understanding of the hybrid material is gained by polarization-dependent SERS measurements which allows for precise correlation of visible disorder within the graphene layer and spectral mode splitting of the 2D band. Furthermore, an improved photostability due to graphene encapsulation resulting in significantly lower photobleaching rates is clearly demonstrated. This is attributed to the efficient protection of the dye molecules from reactions with ambient oxygen by graphene and heat dissipation from the SERS hot spots.

The novel AuDG hybrid structures combine unique properties of three different building blocks within one material. Since every component can be independently tuned, hybrid structures represent a multifunctional tool in fields such as biosensing and bioelectronics. In this context, the addressability of the system introduced by the DNA origami template is highly beneficial since it allows for the precise arrangement of nanoparticles and other functional entities such as dyes, conducting polymers,<sup>[57]</sup> etc. On the other hand, the structures might be suitable for promoting investigations in the field of graphene-enhanced Raman scattering (GERS)<sup>[37,58]</sup> and correlated mechanisms. The main profit in this context is the possibility of using the DNA origami substrate as mediator in order to precisely tune the interaction between NPs and graphene.

### 4. Experimental Section

**Preparation of AuDG Hybrid Structures:** DNA origami structures, DNA-coated AuNPs, as well as AuNP dimers were prepared following a previously published procedure.<sup>[13]</sup> The synthesis of DNA origami structures is based on the M13mp18 virus strand (New England Biolabs) used as scaffold which is folded to triangular shape by the addition of 208 short ssDNA staple strands.<sup>[1]</sup> Eight staple strands (t-1s6e, t1s6i, t-1s8g, t1s8i and t-2s5f, t-2s7f, t2s5f, t2s7f) were extended at the 5'-end by the capture sequence 5'-(AAA)<sub>3</sub>T<sub>4</sub>-3' in order to realize the attachment of two AuNPs per DNA origami substrate. Extended ssDNA strands were purchased

## full papers

from metabion, non-extended from Integrated DNA Technologies. Citrate-capped 40 nm AuNPs from BBI solutions were coated with two different types of TAMRA-modified ssDNA (5'-(TTT)<sub>4</sub> TX-SH-3' or 5'-X-(TTT)<sub>4</sub> T-SH-3'; X = TAMRA) or Cy3-modified ssDNA (5'-(ATT)<sub>3</sub>-T<sub>4</sub>X-SH-3'; X = Cy3) (Metabion) similar to the protocol of Ding et al.<sup>[59]</sup> using adjusted concentrations, reaction times, and 0.02% sodium dodecyl sulfate (SDS, Sigma Aldrich). DNA-coated AuNPs were attached to DNA origami substrates via DNA hybridization. Therefore, a temperature program was applied to a mixture of DNA origami structures and AuNPs (ratio 1:1). After hybridization the solution was used without further purification resulting in a coexistence of AuNP dimers and unbound AuNPs.

**Preparation of Si Substrates:** Si wafers covered with 290 nm thick dry thermal oxide (SiO<sub>2</sub>/Si) (IDB Technologies Ltd.) were cleaned with acetone (absolute), heated to 250 °C for 10 min, and finally cleaned using an ozone cleaner (Diener electronic, ZEPTO) for 10 min. Immediately after ozone cleaning the AuNP dimers (coexisting with unbound AuNPs) were immobilized by transferring a 0.5–1.0 µL drop of the hybridization solution to the Si substrate and adding 40 µL of 10× TAE with 100 × 10<sup>-3</sup> M MgCl<sub>2</sub>. After an incubation time of 60 min Si wafers were rinsed with ethanol (absolute)/Millipore water (1:1) and dried with compressed air.

**Mechanical Exfoliation of Graphene:** Graphene was deposited by the well-established process of micromechanical cleavage.<sup>[16]</sup> Flakes of Kish graphite (Naturgraphite GmbH) were repeatedly cleaved using sticky tape (Nitto Denko ELP BT150ECM) and afterward deposited on top of the AuNP dimers immobilized on Si substrates. As-prepared Si wafers were stored in methyl isobutyl ketone (MIBK, Sigma Aldrich) at room temperature for ≈ 3 h. After removal of the sticky tape, wafers were washed with MIBK and 2-propanol and dried with compressed air. Finally, exfoliated flakes were cleaved another time using sticky tape and flakes of SLG were identified using an optical microscope.

**AFM Imaging:** AFM images were recorded in tapping mode with a Nanosurf FlexAFM using Tap150Al-G cantilevers (force constant 5 N m<sup>-1</sup>) (Budget Sensors). For analysis of AFM images the software Gwyddion 2.34 (freeware) was used.

**Raman Imaging:** For SERS measurements a confocal Raman microscope (WITec alpha300) with an upright optical microscope was used. The 532 nm excitation laser was coupled into a single-mode optical fiber and focused to a diffraction-limited point (1.3 µm<sup>2</sup>) on the sample by passing a 100× objective (Olympus MPlanFL N, NA = 0.9). Raman images in Figure 3a were performed using a laser power of 900–1000 µW and an integration time of 2 s. The SERS spectra of SLG, FLG, and graphite (Figure 3c) were extracted from these Raman images. Further Raman images (including the image in Figure 1b) were recorded with a laser power of 80 µW and an integration time of 10 s, and the SERS spectra a-c and A-C in Figure 3c as well as the spectra in Figure 2 were extracted from these Raman images. All other SERS spectra were obtained by recording single spectra on predefined positions. The laser power was further decreased to 25 µW for polarization-dependent measurements (Figure 4) and time series measurements (Figure 5). Before the beginning of the polarization series (Figure 4) it was ensured that the SERS signal stayed constant over three unpolarized measurements. In all cases, the grating of the spectrograph was set to 600 g mm<sup>-1</sup>. SERS spectra were vertically shifted for better visualization.

## Supporting Information

Supporting Information is available from the Wiley Online Library or from the author.

## Acknowledgements

This research was supported by the Deutsche Forschungsgemeinschaft (DFG), a Marie Curie FP7 Integration Grant within the 7th European Union Framework Programme, the European Regional Development Fund (EFRE), by the University of Potsdam and the Federal Institute of Materials Research (BAM). A.M., J. Pešić, and R.G. acknowledge support from Serbian MPNTR through Projects ON 171005, III 45018, and from the DAAD bilateral project 51-03-01858/2013-09/1 between Republic of Serbia and Germany.

- [1] P. W. K. Rothmund, *Nature* **2006**, *440*, 297.
- [2] S. M. Douglas, H. Dietz, T. Liedl, B. Hogberg, F. Graf, W. M. Shih, *Nature* **2009**, *459*, 414.
- [3] X. Shen, A. Asenjo-Garcia, Q. Liu, Q. Jiang, F. J. G. de Abajo, N. Liu, B. Ding, *Nano Lett.* **2013**, *13*, 2128.
- [4] C. Zhou, X. Duan, N. Liu, *Nat. Commun.* **2015**, *6*, 8102.
- [5] A. Kuzyk, R. Schreiber, Z. Fan, G. Pardatscher, E.-M. Roller, A. Hoge, F. C. Simmel, A. O. Govorov, T. Liedl, *Nature* **2012**, *483*, 311.
- [6] T. Schlichthaerle, M. T. Strauss, F. Schueder, J. B. Woehrstein, R. Jungmann, *Curr. Opin. Biotechnol.* **2016**, *39*, 41.
- [7] G. P. Acuna, F. M. Möller, P. Holzmeister, S. Beater, B. Lalkens, P. Tinnefeld, *Science* **2012**, *338*, 506.
- [8] G. P. Acuna, M. Bucher, I. H. Stein, C. Steinhauer, A. Kuzyk, P. Holzmeister, R. Schreiber, A. Moroz, F. D. Stefani, T. Liedl, F. C. Simmel, P. Tinnefeld, *ACS Nano* **2012**, *6*, 3189.
- [9] J. Prinz, B. Schreiber, L. Olejko, J. Oertel, J. Rackwitz, A. Keller, I. Bald, *J. Phys. Chem. Lett.* **2013**, *4*, 4140.
- [10] V. V. Thacker, L. O. Herrmann, D. O. Sigle, T. Zhang, T. Liedl, J. J. Baumberg, U. F. Keyser, *Nat. Commun.* **2014**, *5*, 3448.
- [11] M. Pilo-Pais, A. Watson, S. Demers, T. H. LaBean, G. Finkelstein, *Nano Lett.* **2014**, *14*, 2099.
- [12] P. Kühler, E.-M. Roller, R. Schreiber, T. Liedl, T. Lohmüller, J. Feldmann, *Nano Lett.* **2014**, *14*, 2914.
- [13] J. Prinz, C. Heck, L. Ellerik, V. Merk, I. Bald, *Nanoscale* **2016**, *8*, 5612.
- [14] C. E. Talley, J. B. Jackson, C. Oubre, N. K. Grady, C. W. Hollars, S. M. Lane, T. R. Huser, P. Nordlander, N. J. Halas, *Nano Lett.* **2005**, *5*, 1569.
- [15] K. L. Wustholz, A.-I. Henry, J. M. McMahon, R. G. Freeman, N. Valley, M. E. Piotti, M. J. Natan, G. C. Schatz, R. P. Van Duyne, *J. Am. Chem. Soc.* **2010**, *132*, 10903.
- [16] K. S. Novoselov, A. K. Geim, S. V. Morozov, D. Jiang, Y. Zhang, S. V. Dubonos, I. V. Grigorieva, A. A. Firsov, *Science* **2004**, *306*, 666.
- [17] A. A. Balandin, S. Ghosh, W. Bao, I. Calizo, D. Teweldebrhan, F. Miao, C. N. Lau, *Nano Lett.* **2008**, *8*, 902.
- [18] J. S. Bunch, S. S. Verbridge, J. S. Alden, A. M. van der Zande, J. M. Parpia, H. G. Craighead, P. L. McEuen, *Nano Lett.* **2008**, *8*, 2458.
- [19] R. R. Nair, P. Blake, A. N. Grigorenko, K. S. Novoselov, T. J. Booth, T. Stauber, N. M. R. Peres, A. K. Geim, *Science* **2008**, *320*, 1308.

- [20] N. Severin, M. Dorn, A. Kalachev, J. P. Rabe, *Nano Lett.* **2011**, *11*, 2436.
- [21] Y. Moon, J. Shin, S. Seo, J. Park, S. R. Dugasani, S. H. Woo, T. Park, S. H. Park, J. R. Ahn, *Appl. Phys. Lett.* **2014**, *104*, 231904.
- [22] A. Matković, B. Vasić, J. Pešić, J. Prinz, I. Bald, A. R. Milosavljević, R. Gajić, *New J. Phys.* **2016**, *18*, 25016.
- [23] X. Ma, Q. Qu, Y. Zhao, Z. Luo, Y. Zhao, K. W. Ng, Y. Zhao, *J. Mater. Chem. B* **2013**, *1*, 6495.
- [24] C. Xu, D. Yang, L. Mei, Q. Li, H. Zhu, T. Wang, *ACS Appl. Mater. Interfaces* **2013**, *5*, 12911.
- [25] S. Mao, G. Lu, K. Yu, Z. Bo, J. Chen, *Adv. Mater.* **2010**, *22*, 3521.
- [26] S. He, K.-K. Liu, S. Su, J. Yan, X. Mao, D. Wang, Y. He, L.-J. Li, S. Song, C. Fan, *Anal. Chem.* **2012**, *84*, 4622.
- [27] K. Balasubramanian, L. Zuccaro, K. Kern, *Adv. Funct. Mater.* **2014**, *24*, 6348.
- [28] F. Schedin, E. Lidorikis, A. Lombardo, V. G. Kravets, A. K. Geim, A. N. Grigorenko, K. S. Novoselov, A. C. Ferrari, *ACS Nano* **2010**, *4*, 5617.
- [29] H. Zhou, C. Qiu, Z. Liu, H. Yang, L. Hu, J. Liu, H. Yang, C. Gu, L. Sun, *J. Am. Chem. Soc.* **2010**, *132*, 944.
- [30] Y. Liu, Y. Hu, J. Zhang, *J. Phys. Chem. C* **2014**, *118*, 8993.
- [31] W. Xu, J. Xiao, Y. Chen, Y. Chen, X. Ling, J. Zhang, *Adv. Mater.* **2013**, *25*, 928.
- [32] S. Heeg, R. Fernandez-Garcia, A. Oikonomou, F. Schedin, R. Narula, S. A. Maier, A. Vijayaraghavan, S. Reich, *Nano Lett.* **2013**, *13*, 301.
- [33] P. Wang, W. Zhang, O. Liang, M. Pantoja, J. Katzer, T. Schroeder, Y.-H. Xie, *ACS Nano* **2012**, *6*, 6244.
- [34] Y. Zhao, Y. Xie, Z. Bao, Y. H. Tsang, L. Xie, Y. Chai, *J. Phys. Chem. C* **2014**, *118*, 11827.
- [35] P. Blake, E. W. Hill, A. H. Castro Neto, K. S. Novoselov, D. Jiang, R. Yang, T. J. Booth, A. K. Geim, *Appl. Phys. Lett.* **2007**, *91*, 63124.
- [36] L. Xie, X. Ling, Y. Fang, J. Zhang, Z. Liu, *J. Am. Chem. Soc.* **2009**, *131*, 9890.
- [37] X. Ling, L. Xie, Y. Fang, H. Xu, H. Zhang, J. Kong, M. S. Dresselhaus, J. Zhang, Z. Liu, *Nano Lett.* **2010**, *10*, 553.
- [38] K. A. Willets, R. P. Van Duyne, *Annu. Rev. Phys. Chem.* **2007**, *58*, 267.
- [39] C. Casiraghi, S. Pisana, K. S. Novoselov, A. K. Geim, A. C. Ferrari, *Appl. Phys. Lett.* **2007**, *91*, 233108.
- [40] A. Das, S. Pisana, B. Chakraborty, S. Piscanec, S. K. Saha, U. V. Waghmare, K. S. Novoselov, H. R. Krishnamurthy, A. K. Geim, A. C. Ferrari, A. K. Sood, *Nat. Nanotechnol.* **2008**, *3*, 210.
- [41] W. X. Wang, S. H. Liang, T. Yu, D. H. Li, Y. B. Li, X. F. Han, *J. Appl. Phys.* **2011**, *109*, 07C501.
- [42] F. Ding, H. Ji, Y. Chen, A. Herklotz, K. Dörr, Y. Mei, A. Rastelli, O. G. Schmidt, *Nano Lett.* **2010**, *10*, 3453.
- [43] M. Huang, H. Yan, T. F. Heinz, J. Hone, *Nano Lett.* **2010**, *10*, 4074.
- [44] T. M. G. Mohiuddin, A. Lombardo, R. R. Nair, A. Bonetti, G. Savini, R. Jalil, N. Bonini, D. M. Basko, C. Galiotis, N. Marzari, K. S. Novoselov, A. K. Geim, A. C. Ferrari, *Phys. Rev. B* **2009**, *79*, 205433.
- [45] Y. Wang, Z. Ni, H. Hu, Y. Hao, C. P. Wong, T. Yu, J. T. L. Thong, Z. X. Shen, *Appl. Phys. Lett.* **2010**, *97*, 163111.
- [46] W. Xu, N. Mao, J. Zhang, *Small* **2013**, *9*, 1206.
- [47] L. Olejko, P. J. Cywinski, I. Bald, *Nanoscale* **2016**, *8*, 10339.
- [48] J. Wirth, F. Garwe, G. Hähnel, A. Csáki, N. Jahr, O. Stranik, W. Paa, W. Fritzsche, *Nano Lett.* **2011**, *11*, 1505.
- [49] J. J. Toppari, J. Wirth, F. Garwe, O. Stranik, A. Csaki, J. Bergmann, W. Paa, W. Fritzsche, *ACS Nano* **2013**, *7*, 1291.
- [50] M. Huang, H. Yan, C. Chen, D. Song, T. F. Heinz, J. Hone, *Proc. Natl. Acad. Sci. USA* **2009**, *106*, 7304.
- [51] E. M. S. Stennett, M. A. Ciuba, M. Levitus, *Chem. Soc. Rev.* **2014**, *43*, 1057.
- [52] A. O. Govorov, H. H. Richardson, *Nano Today* **2007**, *2*, 30.
- [53] C. G. Hübner, A. Renn, I. Renge, U. P. Wild, *J. Chem. Phys.* **2001**, *115*, 9619.
- [54] I. Rasnik, S. A. McKinney, T. Ha, *Nat. Methods* **2006**, *3*, 891.
- [55] L. G. Cançado, A. Jorio, E. H. M. Ferreira, F. Stavale, C. A. Achete, R. B. Capaz, M. V. O. Moutinho, A. Lombardo, T. S. Kulmala, A. C. Ferrari, *Nano Lett.* **2011**, *11*, 3190.
- [56] H. H. Richardson, M. T. Carlson, P. J. Tandler, P. Hernandez, A. O. Govorov, *Nano Lett.* **2009**, *9*, 1139.
- [57] J. B. Knudsen, L. Liu, A. L. B. Kodal, M. Madsen, Q. Li, J. Song, J. B. Woehrstein, S. F. J. Wickham, M. T. Strauss, F. Schueder, J. Vinther, A. Krissanaprasit, D. Gudnason, A. A. A. Smith, R. Ogaki, A. N. Zelikin, F. Besenbacher, V. Birkedal, P. Yin, W. M. Shih, R. Jungmann, M. Dong, K. V. Gothelf, *Nat. Nanotechnol.* **2015**, *10*, 892.
- [58] X. Ling, L. G. Moura, M. A. Pimenta, J. Zhang, *J. Phys. Chem. C* **2012**, *116*, 25112.
- [59] B. Ding, Z. Deng, H. Yan, S. Cabrini, R. N. Zuckermann, J. Bokor, *J. Am. Chem. Soc.* **2010**, *132*, 3248.

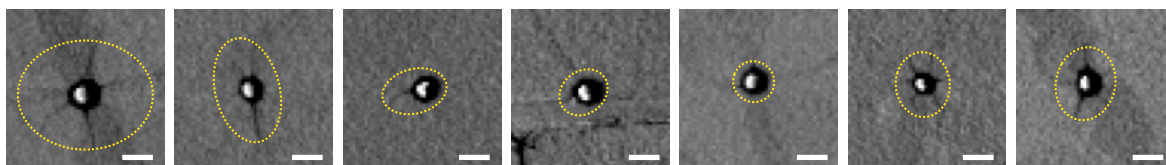
Received: June 6, 2016

Revised: July 8, 2016

Published online: September 4, 2016

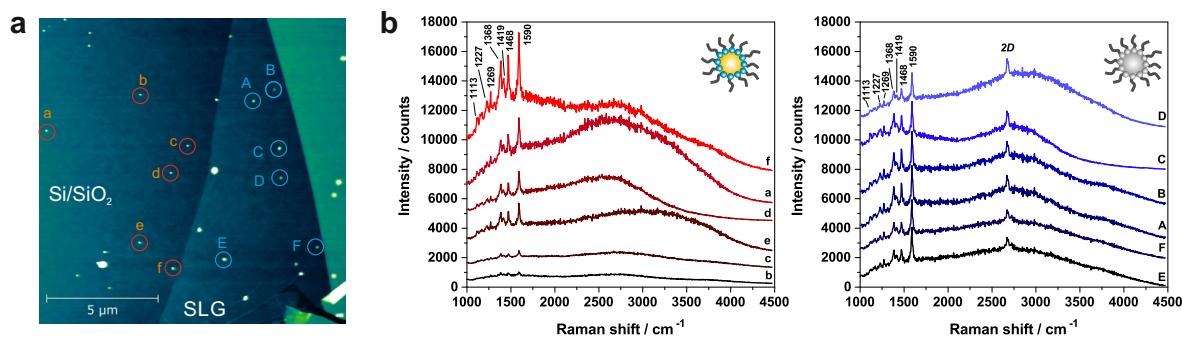
## Supporting Information

## “Hybrid Structures for Surface-Enhanced Raman Scattering: DNA Origami/Gold Nanoparticle Dimer/Graphene”

1. Phase AFM images of single AuNPs ( $5'-(TTT)_4TX-SH-3'$ ; X = TAMRA) covered by SLG

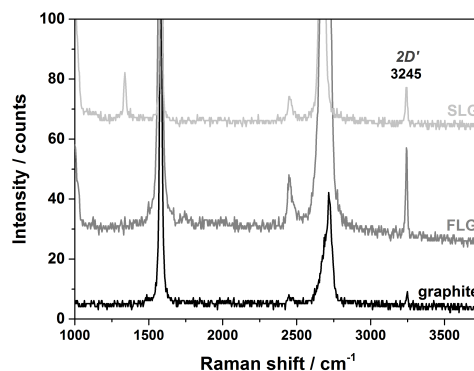
**Figure S1:** Phase AFM images of AuNPs corresponding to the SERS spectra presented in Fig. 2b with highlighted extension of folds. Images from left to right correlate to SERS spectra from top to bottom (Fig. 2b). Scale bars: 200 nm.

## 2. AFM-SERS correlation using Cy3 as Raman reporter molecule



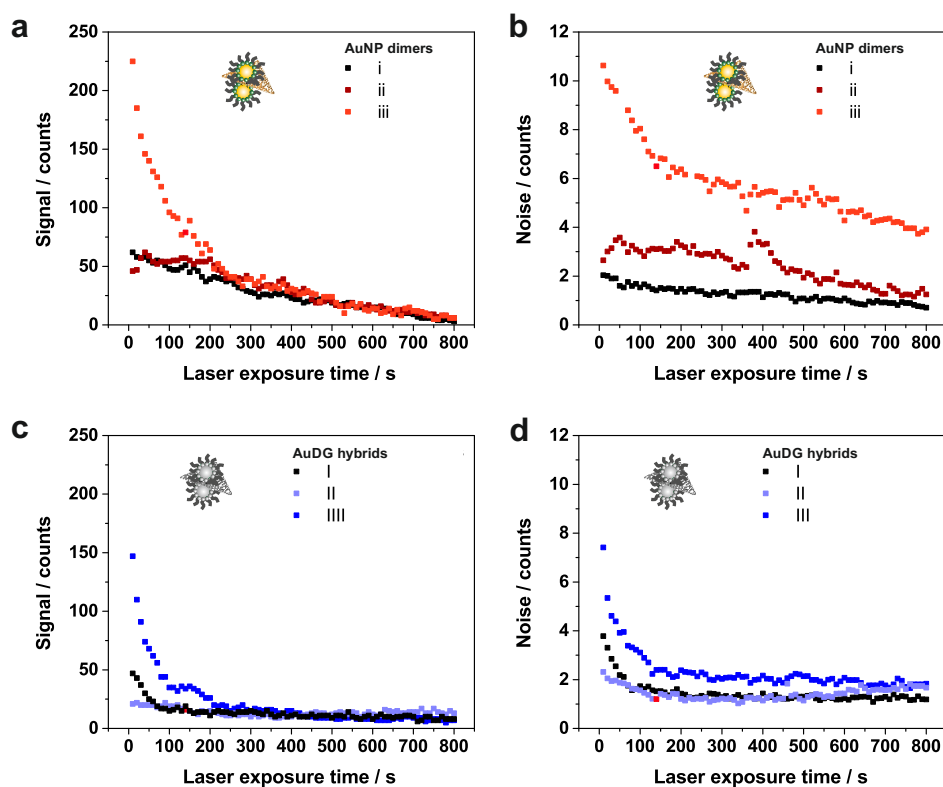
**Figure S2:**(a) AFM image of 40 nm AuNPs coated with Cy3-modified ssDNA (sequence:  $5'-(ATT)_3-T_4X-SH-3'$  (X = Cy3)). A part of the AuNPs is non-covered (a–f), the other part is covered by SLG (A–F). (b) Correlated SERS spectra for the AuNPs shown in (a). As discussed for TAMRA in the main text, the SERS signals of graphene covered AuNPs exhibit a higher reproducibility regarding signal intensities and background appearance.

## 3. SERS spectra of SLG, FLG and graphite



**Figure S3:** SERS spectra of SLG, FLG and graphite including the  $2D'$  peak at approximately  $3245\text{ cm}^{-1}$ .

## 4. Independent time evolutions of signal and noise



*Figure S4:* Time evolutions of signal and noise for AuNP dimers (a, b) as well as for AuDG hybrid structures (c, d) as a function of laser exposure time.



## 6.5. UV photon-induced DNA strand breakage

### “Using DNA Origami Nanostructures To Determine Absolute Cross Sections for UV Photon-Induced DNA Strand Breakage”

*J. Phys. Chem. Lett.* **6**, 4589–4593 (2015).

- Main text: pp. 119–123
- Supporting Information (SI): pp. 124–127

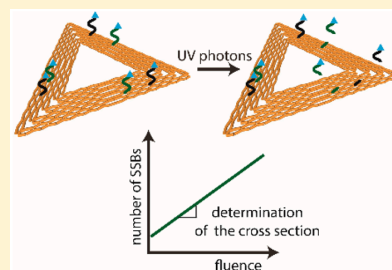


## Using DNA Origami Nanostructures To Determine Absolute Cross Sections for UV Photon-Induced DNA Strand Breakage

Stefanie Vogel,<sup>†</sup> Jenny Rackwitz,<sup>†</sup> Robin Schürman,<sup>†,‡</sup> Julia Prinz,<sup>†</sup> Aleksandar R. Milosavljević,<sup>§,#</sup> Matthieu Réfrégiers,<sup>||</sup> Alexandre Giuliani,<sup>||,⊥</sup> and Ilko Bald<sup>\*,†,‡</sup><sup>†</sup>Institute of Chemistry, University of Potsdam, Karl-Liebknecht-Str. 24-25, 14469 Potsdam, Germany<sup>‡</sup>BAM Federal Institute for Materials Research and Testing, Richard-Willstätter Str. 11, 12489 Berlin, Germany<sup>§</sup>Institute of Physics Belgrade, University of Belgrade, Pregrevica 118, 11080 Belgrade, Serbia<sup>||</sup>Synchrotron SOLEIL, 91192 Gif-sur-Yvette, France<sup>⊥</sup>UAR 1008 CEPIA, INRA, 44316 Nantes, France

## Supporting Information

**ABSTRACT:** We have characterized ultraviolet (UV) photon-induced DNA strand break processes by determination of absolute cross sections for photoabsorption and for sequence-specific DNA single strand breakage induced by photons in an energy range from 6.50 to 8.94 eV. These represent the lowest-energy photons able to induce DNA strand breaks. Oligonucleotide targets are immobilized on a UV transparent substrate in controlled quantities through attachment to DNA origami templates. Photon-induced dissociation of single DNA strands is visualized and quantified using atomic force microscopy. The obtained quantum yields for strand breakage vary between 0.06 and 0.5, indicating highly efficient DNA strand breakage by UV photons, which is clearly dependent on the photon energy. Above the ionization threshold strand breakage becomes clearly the dominant form of DNA radiation damage, which is then also dependent on the nucleotide sequence.



The susceptibility of the DNA molecule to energetic photons, particularly to the ubiquitous ultraviolet (UV) radiation, is the subject of an immense and long-standing research.<sup>1</sup> Because DNA is the carrier of genetic information, any radiation-induced alteration or degradation of its structure directly leads to drastic vital effects such as cell death or tumor genesis.<sup>2,3</sup> It has been shown that absorption in the UV range around 4.7 eV (260 nm), corresponding to resonant  $1\pi\pi^*$  excitation in the nucleobases,<sup>1,4</sup> mainly leads to rapid population of the electronic ground state via conical intersections and to a small extent to nucleobase modifications such as cyclobutane pyrimidine dimers.<sup>1</sup> At higher photon energies (>6 eV) DNA strand breaks become the dominant form of radiation damage.<sup>5,6</sup> To reach a profound understanding of photoinduced DNA strand breakage, which allows modeling the irradiation effects on a macroscopic level, absolute cross sections for a specific DNA damage are needed, particularly their dependence on both the photon energy and the molecular structure.

There has been a persistent effort to quantify the DNA damage induced by vacuum ultraviolet (VUV) irradiation (see refs 5, 7, and 8 and references therein); however, so far the investigations have been typically performed on plasmid DNA, in which the induced damage, such as single and double strand breaks (SSBs and DSBs, respectively), can be recorded by gel electrophoresis. The obtained results indeed provided valuable

information about the yields of SSBs and DSBs as a function of both the irradiation dose and the photon energy, which were important to understand, and model biological effects induced by ionizing radiation.<sup>7</sup> Nevertheless, the quantification of SSBs by gel electrophoresis is error prone,<sup>6</sup> and from the experiments performed on plasmid DNA it remains unknown in which part of the DNA the actual damage occurs and what the influence of both the primary and the secondary structure on the DNA damage is. It has been reported that stacking interactions between the DNA nucleobases lead to a strong modification of their electronic properties and hence their photoinduced fragmentation dynamics.<sup>9</sup> In early attempts to understand the mechanism of UV-induced DNA strand breakage it was already suggested that it depends on the nucleotide sequence. In these experiments chromatographic methods were used to analyze the damage to dinucleotides,<sup>10</sup> however, as was demonstrated recently with low-energy electrons, chromatographic methods fail for the analysis of longer DNA sequences,<sup>11</sup> in which sequence-dependent effects are actually expected to be the most relevant. Consequently, to the best of our knowledge, absolute cross sections for VUV-induced sequence-specific

Received: October 7, 2015

Accepted: November 4, 2015

Published: November 4, 2015



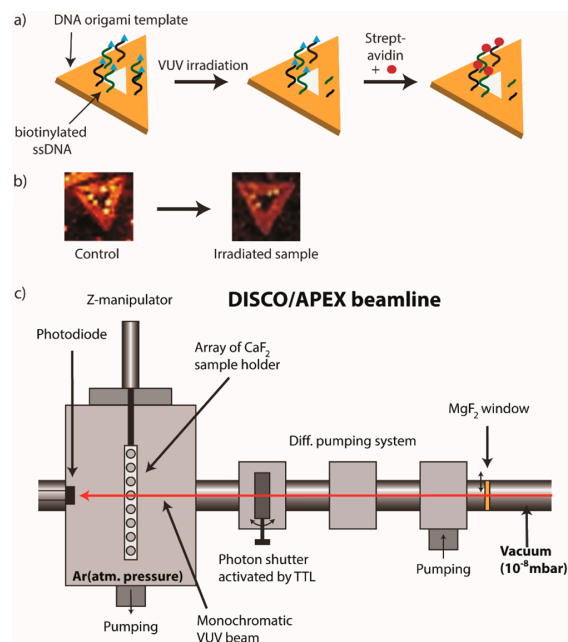
DNA strand breakage of oligonucleotides have not yet been reported.

Furthermore, the results measured for plasmid DNA may depend markedly on the experimental procedure. For example, it has been suggested that variation of the plasmid damage reported by different authors may be due to different sample preparation conditions and different structure of the plasmid DNA as a result of different residual water contentment by the dried plasmid DNA.<sup>5</sup> It has been also pointed out recently that the film thickness can strongly influence the radiation damage by modifying both the molecular structure of the material and the deposition process.<sup>12</sup> Finally, possible effects from either secondary electrons produced in the substrate or an indirect damage cannot be absolutely excluded.<sup>5</sup> Therefore, it appears that there is a serious constraint in the research on UV damage to DNA. On the one hand the photophysics of basic DNA components (e.g., nucleobases or nucleotides) can be studied under well-defined conditions but cannot be simply extrapolated to quantify the damage of the DNA molecule, as the sequence and structure contributions are not taken into consideration. On the other hand, the quantification of degradation of a macroscopic DNA sample cannot be scaled down to unambiguously determine the absolute cross section for the VUV-induced damage of a single DNA molecule with defined sequence.

In the following, we report an unprecedented study on sequence-specific DNA damage induced by VUV photons on the single-molecule level. By using DNA origami-based DNA nanoarrays, we are able to visualize the dissociation of single chemical bonds by atomic force microscopy (AFM)<sup>13–15</sup> and determine the absolute cross sections for strand breakage ( $\sigma_{\text{SSB}}$ ) in specific oligonucleotides at various photon energies. The basic experimental procedure is illustrated in Figure 1a.

Triangular DNA origami substrates are used due to their rigidity and their low tendency to form clusters. Because the target sequences are arranged in a pattern recognizable in AFM images, two target sequences can be studied simultaneously within one irradiation experiment. The samples are deposited on a UV transparent  $\text{CaF}_2$  substrate to avoid any secondary effects due to absorption by the substrate and are irradiated under normal atmospheric pressure in a transparent Ar atmosphere. Under the dry conditions the direct interaction of VUV photons with DNA is probed and the contribution of OH radical-induced DNA damage can be ruled out. The target sequences are modified with a biotin marker on the 5' end. After irradiation the DNA nanoarrays on the  $\text{CaF}_2$  substrates are treated with a solution of streptavidin (SAv), which binds to the biotin markers of the intact target oligonucleotides. The SAv can then be easily recognized in AFM images and thus the number and position of damaged target oligonucleotides can be determined. The method is intrinsically digital regarding the information on both the strand breakage and the target sequence; therefore, it allows fast and parallel determination of  $\sigma_{\text{SSB}}$  with unprecedented control over the DNA's primary and also secondary structure.<sup>16,17</sup> The  $\sigma_{\text{SSB}}$  values have been determined by measuring dose–response curves.<sup>18</sup> The results clearly indicate a dependence of  $\sigma_{\text{SSB}}$  on the photon energy and to some extent also on the sequence. By measuring the photon absorption cross sections ( $\sigma_{\text{PA}}$ ) of the same target sequences at the same photon energies, we additionally obtain the quantum yield of DNA strand breakage.

DNA origami nanostructures were prepared from the M13mp18 scaffold strand and a set of 208 short oligonucleo-

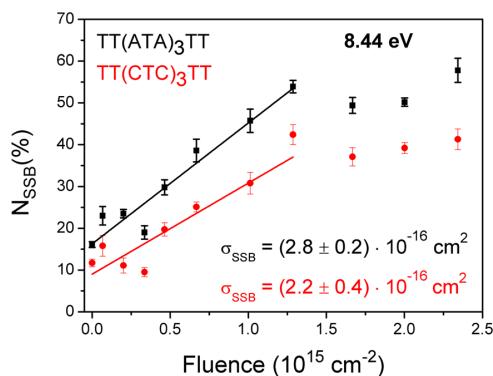


**Figure 1.** (a) Scheme of the DNA origami triangles which serve as a support of the oligonucleotide target structures. (b) Typical AFM images of a nonirradiated control sample (left) and a sample irradiated with VUV light (right). (c) Schematic view of the experimental setup.

tides according to a well-established procedure.<sup>13,19</sup> In brief, the DNA strands are mixed in TAE buffer with 10 mM  $\text{MgCl}_2$  and annealed from 80 °C to room temperature within 4–6 h, and the nonassembled excess strands are removed by spin-filtering. The assembled structures are deposited in 1× TAE buffer with 10 mM  $\text{MgCl}_2$  on  $\text{CaF}_2$  substrates. The excess solution is removed by washing with 4 mL of ethanol/water (1/1) mixture, and subsequently the sample is dried with a blow of nitrogen. Then, the samples are transferred into the irradiation chamber and exposed to VUV photons. After irradiation the samples are rinsed again with ethanol/water to remove fragmentation products and then incubated in a 50 nM solution of streptavidin (SAv) for 2 min, washed again, and dried. Then, the samples are analyzed with AFM (Figure 1b). Within the accuracy of the experiment the strand break cross section is independent of the position of target strands on the DNA origami template. Compared with isolated oligonucleotides the target sequences in the present experiment are attached to the DNA origami template and have thus one more potential site that can be broken to be detected as a strand break. A schematic view of the experimental setup is given in Figure 1c. The irradiation chamber has been connected to the APEX branch of the DISCO beamline<sup>20</sup> of the SOLEIL synchrotron facility (France) and filled with argon gas under normal atmospheric pressure through the differential pumping stage of the branch.<sup>21</sup> For the present energy range, the second-order light has been filtered off by a  $\text{MgF}_2$  window mounted on the window valve isolating the differential pumping. Because  $\text{CaF}_2$  holders are used any secondary effects that could result from substrate irradiation (secondary electrons, heating, etc.) are practically excluded. Because we are working on a single-molecule level the photon irradiation above the ionization

threshold of DNA is not expected to modify the strand breakage or to lead to significant charging of the DNA. The samples are inserted in front of the VUV beam by using a Z-manipulator and irradiated for a defined period. The beam diameter is larger than the exposed sample and the photon flux is measured only for the exposed, active sample area. The irradiation time was controlled by using a rotatable shutter activated by a TTL signal. The photon flux has been constantly monitored during the irradiation period by using a calibrated photodiode (AXUV 100, International Radiation Detectors) placed downstream the sample holder. The photon flux used to evaluate the absolute cross sections has been measured with the sample holder pulled out. A series of samples was irradiated with different photon fluence at a fixed photon energy. The relative number of strand breaks  $N_{\text{SSB}}$  was extracted from AFM images by comparing the number of specifically bound SA<sub>v</sub> on irradiated and nonirradiated triangular DNA origami structures with the expected maximum coverage. For each irradiated sample, about ten AFM images, that is, 500–1000 DNA origami structures, have been recorded and analyzed.

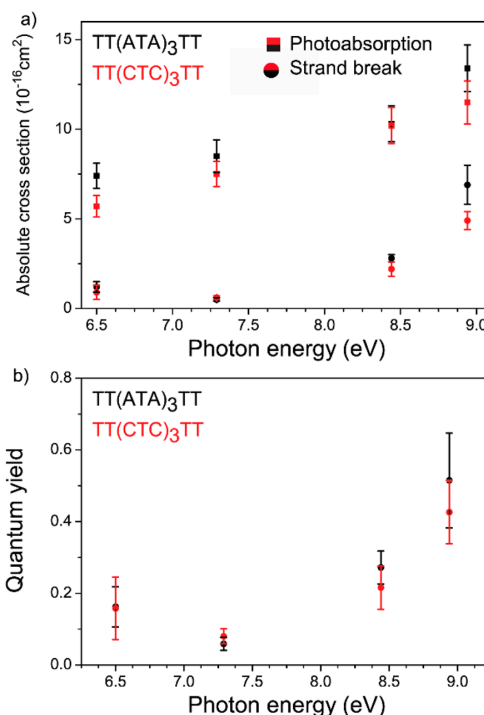
The fluence ( $\Phi$ ) dependence of  $N_{\text{SSB}}$  at 8.44 eV photon energy is shown in Figure 2. It shows a linear increase of  $N_{\text{SSB}}$



**Figure 2.** Relative number of strand breaks plotted as a function of the photon fluence at 8.44 eV. From the slopes of the linear fits in the low-fluence regime the absolute cross sections for strand breakage are extracted.

until a saturation is reached at  $\sim 1.3 \times 10^{15} \text{ cm}^{-2}$ . The DNA origami structures are modified with two different oligonucleotide sequences (TT(ATA)<sub>3</sub>TT and TT(CTC)<sub>3</sub>TT), which can be independently analyzed by AFM. From the slope of the linear fit in the low fluence regime  $\sigma_{\text{SSB}}$  is determined:  $N_{\text{SSB}} = \sigma_{\text{SSB}} \cdot \Phi$ .<sup>15,18</sup> The strand break cross sections for the two different DNA sequences at four different photon energies are summarized in Supplementary Table 1 and displayed in Figure 3. They vary between  $0.9 \times 10^{-16}$  and  $6.9 \times 10^{-16} \text{ cm}^2$  depending on the photon energy and the oligonucleotide sequence.

Photoabsorption cross sections ( $\sigma_{\text{PA}}$ ) for the oligonucleotides have been measured in solution from 350 (3.54 eV) to 190 nm (6.52 eV) using both a double spectrophotometer and the synchrotron radiation circular dichroism branch of the DISCO beamline.<sup>22</sup> Absorption measurements have been carried out on thin films of oligonucleotides deposited on CaF<sub>2</sub> windows to reach for shorter wavelengths. The condensed phase measurements have been scaled to absolute cross sections obtained from the solution phase. Although UV



**Figure 3.** (a) Absolute cross sections for DNA photoabsorption (open symbols) and strand breakage (full symbols) for two different oligonucleotides determined at four different photon energies. (b) Quantum yield for strand breaks for the two oligonucleotides obtained from the data in panel a.

spectroscopy is known to be indicative of higher order structure of biological polymers, the effect of the physical state on the absorption cross sections is not drastic and both measurements can be compared, as previously done for other biomolecules.<sup>23</sup> The procedure is described in detail in the Supporting Information.

The photon energy dependence of  $\sigma_{\text{SSB}}$  is displayed in Figure 3a (circles) and shows a minimum around 7.29 eV. At lower energy (6.50 eV)  $\sigma_{\text{SSB}}$  is slightly larger, and toward higher energies  $\sigma_{\text{SSB}}$  rises steeply. The slight increase in  $\sigma_{\text{SSB}}$  at 6.50 eV indicates a resonant process and contrasts with the  $\sigma_{\text{PA}}$ , which increases monotonically from 6.5 to 8.94 eV, as shown in the top of Figure 3a (square symbols). The excitation in the 6.3 to 6.5 eV range is ascribed to a  $\pi-\pi^*$  transition within the nucleobases.<sup>24</sup> In recent tandem mass spectrometric experiments using protonated adenine-5'-monophosphate stored in an ion trap and irradiated with VUV photons, a resonant fragmentation around 6.50 eV was found resulting in the formation of protonated adenine due to an N-glycosidic bond cleavage.<sup>4</sup> The current data show that the  $\pi-\pi^*$  transition at 6.50 eV results not only in base abstraction but also in a more efficient DNA strand breakage, that is, a bond cleavage within the sugar-phosphate backbone.

At the higher energies investigated here the oligonucleotides can be ionized at the nucleobases because the vertical ionization energy (IE) of isolated A is 8.44 eV and the vertical IE of C is 8.94 eV.<sup>25</sup> The IEs of stacked nucleobases are slightly lower<sup>15</sup> and the ionization threshold of the DNA sugar 2'-deoxy-D-ribose was recently found to be 9.4 eV,<sup>26</sup> which is clearly above

the energies considered here.  $\sigma_{\text{SSB}}$  increases steeply at these energies, indicating more efficient strand breakage from ionized DNA compared with the strand breakage from electronically excited states. In a previous study on single strand breakage in plasmid DNA by 8.3 eV photons a cross section of  $8.1 \times 10^{-15} \text{ cm}^2$  was found.<sup>27</sup> The lower values of  $\sigma_{\text{SSB}}$  found in the present study are ascribed to the fact that we have used 13mer oligonucleotides compared with the plasmid DNA used by Hieda et al., which consists of several thousand base pairs. At higher photon energy of 26.5 eV an SSB cross section of  $(2 \text{ to } 3) \times 10^{-13} \text{ cm}^2$  was recently reported.<sup>28</sup> In previous experiments using low-energy electrons, strand break cross sections on the order  $10^{-14} \text{ cm}^2$  have been reported for both plasmid DNA<sup>18,29</sup> and oligonucleotides.<sup>15</sup> Such high damage cross sections are due to the dissociative electron attachment mechanism, which proceeds through a transient anionic state and is very efficient at low electron energies.<sup>30,31</sup>

The two different oligonucleotide sequences investigated here (TT(ATA)<sub>3</sub>TT and TT(CTC)<sub>3</sub>TT) exhibit very similar properties, but distinct differences appear for  $\sigma_{\text{SSB}}$  at higher energies (8.44 and 8.94 eV, see Figure 3a). That is,  $\sigma_{\text{SSB}}$  is higher for the TT(ATA)<sub>3</sub>TT sequence than for the TT-(CTC)<sub>3</sub>TT sequence by a factor of 1.3 at 8.44 eV and by a factor of 1.4 at 8.94 eV. The comparison with the absorption cross section of the two oligonucleotides (Figure 3a, square symbols) indicates that the higher sensitivity of the A-containing sequence can partly be attributed to a higher photoabsorption. Nevertheless, a very recent study found that the energy threshold for DNA photo damage at the sugar-phosphate backbone is considerably lower (4.2 eV) than that for damage at the nucleobases (6.9 eV).<sup>32</sup> Such low-energy thresholds might be associated with low ionization energies that have been reported for the negatively charged phosphate in DNA.<sup>33</sup> Thus, the strand breakage at low energies proceeds most likely via the DNA backbone, and at higher energies fragmentation pathways involving the nucleobases start to be operative, resulting in more distinct values of  $\sigma_{\text{SSB}}$  for the two different sequences. At 8.44 and 8.94 eV a radical cation might be formed on one of the nucleobases. Previously, it was shown that excited nucleobase radical cations are transferred into sugar radicals through a hole and proton transfer.<sup>34–36</sup> These sugar radicals represent important precursors for DNA strand breakage, and they might be formed more efficiently in the A containing sequence than in the C containing sequence.

The energy dependence of the strand break quantum yield is presented in Figure 3b. For both molecules, the yields range from 16% at 6.5 eV to 40–50% at 8.94 eV, with a minimum at 7.29 eV of 6–8%. Interestingly, the minimum at 7.24 eV observed in Figure 3b indicates that a relaxation mechanism other than strand breakages becomes predominant at 7.24 eV. Nevertheless, the quantum yields demonstrate the extremely high efficiency of DNA strand breakage upon absorption of UV photons. Thus, the strand breakage is most likely a direct result of the excitation/ionization either of the DNA backbone or the nucleobases and is not due to a combined process such as the production of secondary low-energy electrons, which then react with the target sequence. Furthermore, the quantum yields indicate that strand breakage is the dominant decay channel after photon absorption at energies above the ionization threshold.

In conclusion, we present for the first time absolute cross sections and quantum yields for the strand breakage of specific oligonucleotide sequences (TT(ATA)<sub>3</sub>TT and TT(CTC)<sub>3</sub>TT)

induced by VUV photons with energies around the ionization threshold (6.50, 7.29, 8.44, and 8.94 eV). The strand break cross sections vary between  $0.9 \times 10^{-16}$  and  $6.9 \times 10^{-16} \text{ cm}^2$  depending on both the oligonucleotide sequence and the photon energy. DNA strand breakage takes place both from the  $\pi-\pi^*$  transition at 6.50 eV and presumably from ionized states accessed at higher photon energies. The strand breakage is highly efficient, which is reflected by quantum yields ranging from 6 to 50%. The sequence dependence of  $\sigma_{\text{SSB}}$  is most pronounced at the higher energies investigated here and is reflected in a higher sensitivity of the A-containing sequence, which could be due to a stronger delocalization of excited/ionized states in stacked A bases. The present experiments are based on a novel DNA origami technique, which allows us to determine absolute cross sections for strand breakage in well-defined oligonucleotide sequences. This is the basis for a thorough and comprehensive investigation of photoinduced DNA strand break mechanisms.

## ■ ASSOCIATED CONTENT

### ■ Supporting Information

The Supporting Information is available free of charge on the ACS Publications website at DOI: 10.1021/acs.jpcllett.5b02238.

Additional AFM images of DNA nanostructures irradiated on CaF<sub>2</sub>, additional measurements indicating the biotin stability, dose–response curves for the irradiation energies 6.50, 7.29, and 8.94 eV, detailed information about the measurements of the photo-absorption cross sections of the different DNA sequences, and complete refs 20–22. (PDF)

## ■ AUTHOR INFORMATION

### ■ Corresponding Author

\*E-mail: bald@uni-potsdam.de.

### ■ Present Address

#A.R.M.: Radiation Laboratory, University of Notre Dame, Notre Dame, Indiana 46556, USA.

### ■ Notes

The authors declare no competing financial interest.

## ■ ACKNOWLEDGMENTS

This research was supported by a Marie Curie FP7 Integration Grant within the seventh European Union Framework Programme and by the Deutsche Forschungsgemeinschaft (DFG). We are grateful to the synchrotron SOLEIL for providing beamtime and support under project no. 20131271 and to a bilateral grant between Serbia and Germany through the German Academic Exchange Service (DAAD, project no. 57055766) supported by the German Federal Ministry of Education and Research. A.R.M. acknowledges support by the MESTD of RS (171020) and the COST Action MP1002 (Nano-IBCT).

## ■ REFERENCES

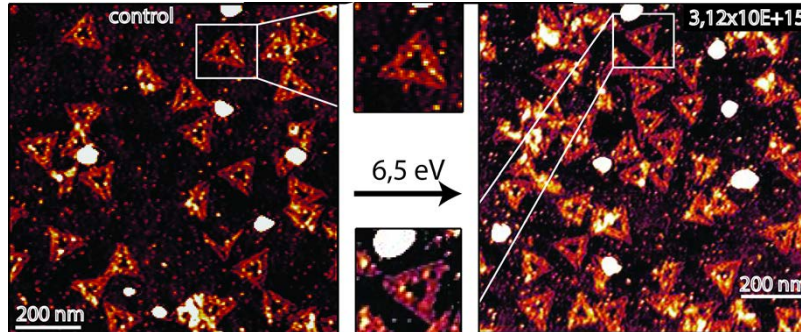
- (1) Middleton, C. T.; de La Harpe, K.; Su, C.; Law, Y. K.; Crespo-Hernández, C. E.; Kohler, B. DNA Excited-State Dynamics: From Single Bases to the Double Helix. *Annu. Rev. Phys. Chem.* **2009**, *60*, 217–239.
- (2) Baccarelli, I.; Bald, I.; Gianturco, F. A.; Illenberger, E.; Kopyra, J. Electron-Induced Damage of DNA and its Components: Experiments and Theoretical Models. *Phys. Rep.* **2011**, *508*, 1–44.

- (3) Alizadeh, E.; Sanche, L. Precursors of Solvated Electrons in Radiobiological Physics and Chemistry. *Chem. Rev.* **2012**, *112*, 5578–5602.
- (4) Milosavljević, A. R.; Cerovski, V. Z.; Canon, F.; Ranković, M. L.; Škoro, N.; Nahon, L.; Giuliani, A. Energy-Dependent UV Photo-dissociation of Gas-Phase Adenosine Monophosphate Nucleotide Ions: The Role of a Single Solvent Molecule. *J. Phys. Chem. Lett.* **2014**, *5*, 1994–1999.
- (5) Prise, K. M.; Folkard, M.; Michael, B. D.; Vojnovic, B.; Brocklehurst, B.; Hopkirk, A.; Munro, I. H. Critical Energies for SSB and DSB Induction in Plasmid DNA by Low-Energy Photons: Action Spectra for Strand-Break Induction in Plasmid DNA Irradiated in Vacuum. *Int. J. Radiat. Biol.* **2000**, *76*, 881–890.
- (6) Śmialek, M. A.; Moore, S. A.; Mason, N. J.; Shuker, David E. G. Quantification of Radiation-Induced Single-Strand Breaks in Plasmid DNA using a TUNEL/ELISA-Based Assay. *Radiat. Res.* **2009**, *172*, 529–536.
- (7) Folkard, M.; Prise, K. M.; Vojnovic, B.; Brocklehurst, B.; Michael, B. D. Critical Energies for SSB and DSB Induction in Plasmid DNA by Vacuum-UV Photons: an Arrangement for Irradiating Dry or Hydrated DNA with Monochromatic Photons. *Int. J. Radiat. Biol.* **2000**, *76*, 763–771.
- (8) Folkard, M.; Prise, K. M.; Turner, C. J.; Michael, B. D. The Production of Single Strand and Double Strand Breaks in DNA in Aqueous Solution by Vacuum UV Photons Below 10 eV. *Radiat. Prot. Dosim.* **2002**, *99*, 147–149.
- (9) Kadhane, U.; Holm, Anne, I. S.; Hoffmann, S. V.; Nielsen, S. B. Strong Coupling between Adenine Nucleobases in DNA Single Strands Revealed by Circular Dichroism using Synchrotron Radiation. *Phys. Rev. E* **2008**, *77*, 021901.
- (10) Ito, T.; Saito, M. Degradation of Oligonucleotides by Vacuum-UV Radiation in Solid: Roles of the Phosphate Group and Bases. *Photochem. Photobiol.* **1988**, *48*, 567–572.
- (11) Li, Z. J.; Cloutier, P.; Sanche, L.; Wagner, J. R. Low-Energy Electron-Induced DNA Damage: Effect of Base Sequence in Oligonucleotide Trimers. *J. Am. Chem. Soc.* **2010**, *132*, 5422–5427.
- (12) Alizadeh, E.; Sanche, L. Absolute Measurements of Radiation Damage in Nanometer-Thick Films. *Radiat. Prot. Dosim.* **2012**, *151*, 591–599.
- (13) Keller, A.; Bald, I.; Rotaru, A.; Cauet, E.; Gothelf, K. V.; Besenbacher, F. Probing Electron-Induced Bond Cleavage at the Single-Molecule Level Using DNA Origami Templates. *ACS Nano* **2012**, *6*, 4392–4399.
- (14) Keller, A.; Kopyra, J.; Gothelf, K. V.; Bald, I. Electron-Induced Damage of Biotin Studied in the Gas Phase and in the Condensed Phase at a Single-Molecule Level. *New J. Phys.* **2013**, *15*, 083045.
- (15) Keller, A.; Rackwitz, J.; Cauet, E.; Lievin, J.; Körzdörfer, T.; Rotaru, A.; Gothelf, K. V.; Besenbacher, F.; Bald, I. Sequence Dependence of Electron-Induced DNA Strand Breakage Revealed by DNA Nanoarrays. *Sci. Rep.* **2014**, *4*, 7391.
- (16) Bald, I.; Keller, A. Molecular Processes Studied at a Single-Molecule Level Using DNA Origami Nanostructures and Atomic Force Microscopy. *Molecules* **2014**, *19*, 13803–13823.
- (17) Olejko, L.; Cywinski, P. J.; Bald, I. Ion-Selective Formation of a Guanine Quadruplex on DNA Origami Structures. *Angew. Chem., Int. Ed.* **2015**, *54*, 673–677.
- (18) Panajotovic, R.; Martin, F.; Cloutier, P.; Hunting, D.; Sanche, L. Effective Cross Sections for Production of Single-Strand Breaks in Plasmid DNA by 0.1 to 4.7 eV Electrons. *Radiat. Res.* **2006**, *165*, 452–459.
- (19) Rothmund, Paul W. K. Folding DNA to Create Nanoscale Shapes and Patterns. *Nature* **2006**, *440*, 297–302.
- (20) Giuliani, A.; Jamme, F.; Rouam, V.; Wien, F.; Giorgetta, J.-L.; Lagarde, B.; Chubar, O.; Bac, S.; Yao, I.; Rey, S.; et al. DISCO: A Low-Energy Multipurpose Beamline at Synchrotron SOLEIL. *J. Synchrotron Radiat.* **2009**, *16*, 835–841.
- (21) Giuliani, A.; Yao, I.; Lagarde, B.; Rey, S.; Duval, J.-P.; Rommeluere, P.; Jamme, F.; Rouam, V.; Wein, F.; De Oliveira, C.; et al. A Differential Pumping System to Deliver Windowless VUV Photons at Atmospheric Pressure. *J. Synchrotron Radiat.* **2011**, *18*, 546–549.
- (22) Refregiers, M.; Wien, F.; Ta, H.-P.; Premvardhan, L.; Bac, S.; Jamme, F.; Rouam, V.; Lagarde, B.; Polack, F.; Giorgetta, J.-L.; et al. DISCO Synchrotron-Radiation Circular-Dichroism Endstation at SOLEIL. *J. Synchrotron Radiat.* **2012**, *19*, 831–835.
- (23) Meinert, C.; Bredehöft, J. H.; Filippi, J.-J.; Baraud, Y.; Nahon, L.; Wien, F.; Jones, N. C.; Hoffmann, S. V.; Meierhenrich, U. J. Anisotropy Spectra of Amino Acids. *Angew. Chem., Int. Ed.* **2012**, *51*, 4484–4487.
- (24) Szalay, P. G.; Watson, T.; Perera, A.; Lotrich, V. F.; Bartlett, R. J. Benchmark Studies on the Building Blocks of DNA. 1. Superiority of Coupled Cluster Methods in Describing the Excited States of Nucleobases in the Franck–Condon Region. *J. Phys. Chem. A* **2012**, *116*, 6702–6710.
- (25) Cauët, E.; Dehareng, D.; Liévin, J. Ab Initio Study of the Ionization of the DNA Bases: Ionization Potentials and Excited States of the Cations. *J. Phys. Chem. A* **2006**, *110*, 9200–9211.
- (26) Ghosh, D.; Golan, A.; Takahashi, L. K.; Krylov, A. I.; Ahmed, M. A VUV Photoionization and Ab Initio Determination of the Ionization Energy of a Gas-Phase Sugar (Deoxyribose). *J. Phys. Chem. Lett.* **2012**, *3*, 97–101.
- (27) Hieda, K. DNA Damage Induced by Vacuum and Soft X-ray Photons from Synchrotron Radiation. *Int. J. Radiat. Biol.* **1994**, *66*, 561–567.
- (28) Nováková, E.; Vyšín, L.; Burian, T.; Juha, L.; Davidková, M.; Múčka, V.; Čuba, V.; Grisham, M. E.; Heinbuch, S.; Rocca, J. J. Breaking DNA Strands by Extreme-Ultraviolet Laser Pulses in Vacuum. *Phys. Rev. E* **2015**, *91*, 042718.
- (29) Boulanouar, O.; Fromm, M.; Bass, A. D.; Cloutier, P.; Sanche, L. Absolute Cross Section for Loss of Supercoiled Topology Induced by 10 eV Electrons in Highly Uniform /DNA/1,3-Diaminopropane Films Deposited on Highly Ordered Pyrolytic Graphite. *J. Chem. Phys.* **2013**, *139*, 055104.
- (30) Bald, I.; Dabkowska, I.; Illenberger, E. Probing Biomolecules by Laser-Induced Acoustic Desorption: Electrons at Near Zero Electron Volts Trigger Sugar-Phosphate Cleavage. *Angew. Chem., Int. Ed.* **2008**, *47*, 8518–8520.
- (31) Bald, I.; Kopyra, J.; Dąbkowska, I.; Antonsson, E.; Illenberger, E. Low Energy Electron-Induced Reactions in Gas Phase 1,2,3,5-Tetra-O-Acetyl-β-D-Ribofuranose: A Model System for the Behavior of Sugar in DNA. *J. Chem. Phys.* **2007**, *126*, 074308.
- (32) Gomes, P. J.; Ferraria, A. M.; Botelho do Rego, A. M.; Hoffmann, S. V.; Ribeiro, P. A.; Raposo, M. Energy Thresholds of DNA Damage Induced by UV Radiation: An XPS Study. *J. Phys. Chem. B* **2015**, *119*, 5404–5411.
- (33) Kim, N. S.; Zhu, Q.; LeBreton, P. R. Aqueous Ionization and Electron-Donating Properties of Dinucleotides: Sequence-Specific Electronic Effects on DNA Alkylation. *J. Am. Chem. Soc.* **1999**, *121*, 11516–11530.
- (34) Adhikary, A. UVA-Visible Photo-Excitation of Guanine Radical Cations Produces Sugar Radicals in DNA and Model Structures. *Nucleic Acids Res.* **2005**, *33*, 5553–5564.
- (35) Adhikary, A.; Kumar, A.; Sevilla, M. D. Photo-Induced Hole Transfer from Base to Sugar in DNA: Relationship to Primary Radiation Damage. *Radiat. Res.* **2006**, *165*, 479–484.
- (36) Khanduri, D.; Adhikary, A.; Sevilla, M. D. Highly Oxidizing Excited States of One-Electron-Oxidized Guanine in DNA: Wavelength and pH Dependence. *J. Am. Chem. Soc.* **2011**, *133*, 4527–4537.

## Supporting Information

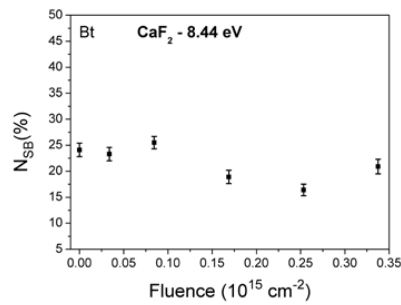
### “Using DNA Origami Nanostructures to Determine Absolute Cross Sections for UV Photon-Induced DNA Strand Breakage”

#### 1. AFM images



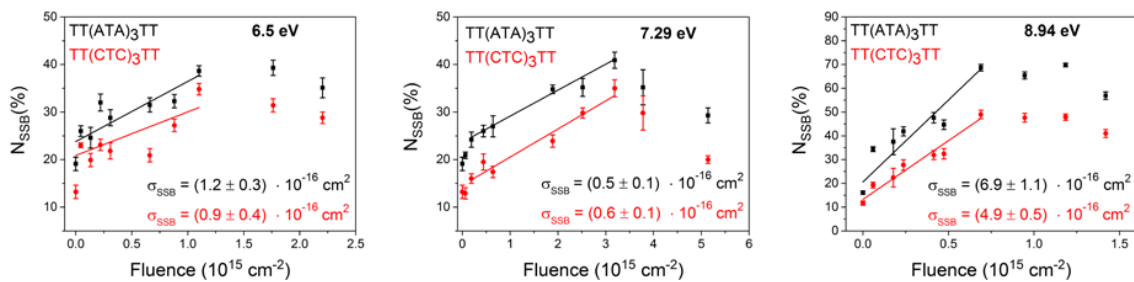
**Figure S1:** Typical AFM images of modified DNA origami structures irradiated on CaF<sub>2</sub> with 6.5 eV.

#### 2. Determination of biotin stability



**Figure S2:** To test the VUV stability of the biotin (Bt) label a single biotin modification was attached to the DNA origami templates and the irradiation was performed at 8.44 eV. No increase in Bt damage can be observed.

#### 3. Determination of strand break cross sections



**Figure S3:** Relative number of strand breaks plotted as a function of the photon fluence at 6.50 eV, 7.29 eV, and 8.94 eV.

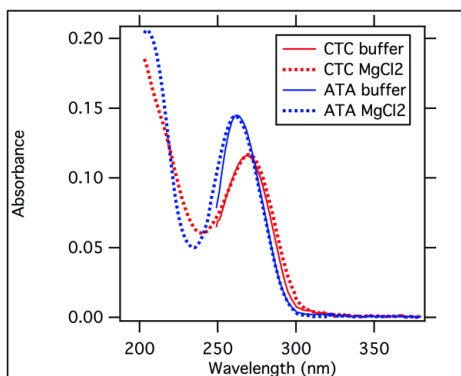


#### 4. Measurements of the photoabsorption cross sections

The photoabsorption cross section of the TT(CTC)<sub>3</sub>TT and TT(ATA)<sub>3</sub>TT oligonucleotides have been measured for solutions and for thin films using two instruments: a double beam spectrophotometer and a synchrotron radiation circular dichroism spectrometer. The details of the measurements and of the data treatment are given below. We will refer to CTC and ATA in the following for TT(CTC)<sub>3</sub>TT and TT(ATA)<sub>3</sub>TT, respectively. Stock solutions of ATA and CTC were received from the supplier (Metabion, Germany) with a claimed concentration of 100 μM in water.

##### Solution phase

The stock solutions of ATA and CTC were diluted in TAE buffer and in MgCl<sub>2</sub> solution to 1 μM. Measurements were made in 1 cm quartz cuvette using a Specord 210 (Analytic Jena), which is a double beam spectrophotometer with 0.5 nm wavelength accuracy.



**Figure S4:** Photoabsorption spectra of CTC and ATA measured in the TAE buffer and in the MgCl<sub>2</sub> solution.

Figure S2 presents the absorbance spectra. The TAE buffer becomes opaque at wavelength shorter than 250 nm. In contrast, when using a MgCl<sub>2</sub> solution 200 nm can be reached. The spectrum is not affected by the type of buffer.

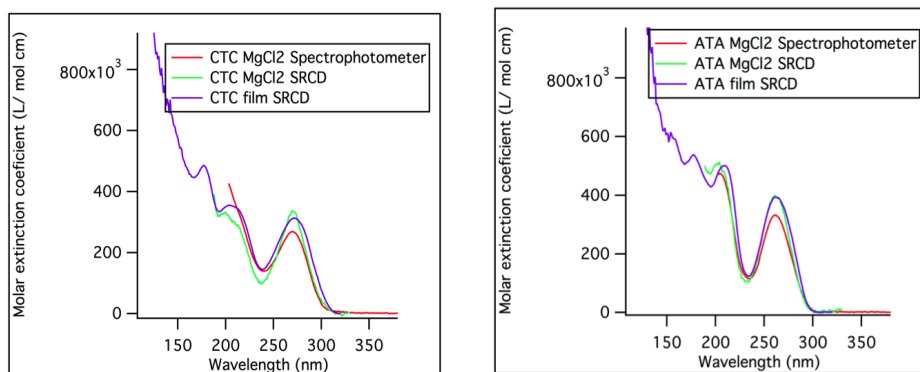
In order to reach shorter wavelength, experiments were carried out using the SRCD spectrometer [1] of the DISCO beamline [2] at the SOLEIL facility. The SRCD branch allows measurements down to 125 nm. We used fixed exit slits giving a spectral resolution ranging from 2 nm to 1 nm over the spectral range investigated. Owing to the strong absorbance of the TAE buffer, we used MgCl<sub>2</sub> solutions only in CaF<sub>2</sub> cells (Hellma) with 58 μm path length. Spectra of the blank (MgCl<sub>2</sub> solution) and the solution were recorded in triplicate. We have followed the method described by Sutherland and coworkers [3] in which the dependency of the gain of the photomultiplier with the wavelength is used to obtain absorbance. The photoabsorption spectra are presented in Figure S3 (green curve) and compared to those made with the spectrophotometer (red curve). Both data agree well, the difference in the band shape arises from higher spectral resolution of the SRCD spectrometer. The SRCD measurements extend the data down to 190 nm. The absorbances were converted in molar extinction coefficient by:

$$\epsilon = \frac{A}{c \cdot l}$$

where  $A$  is the absorbance,  $c$  the concentration in mol/L,  $l$  the optical path length in cm, and  $\epsilon$  the molar extinction coefficient in L/mol cm. The absorbances measured in Log10 were divided by 0.43429 according to Berkowitz. [4]

## Films measurements

To reach shorter wavelength, thin films of the oligonucleotides were deposited on  $\text{CaF}_2$  windows. The films were prepared by spraying the mother solution using an APCI probe (Thermo Finigan). The sheath gas entry of the ion source was connected to 4 bar of nitrogen and the solution was infused using a syringe pump at  $10 \mu\text{L}/\text{min}$ . The solution was sprayed out of a fused silica capillary ( $100 \mu\text{m}$  internal diameter) by the compressed gas surrounding the capillary. The ion source was placed in a vertical position above the  $\text{CaF}_2$  window for a certain amount of time, which allowed controlling the film thickness. The spraying time was gradually increased until a measurable absorption signal was obtained over the wavelength range of interest. To avoid measuring contributions from the buffer, the films were prepared by spraying the mother aqueous solution. The  $\text{CaF}_2$  window was first measured without any film deposited to obtain the blank spectrum. Then the film was deposited on the window and was measured in the same conditions. Three (3) spectra were averaged and the Sutherland's [3] procedure was used. The absorbances measured for the thin films were scaled to the molar extinction coefficients measured for the solutions using the SRCD spectrometer. The scaling factor was chosen in order to minimize the difference between the film and solution spectra where overlapping. We estimate this process to be accurate by 10%. Therefore the photoabsorption coefficient and cross section from the thin films are given with 10% error. The spectra are presented in Figure S3.



**Figure S5:** Photoabsorption spectra (expressed in molar extinction coefficient  $\epsilon$ ) of CTC (left panel) and ATA (right panel) oligonucleotides obtained in solution using the Specord 210 spectrophotometer (red curves) and the SRCD spectrometer (green curves). Thin film measurements made using the SRCD spectrometer are presented in blue.

The molar extinction coefficient  $\epsilon$  is converted into a cross section  $\sigma$  using the following equation from Berkowitz [4]:

$$\epsilon \left[ \frac{\text{L}}{\text{mol} \cdot \text{cm}} \right] = \sigma [\text{Mb}] \cdot 6.020389 \cdot 10^2$$

**Supplementary Table 1:** Photoabsorption and single strand break absolute cross section in  $10^{-16}$  cm<sup>2</sup> for the two different oligonucleotides at different photon energies. Strand break quantum yields are given for each oligonucleotide.

Photon energy / eV	TT(CTC) <sub>3</sub> TT			TT(ATA) <sub>3</sub> TT		
	$\sigma_{PA}$	$\sigma_{SSB}$	$\rho_{SSB}$	$\sigma_{PA}$	$\sigma_{SSB}$	$\rho_{SSB}$
<b>6.50</b>	$5.7 \pm 0.6$	$0.9 \pm 0.4$	$0.16 \pm 0.09$	$7.4 \pm 0.7$	$1.2 \pm 0.3$	$0.16 \pm 0.06$
<b>7.29</b>	$7.5 \pm 0.7$	$0.6 \pm 0.1$	$0.08 \pm 0.02$	$8.5 \pm 0.9$	$0.5 \pm 0.1$	$0.06 \pm 0.02$
<b>8.44</b>	$10.2 \pm 1.0$	$2.2 \pm 0.4$	$0.21 \pm 0.06$	$10.3 \pm 1.0$	$2.8 \pm 0.2$	$0.27 \pm 0.05$
<b>8.94</b>	$11.5 \pm 1.2$	$4.9 \pm 0.5$	$0.43 \pm 0.09$	$13.4 \pm 1.3$	$6.9 \pm 1.1$	$0.51 \pm 0.13$

## References

- [1] M. Réfrégiers, F. Wien, H. P. Ta, L. Premvardhan, S. Bac, F. Jamme, V. Rouam, B. Lagarde, F. Polack, J. L. Giorgetta, J. P. Ricaud, M. Bordessoule, A. Giuliani, “DISCO Synchrotron-Radiation Circular-Dichroism Endstation at SOLEIL”, *Synchrotron Radiat.* **19**, 831–835 (2012).
- [2] A. Giuliani, F. Jamme, V. Rouam, F. Wien, J.-L. Giorgetta, B. Lagarde, O. Chubar, S. Bac, I. Yao, S. Rey, C. Herbeaux, J.-L. Marlats, D. Zerbib, F. Polack, M. Réfrégiers, “DISCO: A Low-Energy Multipurpose Beamline at Synchrotron SOLEIL”, *J. Synchrotron Radiat.* **16**, 835–841 (2009).
- [3] J. C. Sutherland, P. C. Keck, K. P. Griffin, P. Z. Takacs, “Simultaneous Measurement of Absorption and Circular Dichroism in a Synchrotron Spectrometer”, *Nucl. Instruments Methods Phys. Res.* **195**, 375–379 (1982).
- [4] J. Berkowitz, *Photoabsorption, Photoionization, and Photoelectron Spectroscopy*, Academic Press: New York, p xv-xvi (1979).

## Complete References from main text:

- [20] A. Giuliani, F. Jamme, V. Rouam, F. Wien, J.-L. Giorgetta, B. Lagarde, O. Chubar, S. Bac, I. Yao, S. Rey, C. Herbeaux, J.-L. Marlats, D. Zerbib, F. Polack, M. Réfrégiers, “DISCO: A Low-Energy Multipurpose Beamline at Synchrotron SOLEIL” *J. Synchrotron Rad.* **16**, 835–841 (2009).
- [21] A. Giuliani, I. Yao, B. Lagarde, S. Rey, J.-P. Duval, P. Rommeluere, F. Jamme, V. Rouam, F. Wien, C. de Oliveira, M. Ros, A. Lestrade, K. Desjardins, J.-L. Giorgetta, O. Laprevote, C. Herbaux, M. Refregiers, “A Differential Pumping System to Deliver Windowless VUV Photons at Atmospheric Pressure”, *J. Synchrotron Rad.* **18**, 546–549 (2011).
- [22] M. Refregiers, F. Wien, H.-P. Ta, L. Premvardhan, S. Bac, F. Jamme, V. Rouam, B. Lagarde, F. Polack, J.-L. Giorgetta, J.-P. Ricaud, M. Bordessoule, A. Giuliani, “DISCO Synchrotron-Radiation Circular-Dichroism Endstation at SOLEIL”, *J. Synchrotron Rad.* **19**, 831–835 (2012).



## 6.6. Metallized phospholipid nanodiscs

### “Anisotropic metal growth on phospholipid nanodiscs via lipid bilayer expansion”

*Sci. Rep.* **6**, 26718 (2016).

- Main text: pp. 131–139
- Supplementary Information (SI): pp. 140–141



# SCIENTIFIC REPORTS

OPEN

## Anisotropic metal growth on phospholipid nanodiscs via lipid bilayer expansion

Received: 17 February 2016  
Accepted: 05 May 2016  
Published: 24 May 2016

Jana Oertel<sup>1,\*</sup>, Adrian Keller<sup>2,3,\*</sup>, Julia Prinz<sup>4</sup>, Benjamin Schreiber<sup>2,5</sup>, René Hübner<sup>2</sup>, Jochen Kerbusch<sup>2</sup>, Ilko Bald<sup>4,6</sup> & Karim Fahmy<sup>1,5</sup>

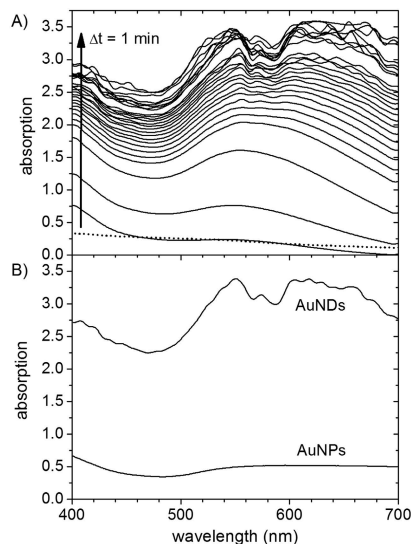
Self-assembling biomolecules provide attractive templates for the preparation of metallic nanostructures. However, the intuitive transfer of the “outer shape” of the assembled macromolecules to the final metallic particle depends on the intermolecular forces among the biomolecules which compete with interactions between template molecules and the metal during metallization. The shape of the bio-template may thus be more dynamic than generally assumed. Here, we have studied the metallization of phospholipid nanodiscs which are discoidal particles of ~10 nm diameter containing a lipid bilayer ~5 nm thick. Using negatively charged lipids, electrostatic adsorption of amine-coated Au nanoparticles was achieved and followed by electroless gold deposition. Whereas Au nanoparticle adsorption preserves the shape of the bio-template, metallization proceeds via invasion of Au into the hydrophobic core of the nanodisc. Thereby, the lipidic phase induces a lateral growth that increases the diameter but not the original thickness of the template. Infrared spectroscopy reveals lipid expansion and suggests the existence of internal gaps in the metallized nanodiscs, which is confirmed by surface-enhanced Raman scattering from the encapsulated lipids. Interference of metallic growth with non-covalent interactions can thus become itself a shape-determining factor in the metallization of particularly soft and structurally anisotropic biomaterials.

In the last two decades, the metallization of biomolecules has received considerable attention as the resulting biomolecule-templated metal nanostructures have great promise for applications in nanoelectronics and plasmonics. A variety of biomolecular complexes including lipid tubules<sup>1</sup>, microtubules<sup>2</sup>, amyloid fibrils<sup>3</sup>, S-layers<sup>4</sup>, and especially DNA<sup>5–11</sup> have been used as templates for metallization. Consequently, a number of techniques have been developed for the deposition of different metals on the biomolecular templates including silver<sup>3,6</sup>, gold<sup>3,8,10</sup>, copper<sup>9</sup>, nickel<sup>1,2</sup>, cobalt<sup>1,2</sup>, platinum<sup>7</sup>, and palladium<sup>4,5,11</sup>. With few exceptions<sup>3</sup>, most of these methods rely on the activation of the biomolecules by a specific immobilization of metal ions, followed by a reduction step which leads to the formation of metallic nanoclusters along the template. These clusters can then be fused together by electroless deposition so that a continuous metallic nanostructure is obtained.

Recently, Schreiber *et al.* reported a different approach that does not rely on a direct binding of metal ions but rather makes use of the negative charge of the DNA backbone to assemble metallic nanoclusters along the DNA strands<sup>12</sup>. To this end, the authors incubated differently shaped DNA nanostructures with positively charged gold nanoparticles (AuNPs) which were then, due to electrostatic interactions with the phosphate groups in the DNA backbone, immobilized on the DNA surface. By electroless gold deposition, the AuNPs could again be fused together, so that DNA-templated AuNPs of defined shape were formed. In this work, we have adapted this approach<sup>12</sup> and applied it to another biomolecular nanostructure of considerable importance, namely phospholipid nanodiscs (NDs).

<sup>1</sup>Institute of Resource Ecology, Helmholtz-Zentrum Dresden-Rossendorf, P.O.B. 510119, 01314 Dresden, Germany.

<sup>2</sup>Institute of Ion Beam Physics and Materials Research, Helmholtz-Zentrum Dresden-Rossendorf, P.O.B. 510119, 01314 Dresden, Germany. <sup>3</sup>Technical and Macromolecular Chemistry, University of Paderborn, Warburger Str. 100, 33098 Paderborn, Germany. <sup>4</sup>Department of Chemistry, University of Potsdam, Karl-Liebknecht-Strasse 24–25, 14476 Potsdam, Germany. <sup>5</sup>Technische Universität Dresden, Mommsenstraße 13, 01069 Dresden, Germany. <sup>6</sup>BAM Federal Institute of Materials Research and Testing, Richard-Willstätter Strasse 11, 12489 Berlin, Germany. \*These authors contributed equally to this work. Correspondence and requests for materials should be addressed to A.K. (email: adrian.keller@uni-paderborn.de) or K.F. (email: k.fahmy@hzdr.de)



**Figure 1.** (A) UV-Vis spectra of AuNDs during electroless deposition recorded at time increments  $\Delta t = 1$  min. The dotted line represents the spectrum of the AuNP-decorated nanodiscs before electroless deposition. (B) UV-Vis spectra of AuNDs and 1.4 nm AuNPs after 21 min of electroless deposition.

Phospholipid NDs are water-soluble planar phospholipid bilayer particles surrounded by two copies of an amphipathic helical protein (membrane scaffold protein, MSP) derived from apolipoprotein ApoA1<sup>13</sup>. NDs exhibit a very well-defined size between 10 and 20 nm depending on the MSP variant used. This allows for the incorporation of single membrane proteins into the NDs<sup>14</sup>. Despite the confinement of the phospholipid bilayer by the MSP, NDs provide a native-like environment for membrane proteins which maintain their native structure and function<sup>15,16</sup>. Therefore, phospholipid NDs represent promising systems for the structural investigation of membrane proteins and their interaction with drug molecules by a variety of spectroscopic techniques including Raman scattering<sup>17</sup> and surface-enhanced infrared spectroscopy (SEIRS)<sup>18</sup>. Furthermore, NDs can also be used as building blocks for the self-assembly of larger hierarchical nanostructures. For instance, DNA-modified NDs have been synthesized by insertion of cholesterol-modified DNA oligonucleotides into the membrane which assembled upon DNA hybridization into wire-like bionanostacks<sup>19</sup>. By utilizing the polyhistidine tag of the MSPs, these bionanostacks could then be used as scaffolds for the controlled arrangement of gold nanoparticles<sup>20</sup>.

Here, we investigate the metallization of NDs and elucidate the fate of the bio-template during metallization by spectroscopic and microscopic techniques. In contrast to DNA, NDs are naturally soft and more fragile due to the confining protein belt, and thus may get deformed and even disrupted during metallization. Therefore, studying the internal structure of the NDs during metallization will be indispensable for understanding the metallization process and potentially exploiting unique features of deformable matrices for the template-directed 2D or 3D growth of metallic layers and especially metal-insulator stacks.

We have followed the metal growth on NDs *in situ* by atomic force, scanning electron, and transmission electron microscopy, as well as optical spectroscopy. Infrared spectroscopy has been employed to detect metallization-induced structural changes of the constituents of the NDs. These investigations reveal that metallization proceeds in the form of a template-directed lateral growth of the AuNPs immobilized on the lipid headgroups which leads to a significant lateral expansion of the ND core. Using infrared spectroscopy and surface-enhanced Raman scattering (SERS) measurements of the AuNDs, we assess their inner structure and demonstrate strong Raman enhancement of the enclosed lipidic phase.

## Results and Discussion

Negatively charged NDs have first been assembled from the MSP variant MSP1D1<sup>21</sup> and negatively charged DMPG (1,2-dimyristoyl-*sn*-glycero-3-phospho-1'-*rac*-glycerol) lipids. The negatively charged DMPG-lipid NDs were then mixed with positively charged amine-coated AuNPs with a diameter of 1.4 nm. Due to the attractive electrostatic interactions with the DMPG head groups, AuNPs got immobilized on both sides of the confined lipid bilayer. After removal of unbound AuNPs by spin filtering, electroless gold deposition was performed and followed *in situ* using UV-Vis spectroscopy. Figure 1A shows the obtained absorption spectra recorded at time increments of  $\Delta t = 1$  min. The absorption is increasing drastically with deposition time at all wavelengths investigated, indicating the continuous deposition of metallic gold. However, the increase of absorption is considerably



slowed down already after a few minutes until almost no further increase is observed for  $t > 20$  min which indicates the depletion of gold ions in the solution. Already after 1 min of deposition, a strong increase of absorption at wavelengths below 440 nm is observed, corresponding to the interband absorption of gold<sup>22</sup>. After 2 min, a second rather broad absorption peak appears around 550 nm, *i.e.*, in the spectral region of the typical plasmon resonances of AuNPs. At longer deposition times, the 550 nm peak becomes narrower and the absorption at wavelengths above 600 nm strongly increases which probably indicates the formation of larger aggregates of AuNDs. The absorption bands measured over the first 10 min scale with the amount of the respective materials and show the successive increase of fully metallized AuNDs in relation to the initially formed metallic gold clusters. At later times, the instrument response saturates, which leads to increased noise and prevents quantitating the formation of aggregates.

Figure 1B compares UV-Vis absorption spectra of AuNDs and pure AuNPs without NDs both after 21 min of electroless deposition. The pure AuNPs show a much lower total absorption and do not exhibit a pronounced plasmon absorption peak. Although the initial amount of gold in solution was identical for the two samples, the colloidal AuNPs have a very small size of 1.4 nm and only a rather small amount of gold was deposited. Since the extinction coefficient of AuNPs in this size range increases about one order of magnitude when the diameter of the particles is doubled<sup>23</sup>, the larger AuNDs also have a much larger extinction. The appearance of the plasmon resonance peaks in the AuND sample is therefore also accompanied by a change of color: the initially clear solution turns purple during deposition when the individual AuNPs are fused together.

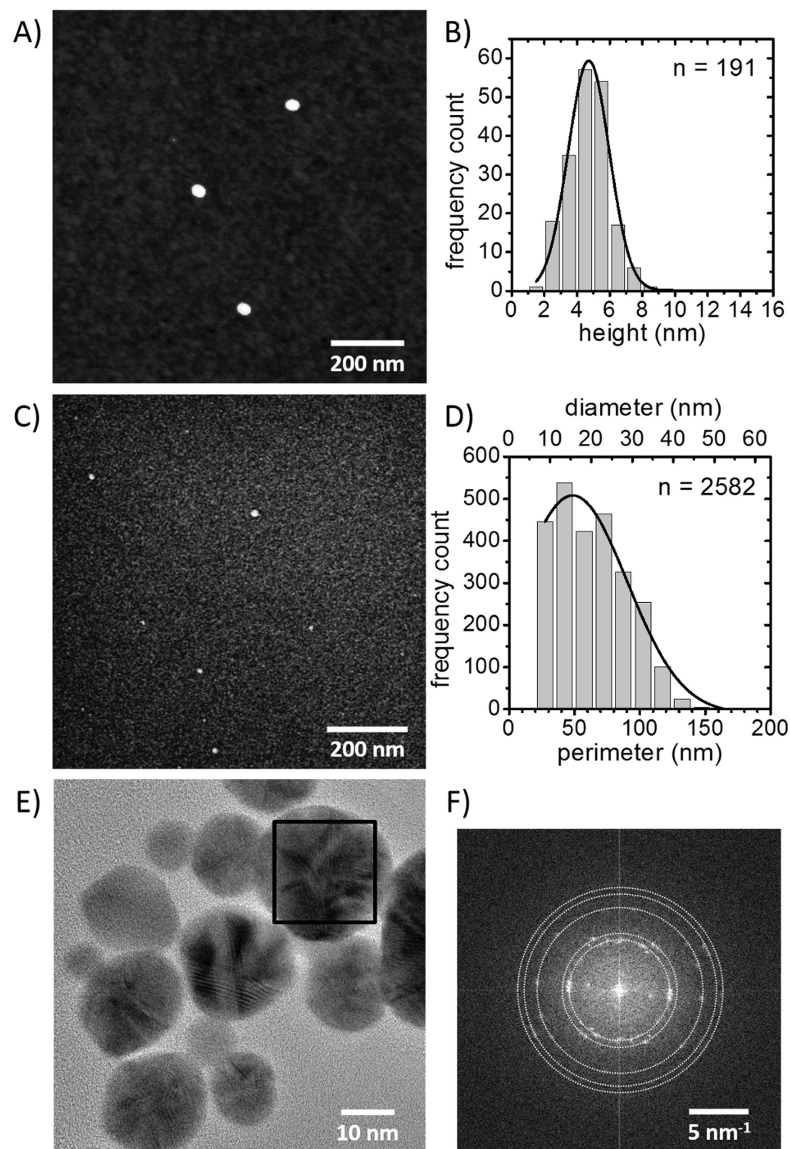
The geometric and crystalline structure of the AuNDs has been assessed by atomic force and electron microscopy. Figure 2A shows an atomic force microscopy (AFM) image of AuNDs immobilized on a silicon surface. Three AuNDs with almost circular shape and similar diameters are clearly observed. Due to the convolution with the AFM tip, however, only the heights of the AuNDs have been determined from the AFM images. The histogram of heights given in Fig. 2B reveals a rather narrow distribution. The Gaussian fit of the distribution indicated by the solid line in Fig. 2B is centered at a height of 4.7 nm and has a full width at half maximum (FWHM) of 2.5 nm. This height value is very similar to the height of non-metallized DMPG-lipid NDs of 5.0 nm as determined by AFM (see Supplementary Information for details) and agrees fairly well with the reported thickness of DMPG bilayers in solution<sup>24</sup>.

In order to accurately characterize the diameter of the AuNDs, scanning electron microscopy (SEM) images of the same sample have been taken. In the SEM image shown in Fig. 2C, AuNDs are clearly resolved due to the high Z contrast between gold and silicon. A stack of 400 individual SEM images has been analyzed to determine the lateral size of the AuNDs. To this end, a lower threshold of 50 nm<sup>2</sup> has been introduced corresponding to a lower AuND diameter of 8 nm, in order to exclude residual free AuNPs from the analysis. The perimeter/diameter histogram and the Gaussian fit shown in Fig. 2D reveal a rather broad distribution centered at a mean AuND diameter of 15.5 nm with a FWHM of 26.5 nm. The fact that AuNDs with diameters larger than 40 nm are observed suggests the presence of aggregates of AuNDs, as already observed in the UV-Vis spectra. Aggregates of a few AuNDs may form during deposition and incubation and get immobilized on the silicon surface. On the other hand, the decoration of the negatively charged DMPG-lipid NDs with the positively charged AuNPs may lead to a local charge inversion on the surface of some of the NDs. This charge inversion might then facilitate the AuNP-mediated aggregation of the NDs prior to electroless deposition.

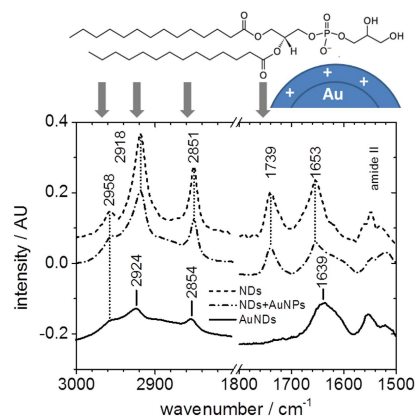
NDs assembled from MSP1D1 exhibit a mean diameter of 9.7 nm as determined by small angle X-ray scattering<sup>21</sup>. Therefore, the rather dominant peak of the size distribution in Fig. 2D at a diameter of 15.5 nm most likely corresponds to the diameter of the AuND monomer. This increase in diameter by ~6 nm is particularly noteworthy as no increase in ND thickness is observed by AFM (Fig. 2B).

The crystalline structure of the AuNDs has been assessed by high-resolution transmission electron microscopy (HR-TEM). The HR-TEM image in Fig. 2E shows AuNDs of different size. The microstructure of the AuNDs can be clearly resolved, revealing their polycrystalline nature. This is even more evident from the Fast Fourier Transform (FFT) given in Fig. 2F, which has been calculated from the square region indicated in the TEM image, *i.e.*, from a single AuND. The FFT consists of several spots arranged on concentric circles evidencing the existence of several crystallites in a single AuND. In particular, the observed spots correspond to lattice spacings of 2.35 Å, 2.04 Å, 1.45 Å, 1.24 Å, and 1.16 Å, which can be assigned to the (111), (200), (220), (311), and (222) lattice planes of gold, respectively. Interference of lattice fringes from two crystallites can lead to Moiré fringes, explaining the two inner peaks in the FFT corresponding to a spacing of 3.79 Å. Although the growth of the AuNPs due to electroless gold deposition proceeds epitaxially<sup>25</sup>, the fact that the AuNPs are immobilized with random orientation on the ND leads to the formation of grains and thus polycrystalline AuNDs.

The state of the organic material within the AuNDs was assessed by attenuated total reflection Fourier transform infrared (ATR-FTIR) spectroscopy. As can be seen in Fig. 3, the association of AuNPs with the DMPG-reconstituted NDs does not cause significant changes in the infrared absorption spectrum. The lipid ester and the amide I absorption peaks at 1739 cm<sup>-1</sup> and 1653 cm<sup>-1</sup>, respectively, are visible in both preparations. Likewise, the symmetric (2851 cm<sup>-1</sup>) and antisymmetric (2918 cm<sup>-1</sup>) CH<sub>2</sub> stretching modes are not affected by the electrostatic association of the NDs with the AuNPs. In contrast, extensive spectral changes are observed after electroless gold deposition. The lipid ester carbonyl stretching mode has almost completely disappeared which is indicative of the quenching of its transition dipole moment. Polarization-dependent selection rules of vibrational modes near metallic surfaces<sup>26</sup> can lead to strong alterations of the relative intensities of absorption bands as is known from reflection absorption infrared spectroscopy of lipids on gold support<sup>27</sup>. Only those vibrational modes are observed that have a transition dipole moment perpendicular to the metal surface. Also the CH<sub>2</sub> stretching modes are affected by the metallization. The peak intensity is again reduced and an increased frequency of the symmetric and antisymmetric stretching modes observed. Such a frequency up-shift is typical of decreased packing interactions between acyl chains<sup>28</sup>. Remarkably, the frequency of the antisymmetric CH<sub>2</sub> stretching mode of the acyl chain termini at 2958 cm<sup>-1</sup> is affected neither by electrostatic adsorption of Au nanoparticles nor by



**Figure 2. Structural characterization of the AuNDs.** (A) AFM image of AuNDs (height scale 6 nm) and (B) corresponding histogram of the AuND height. The solid line in (B) corresponds to a Gaussian fit yielding a mean AuND height of 4.7 nm and a FWHM of 2.5 nm. A total of  $n = 191$  AuNDs have been analyzed. (C) SEM image of AuNDs and (D) corresponding histogram of the AuND perimeter/diameter. The solid line in (D) corresponds to a Gaussian fit yielding a mean AuND diameter of 15.5 nm and a FWHM of 26.5 nm. A total of  $n = 2582$  AuNDs have been analyzed. (E) HR-TEM image of AuNDs. (F) Fast Fourier Transform (FFT) of the square region indicated in (E). As a guide to the eye, the Au diffraction rings are marked by dotted circles.

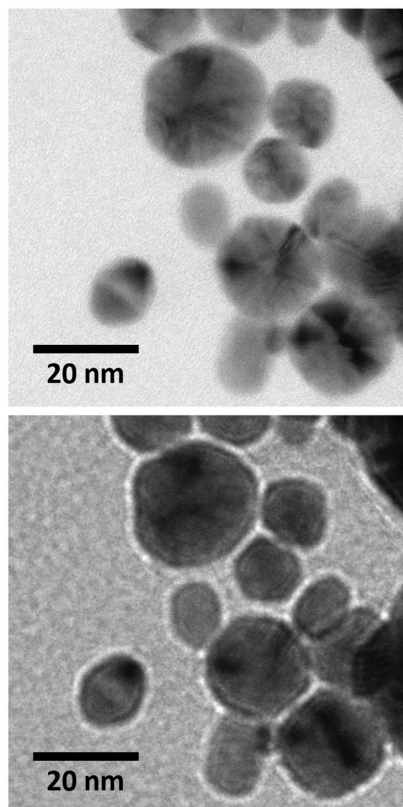


**Figure 3.** ATR-FTIR spectra of NDs at different stages of the metallization process: pure non-metallized NDs (broken line), NDs with immobilized AuNPs before gold deposition (dash-dotted line), fully metallized AuNDs (solid line). All spectra are corrected for background absorption of the respective buffer solutions. The amide II absorption range is shown for completeness but variability in buffer absorption in this range prevents a more precise frequency assignment. The chemical structure of DMPG is shown on top of the spectra. Arrows indicate the IR-spectral range in which the structural elements show major absorption bands. The putative local interaction with positively charged gold particles before electroless metal deposition is symbolized by the blue sphere.

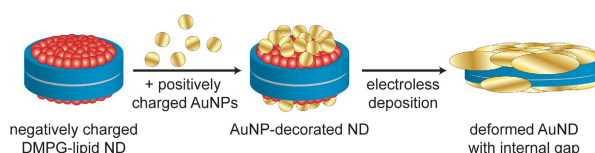
the electroless Au depositions. This suggests that the acyl chain ends in the center of the bilayer do not form inter-leafed structures or become exposed to aqueous or metallic phases during the metallization process. Finally, the broadening and the shift of the amide I mode from 1653 to 1639  $\text{cm}^{-1}$  evidences the unfolding of the helical secondary structure of the MSP. The ensemble of the spectral changes suggests an invasion of metallic gold into the sub-headgroup region of the lipids, thereby pushing acyl chains apart. As a consequence of this lateral expansion, the MSP gets stretched longitudinally, leading to the unfolding of its helical structure. In this picture, gold grows predominantly in a lateral manner between lipid headgroups but also towards the center of the bilayer, such that the acyl methylene absorption becomes partially suppressed. Remarkably, the growth proceeds without increasing the thickness of the NDs as observed by AFM (Fig. 2A,B). This demonstrates that the original bilayer thickness, rather than its circumference, is the predominant template dimension that governs metal growth and which becomes inherited by the final metallic particles. The evidenced preservation of organic material in the AuNDs, however, raises the question to which extent non-metallic voids or gaps persist in the AuNDs.

In an attempt to verify the presence of internal gaps in the AuNDs as suggested by the ATR-FTIR spectra in Fig. 3, the so-called Fresnel contrast has been utilized in TEM imaging<sup>29</sup>. In this imaging mode, Fresnel fringes can be generated wherever the inner potential of the sample changes abruptly by imaging this particular region out of focus. Hence, this technique is particularly useful for imaging voids and embedded bubbles. Figure 4 shows TEM images of the same sample region imaged in focus and with an underfocus of 1.5  $\mu\text{m}$ . In the latter image, Fresnel fringes are clearly visible surrounding the shapes of the AuNDs. Directly inside the AuNDs, however, no clear fringes are visible. There are thus no distinct hints for pores inside the AuNDs. However, disc-shaped internal gaps within sandwich-like Au structures do not provide a strong change in the inner potential and can thus not be resolved by this technique. Therefore, Fresnel imaging in combination with the FTIR results suggests that the AuNDs consist of two parallel gold discs that have partially grown into the membrane region and are separated by a small gap centered at the interface of the two lipid leaflets.

The pathway of ND metallization as deduced from above experimental data is summarized in Fig. 5. Positively charged AuNPs of 1.4 nm diameter are immobilized on both surfaces of the confined DMPG-lipid bilayer due to electrostatic interactions with the negatively charged lipid headgroups. This immobilization affects neither the MSP structure nor the state of the lipids within the NDs as observed in the ATR-FTIR spectra in Fig. 3. During electroless deposition, the immobilized AuNPs grow in size and fuse together. However, instead of isotropic AuNP growth in all directions, the microscopic and spectroscopic data suggest a template-directed lateral growth which leads to a significant increase in ND diameter from about 9.7 to 15.5 nm while the thickness remains largely unaffected (see Fig. 2A–D). Since the observed shift in the amide I band to lower wavenumbers evidences the denaturation of the MSP due to metallization, it appears likely that this lateral growth of the AuNPs leads to a deformation of the ND core of the AuND as depicted in Fig. 5. Although the ATR-FTIR spectra further show the growth of the AuNPs into the membrane region, growth stops before a fully metallized AuND is formed, leaving the AuNDs with an internal, probably lipid-containing, gap. The lack of clear Fresnel fringes inside the AuNDs in



**Figure 4.** Bright-field TEM images of AuNDs taken in focus (upper image) and with an underfocus of  $1.5\ \mu\text{m}$  (lower image).



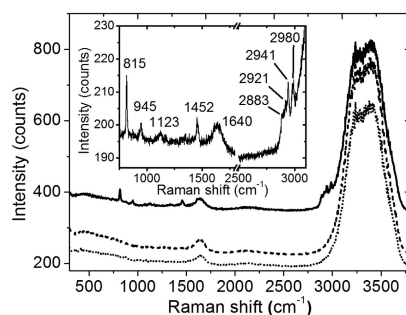
**Figure 5.** Pathway of ND metallization resulting in deformed AuNDs with internal gaps.

the TEM image of Fig. 4 further suggests that this internal gap is not fully embedded in the grown gold matrix but rather represents a thin spacer between two approximately parallel gold discs of about 2 nm thickness.

Similar nanoscale gaps have been observed after electroless deposition onto DNA coated AuNPs<sup>30</sup>. The resulting Au@Au core@shell nanoparticles exhibiting internal gaps of about 1 nm thickness were found to be SERS active due to a strong electromagnetic field enhancement in the nanogaps upon laser irradiation. Therefore, we performed Raman measurements on native NDs and metallized AuNDs in order to evaluate whether the AuNDs are SERS active.

The obtained Raman spectrum of the non-metallized NDs (broken line in Fig. 6) consists of some very intense peaks in the range from about  $2900\ \text{cm}^{-1}$  to about  $3700\ \text{cm}^{-1}$  and a small peak at  $1640\ \text{cm}^{-1}$ , which are identified as OH stretching and bending modes of water and TRIS in the buffer. An almost identical spectrum is obtained for pure buffer without any NDs (dotted line in Fig. 6). In the case of the metallized AuNDs (solid line in Fig. 6),

www.nature.com/scientificreports/



**Figure 6.** Raman spectra of AuNDs (~320 nM, solid line), non-metallized DMPG-lipid NDs (400 nM, broken line), and pure buffer (dotted line) obtained under the same conditions. The inset shows the relevant parts of the AuND Raman spectrum at high resolution with the wavenumbers of the individual Raman peaks indicated. The excitation wavelength was 532 nm.

however, several additional peaks are observed in the spectral regions from  $800\text{ cm}^{-1}$  to  $1500\text{ cm}^{-1}$  and from  $2800\text{ cm}^{-1}$  to  $3000\text{ cm}^{-1}$  which are characteristic for phospholipids<sup>31</sup>. The bands at  $2800\text{ cm}^{-1}$  to  $3000\text{ cm}^{-1}$  correspond to the CH stretching modes of the methylene groups, and the pronounced band at  $1452\text{ cm}^{-1}$  is assigned to the  $\text{CH}_2$  scissoring mode<sup>31</sup>. The signal around  $1123\text{ cm}^{-1}$  consists most likely of different contributions and is attributed to C-C and  $\text{PO}_2^-$  stretching modes. The bands at  $815$  and  $945\text{ cm}^{-1}$  originate most likely from the MSP. The band at  $945\text{ cm}^{-1}$  can be attributed to the N-C<sub>α</sub>-C mode while the band at  $815\text{ cm}^{-1}$  might originate from tyrosine<sup>32</sup>. Since these modes are not observed in non-metallized NDs and taking further into account that the AuNDs were slightly less concentrated, the appearance of these peaks results from a Raman enhancement in the gap region of the metallized DMPG-lipid NDs. This Raman enhancement thus is further evidence for the presence of internal gaps in the AuNDs.

### Conclusion

In the present work, DMPG-lipid NDs have been metallized using electroless gold deposition with colloidal AuNPs as seeds. The seeding process was enabled by the electrostatic interaction of the positively charged AuNPs with the negatively charged DMPG headgroups. UV-Vis spectroscopy revealed the rapid growth of the AuNDs within the first few minutes of deposition, while growth arrest was observed after about 20 min due to the depletion of ionic gold in the solution. The ND efficiently restricts metallization to two-dimensional growth by a mechanism that involves the expansion of the hydrophobic core of the particle at essentially constant thickness. Lateral deformability appears to be the crucial factor for the anisotropic metallization. The obtained discoidal AuNDs are polycrystalline and have a mean height and diameter of 4.7 nm and 15.5 nm, respectively, as determined by atomic force and electron microscopy. The AuNDs furthermore exhibit significant Raman enhancement of the enclosed lipidic phase and thus represent attractive SERS-active substrates.

### Methods

**Assembly of negatively charged DMPG-lipid nanodiscs.** The protocol for the phospholipid nanodisc assembly was adapted from the original publication<sup>13</sup>. In order to enable the metallization of the nanodiscs, however, negatively charged 1,2-dimyristoyl-*sn*-glycero-3-phospho-(1'-*rac*-glycerol) (DMPG; Avanti Lipids) was used. A completely dried DMPG lipid film was solubilized in buffer A, containing cholate as detergent twice the concentration of the lipid, and sonicated until a clear solution was obtained. The respective lipid/sodium cholate solution and MSP1D1 (see Supplementary Information) were mixed to yield a final concentration of 12 mM lipid and 0.2 mM MSP1D1. The mixture was incubated for 1 h at 25 °C. The detergent was removed by Detergent Removal spin columns (Pierce). The size and the homogeneity of the DMPG-lipid NDs were verified by size exclusion chromatography (see Figure S1).

**Metallization of DMPG-lipid nanodiscs.** The metallization process of phospholipid nanodiscs was adapted from the protocol of Schreiber *et al.* who applied it to DNA origami nanostructures<sup>12</sup>. For the whole metallization procedure, buffer A was used in a 1:10 dilution (5 mM Tris-HCl, 20 mM NaCl, pH 7.4). Negatively charged DMPG-lipid nanodiscs (400 nM) were incubated with positively charged, amine-coated 1.4 nm nanogold particles (Nanoprobes) at a final concentration of 1.5 μM for one hour at room temperature. After incubation, the sample was spin filtered twice through an Amicon Ultra-0.5 mL filter (100 kDa MWCO, Millipore) to remove excess nanogold and diluted 1:5 in buffer A to get a final concentration of approximately 100 nM nanodiscs decorated with Au-particles. The controlled growth of the nanogold particles was achieved by electroless gold deposition from solution using the gold enhancement kit (GoldEnhance LM, Nanoprobes) following the instructions of the supplier and mixed 1:1 with the Au-seeded nanodisc sample.

**UV-Vis spectroscopy.** The metallization process was monitored over time with a Lambda 35 UV-Vis spectrometer (Perkin Elmer) in the wavelength range between 400 and 700 nm using quartz cuvettes with a path length of 1 cm. The absorption spectra from Au-seeded nanodiscs without gold enhancement and the enhancement mixture without nanodiscs were recorded as controls and buffer A as reference.

**Atomic force microscopy.** The successful assembly of DMPG-lipid nanodiscs has been verified by atomic force microscopy (AFM). For immobilization, the DMPG-lipid nanodisc sample was diluted 1:10 in buffer A, then mixed 1:25 with 10 mM MgCl<sub>2</sub> solution and incubated for 3 min on a freshly cleaved mica substrate. After incubation, the sample was rinsed with Milli-Q water and dried in a stream of nitrogen. For the AFM and scanning electron microscopy (SEM) characterization of the metallized nanodiscs, silicon wafers were used as substrates. Directly before immobilization, the substrates were cleaned for 3 min in an oxygen plasma, rinsed with ethanol and Milli-Q water, and dried in a stream of nitrogen. The metallized nanodisc sample was mixed 1:1 with 10 mM MgCl<sub>2</sub> and incubated on the silicon wafer for at least one hour in a humidity chamber. The wafer was then carefully rinsed with Milli-Q water and dried in a stream of nitrogen. AFM imaging was performed using a Bruker Multimode8 scanning probe microscope operated in tapping mode in air. Tap150Al-G soft tapping cantilevers (Budget Sensors) were used with a nominal force constant of 5 N/m, a resonance frequency of 150 kHz, and a tip radius <10 nm. The AFM images were analyzed using Gwyddion image processing software<sup>33</sup>.

**Scanning electron microscopy.** Scanning electron microscopy (SEM) was performed using a RAITH 150<sup>TWO</sup> electron beam writer. A total of 400 images was recorded using the Inlens-SE detector. The images were arranged in a 20 × 20 matrix with 2 μm center-to-center distance between each image. A magnification of 100 000 and a beam energy of 10 keV was used. To determine the diameters of the individual nanodiscs, an automated particle analysis was performed with WCIF-ImageJ<sup>34</sup>. To this end, the images were converted into binary images by introducing a grayscale threshold of 130. Then the perimeters of the particles with areas between 50 and 1300 nm<sup>2</sup> were determined and converted into diameters assuming circular shapes.

**Transmission electron microscopy.** Samples for transmission electron microscopy (TEM) were prepared by incubating a drop of metallized nanodiscs on a carbon-coated (15 nm thickness) copper grid for several minutes. After incubation, excess liquid was blotted away with a tissue and the grid was air dried. TEM images were obtained using an image-corrected FEI Titan 80–300 microscope operated at 300 kV accelerating voltage.

**Fourier transform infrared spectroscopy.** Spectra were recorded with an IFS 66v spectrometer (Bruker) equipped with a liquid nitrogen-cooled MCT detector. Samples (10 μL of pure NDs, AuNP-decorated NDs, and metallized AuNDs) were dried on a diamond attenuated total reflectance (ATR) cell (Resultec). The 1:10 diluted buffer A (5 mM Tris-HCl, 20 mM NaCl, pH 7.4) was used as reference for the pure and the AuNP-decorated NDs while as the AuND reference, a sample of AuNPs incubated with gold enhancement solution was used. 256 interferograms were recorded at a resolution of 2 cm<sup>-1</sup> and averaged to obtain absorption spectra in reference to the pure ATR crystal.

**Raman spectroscopy.** For Raman measurements a drop of the corresponding was applied to a freshly cleaned glass slide. Raman measurements have been performed using a confocal Raman microscope (WITec 300α) equipped with an upright optical microscope. The excitation laser light at 532 nm was coupled into a single-mode optical fiber and focused through a 100x objective (Olympus MPlanFL N, NA = 0.9) to a diffraction-limited spot of about 1.3 μm<sup>2</sup>. The laser power was set to 13 mW and the integration time was 10 s for all measurements. Each spectrum has been obtained by an average of three accumulations. The spectra that cover a broad range of wavenumbers have been recorded using a grating with 600 g/mm whereas for the more detailed measurement a grating with 1800 g/mm has been used.

## References

1. Markowitz, M., Baral, S., Brandow, S. & Singh, A. Palladium ion assisted formation and metallization of lipid tubules. *Thin Solid Films* **224**, 242–247 (1993).
2. Mertig, M., Kirsch, R. & Pompe, W. Biomolecular approach to nanotube fabrication. *Appl. Phys. A* **66**, S723–S727 (1998).
3. Scheibel, T. *et al.* Conducting nanowires built by controlled self-assembly of amyloid fibers and selective metal deposition. *Proc. Natl. Acad. Sci.* **100**, 4527–4532 (2003).
4. Aichmayer, B., Mertig, M., Kirchner, A., Paris, O. & Fratzl, P. Small-Angle Scattering of S-Layer Metallization. *Adv. Mater.* **18**, 915–919 (2006).
5. Geng, Y. *et al.* Rapid metallization of lambda DNA and DNA origami using a Pd seeding method. *J. Mater. Chem.* **21**, 12126 (2011).
6. Braun, E., Eichen, Y., Sivan, U. & Ben-Yoseph, G. DNA-templated assembly and electrode attachment of a conducting silver wire. *Nature* **391**, 775–778 (1998).
7. Ford, W. E., Harnack, O., Yasuda, A. & Wessels, J. M. Platinated DNA as Precursors to Templated Chains of Metal Nanoparticles. *Adv. Mater.* **13**, 1793–1797 (2001).
8. Keren, K., Berman, R. S., Buchstab, E., Sivan, U. & Braun, E. DNA-templated carbon nanotube field-effect transistor. *Science* **302**, 1380–1382 (2003).
9. Monson, C. F. & Woolley, A. T. DNA-Templated Construction of Copper Nanowires. *Nano Lett.* **3**, 359–363 (2003).
10. Patolsky, F., Weizmann, Y., Lioubashevski, O. & Willner, I. Au-Nanoparticle Nanowires Based on DNA and Polylysine Templates. *Angew. Chem. Int. Ed.* **41**, 2323–2327 (2002).
11. Richter, J. *et al.* Nanoscale Palladium Metallization of DNA. *Adv. Mater.* **12**, 507–510 (2000).
12. Schreiber, R. *et al.* DNA origami-templated growth of arbitrarily shaped metal nanoparticles. *Small* **7**, 1795–1799 (2011).
13. Bayburt, T. H., Grinkova, Y. V. & Sligar, S. G. Self-Assembly of Discoidal Phospholipid Bilayer Nanoparticles with Membrane Scaffold Proteins. *Nano Lett.* **2**, 853–856 (2002).
14. Bayburt, T. H. & Sligar, S. G. Self-assembly of single integral membrane proteins into soluble nanoscale phospholipid bilayers. *Protein Sci.* **12**, 2476–2481 (2003).
15. Bayburt, T. H. & Sligar, S. G. Membrane protein assembly into Nanodiscs. *FEBS letters* **584**, 1721–1727 (2010).

16. Knepp, A. M., Sakmar, T. P. & Huber, T. Homogeneous time-resolved fluorescence assay to probe folded G protein-coupled receptors. *Methods in enzymology* **522**, 169–189 (2013).
17. Mak, P. J., Denisov, I. G., Grinkova, Y. V., Sligar, S. G. & Kincaid, J. R. Defining CYP3A4 structural responses to substrate binding. Raman spectroscopic studies of a nanodisc-incorporated mammalian cytochrome P450. *J. Am. Chem. Soc.* **133**, 1357–1366 (2011).
18. Zaitseva, E., Saavedra, M., Banerjee, S., Sakmar, T. P. & Vogel, R. SEIRA spectroscopy on a membrane receptor monolayer using lipoprotein particles as carriers. *Biophysical journal* **99**, 2327–2335 (2010).
19. Beales, P. A. *et al.* Reversible assembly of stacked membrane nanodiscs with reduced dimensionality and variable periodicity. *J. Am. Chem. Soc.* **135**, 3335–3338 (2013).
20. Geerts, N. *et al.* Using DNA-driven assembled phospholipid nanodiscs as a scaffold for gold nanoparticle patterning. *Langmuir* **29**, 13089–13094 (2013).
21. Denisov, I. G., Grinkova, Y. V., Lazarides, A. A. & Sligar, S. G. Directed self-assembly of monodisperse phospholipid bilayer Nanodiscs with controlled size. *J. Am. Chem. Soc.* **126**, 3477–3487 (2004).
22. Etchegoin, P. G., Le Ru, E. C. & Meyer, M. An analytic model for the optical properties of gold. *J. Chem. Phys.* **125**, 164705 (2006).
23. Liu, X., Atwater, M., Wang, J. & Huo, Q. Extinction coefficient of gold nanoparticles with different sizes and different capping ligands. *Colloids Surf. B Biointerfaces* **58**, 3–7 (2007).
24. Riske, K. A., Amaral, L. Q. & Lamy-Freund, M. Thermal transitions of DMPG bilayers in aqueous solution: SAXS structural studies. *Biochim. Biophys. Acta-Biomembranes* **1511**, 297–308 (2001).
25. Sau, T. K. & Murphy, C. J. Room temperature, high-yield synthesis of multiple shapes of gold nanoparticles in aqueous solution. *J. Am. Chem. Soc.* **126**, 8648–8649 (2004).
26. Greenler, R. G. Infrared Study of Adsorbed Molecules on Metal Surfaces by Reflection Techniques. *J. Chem. Phys.* **44**, 310 (1966).
27. Anderson, M. R., Ewaniak, M. N. & Zhang, M. Influence of Solvent on the Interfacial Structure of Self-Assembled Alkanethiol Monolayers. *Langmuir* **12**, 2327–2331 (1996).
28. Binder, H., Dietrich, U., Schalke, M. & Pfeiffer, H. Hydration-Induced Deformation of Lipid Aggregates before and after Polymerization. *Langmuir* **15**, 4857–4866 (1999).
29. Williams, D. B. & Carter, C. B. *Transmission electron microscopy. A textbook for materials science.* 2nd ed. (Springer, New York, 2009).
30. Lim, D.-K. *et al.* Highly uniform and reproducible surface-enhanced Raman scattering from DNA-tailorable nanoparticles with 1-nm interior gap. *Nature Nanotechnol.* **6**, 452–460 (2011).
31. Wong, P. T. T. Raman spectroscopy of thermotropic and high-pressure phases of aqueous phospholipid dispersions. *Ann. Rev. Biophys. Bioeng.* **13**, 1–24 (1984).
32. Rygula, A. *et al.* Raman spectroscopy of proteins: a review. *J. Raman Spectrosc.* **44**, 1061–1076 (2013).
33. Nečas, D. & Klapetek, P. Gwyddion: an open-source software for SPM data analysis. *centr.eur.j.phys.* **10**, 181–188 (2012).
34. Rasband, W. S. ImageJ, Image Processing and Analysis in Java: National Institutes of Health, Bethesda, Maryland, USA, <http://rsb.info.nih.gov/ij/> (1997–2004) (date of access 25/10/2014) via <http://www.uhnresearch.ca/facilities/wcif/imagej/>.

#### Acknowledgements

This research was supported by a Marie Curie FP7 Integration Grant within the 7th European Union Framework Programme and the Deutsche Forschungsgemeinschaft (DFG).

#### Author Contributions

J.O., A.K., I.B. and K.F. conceived the experiments, J.O., A.K., J.P., R.H. and J.K. conducted the experiments, J.O., A.K., J.P., B.S., R.H., J.K., I.B. and K.F. analyzed the results, and J.O., A.K., I.B. and K.F. wrote the manuscript. All authors reviewed the manuscript.

#### Additional Information

**Supplementary information** accompanies this paper at <http://www.nature.com/srep>

**Competing financial interests:** The authors declare no competing financial interests.

**How to cite this article:** Oertel, J. *et al.* Anisotropic metal growth on phospholipid nanodiscs via lipid bilayer expansion. *Sci. Rep.* **6**, 26718; doi: 10.1038/srep26718 (2016).



This work is licensed under a Creative Commons Attribution 4.0 International License. The images or other third party material in this article are included in the article's Creative Commons license, unless indicated otherwise in the credit line; if the material is not included under the Creative Commons license, users will need to obtain permission from the license holder to reproduce the material. To view a copy of this license, visit <http://creativecommons.org/licenses/by/4.0/>

## Supplementary Information

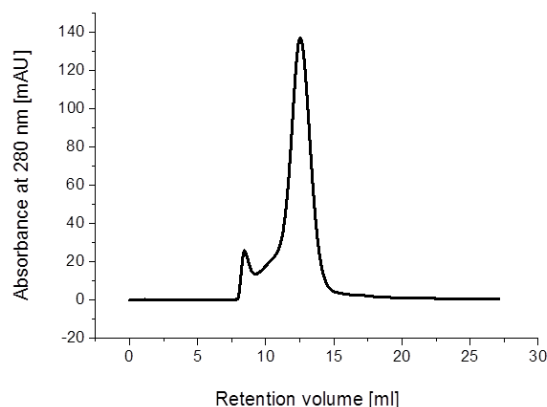
### “Anisotropic metal growth on phospholipid nanodiscs via lipid bilayer expansion”

#### Expression and purification of MSP1D1

The standard expression of MSP1D11 was adapted from literature. [2] Briefly, the MSP1D1-pET28a plasmids were grown over night in BL21Gold (DE3) cells (Agilent Technologies) at 37 °C in double strength YT medium containing 50 µg/mL kanamycin. After induction with 0.3 mM isopropyl- $\beta$ -D-thiogalactopyranoside, the temperature was decreased to 28 °C. The cells were harvested 4 h later, frozen in liquid nitrogen, and stored at -80 °C until further use. For purification, cells were resuspended in buffer A (50 mM Tris-HCl, 200 mM NaCl, pH 7.4) containing protease inhibitors (Roche Applied Science) and lysed twice with a French Press. Cell debris was removed by centrifugation (10 000 *g*, 50 min, 4 °C). Imidazole was added to the supernatant to a final concentration of 25 mM. The sample was loaded onto a Ni-NTA column (GE-Healthcare), equilibrated with buffer B (buffer A containing 25 mM imidazole). The column was washed with buffer B, and the protein was eluted with 5 mL buffer C (buffer A containing 250 mM imidazole), followed by 5 mL buffer D (buffer A containing 500 mM imidazole). Fractions containing MSP1D1 were identified by SDS-PAGE. Imidazole was removed by a desalting step (PD10 column, equilibrated with buffer A; GE Healthcare) and concentrated using Vivaspın4 columns (Satorius). The final protein concentration was determined by measuring the absorbance at 280 nm with a NanoDrop spectrophotometer using a calculated extinction coefficient of 21430 M<sup>-1</sup> cm<sup>-1</sup> and a calculated molecular weight of 24.793 kDa (ProtParam, ExpASy). Purified MSP1D1 was frozen in liquid nitrogen and stored at -80 °C until further use.

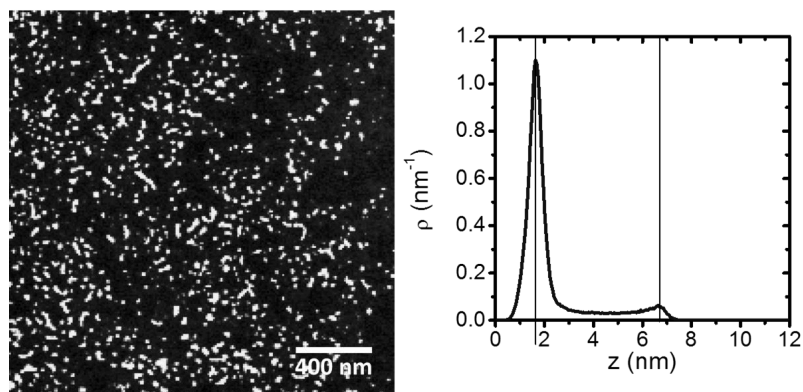
#### Characterization of non-metallized DMPG-lipid nanodiscs

The size and the homogeneity of the DMPG-lipid NDs were verified by size exclusion chromatography (Figure S1) and AFM (Figure S2). The mean height of the non-metallized DMPG-lipid nanodiscs was determined from the height distribution function of the AFM image which exhibits two peaks (see Figure S2, right). The peak at a height of about 1.6 nm corresponds to the bare mica surface while the one at about 6.6 nm corresponds to the nanodiscs. The difference of these peaks thus yields the mean height of the non-metallized nanodiscs, i.e., 5.0 nm, which is very similar to the reported thickness of DMPG bilayers in solution. [3]



**Figure S1:** Size exclusion chromatogram of DMPG-lipid NDs, monitoring the protein absorbance of MSP1 at 280 nm. NDs eluted at  $V = 11.5\text{--}13.5$  mL, while lipid-protein aggregates eluted at  $V = 8.3\text{--}9.1$  mL. A Superdex 200 10/300 GL column from GE Healthcare was used.





**Figure S2:** AFM image of non-metallized DMPG-lipid nanodiscs (height scale 8 nm) and corresponding height distribution function. The vertical lines give the values of the mica (1.6 nm) and the nanodisc height (6.6 nm).

## References

- [1] I. G. Denisov, Y. V. Grinkova, A. A. Lazarides, S. G. Sligar, “Directed self-assembly of monodisperse phospholipid bilayer Nanodiscs with controlled size”, *J. Am. Chem. Soc.* **126**, 3477–3487 (2004).
- [2] S. Inagaki *et al.*, “Modulation of the interaction between neurotensin receptor NTS1 and Gq protein by lipid”, *J. Mol. Biol.* **417**, 95–111 (2012).
- [3] K. A. Riske, L. Q. Amaral, M. Lamy-Freund, “Thermal transitions of DMPG bilayers in aqueous solution: SAXS structural studies”, *Biochim. Biophys. Acta - Biomembranes* **1511**, 297–308 (2001).



## 6.7. Gold nanolenses

### “Gold-nanolenses self-assembled by DNA origami”

*submitted manuscript.*

- Main text: pp. 145–159
- Supporting Information (SI): pp. 160–164



## Gold nanolenses self-assembled by DNA origami

Christian Heck<sup>a,b,c</sup>, Julia Prinz<sup>a</sup>, André Dathe<sup>d</sup>, Virginia Merk<sup>c</sup>, Ondrej Stranik<sup>d</sup>, Wolfgang Fritzsche<sup>d</sup>, Janina Kneipp<sup>b,c</sup>, Ilko Bald<sup>a,b,\*</sup>

<sup>a</sup>University of Potsdam, Department of Chemistry, Karl-Liebknecht-Str. 24-25, 14476 Potsdam, Germany;

<sup>b</sup>BAM Federal Institute for Materials Research and Testing, Richard-Willstätter-Str. 11, 12489 Berlin, Germany;

<sup>c</sup>Humboldt Universität zu Berlin, Department of Chemistry & SALSA, Brook-Taylor-Str. 2, 12489 Berlin, Germany;

<sup>d</sup>IPHT Jena, Albert-Einstein-Straße 9, 07745 Jena, Germany.

\*ilko.bald@uni-potsdam.de

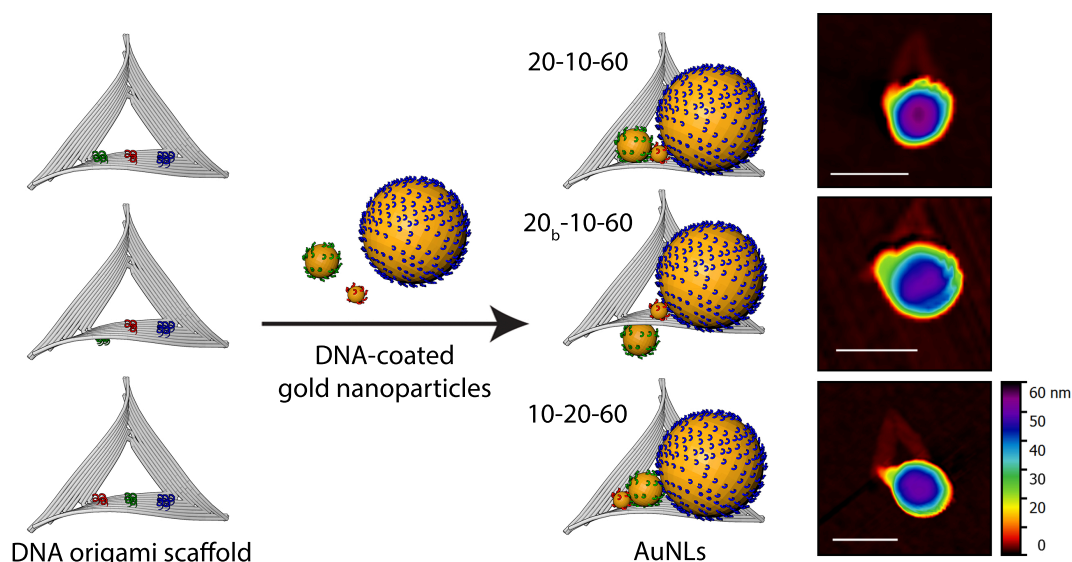
### Abstract

Here, we present a bottom-up approach to create plasmonic gold nanolenses (AuNLs), consisting of three differently-sized gold nanoparticles. The programmable technique of DNA origami is used to self-assemble 10, 20 and 60 nm gold nanoparticles in three different geometrical arrangements in solution and in billions of copies. Correlated atomic force microscopy (AFM), Raman mapping, scanning electron microscopy (SEM) and dark field spectroscopy are used to characterise sets of single AuNLs from each of the three designs. The surface-enhanced Raman scattering (SERS) capabilities of single AuNLs are assessed and the same AuNLs are further characterised by localised surface plasmon resonance (LSPR) spectroscopy. For the design which showed best properties, SERS signals from the two different internal gaps were compared by selectively placing probe dyes. The highest Raman enhancement was found for the gap between the small and medium nanoparticle, which agrees well with theoretical predictions.

Assemblies of plasmonic nanoparticles are promising building blocks in the development of nanoscopic optical devices: They can guide light [1] and focus it [2] at scales far below the diffraction limit. Upon irradiation with light of their resonance wavelength, localised surface plasmons are excited in plasmonic nanoparticles, which amplifies the electromagnetic field in their proximity. If two or more nanoparticles are in close proximity, the individual surface plasmons can couple and create spots of very high field intensity. [3–6] High local fields can be exploited for the enhancement of signals in Raman [7–9], infrared [10,11] and fluorescence spectroscopy [12,13]. In order to build efficient plasmonic nanostructures and to learn more about the basic principles of the signal enhancement in different processes and molecules or materials, control over relative positioning and type of the constituent nanoparticles is needed. [14,15] Collinear assemblies of self-similar gold nanoparticle chains (so-called *gold nanolenses*, AuNLs) are particularly interesting plasmonic objects. [16–19] Due to their incremental architecture, a cascaded enhancement of the electromagnetic field was predicted [20,21] and demonstrated. [22]

In the case of gold nanoparticles, highly versatile interactions with organic molecules can be exploited to control their positions and interaction. Thanks to the programmable nature of DNA-DNA interaction, DNA nanotechnology [23], and namely scaffolded DNA origami [24], have developed into key technologies for self-assembling nanocomponents of many kinds. [25,26] Gold nanoparticles that have been coated with DNA strands [27,28] can be bound at defined positions on such DNA origami scaffolds. [29–32] When orthogonal coating strand sequences are chosen, different nanoparticles can be programmed to bind at specific positions. By using this self-assembly principle, we present a bottom-up technique to synthesise AuNLs in solution in billions of copies, in contrast to typical top-down methods. [33] Several approaches that use DNA origami to assemble metal nanoparticle homomers for surface-enhanced Raman scattering (SERS) measurements have been reported [34–37], utilizing two to four nanoparticles of the same kind, and recently reaching single molecule sensitivity. [38] In the structures discussed here, we introduce a further dimension of complexity by controlling not just positions, but also relative sizes of the nanocomponents. As will be demonstrated here for nanoparticles with diameters of 10 nm, 20 nm, and 60 nm, this opens the door for arranging individual gold nanoparticles of different sizes in strictly defined patterns in solution, in a way that they act as nanolenses. The results of the experiments and theoretical considerations reported here indicate that the gold nanoparticle assemblies enable efficient plasmon coupling, and the generation of high local optical fields.

By assembling AuNLs consisting of three different gold nanoparticles (10, 20 and 60 nm in diameter) in three spatial arrangements (Figure 1), we show that DNA origami can assemble gold nanoparticles in different, defined geometric varieties. The collinearity and order of the assemblies are controlled by capture strands with specific recognition sequences on the DNA origami scaffold. With applications of complex plasmonic structures in mind, and with the need for experimental systems to study plasmon-enhanced spectroscopic effects, it is desirable to control both the geometry and also the position of probe molecules. Using DNA origami technology, it is easy to incorporate binding functionalities that immobilise defined numbers of analyte molecules at defined positions on the DNA origami scaffold. [39] For one of the nanolens designs discussed here, SERS signals from the two internal gaps are compared by selectively labelling gold nanoparticles with Raman probes. As predicted in the literature [20], the strongest enhancement is found located between the medium-sized and smallest nanoparticle.



**Figure 1:** Scheme and representative AFM images of the three AuNL assemblies. Triangular DNA origami scaffolds [40,41] with capture strands (coloured) bind gold nanoparticles coated with complementary DNA sequences. In AuNL 20<sub>b</sub>-10-60, the 20 nm gold nanoparticle is positioned on the opposing face of the DNA origami scaffold. Scale bars: 100 nm.

## Results

As base for our assemblies, the sharp triangle introduced by Rothemund [24] is used, which has a side length of 127 nm and consists of a single layer of double-stranded DNA. It self-assembles when 208 short ssDNA strands, termed staple strands, and the long scaffold ssDNA M13mp18 are subjected to a temperature program. Extended staple strands are placed at those positions on the DNA origami scaffold where gold nanoparticles are to be bound (extension typically by 28 bases, see S6 – S8 in the SI for sequences). If the sequence of such an exposed capture strand is complementary to the DNA on a specific nanoparticle, both strands hybridize and the nanoparticle is immobilized at the respective position. The number of capture strands on the DNA origami scaffold was adjusted with respect to gold nanoparticle size: 60 nm particles are bound by four to five capture strands, 20 nm particles by four, and 10 nm particles by three. The capture strand positions used to realize the three different AuNL geometries are displayed in the SI (S6–S8).

Gold nanoparticles have been coated with 3' thiol-modified DNA using a protocol modified from Zhang *et al.* [42] The DNA coating of the nanoparticles serves two purposes: (i) the selective hybridization to complementary capture strands on the DNA origami scaffold, and (ii) stabilization against aggregation in the high ionic strength buffer that is required for DNA origami integrity. At the same time, the DNA coating should allow optimum plasmon coupling between the gold nanoparticles. Thus we have minimized the length of coating strands to 13 bases, with 9 base recognition sequences. For shorter lengths, a rapid loss in stabilization efficiency was reported. [43] The coating strands have the sequence (XTT)<sub>3</sub>T<sub>4</sub>-SH, with X representing A, G, or T, respectively. In order to enable the characterization of AuNLs regarding their ability to enhance Raman scattering signals by SERS, the 10 nm gold nanoparticles carry the fluorescent dye tetramethylrhodamine (TAMRA). TAMRA is attached at the solution-facing 5'-end of the DNA coating. This lack of interaction of the dye with the gold nanoparticle surface should lead to very small or negligible contributions of chemical enhancement effects, and a main contribution to potential SERS enhancement by

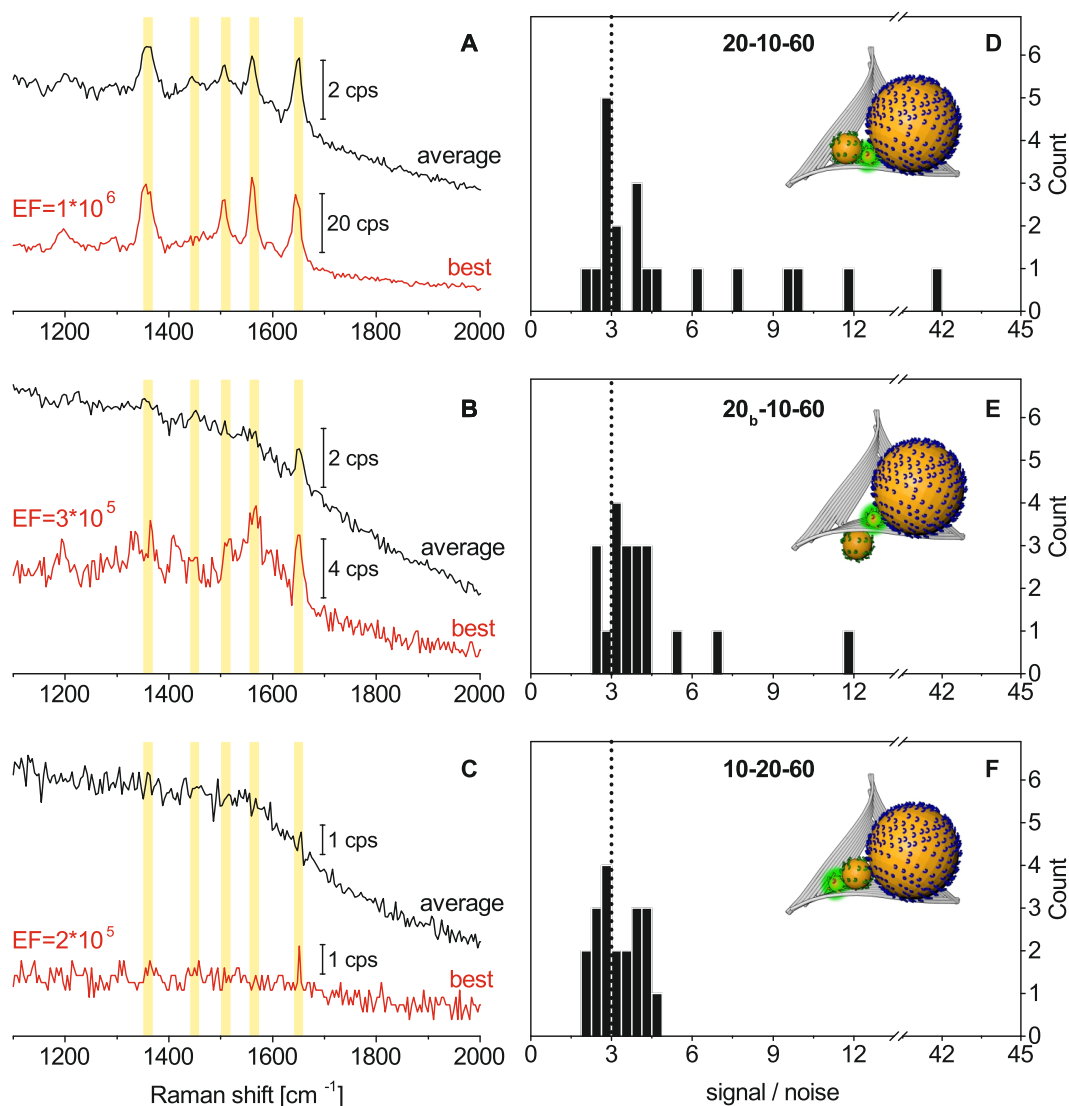
electromagnetic enhancement.

Coated gold nanoparticles are bound to the DNA origami scaffold in several steps: for AuNLs 20-10-60 and 20<sub>b</sub>-10-60 (see Figure 1 for schematic structures), the small 10 nm particle is first immobilized at the middle position, then 20 nm and 60 nm particles for the peripheral positions are added. AuNL 10-20-60 is assembled in three steps, in the order 10 nm, 20 nm, 60 nm. The first hybridization step is facilitated by a temperature ramp from 45 °C to 25 °C over 71 min. In order to prevent the detachment of nanoparticles, subsequent hybridization steps have been performed at room temperature (90 min). A ratio of 1:1 between DNA origami scaffold and the respective gold nanoparticles was found to show the best assembly yield. The stepwise hybridization enables process control by AFM: with binding yields of almost 100% in the first step, each AuNL includes one 10 nm gold nanoparticle. Additionally, the characteristic SERS signals of TAMRA from individual AuNLs serve as final proof for the presence of the 10 nm gold nanoparticle in the AuNLs. In AFM or SEM images, the 10 nm-sized particles are often covered by the larger particles.

Unbound gold nanoparticles are typically removed by agarose gel electrophoresis. Bands in the gel containing the assembled AuNLs are isolated by electroelution into a sucrose-filled pocket [44] and concentrated by centrifugation. For further characterization, the samples are deposited onto silicon wafers. Areas of  $25 \times 25 \mu\text{m}^2$  around a scratch on the silicon wafer are mapped with a Raman microscope and then scanned by AFM. Both images are superimposed and the detailed structures of those AuNLs giving SERS signals are determined.

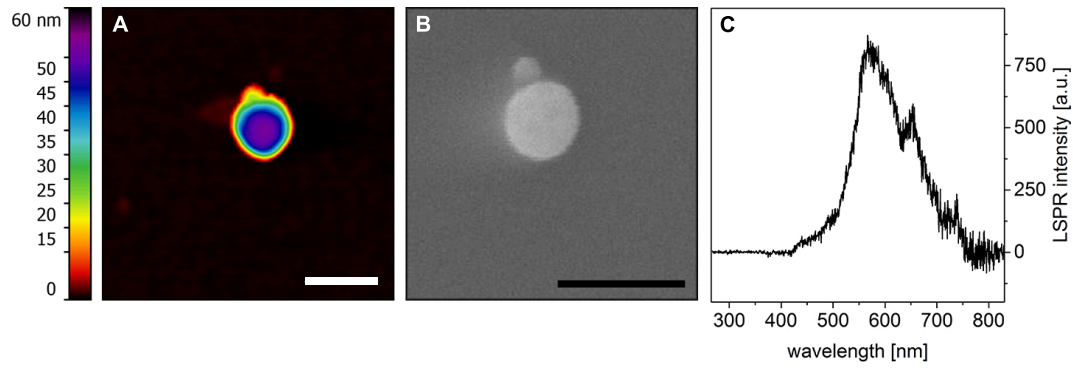
Apart from the electromagnetic enhancement occurring due to the high local field, the SERS signal from an individual AuNL is related to the number of TAMRA molecules participating in the SERS process, and hence to the number of TAMRA-modified DNA strands on the surface of the labelled gold nanoparticles. In order to determine this number, a protocol from Hurst *et al.* [45] was applied. The average number was 99 TAMRA molecules for the 10 nm particles in AuNLs 20-10-60 and 20<sub>b</sub>-10-60, and 39 TAMRA molecules for the 10 nm particles in AuNLs 10-20-60. For each design, a set of 20 single AuNLs was examined; the resulting average SERS spectra and respective SERS spectra with strongest signal are shown in Figure 2 A–C. The average SERS spectra of the three AuNL designs exhibit several differences, with 20-10-60 showing the strongest SERS signal, followed by 20<sub>b</sub>-10-60, whereas design 10-20-60 has the weakest one. The single AuNL analysis enables a close look at how differences in average SERS signals between designs are constituted: in the histograms of Figure 2 D–F, each design yields a majority of spectra with relatively low signals just around the limit of detection. The main difference between the three designs lies in the number and intensity of the small amount of spectra of relatively high intensity, obtained with each respective design (compare Figures 2D, 2E, and 2F). Whereas six AuNLs of design 20-10-60 yield a signal-to-noise ratio above six, for design 20<sub>b</sub>-10-60 only two individual AuNLs showed SERS signals of similar intensity. For design 10-20-60, none of the 20 examined AuNL yielded signals of this strength.





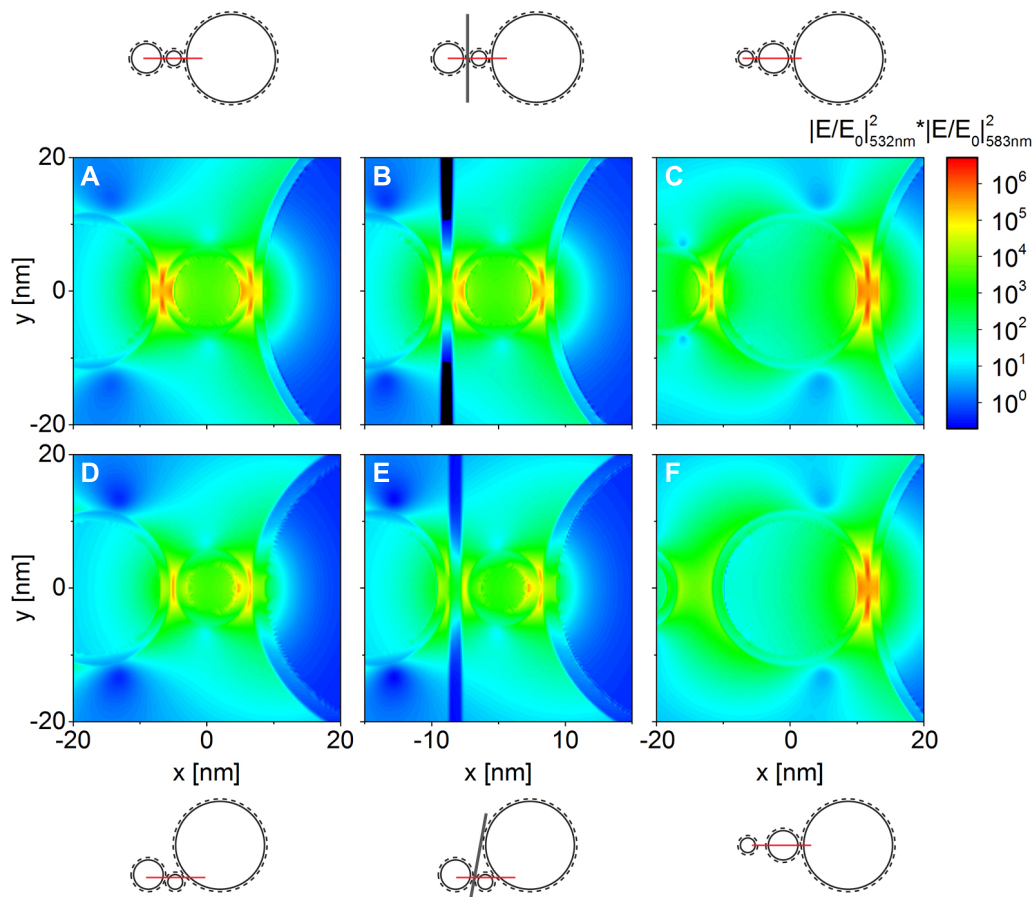
**Figure 2:** (A–C) Average spectrum and most intense Raman spectrum obtained from each respective AuNL design: (A) 20-10-60, (B) 20<sub>b</sub>-10-60, (C) 10-20-60. Characteristic bands of TAMRA are highlighted in yellow. (D–F) Distribution of signal-to-noise in the individual SERS spectra: (D) 20-10-60, (E) 20<sub>b</sub>-10-60, (F) 10-20-60. The intensity of the most prominent TAMRA band of each respective spectrum is divided by the noise  $\sigma$ . The limit of detection is indicated by a dotted line.

One AuNL of design 20-10-60 showed a particularly strong SERS signal (Figure 2 A, red), relating to an enhancement factor (EF) of  $1.4 \times 10^6$ . This EF is underestimated, because it is determined based on the total number of TAMRA molecules. Only a fraction of them are in the region where the local field is very high, therefore, the number of molecules that contribute to the SERS signals is expected to be considerably smaller. Further effects such as the additional resonance of the TAMRA molecules at the wavelength of the excitation laser (532 nm) alter the electromagnetic enhancement of SERS. The corresponding AFM, SEM and localized surface plasmon resonance (LSPR) data for this well-performing AuNL are displayed in Figure 3. A complimentary data set for a AuNL with low enhancement is shown in Figure S1 of the SI.



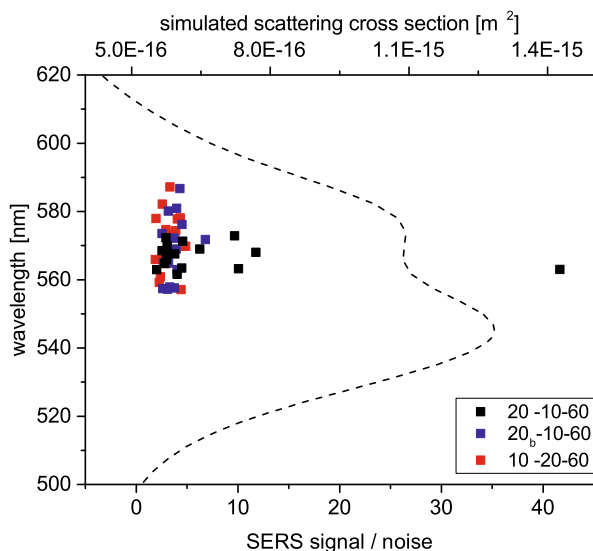
**Figure 3:** (A) AFM, (B) SEM, and (C) LSPR data for the AuNL of design 20-10-60 with a particularly strong SERS signal (spectrum displayed in Figure 2 A). The AFM image reveals the DNA origami structure beneath the AuNL. Scale bars: 100 nm.

The estimates of the enhancement are on the same order of magnitude as those found by Finite Difference Time Domain (FDTD) simulations (Figure 4). The simulation results demonstrate how the electric field enhancement is affected, when gold nanoparticle positions differ in the different nanolens designs. It should be noted that the actual geometry of an individual AuNL might deviate from the collinear arrangement, since in the experiments reported here (i) the AuNLs are dried on the surface, (ii) the nanoparticles are assembled on a planar DNA origami scaffold, and (iii) the nanoparticle-anchoring strands allow for some flexibility and imply variation between individual nanolenses. The SERS enhancement of the different AuNL designs strongly depends on how closely individual structures match ideal collinear geometries with smallest gaps (Figure 4 A–C). The relatively small enhancement obtained with design 10-20-60 (see Figure 2 C for SERS spectra) can be explained by the flexibility of the 10 nm gold nanoparticle: in AuNL 10-20-60, the TAMRA-labelled 10 nm particle is free to move as the DNA tethers allow, whereas in the other designs, it is wedged between the larger particles. The simulation shows that an additional 5 nm gap between 10 nm and 20 nm gold nanoparticle causes the SERS signal in design 10-20-60 to drop by two orders of magnitude (Figure 4 C, F). This effect is considerably stronger than the variations expected for designs 20-10-60 and 20<sub>b</sub>-10-60, with EF decreasing by one order of magnitude in the least favourable case (Figure 4 D, E). The strong SERS enhancement for some structures of design 20-10-60 indicates an optimal plasmonic coupling with a geometry closer to the one shown in Figure 4 A than in 4 D for those structures. AuNLs of type 20<sub>b</sub>-10-60 suffer from the additional DNA origami spacer separating the 20 nm gold nanoparticle (Figure 4 B, E).



**Figure 4:** Electromagnetic SERS enhancement based on FDTD simulations of the local fields for the three designs at the excitation wavelength (532 nm) and at the wavelength corresponding to the TAMRA signal at  $1650\text{ cm}^{-1}$  (583 nm). (A–C) in-line, no gap (D, E) out-of-line, (F) 5-nm-gap arrangement. The polarization direction of the incident light is along the longitudinal axis of the AuNLs. The red line in the schematics illustrates the plane of observation; the plane is chosen to intersect the position of greatest field intensity. The DNA origami scaffold separating the 20 nm gold nanoparticle in  $20_b$ -10-60 AuNLs (B, E) is indicated in grey.

LSPR spectra from the same sets of AuNLs have been obtained by dark field spectroscopy. The wavelengths of the absorbance maxima,  $\lambda_{\text{max}}$ , have been determined and Figure 5 shows them plotted versus SERS intensity of the respective AuNLs. There is no correlation between far field  $\lambda_{\text{max}}$  and the SERS signals observed in the Raman experiments. Interestingly, the  $\lambda_{\text{max}}$  distribution for sample 20-10-60 is narrower than for  $20_b$ -10-60 and 10-20-60. At the same time, 20-10-60 is the design that yields the highest signals in individual SERS spectra. The values for  $\lambda_{\text{max}}$  are in good accordance with scattering spectra simulated by the FDTD method (dashed line in Figure 5). Localized surface plasmons can potentially interact with the underlying silicon substrate, and, due to the high refractive index of silicon, a red-shifted p-mode can be excited under the high angle of incidence used in the dark-field configuration. It was reported that LSPR spectra of single gold nanoparticles on silicon substrates are dominated by this mode, with their  $\lambda_{\text{max}}$  values red-shifted compared to particle dimers on the same substrate. [46] In the experiments reported here, a similar phenomenon would explain why the  $\lambda_{\text{max}}$  values for the  $20_b$ -10-60 and 10-20-60 AuNLs (blue and red dots in Figure 5) are distributed at higher wavelengths than for 20-10-60 AuNLs (black dots, resp.). An exemplary LSPR spectrum, for the AuNL with the overall highest SERS intensity (design 20-10-60), is displayed in Figure 3 C.



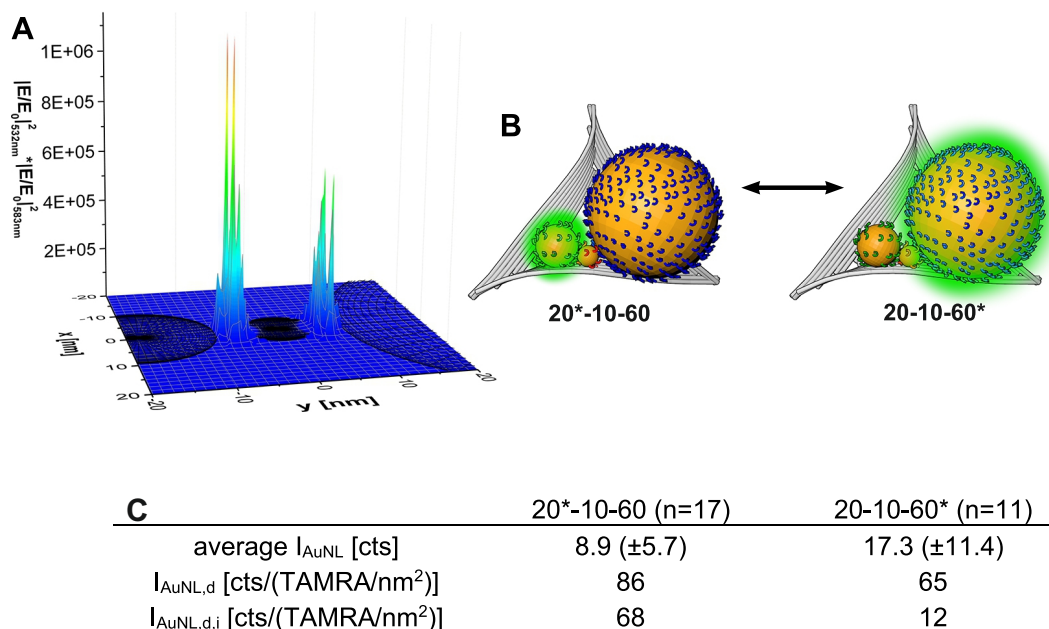
**Figure 5:** Dots display wavelength of LSPR maximum ( $\lambda_{\max}$ ) vs. SERS signal/noise for individual AuNLs. The dashed line shows the simulated Rayleigh scattering cross section as a function of wavelength for design 20-10-60 with ideal geometry. For  $20_b$ -10-60 and 10-20-60 see Figure S3 in the SI.

### Comparison of SERS signals from different gaps

Previously, it was predicted that the electromagnetic field and thus the SERS signal is higher in the gap between the small and the medium-sized particle, compared to the gap between the small and the large particle. [17,20] In order to learn more about the distribution of the electromagnetic enhancement within AuNLs, experiments with 20-10-60 AuNLs were carried out, where either 20 nm ( $20^*$ -10-60) or 60 nm (20-10-60 $^*$ ) gold nanoparticles were TAMRA-labeled, respectively (Figure 6 B). In this way, the Raman signal is only enhanced in one of the two gaps and the signal intensities can directly be compared from the two experiments. SERS spectra from 17 single  $20^*$ -10-60 AuNLs and 11 single 20-10-60 $^*$  AuNLs have been measured and the intensity of the strongest TAMRA signal in each spectrum has been determined. For the comparison of signals from the two individual gaps, the different numbers of TAMRA molecules in the gaps are considered, since nanoparticles of different size support different densities of dye molecules. The SERS signals are normalized by the densities of TAMRA molecules on the gold nanoparticles, assuming that the SERS signal is proportional to the number of dye molecules in the area of highest enhancement, and that for both gaps these areas share similar size. The resulting average SERS signal  $I_{\text{AuNL,d}}$  from  $20^*$ -10-60 is approximately 30% higher than the one from 20-10-60 $^*$  (Figure 6 C).

When the incident light is polarized parallel to the longitudinal axis of the nanolens, the regions of high fields are located in the gaps between the particles. For light polarized perpendicular to the longitudinal axis, mainly transverse modes are excited that should provide field enhancements similar to single-particle modes. [47,48] Under the illumination used in our experiments, both, longitudinal and transverse modes are excited. Therefore, also the enhancement contributed by the whole nanoparticle surfaces, apart from the gaps, must be taken into account, and average SERS signals from TAMRA-coated, isolated nanoparticles of the respective size are subtracted from the signal obtained with the nanolenses. The difference in SERS intensity between the gaps increases considerably: the signal  $I_{\text{AuNL,d,i}}$  from the gap between 20 nm and 10 nm gold nanoparticle then is approximately 6 times higher than that

from the other gap (between the 10 nm and 60 nm gold nanoparticle). This matches well with the FDTD simulations, which predict a factor of 2 for a 3.4 nm gap of DNA coating between the particles (Figure 6 A). With smaller gap sizes, larger factors were predicted. In spite of the signal fluctuations and a relatively low number of analyzed AuNLs, these results provide an experimental indication that the gap between medium and small nanoparticle in AuNLs provides stronger field enhancement than that between the large and the small nanoparticle.



**Figure 6:** (A) FDTD simulation result indicating the electromagnetic Raman enhancement of the two gaps in AuNL 20-10-60. Positions of gold nanoparticles are shown by the black wireframes. (B) Schematic of the selective placement of TAMRA molecules (bright green) for probing of the different inter-particle gaps. (C) SERS signals from AuNLs with TAMRA-labeled 20 nm or 60 nm gold nanoparticles. The SERS signal from single AuNLs ( $I_{\text{AuNL}}$ ) is corrected for TAMRA-density ( $I_{\text{AuNL,d}}$ ) and for signal contribution from isolated, TAMRA-labeled gold nanoparticles ( $I_{\text{AuNL,d,i}}$ ).

## Discussion

In summary, we assembled plasmonic AuNLs from 10, 20 and 60 nm gold nanoparticles in three different designs (20-10-60, 20<sub>b</sub>-10-60 and 10-20-60) and present a systematic investigation of these nanolenses. For sets of single AuNLs from each arrangement, AFM images, SEM images, LSPR spectra and SERS signals of a probe dye have been determined, which gives deep insight into the Raman enhancement of the different arrangements and into the distribution of SERS signals from individual structures. Experiments on single AuNLs indicate that design 20-10-60 yields the most structures with strong SERS enhancement and also shows a narrow distribution of LSPR wavelengths. The localization of SERS enhancement in 20-10-60 AuNLs has been examined further by selectively labelling the 20 nm and 60 nm gold nanoparticles, respectively, with TAMRA. The highest enhancement is located in the gap between the 20 nm and 10 nm gold nanoparticle, in accordance with theoretical predictions. In order to reach the giant Raman enhancements predicted for this and similar structures in the literature, [20,21] it will be of crucial importance to further increase the number of coupled nanoparticles and to decrease the thickness of the DNA coating. The former will require additional sets of capture strands on the present DNA origami scaffold.

The latter will be realized by hybrid coatings with separated functionalities for binding and stabilization. The structures presented here are prepared by self-assembly in solution, in billions of copies. They will be useful for a number of practical applications, since analyte binding functionalities with defined number and position can be easily incorporated into the DNA origami scaffold. Besides potential analytical applications, the DNA origami platforms will enable fundamental investigations of plasmon-related processes.

## Methods

### DNA origami scaffolds

DNA origami scaffolds are assembled in 1x TAE buffer with 11 mM MgCl<sub>2</sub> as described earlier. [34] Staple strand and capture strand sequences can be found in the SI (S6–S8).

### Gold nanoparticle coating

Citrate-stabilized gold nanoparticle solution (BBI Solutions, 1 nM (60 nm), 10 nM (20 nm), 5 nM (10 nm)) in 0.02% sodium dodecyl sulfate (SDS) is mixed with DNA coating strands (metabion, 15 μM (60 nm), 22.5 μM (20 nm), 2.5 μM (10 nm), respectively) and incubated for 30 min. 0.5 M citrate buffer (pH 3) is added to a final concentration of 10 mM and the solution is incubated for another 45 min. 2.5 M NaCl is added to a final concentration of 300 mM and after shaking for 3 h, 2.5 M NaCl is added again to a final concentration of 600 mM. After overnight incubation, 400 μL 1x TAE with 11 mM MgCl<sub>2</sub> and 0.02% SDS are added. Gold nanoparticles are either sedimented by centrifugation (60, 20 nm particles) or separated by centrifugal filters (10 nm particles, Amicon Ultra 0.5 100 kDa, Millipore) and supernatant/flow through are removed. After four more cycles of buffer addition and centrifugation, particles are stored at 4 °C. For the experiments with TAMRA-labeled 60 nm gold nanoparticles, a 1:1 mix of 5'-TAMRA-labeled / unlabeled (TTT)<sub>3</sub>T<sub>4</sub>-SH strands is used for coating.

The pH 3-coating procedure does not yield stable 20 nm nanoparticles with TAMRA-(GTT)<sub>3</sub>T<sub>4</sub>-SH DNA. Instead, a small-step salt-aging protocol at pH 7 is applied: citrate-stabilized 20 nm gold nanoparticles (BBI Solutions) are phosphinated as described earlier. [34] A solution of 6 nM bis(p-sulfonatophenyl)phenylphosphine-coated 20 nm particles with 13.5 μM thiol-modified DNA (metabion, 1:1 mix TAMRA-(GTT)<sub>3</sub>T<sub>4</sub>-SH / (GTT)<sub>3</sub>T<sub>4</sub>-SH) in 0.02% SDS, 50 mM NaCl and 0.5x TAE is incubated for 1 h, then NaCl concentration is increased to 100 mM and the solution is left shaking overnight. The next day, NaCl concentration is increased to 700 mM in 50 mM steps every 40 min. After overnight incubation, particles are purified by five cycles of buffer addition (400 μL 1x TAE with 11 mM MgCl<sub>2</sub> and 0.02% SDS), centrifugation and supernatant removal.

The surface coverage with TAMRA-strands is determined by the dithiothreitol replacement technique [45]: DNA-coated gold nanoparticles are mixed with 0.5 M dithiothreitol, which replaces DNA on the particle surface. After overnight incubation, gold nanoparticles are separated by centrifugation. The concentration of TAMRA-DNA in the supernatant is determined by fluorescence spectroscopy. The data for 60 nm and 20 nm TAMRA-coated gold nanoparticles is displayed in Figure S5 in the SI.

### Si sample preparation

6 μL of the sample solution are placed onto a plasma-cleaned ≈ 1 cm<sup>2</sup> silicon wafer (CrysTec) and 30 μL 110 mM MgCl<sub>2</sub> 10x TAE buffer are added. The sample is incubated for 1 h, washed with 4 mL ethanol/water 1:1 and blow-dried with compressed air.

### Raman measurements

Raman measurements were carried out on a WITec alpha300 confocal Raman microscope with a 100x Olympus MPlanFL N objective (NA = 0.9), 600 gr/mm grating and 532 nm excitation laser. Areas of  $25 \times 25 \mu\text{m}^2$  were scanned with  $0.5 \mu\text{m}$  step size, 4 s integration time and  $2.0 \times 10^4 \text{ W/cm}^2$  laser power. The diffraction-limited spot was estimated to be  $1.3 \mu\text{m}$  wide.

### Estimation of enhancement factors

TAMRA's fluorescence under 532 nm illumination prevents bulk Raman measurements of the non-enhanced dye. Since EFs for single 60 nm gold nanoparticles ( $\text{EF}_{\text{AuNP}}$ ) are known from literature, EFs for AuNLs ( $\text{EF}_{\text{AuNL}}$ ) can be determined indirectly when AuNLs and TAMRA-coated, single 60 nm gold nanoparticles are measured under the same conditions.  $\text{EF}_{\text{AuNL}}$  then can be defined as:

$$\text{EF}_{\text{AuNL}} = \frac{I_{\text{AuNL}}}{I_{\text{AuNP}}} \cdot \frac{N_{\text{AuNP}}}{N_{\text{AuNL}}} \cdot \text{EF}_{\text{AuNP}}$$

with  $I_{\text{AuNL}}$  – SERS intensity of strongest TAMRA band from single AuNL,  $I_{\text{AuNP}}$  – average SERS intensity from single, TAMRA-labeled 60 nm gold nanoparticles (13.9 cts,  $n = 14$ ),  $N_{\text{AuNP}}$  – number of TAMRA molecules on single 60 nm gold nanoparticles,  $N_{\text{AuNL}}$  – number of TAMRA molecules on single 10 nm gold nanoparticles,  $\text{EF}_{\text{AuNP}}$  – enhancement factor of single 60 nm gold nanoparticles ( $7.5 \times 10^3$ ). [49]

### FDTD simulations

FDTD simulations for all AuNLs were carried out with Lumerical FDTD Solutions 8.6.3, using a mesh size of 0.25 nm in the plotted area. Thickness (1.7 nm) and refractive index (1.7) of the ssDNA coating are based on the findings of Thacker *et al.* [35] Since in Raman scattering, exciting and emitted light are wavelength-shifted and thus experience different enhancement, the electric field intensity enhancements at 532 nm (laser) and 583 nm ( $\lambda$  of the usually most prominent TAMRA band,  $\hat{=} 1650 \text{ cm}^{-1}$ ) are multiplied. For Rayleigh scattering simulations, substrate layers were modeled with thicknesses of 2 nm (DNA origami scaffold), 2 nm ( $\text{SiO}_2$  substrate) and an infinite layer of silicon below. Scattering cross sections from s and p polarized light were added incoherently to account for the unpolarised illumination used in the dark field setup. The following refractive indices were used: DNA origami scaffold: 2.1, gold: Johnson and Christy [50], silicon and  $\text{SiO}_2$ : Palik [51], surrounding medium: 1.0. The used 3D models are shown in Figures S2 and S4 in the SI.

### LSPR measurements

For LSPR measurements, a microscope (AxioImager.Z1, Carl-Zeiss AG) in upright dark-field configuration with a 100x objective (LD EC Epiplan-Neofluar 100x 0.75 HD DIC, Carl-Zeiss AG) and a 100 W halogen light source was utilized. Spectral acquisition of individual nanostructures was accomplished by placement of a home-built optical fiber into the image plane of the microscope beam path towards the entrance slit of an external spectrometer (SpectraPro 2300i, Princeton Instruments) with 150 gr/mm. The measurements were conducted with 10 s integration time and averaging over 6 acquisitions.

### Comparison of SERS signals from different gaps

Correction for different densities of TAMRA on the gold nanoparticles:

$$I_{\text{AuNL,d}} = \frac{I_{\text{AuNL}} \cdot \pi d^2}{n}$$

with  $n$  - number of TAMRA strands on the coated gold nanoparticles (2988 for 60 nm particles,

130 for 20 nm particles, see S5 in the SI for details),  $d$  – particle diameter. Correction for signal contribution of isolated TAMRA-coated gold nanoparticles:

$$I_{\text{AuNL},d,i} = I_{\text{AuNL},d} - I_{\text{AuNP},d}$$

with  $I_{\text{AuNP},d}$  – density-corrected SERS intensity of strongest TAMRA band from isolated gold nanoparticles (53 cts/(TAMRA/nm<sup>2</sup>) for 60 nm particles ( $n = 14$ ), 18 cts/(TAMRA/nm<sup>2</sup>) for 20 nm particles ( $n = 11$ )).

### Acknowledgements

This research was supported by the Deutsche Forschungsgemeinschaft (DFG), a Marie Curie FP7 Integration Grant within the 7th European Union Framework Programme, the European Regional Development Fund (EFRE), by the University of Potsdam and the Federal Institute of Materials Research (BAM). V.M. & J.K. acknowledge an ERC Grant (259462, MULTI-BIOPHOT); C.H. & V.M. are grateful for funding through the DFG (GSC 1013, SALSA). We thank Franka Jahn (IPHT Jena) for SEM imaging.

### References

- [1] S. A. Maier *et al.*, “Plasmonics – a route to nanoscale optical devices”, *Adv. Mater.* **13**, 1501–1505 (2001).
- [2] K. L. Kelly, E. Coronado, L. K. Zhao, G. C. Schatz, “The optical properties of metal nanoparticles: the influence of size, shape, and dielectric environment”, *J. Phys. Chem. B* **107**, 668–677 (2003).
- [3] K. A. Willets, R. P. van Duyne, “Localized surface plasmon resonance spectroscopy and sensing”, *Annu. Rev. Phys. Chem.* **58**, 267–297 (2007).
- [4] N. J. Halas, S. Lal, W.-S. Chang, S. Link, P. Nordlander, “Plasmons in strongly coupled metallic nanostructures”, *Chem. Rev.* **111**, 3913–3961 (2011).
- [5] M. I. Stockman, “Nanoplasmonics: past, present, and glimpse into future”, *Opt. Express* **19**, 22029–22106 (2011).
- [6] J. M. McMahon, S. K. Gray, G. C. Schatz, “Fundamental behavior of electric field enhancements in the gaps between closely spaced nanostructures”, *Phys. Rev. B* **83**, 115428 (2011).
- [7] K. Kneipp, H. Kneipp, I. Itzkan, R. R. Dasari, M. S. Feld, “Surface-enhanced Raman scattering and biophysics”, *J. Phys.: Condens. Matter* **14**, 597–624 (2002).
- [8] S. Schlücker, “Surface-enhanced Raman spectroscopy: concepts and chemical applications”, *Angew. Chem. Int. Ed.* **53**, 4756–4795 (2014).
- [9] J.-H. Lee *et al.*, “Tuning and maximizing the single-molecule surface-enhanced Raman scattering from DNA-tethered nanodumbbells”, *ACS Nano* **6**, 9574–9584 (2012).
- [10] R. F. Aroca, D. J. Ross, C. Domingo, “Surface-enhanced infrared spectroscopy”, *Appl. Spectros.* **58**, 324A–338A (2004).
- [11] K. Ataka, S. T. Stripp, J. Heberle, “Surface-enhanced infrared absorption spectroscopy (SEIRAS) to probe monolayers of membrane proteins”, *Biochimica et Biophysica Acta (BBA)-Biomembranes* **1828**, 2283–2293 (2013).



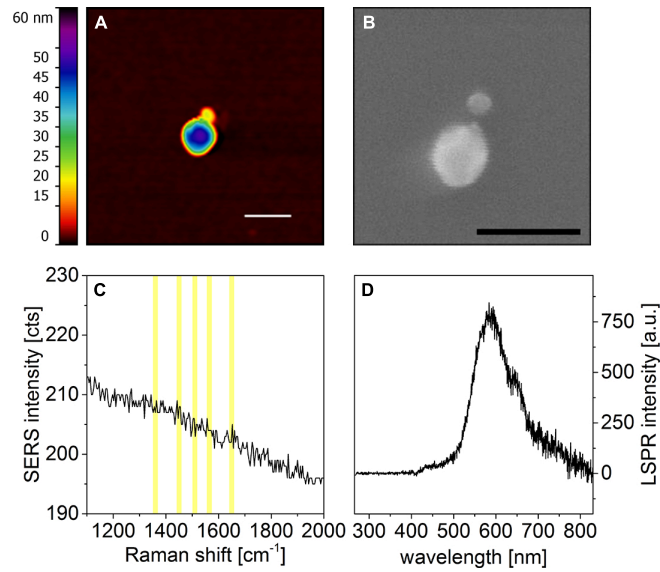
- 
- [12] E. Fort, S. Grésillon, “Surface enhanced fluorescence”, *J. Phys. D: Appl. Phys.* **41**, 13001 (2007).
- [13] A. Puchkova *et al.*, “DNA origami nanoantennas with over 5000-fold fluorescence enhancement and single-molecule detection at 25  $\mu\text{M}$ ”, *Nano Lett.* **15**, 8354–8359 (2015).
- [14] K. L. Wustholz *et al.*, “Structure-activity relationships in gold nanoparticle dimers and trimers for surface-enhanced Raman spectroscopy”, *J. Am. Chem. Soc.* **132**, 10903–10910 (2010).
- [15] H. Lee *et al.*, “Quantitative Plasmon Mode and Surface-Enhanced Raman Scattering Analyses of Strongly Coupled Plasmonic Nanotrimers with Diverse Geometries”, *Nano Lett.* **15**, 4628–4636 (2015).
- [16] S. Bidault, J. F. García de Abajo, A. Polman, “Plasmon-based nanolenses assembled on a well-defined DNA template”, *J. Am. Chem. Soc.* **130**, 2750–2751 (2008).
- [17] J. Kneipp *et al.*, “Gold nanolenses generated by laser ablation-efficient enhancing structure for surface enhanced Raman scattering Analytics and Sensing”, *Anal. Chem.* **80**, 4247–4251 (2008).
- [18] K. Li, X. Li, M. I. Stockman, D. J. Bergman, “Surface plasmon amplification by stimulated emission in nanolenses”, *Phys. Rev. B* **71**, 115409 (2005).
- [19] K. Li, M. I. Stockman, D. J. Bergman, “Enhanced second harmonic generation in a self-similar chain of metal nanospheres”, *Phys. Rev. B* **72**, 153401 (2005).
- [20] K. Li, M. I. Stockman, D. J. Bergman, “Self-similar chain of metal nanospheres as an efficient nanolens”, *Phys. Rev. Lett.* **91**, 227402 (2003).
- [21] J. Dai, F. Čajko, I. Tsukerman, M. I. Stockman, “Electrodynamic effects in plasmonic nanolenses”, *Phys. Rev. B* **77**, 115419 (2008).
- [22] C. Höppener, Z. J. Lapin, P. Bharadwaj, L. Novotny, “Self-similar gold-nanoparticle antennas for a cascaded enhancement of the optical field”, *Phys. Rev. Lett.* **109**, 17402 (2012).
- [23] N. C. Seeman, “DNA in a material world”, *Nature* **421**, 427–431 (2003).
- [24] P. W. K. Rothmund, “Folding DNA to create nanoscale shapes and patterns”, *Nature* **440**, 297–302 (2006).
- [25] A. Kuzyk *et al.*, “A light-driven three-dimensional plasmonic nanosystem that translates molecular motion into reversible chiroptical function”, *Nat. Commun.* **7**, 10591 (2016).
- [26] M. R. Jones, N. C. Seeman, C. A. Mirkin, “Programmable materials and the nature of the DNA bond”, *Science* **347**, 1260901 (2015).
- [27] C. A. Mirkin, R. L. Letsinger, R. C. Mucic, J. J. Storhoff, “A DNA-based method for rationally assembling nanoparticles into macroscopic materials”, *Nature* **382**, 607–609 (1996).
- [28] A. P. Alivisatos *et al.*, “Organization of nanocrystal molecules using DNA”, *Nature* **382**, 609–611 (1996).
- [29] J. Sharma *et al.*, “Toward reliable gold nanoparticle patterning on self-assembled DNA nanoscaffold”, *J. Am. Chem. Soc.* **130**, 7820–7821 (2008).

- [30] B. Ding *et al.*, “Gold nanoparticle self-similar chain structure organized by DNA origami”, *J. Am. Chem. Soc.* **132**, 3248–3249 (2010).
- [31] B. Teschome, S. Facsko, K. V. Gothelf, A. Keller, “Alignment of gold nanoparticle-decorated DNA origami nanotubes: substrate prepatterning versus molecular combing”, *Langmuir* **31**, 12823–12829 (2015).
- [32] F. N. Gür, F. W. Schwarz, J. Ye, S. Diez, T. L. Schmidt, “Towards self-assembled plasmonic devices: high-yield arrangement of gold nanoparticles on DNA origami templates”, *ACS Nano* **10**, 5374–5382 (2016).
- [33] V. G. Kravets *et al.*, “Cascaded optical field enhancement in composite plasmonic nanostructures”, *Phys. Rev. Lett.* **105**, 246806 (2010).
- [34] J. Prinz *et al.*, “DNA origami substrates for highly sensitive surface-enhanced Raman scattering”, *J. Phys. Chem. Lett.* **4**, 4140–4145 (2013).
- [35] V. V. Thacker *et al.*, “DNA origami based assembly of gold nanoparticle dimers for surface-enhanced Raman scattering”, *Nat. Commun.* **5**, 3448 (2014).
- [36] M. Pilo-Pais, A. Watson, S. Demers, T. H. LaBean, G. Finkelstein, “Surface-enhanced Raman scattering plasmonic enhancement using DNA origami-based complex metallic nanostructures”, *Nano Lett.* **14**, 2099–2104 (2014).
- [37] P. Kühler *et al.*, “Plasmonic DNA-origami nanoantennas for surface-enhanced Raman spectroscopy”, *Nano Lett.* **14**, 2914–2919 (2014).
- [38] J. Prinz, C. Heck, L. Ellerik, V. Merk, I. Bald, “DNA origami based Au-Ag-core-shell nanoparticle dimers with single-molecule SERS sensitivity”, *Nanoscale* **8**, 5612–5620 (2016).
- [39] S. Rinker, Y. Ke, Y. Liu, R. Chhabra, H. Yan, “Self-assembled DNA nanostructures for distance-dependent multivalent ligand–protein binding”, *Nat. Nanotechnol.* **3**, 418–422 (2008).
- [40] S. M. Douglas *et al.*, “Rapid prototyping of 3D DNA-origami shapes with caDNAo”, *Nucl. Acid. Res.* **37**, 1–6 (2009).
- [41] C. E. Castro *et al.*, “A primer to scaffolded DNA origami”, *Nat. Method.* **8**, 221–229 (2011).
- [42] X. Zhang *et al.*, “Toward fast and quantitative modification of large gold nanoparticles by thiolated DNA: scaling of nanoscale forces, kinetics, and the need for thiol reduction”, *J. Phys. Chem. C.* **117**, 15677–15684 (2013).
- [43] J. J. Storhoff, R. Elghanian, C. A. Mirkin, R. L. Letsinger, “Sequence-dependent stability of DNA-modified gold nanoparticles”, *Langmuir* **18**, 6666–6670 (2002).
- [44] G. Bellot, M. A. McClintock, C. Lin, W. M. Shih, “Recovery of intact DNA nanostructures after agarose gel–based separation”, *Nat. Method.* **8**, 192–194 (2011).
- [45] S. J. Hurst, A. K. R. Lytton-Jean, C. A. Mirkin, “Maximizing DNA loading on a range of gold nanoparticle sizes”, *Anal. Chem.* **78**, 8313–8318 (2006).
- [46] V. Pini *et al.*, “Spatially multiplexed dark-field microspectrophotometry for nanoplasmonics”, *Sci. Rep.* **6**, 22836 (2016).

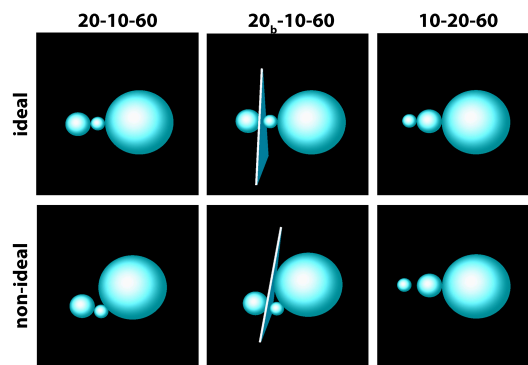
- [47] L. V. Brown, H. Sobhani, J. B. Lassiter, P. Nordlander, N. J. Halas, “Heterodimers: plasmonic properties of mismatched nanoparticle pairs”, *ACS Nano* **4**, 819–832 (2010).
- [48] K. Yoshida *et al.*, “Quantitative evaluation of electromagnetic enhancement in surface-enhanced resonance Raman scattering from plasmonic properties and morphologies of individual Ag nanostructures”, *Phys. Rev. B* **81**, 115406 (2010).
- [49] Z. Zhu, T. Zhu, Z. Liu, “Raman scattering enhancement contributed from individual gold nanoparticles and interparticle coupling”, *Nanotechnology* **15**, 357 (2004).
- [50] P. B. Johnson, R. W. Christy, “Optical constants of the noble metals”, *Phys. Rev. B* **6**, 4370–4379 (1972).
- [51] E. D. Palik, *Handbook of optical constants of solids*, Academic press, 1998.

## Supporting Information

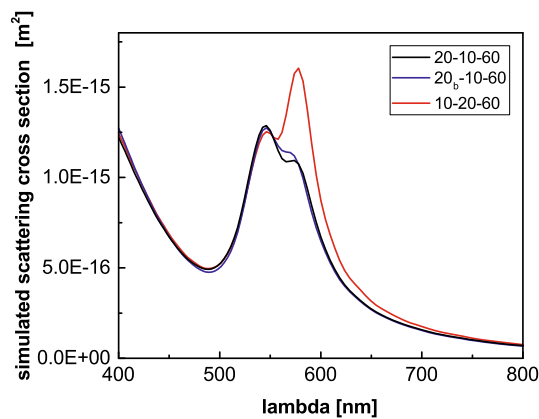
## “Gold nanolenses self-assembled by DNA origami”



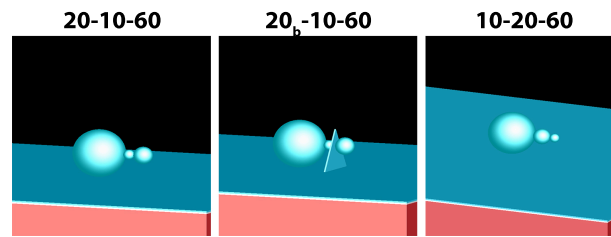
**Figure S1:** AFM (A), SEM (B), SERS (C) and LSPR (D) data for a AuNL of design 20-10-60 with low Raman enhancement. The SEM data indicates a large interparticle gap to be the reason.



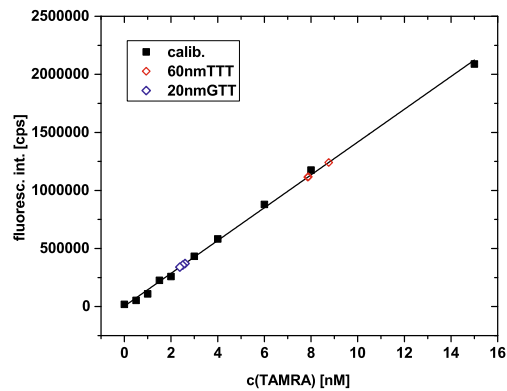
**Figure S2:** 3D models used for simulating electromagnetic enhancements.



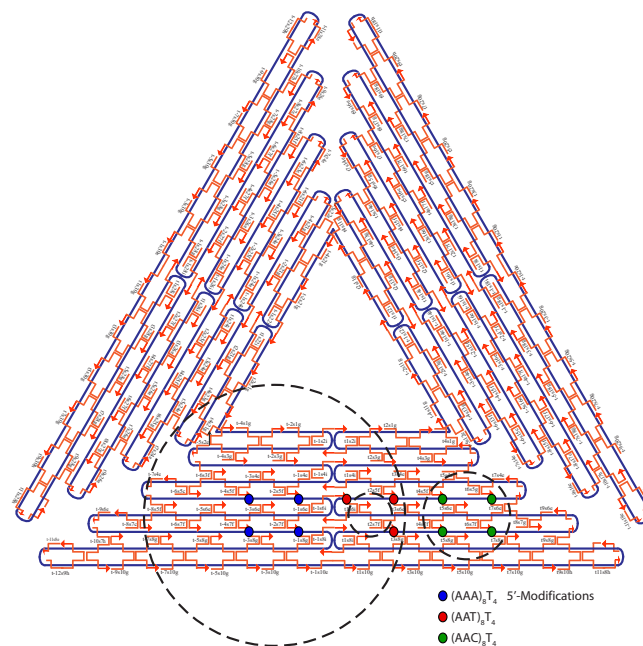
**Figure S3:** Simulated scattering cross sections for the three AuNL designs.



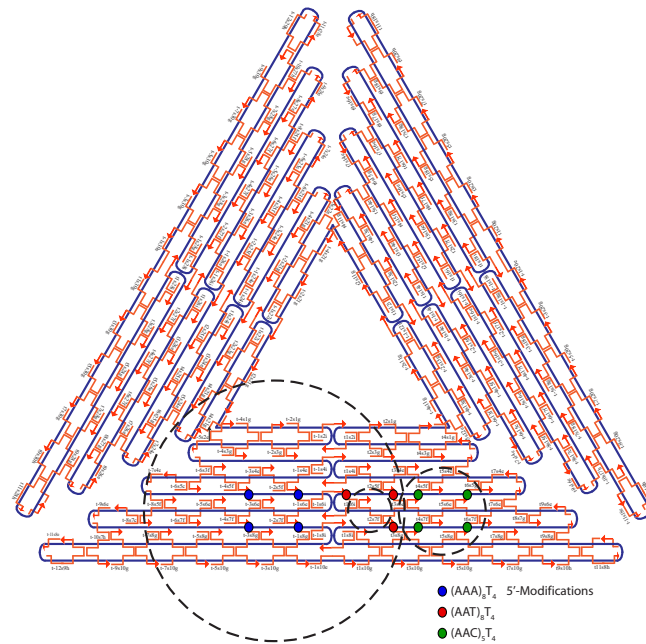
**Figure S4:** 3D models used for simulating scattering cross sections. Color coding: blue – DNA, white – SiO<sub>2</sub>, red – Si.



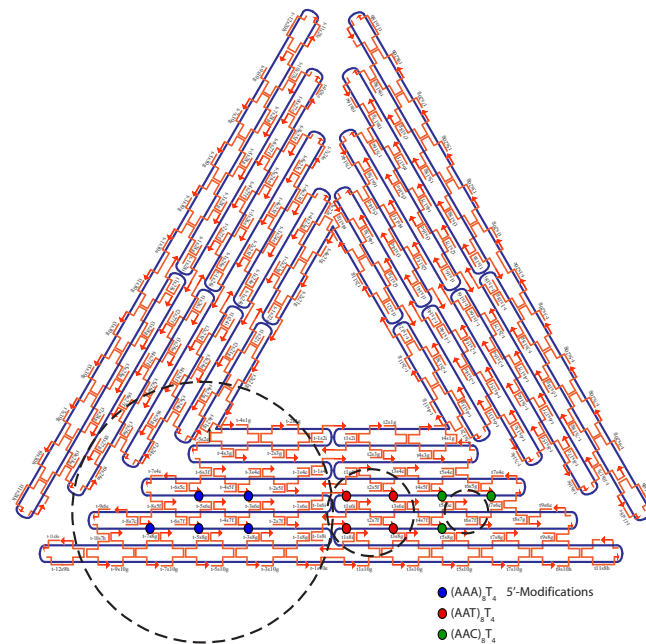
**Figure S5:** Fluorescence data for determination of TAMRA-modified DNA concentration after dithiothreitol replacement on 60 nm (red) or 20 nm (blue) gold nanoparticles, respectively. The calibration curve is shown in black. The absolute TAMRA concentrations were divided by the respective gold nanoparticle concentrations to yield the number of TAMRA strands per particle.



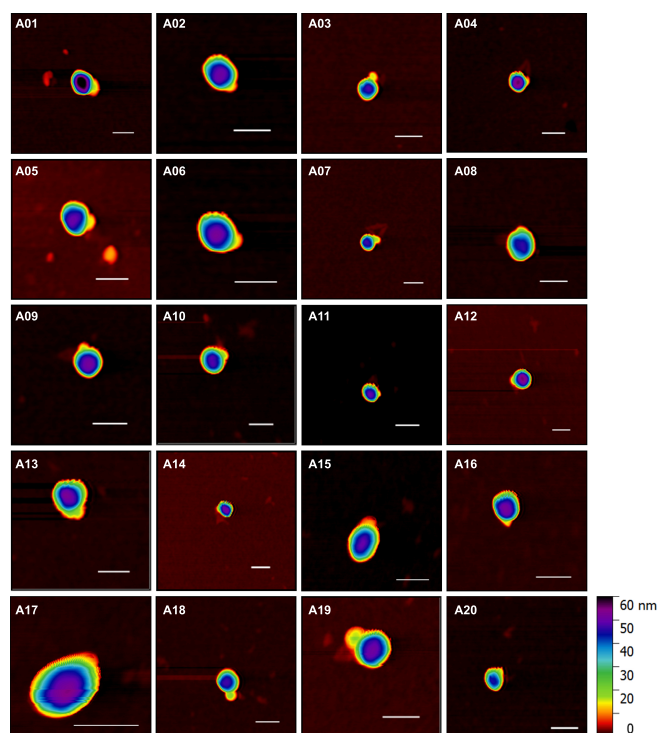
**Figure S6:** Map of the DNA origami scaffold for design 20-10-60. 5' staple modifications are indicated by colored dots. Staple nomenclature and sequences correspond to the original sharp triangle presented by Rothmund. [1] Dashed lines indicate gold nanoparticle positions.



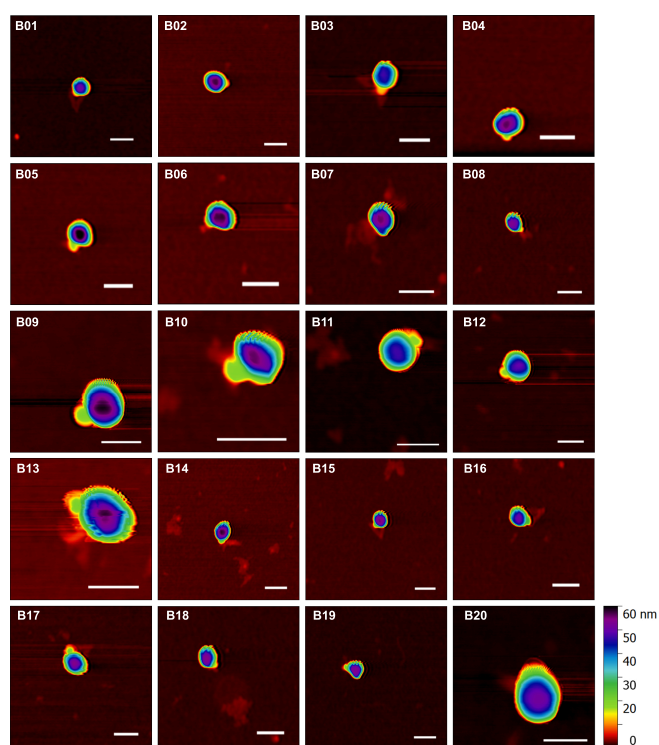
**Figure S7:** Map of the DNA origami scaffold for design 20<sub>b</sub>-10-60. 5' staple modifications are indicated by colored dots. Dashed lines indicate the gold nanoparticle positions. Please note that for this particular design the extensions of the staples marked in green are expected to protrude on the origami face opposite to all the other extensions. The different protrusion angles are enabled by the torsion of the DNA double helix constituting the DNA origami scaffold.



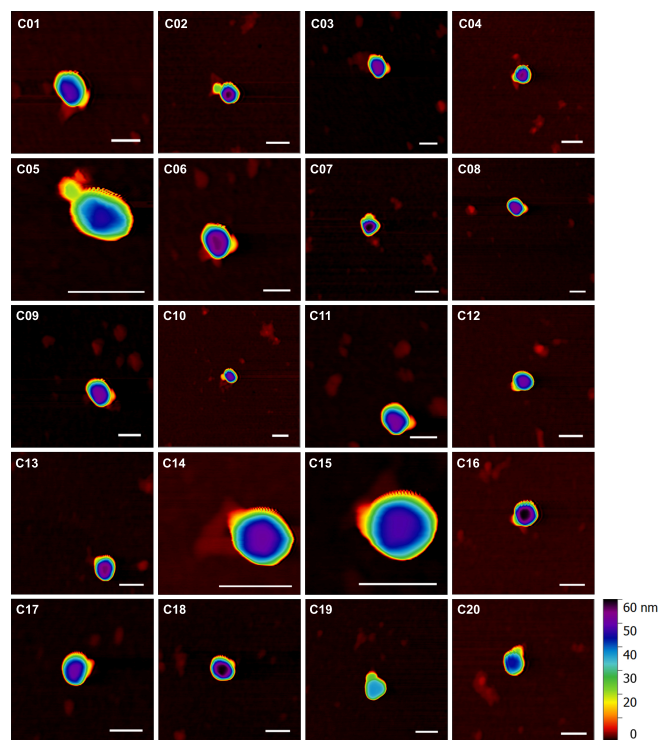
**Figure S8:** Map of the DNA origami scaffold for design 10-20-60. 5' staple modifications are indicated by colored dots. Dashed lines indicate the gold nanoparticle positions.



**Figure S9:** AFM images of the single 20-10-60 AuNLs used for the AuNL design comparison. Scale bars: 100 nm.



**Figure S10:** AFM images of the single 20<sub>b</sub>-10-60 AuNLs used for the AuNL design comparison. Scale bars: 100 nm.



**Figure S11:** AFM images of the single 10-20-60 AuNPs used for the AuNP design comparison. Scale bars: 100 nm.

## Reference

- [1] P. W. K. Rothemund, “Folding DNA to create nanoscale shapes and patterns”, *Nature* **440**, 297–302 (2006).





## Appendix

**Table A.1.:** List of DNA staple strands for the basic DNA origami triangle according to the nomenclature used by ROTHEMUND<sup>[11]</sup>.

position	sequence
t8s27g	CGCGAACTAAAACAGAGGTGAGGCTTAGAAGTATT
t8s7g	AGCCATTTAAACGTCACCAATGAACACCAGAACCA
t9s10h	TATCTTACCGAAGCCAAACGCAATAATAACGAAAATCACCAG
t9s16e	ACTAAAGTACGGTGTCTGAATATAA
t9s18g	TGCTGTAGATCCCCCTCAAATGCTGCGAGAGGCTTTTGCA
t9s20h	AAAGAAGTTTTGCCAGCATAAATATTCATTGACTCAACATGTT
t9s26e	ACCACCAGCAGAAGATGATAGCCC
t9s28g	TAAAACATTAGAAGAACTCAAACCTTTTTATAATCAGTGAG
t9s30h	GCCACCGAGTAAAAGAACATCACTTGCCCTGAGCGCCATTAATA
t9s6e	CCATTAGCAAGGCCGGGGGAATTA
t9s8g	GAGCCAGCGAATACCCAAAAGAACATGAAATAGCAATAGC
t-10s17h	ACCAACCTAAAAAATCAACGTAACAAATAAATTGGGCTTGAGA
t-10s27h	AACTCACATTTATTGAGTGTTGTTCCAGAAAACCGTCTATCAGGG
t-10s7h	ACGACAATAAATCCCGACTTGCGGGAGATCCTGAATCTTACCA
t-12s19h	CCTGACGAGAAAACACCAGAACGAGTAGGCTGCTCATTCAAGTGA
t-12s29h	ACGTGGACTCCAACGTCAAAGGGCGAATTTGGAACAAGAGTCC
t-12s9h	TGCTATTTTGCACCCAGCTACAATTTTGTGTTTGAAGCCTTAAA
t-1s10e	AGAGAATAACATAAAAAACAGGGAAGCGCATT
t-1s12i	AGGATAGCTCAGAGCCACCACCCCATGTCAA
t-1s14e	ATTTTCTGTCAGCGGAGTGAGAATACCGATAT
t-1s14i	CAACAGTTTATGGGATTTTGTCTAATCAAAAAGG
t-1s16e	ATTCCGGTCTGCGGGATCGTCAACCCGAAATCCG
t-1s16i	GCCGCTTTGCTGAGGCTTGCAGGGGAAAAGGT
t-1s18g	CGACCTGCGGTCAATCATAAGGGAACGGAACAACATTATT
t-1s18i	GCGCAGACTCCATGTTACTTAGCCCGTTTTTAA
t-1s20e	ACAGGTAGAAAGATTCATCAGTTGAGATTTAG
t-1s22i	CGCGTCTGATAGGAACGCCATCAACTTTTACA
t-1s24e	CAGTTTGACGCACTCCAGCCAGCTAAACGACG
t-1s24i	AGGAAGATGGGGACGACGACAGTAATCATATT
t-1s26e	GCCAGTGCGATCCCCGGGTACCGAGTTTTTCT
t-1s26i	CTCTAGAGCAAGCTTGCATGCCTGGTCAGTTG
t-1s28g	TTTCACCAGCCTGGCCCTGAGAGAAAGCCGGCGAACGTGG
t-1s28i	CCTTCACCGTGAGACGGGCAACAGCAGTCACA
t-1s2i	CCTTTTTTTCATTTAACAATTTTCATAGGATTAG
t-1s30e	CGAGAAAGGAAGGGAAGCGTACTATGGTTGCT
t-1s4e	TTATCAAACCGGCTTAGGTTGGGTAAGCCTGT
t-1s4i	TTTTAACCTATCATAGGCTGAGAGTTCCAGTA
t-1s6e	TTAGTATCGCCAACGCTCAACAGTCCGGCTGTC
t-1s6i	AGTATAAAATATGCGTTATACAAAAGCCATCTT
t-1s8g	TTTCCTTAGCACTCATCGAGAACAATAGCAGCCTTTACAG

*continued on next page*

*continued from previous page*

position	sequence
t-1s8i	CAAGTACCTCATTCCAAGAACGGGAAATTCAT
t-2s11g	CCTCAGAACC GCCACCCAAAGCCCAATAGGAACGTAAATGA
t-2s13g	AGACGTTACCATGTACCGTAACACCCCTCAGAACC GCCAC
t-2s15f	CACGCATAAGAAAGGAACAACCTAAGTCTTTCC
t-2s17f	ATTGTGTCTCAGCAGCGAAAGACACCATCGCC
t-2s1g	AAAACAAAATTAATTAATGAAAACAGTACATTAGTGAAT
t-2s21g	GCTCATTTTTTTAACCAGCCTTCCTGTAGCCAGGCATCTGC
t-2s23g	GTAACCGTCTTTTCATCAACATTA AAAATTTTTGTAAATCA
t-2s25f	ACGTTGTATTCCGGCACCGCTTCTGGCGCATC
t-2s27f	CCAGGGTGGCTCGAATTCGTAATCCAGTCACG
t-2s3g	AGAGTCAAAAATCAATATATGTGATGAAACAAACATCAAG
t-2s5f	ACTAGAAATATATAACTATATGTACGCTGAGA
t-2s7f	TCAATAATAGGGCTTAATTGAGAATCATAATT
t-3s10g	AACGTCAAAAATGAAAAGCAAGCCGTTTTTATGAAACCAA
t-3s14e	GTTTTGTGTCAGGAATTGCGAATAATCCGACAAT
t-3s16e	GACAACAAGCATCGGAACGAGGGTGAGATTTG
t-3s18g	TATCATCGTTGAAAGAGGACAGATGGAAGAAAAATCTACG
t-3s20g	TTAATAAAACGAACCTAACCGAAGTACCAACTCCTGATAA
t-3s24e	TGTAGATGGGTGCCGAAACCAGGAACGCCAG
t-3s26e	GGTTTTCCATGGTCATAGCTGTTTGAGAGGCG
t-3s28g	GTTTTGCGTACGCTGGTTTTGCCCAAGGGAGCCCCCGATT
t-3s30g	TAGAGCTTGACGGGGAGTTGCAGCAAGCGGTCATTGGGCG
t-3s4e	GATTAAGAAATGCTGATGCAAATCAGAATAAAA
t-3s6e	CACCGGAATCGCCATATTTAACAAAATTTACG
t-3s8g	AGCATGTATTTTCATCGTAGGAATCAAACGATTTTTTTGTTT
t-4s11g	AGGTTTAGTACCGCCATGAGTTTCGTCACCAGGATCTAAA
t-4s13g	AGCGTAACTACAAACTACAACGCCTATCACCGTACTCAGG
t-4s15f	TAGTTGCGAATTTTTTTCACGTTGATCATAGTT
t-4s17f	GTACAACGAGCAACGGCTACAGAGGATACCGA
t-4s1g	GAGCAAAAAGAAGATGAGTGAATAACCTTGCTTATAGCTTA
t-4s21g	GTTAAAATTCGCATTAATGTGAGCGAGTAACACACGTTGG
t-4s23g	GGATAGGTACCCGTCGATTCTCCTAAACGTTAATATTTTT
t-4s25f	AGTTGGGTCAAAGCGCCATTCGCCCCGTAATG
t-4s27f	CGCGCGGGCCTGTGTGAAATTTGTTGGCGATTA
t-4s3g	ACATAGCGCTGTA AATCGTCGCTATTCATTTCAATTACCT
t-4s5f	GTTAAATACAATCGCAAGACAAAGCCTTGAAA
t-4s7f	CCATCCTCGCCAACATGTAATTTAATAAGGC
t-5s10g	TCCCAATCCAAATAAGATTACCGCGCCCAATAAATAATAT
t-5s16e	AACAGCTTGCTTTGAGGACTAAAGCGATTATA
t-5s18g	CCAAGCGCAGGCGCATAGGCTGGCAGAACTGGCTCATTAT
t-5s20g	ACCAGTCAGGACGTTGGAACGGTGTACAGACCGAAACAAA
t-5s26e	TGCTGCAAATCCGCTCACAAATTCAGCTGCA
t-5s28g	TTAATGAAGTTTGATGGTGGTTCCGAGGTGCCGTAAAGCA
t-5s30g	CTAAATCGGAACCCTAAGCAGCGCAAATCCTTCGGCCAA
t-5s6e	GTGTGATAAGGCAGAGGCATTTTCAGTCCTGA
t-5s8g	ACAAGAAAGCAAGCAAATCAGATAACAGCCATATTATTTA
t-6s13f	ACAGACAGCCCAAATCTCCAAAAAATAATTTCTTA
t-6s15c	CGAGGTGAGGCTCCAAAAGGAGCC
t-6s17f	ACCCCAGACTTTTTTCATGAGGAACTTGCTTT
t-6s23f	CGG CGG ATT GAA TTC AGG CTG CGC AAC GGG GGA TG
t-6s25c	TGG CGA AAT GTT GGG AAG GGC GAT
t-6s27f	TGT CGT GCA CAC AAC ATA CGA GCC ACG CCA GC
t-6s3f	TCC CTT AGA ATA ACG CGA GAA AAC TTT TAC CGA CC
t-6s5c	GTT TGA AAT TCA AAT ATA TTT TAG
t-6s7f	AAT AGA TAG AGC CAG TAA TAA GAG ATT TAA TG
t-7s10g	GCC AGT TAC AAA ATA ATA GAA GGC TTA TCC GGT TAT CAA C
t-7s18g	AAA ACA CTT AAT CTT GAC AAG AAC TTA ATC ATT GTG AAT T
t-7s20g	ACC TTA TGC GAT TTT ATG ACC TTC ATC AAG AGC ATC TTT G
t-7s28g	TTC CAG TCC TTA TAA ATC AAA AGA GAA CCA TCA CCC AAA T
t-7s30g	CAA GTT TTT TGG GGT CGA AAT CGG CAA AAT CCG GGA AAC C
t-7s8g	GCG CCT GTT ATT CTA AGA ACG CGA TTC CAG AGC CTA ATT T
t-8s15f	CGG TTT ATC AGG TTT CCA TTA AAC GGG AAT ACA CT
t-8s17c	GGC AAA AGT AAA ATA CGT AAT GCC
t-8s25f	TCT TCG CTA TTG GAA GCA TAA AGT GTA TGC CCG CT
t-8s27c	GCG CTC ACA AGC CTG GGG TGC CTA
t-8s5f	TTC TGA CCT AAA ATA TAA AGT ACC GAC TGC AGA AC

*continued on next page*

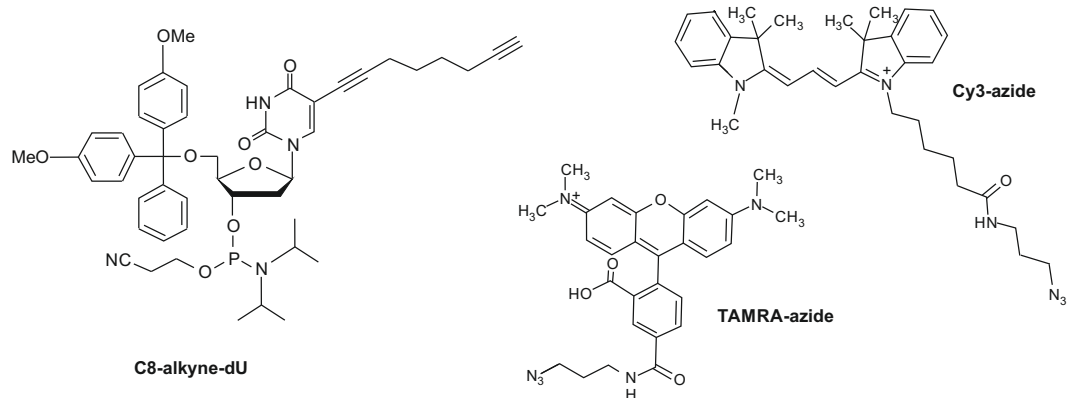
continued from previous page

position	sequence
t-8s7c	TCA GCT AAA AAA GGT AAA GTA ATT
t-9s10g	ACG CTA ACG AGC GTC TGG CGT TTT AGC GAA CCC AAC ATG T
t-9s20g	TGG TTT AAT TTC AAC TCG GAT ATT CAT TAC CCA CGA AAG A
t-9s30g	CGA TGG CCC ACT ACG TAT AGC CCG AGA TAG GGA TTG CGT T
ts-rem1	GCG CTT AAT GCG CCG CTA CAG GGC
t-5s2e-t6s23c-3T	TTA ATT AAT TTT TTA CCA TAT CAA A
t-7s4e-t8s25c-2T	TTA ATT TCA TCT TAG ACT TTA CAA
t-9s6e-t10s27c-1T	CTG TCC AGA CGT ATA CCG AAC GA
t-11s8e-t12s29c-0T	TCA AGA TTA GTG TAG CAA TAC T
t-5s12e-t6s3c-3T	TGT AGC ATT CCT TTT ATA AAC AGT T
t-7s14e-t8s5c-2T	TTT AAT TGT ATT TCC ACC AGA GCC
t-9s16e-t10s7c-1T	ACT ACG AAG GCT TAG CAC CAT TA
t-11s18e-t12s9c-0T	ATA AGG CTT GCA ACA AAG TTA C
t-5s22e-t6s13c-3T	GTG GGA ACA AAT TTC TAT TTT TGA G
t-7s24e-t8s15c-2T	CGG TGC GGG CCT TCC AAA AAC ATT
t-9s26e-t10s17c-1T	ATG AGT GAG CTT TTA AAT ATG CA
t-11s28e-t12s19c-0T	ACT ATT AAA GAG GAT AGC GTC C
t11s18h	AAT ACT GCG GAA TCG TAG GGG GTA ATA GTA AAA TGT TTA GAC T
t11s28h	TCT TTG ATT AGT AAT AGT CTG TCC ATC ACG CAA ATT AAC CGT T
t11s8h	CAG AAG GAA ACC GAG GTT TTT AAG AAA AGT AAG CAG ATA GCC G
t1s10g	GAC GGG AGA ATT AAC TCG GAA TAA GTT TAT TTC CAG CGC C
t1s12i	TCA TAT GTG TAA TCG TAA AAC TAG TCA TTT TC
t1s14i	GTG AGA AAA TGT GTA GGT AAA GAT ACA ACT TT
t1s16i	GGC ATC AAA TTT GGG GCG CGA GCT AGT TAA AG
t1s18i	TTC GAG CTA AGA CTT CAA ATA TCG GGA ACG AG
t1s20g	GAA TAC CAC ATT CAA CTT AAG AGG AAG CCC GAT CAA AGC G
t1s22i	TCG GGA GAT ATA CAG TAA CAG TAC AAA TAA TT
t1s24i	CCT GAT TAA AGG AGC GGA ATT ATC TCG GCC TC
t1s26i	GCA AAT CAC CTC AAT CAA TAT CTG CAG GTC GA
t1s28i	CGA CCA GTA CAT TGG CAG ATT CAC CTG ATT GC
t1s2i	CGG GGT TTC CTC AAG AGA AGG ATT TTG AAT TA
t1s30g	TTG ACG AGC ACG TAT ACT GAA ATG GAT TAT TTA ATA AAA G
t1s4i	AGC GTC ATG TCT CTG AAT TTA CCG ACT ACC TT
t1s6i	TTC ATA ATC CCC TTA TTA GCG TTT TTC TTA CC
t1s8i	ATG GTT TAT GTC ACA ATC AAT AGA TAT TAA AC
t2s11g	AGA AAA GCC CCA AAA AGA GTC TGG AGC AAA CAA TCA CCA T
t2s13g	ACA GTC AAA GAG AAT CGA TGA ACG ACC CCG GTT GAT AAT C
t2s15f	ATA GTA GTA TGC AAT GCC TGA GTA GGC CGG AG
t2s17f	AAC CAG ACG TTT AGC TAT ATT TTC TTC TAC TA
t2s1g	GAT AAG TGC CGT CGA GCT GAA ACA TGA AAG TAT ACA GGA G
t2s21g	CCT GAT TGC TTT GAA TTG CGT AGA TTT TCA GGC ATC AAT A
t2s23g	TGG CAA TTT TTA ACG TCA GAT GAA AAC AAT AAC GGA TTC G
t2s25f	AAG GAA TTA CAA AGA AAC CAC CAG TCA GAT GA
t2s27f	GGA CAT TCA CCT CAA ATA TCA AAC ACA GTT GA
t2s3g	TTT GAT GAT TAA GAG GCT GAG ACT TGC TCA GTA CCA GGC G
t2s5f	CCG GAA CCC AGA ATG GAA AGC GCA ACA TGG CT
t2s7f	AAA GAC AAC ATT TTC GGT CAT AGC CAA AAT CA
t3s10g	GTC AGA GGG TAA TTG ATG GCA ACA TAT AAA AGC GAT TGA G
t3s14e	CAA TAT GAC CCT CAT ATA TTT TAA AGC ATT AA
t3s16e	CAT CCA ATA AAT GGT CAA TAA CCT CGG AAG CA
t3s18g	AAC TCC AAG ATT GCA TCA AAA AGA TAA TGC AGA TAC ATA A
t3s20g	CGC CAA AAG GAA TTA CAG TCA GAA GCA AAG CGC AGG TCA G
t3s24e	TAA TCC TGA TTA TCA TTT TGC GGA GAG GAA GG
t3s26e	TTA TCT AAA GCA TCA CCT TGC TGA TGG CCA AC
t3s28g	AGA GAT AGT TTG ACG CTC AAT CGT ACG TGC TTT CCT CGT T
t3s30g	AGA ATC AGA GCG GGA GAT GGA AAT ACC TAC ATA ACC CTT C
t3s4e	TGT ACT GGA AAT CCT CAT TAA AGC AGA GCC AC
t3s6e	CAC CGG AAA GCG CGT TTT CAT CGG AAG GGC GA
t3s8g	CAT TCA ACA AAC GCA AAG ACA CCA GAA CAC CCT GAA CAA A
t4s11g	GCA AAT ATT TAA ATT GAG ATC TAC AAA GGC TAC TGA TAA A
t4s13g	CGT TCT AGT CAG GTC ATT GCC TGA CAG GAA GAT TGT ATA A
t4s15f	CAG GCA AGA TAA AAA TTT TTA GAA TAT TCA AC
t4s17f	GAT TAG AGA TTA GAT ACA TTT CGC AAA TCA TA
t4s1g	TAG CCC GGA ATA GGT GAA TGC CCC CTG CCT ATG GTC AGT G
t4s21g	GCG CAG AGG CGA ATT AAT TAT TTG CAC GTA AAT TCT GAA T
t4s23g	GAT TAT ACA CAG AAA TAA AGA AAT ACC AAG TTA CAA AAT C

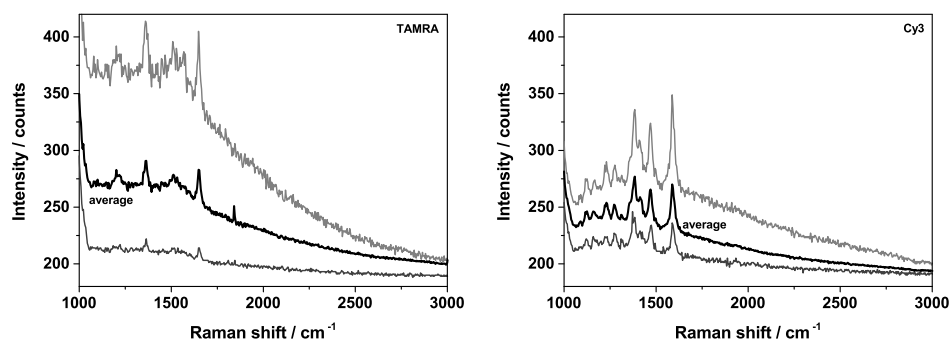
continued on next page

*continued from previous page*

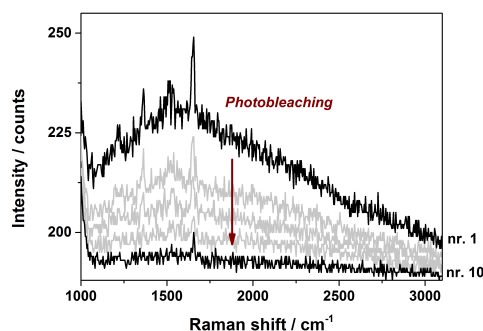
<b>position</b>	<b>sequence</b>
t4s25f	TAG GAG CAT AAA AGT TTG AGT AAC ATT GTT TG
t4s27f	TGA CCT GAC AAA TGA AAA ATC TAA AAT ATC TT
t4s3g	TTT AAC GGT TCG GAA CCT ATT ATT AGG GTT GAT ATA AGT A
t4s5f	CTC AGA GCA TAT TCA CAA ACA AAT TAA TAA GT
t4s7f	GGG GGG AAT TTA GCG TCA GAC TGT CCG CCT CC
t5s10g	GAT AAC CCA CAA GAA TGT TAG CAA ACG TAG AAA ATT ATT C
t5s14e	TTA ATG CCT TAT TTC AAC GCA AGG GCA AAG AA
t5s16e	TTA GCA AAT AGA TTT AGT TTG ACC AGT ACC TT
t5s18g	TAA TTG CTT TAC CCT GAC TAT TAT GAG GCA TAG TAA GAG C
t5s20g	AAC ACT ATC ATA ACC CAT CAA AAA TCA GGT CTC CTT TTG A
t5s24e	AAT GGA AGC GAA CGT TAT TAA TTT CTA ACA AC
t5s26e	TAA TAG ATC GCT GAG AGC CAG CAG AAG CGT AA
t5s28g	GAA TAC GTA ACA GGA AAA ACG CTC CTA AAC AGG AGG CCG A
t5s30g	TTA AAG GGA TTT TAG ATA CCG CCA GCC ATT GCG GCA CAG A
t5s4e	CCT TGA GTC AGA CGA TTG GCC TTG CGC CAC CC
t5s6e	TCA GAA CCC AGA ATC AAG TTT GCC GGT AAA TA
t5s8g	TTG ACG GAA ATA CAT ACA TAA AGG GCG CTA ATA TCA GAG A
t6s15g	ATA AAG CCT TTG CGG GAG AAG CCT GGA GAG GGT AG
t6s17f	TAA GAG GTC AAT TCT GCG AAC GAG ATT AAG CA
t6s25g	TCA ATA GAT ATT AAA TCC TTT GCC GGT TAG AAC CT
t6s27f	CAA TAT TTG CCT GCA ACA GTG CCA TAG AGC CG
t6s5g	CAG AGC CAG GAG GTT GAG GCA GGT AAC AGT GCC CG
t6s7f	ATT AAA GGC CGT AAT CAG TAG CGA GCC ACC CT
t7s10g	ATA AGA GCA AGA AAC ATG GCA TGA TTA AGA CTC CGA CTT G
t7s14e	ATG ACC CTG TAA TAC TTC AGA GCA
t7s16e	TAA AGC TAT ATA ACA GTT GAT TCC CAT TTT TG
t7s18g	CGG ATG GCA CGA GAA TGA CCA TAA TCG TTT ACC AGA CGA C
t7s20g	GAT AAA AAC CAA AAT ATT AAA CAG TTC AGA AAT TAG AGC T
t7s24e	ACA ATT CGA CAA CTC GTA ATA CAT
t7s26e	TTG AGG ATG GTC AGT ATT AAC ACC TTG AAT GG
t7s28g	CTA TTA GTA TAT CCA GAA CAA TAT CAG GAA CGG TAC GCC A
t7s30g	GAA TCC TGA GAA GTG TAT CGG CCT TGC TGG TAC TTT AAT G
t7s4e	GCC GCC AGC ATT GAC ACC ACC CTC
t7s6e	AGA GCC GCA CCA TCG ATA GCA GCA TGA ATT AT
t7s8g	CAC CGT CAC CTT ATT ACG CAG TAT TGA GTT AAG CCC AAT A
t8s17g	TAA TTG CTT GGA AGT TTC ATT CCA AAT CGG TTG TA



**Figure A.1.:** Molecular structures of the precursors for click chemistry. Within the C8-alkyne-dU molecule the 3'-OH position carries a phosphoramidite group to increase the reactivity of the nucleotide. Additionally, the 5'-OH is protected by an acid-labile dimethoxy-trityl group which is removed at the beginning of each synthesis cycle to enable the introduction of a new nucleotide. The TAMRA-azide or the Cy3-azide can be linked to the C8-alkyne-dU via a [3+2]-cycloaddition (click chemistry).



**Figure A.2.:** SERS spectra from 60 nm AuNPs covered with dye-modified ssDNA. The AuNPs are covered with 5'-(TTT)<sub>4</sub>TX-SH-3'; X = TAMRA (left), X = Cy3 (right). For both dyes the most and the less intense spectra are shown as well as an average spectrum obtained from 15 individual 60 nm AuNPs.  $\lambda_{\text{exc}} = 532$  nm, laser power: 400–500  $\mu\text{W}$ , integration time: 10 s.



**Figure A.3.:** Photobleaching of TAMRA occurring in a series measurement with 10 successively recorded SERS spectra. The spectra were obtained from an undefined number of single 15 nm AuNPs coated with 5'-(TTT)<sub>4</sub>TX-SH-3' (X = TAMRA).  $\lambda_{\text{exc}} = 532$  nm, laser power: 900–1000  $\mu\text{W}$ , integration time: 2 s.



## Bibliography

- [1] P. Kumar, I. Roy, “Applications of Gold Nanoparticles in Clinical Medicine”, *Int. J. Pharm. Pharm. Sci.* **8**, 9–16 (2016).
- [2] M. Fleischmann, P. J. Hendra, A. J. McQuillan, “Raman spectra of pyridine adsorbed at a silver electrode”, *Chem. Phys. Lett.* **26**, 163–166 (1974).
- [3] D. L. Jeanmaire, R. P. Van Duyne, “Surface Raman spectroelectrochemistry Part I. Heterocyclic, aromatic, and aliphatic amines adsorbed on the anodized silver electrode”, *J. Electroanal. Chem.* **84**, 1–20 (1977).
- [4] C. E. Talley, J. B. Jackson, C. Oubre, N. K. Grady, C. W. Hollars, S. M. Lane, T. R. Huser, P. Nordlander, N. J. Halas, “Surface-Enhanced Raman Scattering from Individual Au Nanoparticles and Nanoparticle Dimer Substrates”, *Nano Lett.* **5**, 1569–1574 (2005).
- [5] K. L. Wustholz, A.-I. Henry, J. M. McMahon, R. G. Freeman, N. Valley, M. E. Piotti, M. J. Natan, G. C. Schatz, R. P. Van Duyne, “Structure–Activity Relationships in Gold Nanoparticle Dimers and Trimers for Surface-Enhanced Raman Spectroscopy”, *J. Am. Chem. Soc.* **132**, 10903–10910 (2010).
- [6] S. Nie, S. R. Emory, “Probing Single Molecules and Single Nanoparticles by Surface-Enhanced Raman Scattering”, *Science* **275**, 1102–1106 (1997).
- [7] K. Kneipp, Y. Wang, H. Kneipp, L. T. Perelman, I. Itzkan, R. R. Dasari, M. S. Feld, “Single Molecule Detection Using Surface-Enhanced Raman Scattering (SERS)”, *Phys. Rev. Lett.* **78**, 1667–1670 (1997).
- [8] E. C. Le Ru, M. Meyer, P. G. Etchegoin, “Proof of Single-Molecule Sensitivity in Surface Enhanced Raman Scattering (SERS) by Means of a Two-Analyte Technique”, *J. Phys. Chem. B* **110**, 1944–1948 (2006).
- [9] B. Vlčková, M. Moskovits, I. Pavel, K. Šišková, M. Sládková, M. Šlouf, “Single-molecule surface-enhanced Raman spectroscopy from a molecularly-bridged silver nanoparticle dimer”, *Chem. Phys. Lett.* **455**, 131–134 (2008).
- [10] D.-K. Lim, K.-S. Jeon, H. M. Kim, J.-M. Nam, Y. D. Suh, “Nanogap-engineerable Raman-active nanodumbbells for single-molecule detection”, *Nat. Mater.* **9**, 60–67 (2010).
- [11] P. W. K. Rothmund, “Folding DNA to create nanoscale shapes and patterns”, *Nature* **440**, 297–302 (2006).
- [12] Y. Liu, Y. Hu, J. Zhang, “Few-Layer Graphene-Encapsulated Metal Nanoparticles for Surface-Enhanced Raman Spectroscopy”, *J. Phys. Chem. C* **118**, 8993–8998 (2014).
- [13] Y. Zhao, Y. Xie, Z. Bao, Y. H. Tsang, L. Xie, Y. Chai, “Enhanced SERS Stability of R6G Molecules with Monolayer Graphene”, *J. Phys. Chem. C* **118**, 11827–11832 (2014).

- [14] C. V. Raman, "Part II.-The Raman effect. Investigation of molecular structure by light scattering", *Trans. Faraday Soc.* **25**, 781–792 (1929).
- [15] P. Larkin, *Infrared and Raman Spectroscopy: Principles and Spectral Interpretation*, Elsevier, USA, 2011.
- [16] T. Dieing, O. Hollricher, J. Toporski, editors, *Confocal Raman microscopy*, Springer, Heidelberg, Germany, 2010.
- [17] J. R. Lakowicz, *Principles of Fluorescence Spectroscopy*, Springer, New York, USA, 2006.
- [18] E. Le Ru, P. G. Etchegoin, *Principles of Surface Enhanced Raman Spectroscopy and related plasmonic effects*, Elsevier, Amsterdam, The Netherlands, 2009.
- [19] S. Schlücker, "Surface-Enhanced Raman Spectroscopy: Concepts and Chemical Applications", *Angew. Chem. Int. Ed.* **53**, 4756–4795 (2014).
- [20] R. L. McCreery, *Raman Spectroscopy for Chemical Analysis*, WILEY-INTERSCIENCE, USA, 2000.
- [21] M. Hesse, H. Meier, B. Zeeh, *Spektroskopische Methoden in der organischen Chemie*, Thieme, 2002.
- [22] E. C. Le Ru, P. G. Etchegoin, "Single-Molecule Surface-Enhanced Raman Spectroscopy", *Annu. Rev. Phys. Chem.* **63**, 65–87 (2012).
- [23] J. Kneipp, H. Kneipp, K. Kneipp, "SERS—a single-molecule and nanoscale tool for bioanalytics", *Chem. Soc. Rev.* **37**, 1052–1060 (2008).
- [24] K. Kneipp, H. Kneipp, "Single Molecule Raman Scattering", *Appl. Spectrosc.* **60**, 322A–334A (2006).
- [25] S. A. Maier, *Plasmonics: Fundamentals and Applications*, Springer, New York, USA, 2007.
- [26] O. Madelung, *Introduction to Solid-State Theory*, Springer, Berlin, Germany, 1978.
- [27] S. Schlücker, editor, *Surface Enhanced Raman Spectroscopy: Analytical, Biophysical and Life Science Applications*, WILEY-VCH, Weinheim, Germany, 2011.
- [28] P. B. Johnson, R. W. Christy, "Optical Constants of the Noble Metals", *Phys. Rev. B* **6**, 4370–4379 (1972).
- [29] K. A. Willets, R. P. Van Duyne, "Localized Surface Plasmon Resonance Spectroscopy and Sensing", *Annu. Rev. Phys. Chem.* **58**, 267–297 (2007).
- [30] P. K. Jain, M. A. El-Sayed, "Plasmonic coupling in noble metal nanostructures", *Chem. Phys. Lett.* **487**, 153–164 (2010).
- [31] J. H. Yoon, Y. Zhou, M. G. Blaber, G. C. Schatz, S. Yoon, "Surface Plasmon Coupling of Compositionally Heterogeneous Core–Satellite Nanoassemblies", *J. Phys. Chem. Lett.* **4**, 1371–1378 (2013).
- [32] C. L. Haynes, A. D. McFarland, R. P. Van Duyne, "Surface-Enhanced Raman Spectroscopy", *Anal. Chem.* **77**, 338 A–346 A (2005).



- [33] E. Petryayeva, U. J. Krull, “Localized surface plasmon resonance: Nanostructures, bioassays and biosensing—A review”, *Anal. Chim. Acta* **706**, 8–24 (2011).
- [34] J. Gersten, A. Nitzan, “Electromagnetic theory of enhanced Raman scattering by molecules adsorbed on rough surfaces”, *J. Chem. Phys.* **73**, 3023–3037 (1980).
- [35] N. J. Halas, S. Lal, W.-S. Chang, S. Link, P. Nordlander, “Plasmons in Strongly Coupled Metallic Nanostructures”, *Chem. Rev.* **111**, 3913–3961 (2011).
- [36] E. Prodan, C. Radloff, N. J. Halas, P. Nordlander, “A Hybridization Model for the Plasmon Response of Complex Nanostructures”, *Science* **302**, 419–422 (2003).
- [37] A. M. Funston, C. Novo, T. J. Davis, P. Mulvaney, “Plasmon Coupling of Gold Nanorods at Short Distances and in Different Geometries”, *Nano Lett.* **9**, 1651–1658 (2009).
- [38] B. Willingham, D. W. Brandl, P. Nordlander, “Plasmon hybridization in nanorod dimers”, *Appl. Phys. B* **93**, 209–216 (2008).
- [39] F. Hao, C. L. Nehl, J. H. Hafner, P. Nordlander, “Plasmon Resonances of a Gold Nanostar”, *Nano Lett.* **7**, 729–732 (2007).
- [40] Y. Chen, H. Wu, Z. Li, P. Wang, L. Yang, Y. Fang, “The Study of Surface Plasmon in Au/Ag Core/Shell Compound Nanoparticles”, *Plasmonics* **7**, 509–513 (2012).
- [41] Y. Liu, J. Zhou, B. Wang, T. Jiang, H.-P. Ho, L. Petti, P. Mormile, “Au@Ag core-shell nanocubes: epitaxial growth synthesis and surface-enhanced Raman scattering performance”, *Phys. Chem. Chem. Phys.* **17**, 6819–6826 (2015).
- [42] S. Sheikholeslami, Y.-W. Jun, P. K. Jain, A. P. Alivisatos, “Coupling of Optical Resonances in a Compositionally Asymmetric Plasmonic Nanoparticle Dimer”, *Nano Lett.* **10**, 2655–2660 (2010).
- [43] P. Nordlander, C. Oubre, E. Prodan, K. Li, M. I. Stockman, “Plasmon Hybridization in Nanoparticle Dimers”, *Nano Lett.* **4**, 899–903 (2004).
- [44] E. Prodan, P. Nordlander, “Electronic structure and polarizability of metallic nanoshells”, *Chem. Phys. Lett.* **352**, 140–146 (2002).
- [45] E. C. Le Ru, E. Blackie, M. Meyer, P. G. Etchegoin, “Surface Enhanced Raman Scattering Enhancement Factors - A Comprehensive Study”, *J. Phys. Chem. C* **111**, 13794–13803 (2007).
- [46] H. M. Lee, S. M. Jin, H. M. Kim, Y. D. Suh, “Single-molecule surface-enhanced Raman spectroscopy: a perspective on the current status”, *Phys. Chem. Chem. Phys.* **15**, 5276–5287 (2013).
- [47] A. Jabłoński, “Über den Mechanisms der Photolumineszenz von Farbstoffphosphoren”, *Z. Phys.* **94**, 38–46 (1935).
- [48] P. Anger, P. Bharadwaj, L. Novotny, “Enhancement and Quenching of Single-Molecule Fluorescence”, *Phys. Rev. Lett.* **96**, 113002 (2006).
- [49] A. Cecconello, C.-H. Lu, J. Elbaz, I. Willner, “Au Nanoparticle/DNA Rotaxane Hybrid Nanostructures Exhibiting Switchable Fluorescence Properties”, *Nano Lett.* **13**, 6275–6280 (2013).

- [50] E. C. Le Ru, P. G. Etchegoin, J. Grand, N. Féliidj, J. Aubard, G. Lévi, “Mechanisms of Spectral Profile Modification in Surface-Enhanced Fluorescence”, *J. Phys. Chem. C* **111**, 16076–16079 (2007).
- [51] E. M. S. Stennett, M. A. Ciuba, M. Levitus, “Photophysical processes in single molecule organic fluorescent probes”, *Chem. Soc. Rev.* **43**, 1057–1075 (2014).
- [52] J. V. Pellegrotti, G. P. Acuna, A. Puchkova, P. Holzmeister, A. Gietl, B. Lalkens, F. D. Stefani, P. Tinnefeld, “Controlled Reduction of Photobleaching in DNA Origami–Gold Nanoparticle Hybrids”, *Nano Lett.* **14**, 2831–2836 (2014).
- [53] J. Widengren, A. Chmyrov, C. Eggeling, P.-Å. Löfdahl, C. A. M. Seidel, “Strategies to Improve Photostabilities in Ultrasensitive Fluorescence Spectroscopy”, *J. Phys. Chem. A* **111**, 429–440 (2007).
- [54] I. Rasnik, S. A. McKinney, T. Ha, “Nonblinking and long-lasting single-molecule fluorescence imaging”, *Nat. Methods* **3**, 891–893 (2006).
- [55] J. Vogelsang, R. Kasper, C. Steinhauer, B. Person, M. Heilemann, M. Sauer, P. Tinnefeld, “A Reducing and Oxidizing System Minimizes Photobleaching and Blinking of Fluorescent Dyes”, *Angew. Chem. Int. Ed.* **47**, 5465–5469 (2008).
- [56] H. Cang, Y. Liu, Y. Wang, X. Yin, X. Zhang, “Giant Suppression of Photobleaching for Single Molecule Detection via the Purcell Effect”, *Nano Lett.* **13**, 5949–5953 (2013).
- [57] J. A. Dieringer, R. B. Lettan II, K. A. Scheidt, R. P. Van Duyne, “A Frequency Domain Existence Proof of Single-Molecule Surface-Enhanced Raman Spectroscopy”, *J. Am. Chem. Soc.* **129**, 16249–16256 (2007).
- [58] E. Blackie, E. C. Le Ru, M. Meyer, M. Timmer, B. Burkett, P. Northcote, P. G. Etchegoin, “Bi-analyte SERS with isotopically edited dyes”, *Phys. Chem. Chem. Phys.* **10**, 4147–4153 (2008).
- [59] S. L. Kleinman, E. Ringe, N. Valley, K. L. Wustholz, E. Phillips, K. A. Scheidt, G. C. Schatz, R. P. Van Duyne, “Single-Molecule Surface-Enhanced Raman Spectroscopy of Crystal Violet Isotopologues: Theory and Experiment”, *J. Am. Chem. Soc.* **133**, 4115–4122 (2011).
- [60] L. Guerrini, D. Graham, “Molecularly-mediated assemblies of plasmonic nanoparticles for Surface-Enhanced Raman Spectroscopy applications”, *Chem. Soc. Rev.* **41**, 7085–7107 (2012).
- [61] D. J. Anderson, M. Moskovits, “A SERS-Active System Based on Silver Nanoparticles Tethered to a Deposited Silver Film”, *J. Phys. Chem. B* **110**, 13722–13727 (2006).
- [62] S. J. Lee, A. R. Morrill, M. Moskovits, “Hot Spots in Silver Nanowire Bundles for Surface-Enhanced Raman Spectroscopy”, *J. Am. Chem. Soc.* **128**, 2200–2201 (2006).
- [63] G. Braun, I. Pavel, A. R. Morrill, D. S. Seferos, G. C. Bazan, N. O. Reich, M. Moskovits, “Chemically Patterned Microspheres for Controlled Nanoparticle Assembly in the Construction of SERS Hot Spots”, *J. Am. Chem. Soc.* **129**, 7760–7761 (2007).
- [64] R. Dahm, “Discovering DNA: Friedrich Miescher and the early years of nucleic acid research”, *Hum. Genet.* **122**, 565–581 (2008).

- [65] O. T. Avery, C. M. MacLeod, M. McCarty, “Studies on the chemical nature of the substance inducing transformation of pneumococcal types: Induction of transformation by a desoxyribonucleic acid fraction isolated from *Pneumococcus* type III”, *J. Exp. Med.* **79**, 137–158 (1944).
- [66] J. D. Watson, F. H. C. Crick, “Molecular Structure of Nucleic Acids: A Structure for Deoxyribose Nucleic Acid”, *Nature* **171**, 737–738 (1953).
- [67] N. Michelotti, A. Johnson-Buck, A. J. Manzo, N. G. Walter, “Beyond DNA origami: the unfolding prospects of nucleic acid nanotechnology”, *WIREs Nanomed. Nanobiotechnol.* **4**, 139–152 (2012).
- [68] B. Bhushan, D. Luo, S. R. Schrick, W. Sigmund, S. Zauscher, editors, *Handbook of Nanomaterials Properties*, Springer, Berlin-Heidelberg, Germany, 2014.
- [69] E. Hofmann, *Medizinische Biochemie systematisch*, UNI-MED Verlag, Bremen, Germany, 2006.
- [70] I. Saaem, T. H. LaBean, “Overview of DNA origami for molecular self-assembly”, *WIREs Nanomed. Nanobiotechnol.* **5**, 150–162 (2013).
- [71] P. Yakovchuk, E. Protozanova, M. D. Frank-Kamenetskii, “Base-stacking and base-pairing contributions into thermal stability of the DNA double helix”, *Nucl. Acids Res.* **34**, 564–574 (2006).
- [72] M. Caruthers, “Gene synthesis machines: DNA chemistry and its uses”, *Science* **230**, 281–285 (1985).
- [73] N. C. Seeman, “Nucleic acid junctions and lattices”, *J. Theoret. Biol.* **99**, 237–247 (1982).
- [74] S. N. Cohen, A. C. Y. Chang, H. W. Boyer, R. B. Helling, “Construction of Biologically Functional Bacterial Plasmids *In Vitro*”, *Proc. Natl. Acad. Sci. USA* **70**, 3240–3244 (1973).
- [75] N. C. Seeman, “Nanomaterials Based on DNA”, *Annu. Rev. Biochem.* **79**, 65–87 (2010).
- [76] N. C. Seeman, *Structural DNA Nanotechnology*, Cambridge University Press, Cambridge, United Kingdom, 2015.
- [77] J. Zhang, Y. Liu, Y. Ke, H. Yan, “Periodic Square-Like Gold Nanoparticle Arrays Templated by Self-Assembled 2D DNA Nanogrids on a Surface”, *Nano Lett.* **6**, 248–251 (2006).
- [78] J. Zheng, P. E. Constantinou, C. Micheel, A. P. Alivisatos, R. A. Kiehl, N. C. Seeman, “Two-Dimensional Nanoparticle Arrays Show the Organizational Power of Robust DNA Motifs”, *Nano Lett.* **6**, 1502–1504 (2006).
- [79] F. A. Aldaye, A. L. Palmer, H. F. Sleiman, “Assembling Materials with DNA as the Guide”, *Science* **321**, 1795–1799 (2008).
- [80] P. E. Constantinou, T. Wang, J. Kopatsch, L. B. Israel, X. Zhang, B. Ding, W. B. Sherman, X. Wang, J. Zheng, R. Sha, N. C. Seeman, “Double cohesion in structural DNA nanotechnology”, *Org. Biomol. Chem.* **4**, 3414–3419 (2006).

- [81] F. Mathieu, S. Liao, J. Kopatsch, T. Wang, C. Mao, N. C. Seeman, “Six-Helix Bundles Designed from DNA”, *Nano Lett.* **5**, 661–665 (2005).
- [82] J. Chen, N. C. Seeman, “Synthesis from DNA of a molecule with the connectivity of a cube”, *Nature* **350**, 631–633 (1991).
- [83] Y. He, T. Ye, M. Su, C. Zhang, A. E. Ribbe, W. Jiang, C. Mao, “Hierarchical self-assembly of DNA into symmetric supramolecular polyhedra”, *Nature* **452**, 198–201 (2008).
- [84] E. Winfree, F. Liu, L. A. Wenzler, N. C. Seeman, “Design and self-assembly of two-dimensional DNA crystals”, *Nature* **394**, 539–544 (1998).
- [85] H. Liu, Y. He, A. E. Ribbe, C. Mao, “Two-Dimensional (2D) DNA Crystals Assembled from Two DNA Strands”, *Biomacromolecules* **6**, 2943–2945 (2005).
- [86] J. Zheng, J. J. Birktoft, Y. Chen, T. Wang, R. Sha, P. E. Constantinou, S. L. Ginell, C. Mao, N. C. Seeman, “From molecular to macroscopic via the rational design of a self-assembled 3D DNA crystal”, *Nature* **461**, 74–77 (2009).
- [87] J. Malo, J. C. Mitchell, C. Vénien-Bryan, J. R. Harris, H. Wille, D. J. Sherratt, A. J. Turberfield, “Engineering a 2D Protein–DNA Crystal”, *Angew. Chem. Int. Ed.* **44**, 3057–3061 (2005).
- [88] H. Yan, S. H. Park, G. Finkelstein, J. H. Reif, T. H. LaBean, “DNA-Templated Self-Assembly of Protein Arrays and Highly Conductive Nanowires”, *Science* **301**, 1882–1884 (2003).
- [89] R. M. Zadegan, M. L. Norton, “Structural DNA Nanotechnology: From Design to Applications”, *Int. J. Mol. Sci.* **13**, 7149–7162 (2012).
- [90] J. R. Williamson, “RNA origami”, *Nat. Struct. Mol. Biol.* **1**, 270–272 (1994).
- [91] T. H. LaBean, E. Winfree, J. H. Reif, “Experimental Progress in Computation by Self-Assembly of DNA Tilings”, *DIMACS Series in Discrete Mathematics and Theoretical Computer Science* **54**, 123–140 (2000).
- [92] H. Yan, T. H. LaBean, L. Feng, J. H. Reif, “Directed nucleation assembly of DNA tile complexes for barcode-patterned lattices”, *Proc. Natl. Acad. Sci. USA* **100**, 8103–8108 (2003).
- [93] W. M. Shih, J. D. Quispe, G. F. Joyce, “A 1.7-kilobase single-stranded DNA that folds into a nanoscale octahedron”, *Nature* **427**, 618–621 (2004).
- [94] B. Ding, Z. Deng, H. Yan, S. Cabrini, R. N. Zuckermann, J. Bokor, “Gold Nanoparticle Self-Similar Chain Structure Organized by DNA Origami”, *J. Am. Chem. Soc.* **132**, 3248–3249 (2010).
- [95] L. Olejko, P. J. Cywinski, I. Bald, “Ion-Selective Formation of a Guanine Quadruplex on DNA Origami Structures”, *Angew. Chem. Int. Ed.* **54**, 673–677 (2015).
- [96] G. P. Acuna, M. Bucher, I. H. Stein, C. Steinhauer, A. Kuzyk, P. Holzmeister, R. Schreiber, A. Moroz, F. D. Stefani, T. Liedl, F. C. Simmel, P. Tinnefeld, “Distance Dependence of Single-Fluorophore Quenching by Gold Nanoparticles Studied on DNA Origami”, *ACS Nano* **6**, 3189–3195 (2012).

- [97] S. M. Douglas, H. Dietz, T. Liedl, B. Högberg, F. Graf, W. M. Shih, “Self-assembly of DNA into nanoscale three-dimensional shapes”, *Nature* **459**, 414–418 (2009).
- [98] H. Dietz, S. M. Douglas, W. M. Shih, “Folding DNA into Twisted and Curved Nanoscale Shapes”, *Science* **325**, 725–730 (2009).
- [99] D. Han, S. Pal, J. Nangreave, Z. Deng, Y. Liu, H. Yan, “DNA Origami with Complex Curvatures in Three-Dimensional Space”, *Science* **332**, 342–346 (2011).
- [100] M. Endo, K. Hidaka, T. Kato, K. Namba, H. Sugiyama, “DNA Prism Structures Constructed by Folding of Multiple Rectangular Arms”, *J. Am. Chem. Soc.* **131**, 15570–15571 (2009).
- [101] E. S. Andersen, M. Dong, M. M. Nielsen, K. Jahn, R. Subramani, W. Mamdouh, M. M. Golas, B. Sander, H. Stark, C. L. P. Oliveira, J. S. Pedersen, V. Birkedal, F. Besenbacher, K. V. Gothelf, J. Kjems, “Self-assembly of a nanoscale DNA box with a controllable lid”, *Nature* **459**, 73–76 (2009).
- [102] W. Liu, H. Zhong, R. Wang, N. C. Seeman, “Crystalline Two-Dimensional DNA-Origami Arrays”, *Angew. Chem. Int. Ed.* **50**, 264–267 (2011).
- [103] S. Woo, P. W. K. Rothemund, “Programmable molecular recognition based on the geometry of DNA nanostructures”, *Nat. Chem.* **3**, 620–627 (2011).
- [104] H. Zhang, J. Chao, D. Pan, H. Liu, Q. Huang, C. Fan, “Folding super-sized DNA origami with scaffold strands from long-range PCR”, *Chem. Commun.* **48**, 6405–6407 (2012).
- [105] A. N. Marchi, I. Saaem, B. N. Vogen, S. Brown, T. H. LaBean, “Toward Larger DNA Origami”, *Nano Lett.* **14**, 5740–5747 (2014).
- [106] B. Högberg, T. Liedl, W. M. Shih, “Folding DNA Origami from a Double-Stranded Source of Scaffold”, *J. Am. Chem. Soc.* **131**, 9154–9155 (2009).
- [107] S. Brown, J. Majikes, A. Martinez, T. M. Girón, H. Fennell, E. C. Samano, T. H. LaBean, “An easy-to-prepare mini-scaffold for DNA origami”, *Nanoscale* **7**, 16621–16624 (2015).
- [108] C. Mao, W. Sun, Z. Shen, N. C. Seeman, “A nanomechanical device based on the B-Z transition of DNA”, *Nature* **397**, 144–146 (1999).
- [109] B. Yurke, A. J. Turberfield, A. P. Mills, F. C. Simmel, J. L. Neumann, “A DNA-fuelled molecular machine made of DNA”, *Nature* **406**, 605–608 (2000).
- [110] H. Yan, X. Zhang, Z. Shen, N. C. Seeman, “A robust DNA mechanical device controlled by hybridization topology”, *Nature* **415**, 62–65 (2002).
- [111] D. Han, S. Pal, Y. Liu, H. Yan, “Folding and cutting DNA into reconfigurable topological nanostructures”, *Nat. Nanotechnol.* **5**, 712–717 (2010).
- [112] A. Kuzuya, Y. Sakai, T. Yamazaki, Y. Xu, M. Komiyama, “Nanomechanical DNA origami ‘single-molecule beacons’ directly imaged by atomic force microscopy”, *Nat. Commun.* **2**, 449 (2011).
- [113] F. Zhang, J. Nangreave, Y. Liu, H. Yan, “Reconfigurable DNA Origami to Generate Quasifractal Patterns”, *Nano Lett.* **12**, 3290–3295 (2012).

- [114] A. Kuzyk, R. Schreiber, H. Zhang, A. O. Govorov, T. Liedl, N. Liu, “Reconfigurable 3D plasmonic metamolecules”, *Nat. Mater.* **13**, 862–866 (2014).
- [115] K. Lund, A. J. Manzo, N. Dabby, N. Michelotti, A. Johnson-Buck, J. Nangreave, S. Taylor, R. Pei, M. N. Stojanovic, N. G. Walter, E. Winfree, H. Yan, “Molecular robots guided by prescriptive landscapes”, *Nature* **465**, 206–210 (2010).
- [116] H. Gu, J. Chao, S.-J. Xiao, N. C. Seeman, “A proximity-based programmable DNA nanoscale assembly line”, *Nature* **465**, 202–205 (2010).
- [117] S. F. J. Wickham, M. Endo, Y. Katsuda, K. Hidaka, J. Bath, H. Sugiyama, A. J. Turberfield, “Direct observation of stepwise movement of a synthetic molecular transporter”, *Nat. Nanotechnol.* **6**, 166–169 (2011).
- [118] F. Zhang, J. Nangreave, Y. Liu, H. Yan, “Structural DNA Nanotechnology: State of the Art and Future Perspective”, *J. Am. Chem. Soc.* **136**, 11198–11211 (2014).
- [119] S. M. Douglas, A. H. Marblestone, S. Teerapittayanon, A. Vazquez, G. M. Church, W. M. Shih, “Rapid prototyping of 3D DNA-origami shapes with caDNAno”, *Nucl. Acids Res.* **37**, 5001–5006 (2009).
- [120] C. E. Castro, F. Kilchherr, D.-N. Kim, E. L. Shiao, T. Wauer, P. Wortmann, M. Bathe, H. Dietz, “A primer to scaffolded DNA origami”, *Nat. Methods* **8**, 221–229 (2011).
- [121] C. A. Mirkin, R. L. Letsinger, R. C. Mucic, J. J. Storhoff, “A DNA-based method for rationally assembling nanoparticles into macroscopic materials”, *Nature* **382**, 607–609 (1996).
- [122] A. P. Alivisatos, K. P. Johnsson, X. Peng, T. E. Wilson, C. J. Loweth, M. P. Bruchez Jr, P. G. Schultz, “Organization of ‘nanocrystal molecules’ using DNA”, *Nature* **382**, 609–611 (1996).
- [123] J. I. Cutler, E. Auyeung, C. A. Mirkin, “Spherical Nucleic Acids”, *J. Am. Chem. Soc.* **134**, 1376–1391 (2012).
- [124] S. Xiao, F. Liu, A. E. Rosen, J. F. Hainfeld, N. C. Seeman, K. Musier-Forsyth, R. A. Kiehl, “Selfassembly of Metallic Nanoparticle Arrays by DNA Scaffolding”, *J. Nanopart. Res.* **4**, 313–317 (2002).
- [125] Y. Y. Pinto, J. D. Le, N. C. Seeman, K. Musier-Forsyth, T. A. Taton, R. A. Kiehl, “Sequence-Encoded Self-Assembly of Multiple-Nanocomponent Arrays by 2D DNA Scaffolding”, *Nano Lett.* **5**, 2399–2402 (2005).
- [126] X. Zhang, M. R. Servos, J. Liu, “Surface Science of DNA Adsorption onto Citrate-Capped Gold Nanoparticles”, *Langmuir* **28**, 3896–3902 (2012).
- [127] X. Zhang, M. R. Servos, J. Liu, “Instantaneous and Quantitative Functionalization of Gold Nanoparticles with Thiolated DNA Using a pH-Assisted and Surfactant-Free Route”, *J. Am. Chem. Soc.* **134**, 7266–7269 (2012).
- [128] H. D. Hill, J. E. Millstone, M. J. Banholzer, C. A. Mirkin, “The Role Radius of Curvature Plays in Thiolated Oligonucleotide Loading on Gold Nanoparticles”, *ACS Nano* **3**, 418–424 (2009).

- [129] X. Zhang, T. Gouriye, K. Göeken, M. R. Servos, R. Gill, J. Liu, “Toward Fast and Quantitative Modification of Large Gold Nanoparticles by Thiolated DNA: Scaling of Nanoscale Forces, Kinetics, and the Need for Thiol Reduction”, *J. Phys. Chem. C* **117**, 15677–15684 (2013).
- [130] J. J. Storhoff, R. Elghanian, R. C. Mucic, C. A. Mirkin, R. L. Letsinger, “One-Pot Colorimetric Differentiation of Polynucleotides with Single Base Imperfections Using Gold Nanoparticle Probes”, *J. Am. Chem. Soc.* **120**, 1959–1964 (1998).
- [131] L. M. Demers, C. A. Mirkin, R. C. Mucic, R. A. Reynolds, III, R. L. Letsinger, R. Elghanian, G. Viswanadham, “A Fluorescence-Based Method for Determining the Surface Coverage and Hybridization Efficiency of Thiol-Capped Oligonucleotides Bound to Gold Thin Films and Nanoparticles”, *Anal. Chem.* **72**, 5535–5541 (2000).
- [132] S. J. Hurst, A. K. R. Lytton-Jean, C. A. Mirkin, “Maximizing DNA Loading on a Range of Gold Nanoparticle Sizes”, *Anal. Chem.* **78**, 8313–8318 (2006).
- [133] A. Barchanski, N. Hashimoto, S. Petersen, C. L. Sajti, S. Barcikowski, “Impact of Spacer and Strand Length on Oligonucleotide Conjugation to the Surface of Ligand-Free Laser-Generated Gold Nanoparticles”, *Bioconjugate Chem.* **23**, 908–915 (2012).
- [134] J. J. Storhoff, R. Elghanian, C. A. Mirkin, R. L. Letsinger, “Sequence-Dependent Stability of DNA-Modified Gold Nanoparticles”, *Langmuir* **18**, 6666–6670 (2002).
- [135] [http://www.nobelprize.org/nobel\\_prizes/physics/laureates/2010/](http://www.nobelprize.org/nobel_prizes/physics/laureates/2010/), “The Nobel Prize in Physics 2010”, August 2016.
- [136] A. K. Geim, “Random Walk to Graphene (Nobel Lecture)”, *Angew. Chem. Int. Ed.* **50**, 6966–6985 (2011).
- [137] M. J. Allen, V. C. Tung, R. B. Kaner, “Honeycomb Carbon: A Review of Graphene”, *Chem. Rev.* **110**, 132–145 (2010).
- [138] K. S. Novoselov, A. K. Geim, S. V. Morozov, D. Jiang, Y. Zhang, S. V. Dubonos, I. V. Grigorieva, A. A. Firsov, “Electric Field Effect in Atomically Thin Carbon Films”, *Science* **306**, 666–669 (2004).
- [139] K. S. Novoselov, V. I. Fal’ko, L. Colombo, P. R. Gellert, M. G. Schwab, K. Kim, “A roadmap for graphene”, *Nature* **490**, 192–200 (2012).
- [140] W. Choi, I. Lahiri, R. Seelaboyina, Y. S. Kang, “Synthesis of Graphene and Its Applications: A Review”, *Crit. Rev. Solid State* **35**, 52–71 (2010).
- [141] L. M. Malard, M. A. Pimenta, G. Dresselhaus, M. S. Dresselhaus, “Raman spectroscopy in graphene”, *Phys. Rep.* **473**, 51–87 (2009).
- [142] C. Casiraghi, S. Pisana, K. S. Novoselov, A. K. Geim, A. C. Ferrari, “Raman fingerprint of charged impurities in graphene”, *Appl. Phys. Lett.* **91**, 233108 (2007).
- [143] V. Georgakilas, M. Otyepka, A. B. Bourlinos, V. Chandra, N. Kim, K. C. Kemp, P. Hobza, R. Zboril, K. S. Kim, “Functionalization of Graphene: Covalent and Non-Covalent Approaches, Derivatives and Applications”, *Chem. Rev.* **112**, 6156–6214 (2012).

- [144] M. A. Bratescu, N. Saito, “Charge Doping of Large-Area Graphene by Gold-Alloy Nanoparticles”, *J. Phys. Chem. C* **117**, 26804–26810 (2013).
- [145] C. Lee, X. Wei, J. W. Kysar, J. Hone, “Measurement of the Elastic Properties and Intrinsic Strength of Monolayer Graphene”, *Science* **321**, 385–388 (2008).
- [146] S. V. Morozov, K. S. Novoselov, M. I. Katsnelson, F. Schedin, D. C. Elias, J. A. Jaszczak, A. K. Geim, “Giant Intrinsic Carrier Mobilities in Graphene and Its Bilayer”, *Phys. Rev. Lett.* **100**, 016602 (2008).
- [147] M. Bruna, S. Borini, “Optical constants of graphene layers in the visible range”, *Appl. Phys. Lett.* **94**, 031901 (2009).
- [148] F. Bonaccorso, Z. Sun, T. Hasan, A. C. Ferrari, “Graphene photonics and optoelectronics”, *Nat. Photonics* **4**, 611–622 (2010).
- [149] A. A. Balandin, S. Ghosh, W. Bao, I. Calizo, D. Teweldebrhan, F. Miao, C. N. Lau, “Superior Thermal Conductivity of Single-Layer Graphene”, *Nano Lett.* **8**, 902–907 (2008).
- [150] J. S. Bunch, S. S. Verbridge, J. S. Alden, A. M. van der Zande, J. M. Parpia, H. G. Craighead, P. L. McEuen, “Impermeable Atomic Membranes from Graphene Sheets”, *Nano Lett.* **8**, 2458–2462 (2008).
- [151] D. C. Elias, R. R. Nair, T. M. G. Mohiuddin, S. V. Morozov, P. Blake, M. P. Halsall, A. C. Ferrari, D. W. Boukhvalov, M. I. Katsnelson, A. K. Geim, K. S. Novoselov, “Control of Graphene’s Properties by Reversible Hydrogenation: Evidence for Graphane”, *Science* **323**, 610–613 (2009).
- [152] R. R. Nair, W. Ren, R. Jalil, I. Riaz, V. G. Kravets, L. Britnell, P. Blake, F. Schedin, A. S. Mayorov, S. Yuan, M. I. Katsnelson, H.-M. Cheng, W. Strupinski, L. G. Bulusheva, A. V. Okotrub, I. V. Grigorieva, A. N. Grigorenko, K. S. Novoselov, A. K. Geim, “Fluorographene: A Two-Dimensional Counterpart of Teflon”, *Small* **6**, 2877–2884 (2010).
- [153] A. C. Ferrari, “Raman spectroscopy of graphene and graphite: Disorder, electron–phonon coupling, doping and nonadiabatic effects”, *Solid State Commun.* **143**, 47–57 (2007).
- [154] S. Pisana, M. Lazzeri, C. Casiraghi, K. S. Novoselov, A. K. Geim, A. C. Ferrari, F. Mauri, “Breakdown of the adiabatic Born-Oppenheimer approximation in graphene”, *Nat. Mater.* **6**, 198–201 (2007).
- [155] A. C. Ferrari, D. M. Basko, “Raman spectroscopy as a versatile tool for studying the properties of graphene”, *Nat. Nanotechnol.* **8**, 235–246 (2013).
- [156] M. Huang, H. Yan, T. F. Heinz, J. Hone, “Probing Strain-Induced Electronic Structure Change in Graphene by Raman Spectroscopy”, *Nano Lett.* **10**, 4074–4079 (2010).
- [157] C. Thomsen, S. Reich, “Double Resonant Raman Scattering in Graphite”, *Phys. Rev. Lett.* **85**, 5214–5217 (2000).
- [158] R. Saito, A. Jorio, A. G. Souza Filho, G. Dresselhaus, M. S. Dresselhaus, M. A. Pimenta, “Probing Phonon Dispersion Relations of Graphite by Double Resonance Raman Scattering”, *Phys. Rev. Lett.* **88**, 027401 (2002).



- [159] V. V. Thacker, L. O. Herrmann, D. O. Sigle, T. Zhang, T. Liedl, J. J. Baumberg, U. F. Keyser, “DNA origami based assembly of gold nanoparticle dimers for surface-enhanced Raman scattering”, *Nat. Commun.* **5**, 3448 (2014).
- [160] P. Blake, E. W. Hill, A. H. Castro Neto, K. S. Novoselov, D. Jiang, R. Yang, T. J. Booth, A. K. Geim, “Making graphene visible”, *Appl. Phys. Lett.* **91**, 063124 (2007).
- [161] WITec, editor, *WITec alpha300 - System Description*, 2008.
- [162] X. Liu, M. Atwater, J. Wang, Q. Huo, “Extinction coefficient of gold nanoparticles with different sizes and different capping ligands”, *Colloids Surf. B Biointerfaces* **58**, 3–7 (2007).
- [163] <https://www.neb.com/tools-and-resources/usage-guidelines/nucleic-acid-data>, “Nucleic Acid Data”, August 2016.
- [164] M. Eigen, R. Rigler, “Sorting single molecules: Application to diagnostics and evolutionary biotechnology”, *Proc. Natl. Acad. Sci. USA* **91**, 5740–5747 (1994).
- [165] S. Nie, D. T. Chiu, R. N. Zare, “Probing individual molecules with confocal fluorescence microscopy”, *Science* **266**, 1018–1021 (1994).
- [166] P. M. Goodwin, W. P. Ambrose, R. A. Keller, “Single-Molecule Detection in Liquids by Laser-Induced Fluorescence”, *Acc. Chem. Res.* **29**, 607–613 (1996).
- [167] L. Gunnarsson, E. J. Bjerneld, H. Xu, S. Petronis, B. Kasemo, M. Käll, “Interparticle coupling effects in nanofabricated substrates for surface-enhanced Raman scattering”, *Appl. Phys. Lett.* **78**, 802–804 (2001).
- [168] J. Chao, Y. Lin, H. Liu, L. Wang, C. Fan, “DNA-based plasmonic nanostructures”, *Mater. Today* **18**, 326–335 (2015).
- [169] J.-H. Lee, J.-M. Nam, K.-S. Jeon, D.-K. Lim, H. Kim, S. Kwon, H. Lee, Y. D. Suh, “Tuning and Maximizing the Single-Molecule Surface-Enhanced Raman Scattering from DNA-Tethered Nanodumbbells”, *ACS Nano* **6**, 9574–9584 (2012).
- [170] H. M. Lee, J.-H. Lee, H. M. Kim, S. M. Jin, H. S. Park, J.-M. Nam, Y. D. Suh, “High-precision measurement-based correlation studies among atomic force microscopy, Rayleigh scattering, and surface-enhanced Raman scattering at the single-molecule level”, *Phys. Chem. Chem. Phys.* **15**, 4243–4249 (2013).
- [171] H. Lee, J.-H. Lee, S. M. Jin, Y. D. Suh, J.-M. Nam, “Single-Molecule and Single-Particle-Based Correlation Studies between Localized Surface Plasmons of Dimeric Nanostructures with  $\sim 1$  nm Gap and Surface-Enhanced Raman Scattering”, *Nano Lett.* **13**, 6113–6121 (2013).
- [172] J. Sharma, R. Chhabra, C. S. Andersen, K. V. Gothelf, H. Yan, Y. Liu, “Toward Reliable Gold Nanoparticle Patterning On Self-Assembled DNA Nanoscaffold”, *J. Am. Chem. Soc.* **130**, 7820–7821 (2008).
- [173] S. Pal, Z. Deng, H. Wang, S. Zou, Y. Liu, H. Yan, “DNA Directed Self-Assembly of Anisotropic Plasmonic Nanostructures”, *J. Am. Chem. Soc.* **133**, 17606–17609 (2011).

- [174] L. Piantanida, D. Naumenko, E. Torelli, M. Marini, D. M. Bauer, L. Fruk, G. Firrao, M. Lazzarino, “Plasmon resonance tuning using DNA origami actuation”, *Chem. Commun.* **51**, 4789–4792 (2015).
- [175] G. P. Acuna, F. M. Möller, P. Holzmeister, S. Beater, B. Lalkens, P. Tinnefeld, “Fluorescence Enhancement at Docking Sites of DNA-Directed Self-Assembled Nanoantennas”, *Science* **338**, 506–510 (2012).
- [176] W. P. Klein, C. N. Schmidt, B. Rapp, S. Takabayashi, W. B. Knowlton, J. Lee, B. Yurke, W. L. Hughes, E. Graugnard, W. Kuang, “Multiscaffold DNA Origami Nanoparticle Waveguides”, *Nano Lett.* **13**, 3850–3856 (2013).
- [177] X. Shen, C. Song, J. Wang, D. Shi, Z. Wang, N. Liu, B. Ding, “Rolling Up Gold Nanoparticle-Dressed DNA Origami into Three-Dimensional Plasmonic Chiral Nanostructures”, *J. Am. Chem. Soc.* **134**, 146–149 (2012).
- [178] A. Kuzyk, R. Schreiber, Z. Fan, G. Pardatscher, E.-M. Roller, A. Högele, F. C. Simmel, A. O. Govorov, T. Liedl, “DNA-based self-assembly of chiral plasmonic nanostructures with tailored optical response”, *Nature* **483**, 311–314 (2012).
- [179] X. Shen, A. Asenjo-Garcia, Q. Liu, Q. Jiang, F. J. García de Abajo, N. Liu, B. Ding, “Three-Dimensional Plasmonic Chiral Tetramers Assembled by DNA Origami”, *Nano Lett.* **13**, 2128–2133 (2013).
- [180] D.-K. Lim, K.-S. Jeon, J.-H. Hwang, H. Kim, S. Kwon, Y. D. Suh, J.-M. Nam, “Highly uniform and reproducible surface-enhanced Raman scattering from DNA-tailorable nanoparticles with 1-nm interior gap”, *Nat. Nanotechnol.* **6**, 452–460 (2011).
- [181] M. Pilo-Pais, A. Watson, S. Demers, T. H. LaBean, G. Finkelstein, “Surface-Enhanced Raman Scattering Plasmonic Enhancement Using DNA Origami-Based Complex Metallic Nanostructures”, *Nano Lett.* **14**, 2099–2104 (2014).
- [182] P. Kühler, E.-M. Roller, R. Schreiber, T. Liedl, T. Lohmüller, J. Feldmann, “Plasmonic DNA-Origami Nanoantennas for Surface-Enhanced Raman Spectroscopy”, *Nano Lett.* **14**, 2914–2919 (2014).
- [183] S. Pal, J. Sharma, H. Yan, Y. Liu, “Stable silver nanoparticle-DNA conjugates for directed self-assembly of core-satellite silver-gold nanoclusters”, *Chem. Commun.* , 6059–6061 (2009).
- [184] J.-S. Lee, A. K. R. Lytton-Jean, S. J. Hurst, C. A. Mirkin, “Silver Nanoparticle–Oligonucleotide Conjugates Based on DNA with Triple Cyclic Disulfide Moieties”, *Nano Lett.* **7**, 2112–2115 (2007).
- [185] J. A. Dougan, C. Karlsson, W. E. Smith, D. Graham, “Enhanced oligonucleotide–nanoparticle conjugate stability using thioctic acid modified oligonucleotides”, *Nucl. Acids Res.* **35**, 3668–3675 (2007).
- [186] S. Pal, Z. Deng, B. Ding, H. Yan, Y. Liu, “DNA-Origami-Directed Self-Assembly of Discrete Silver-Nanoparticle Architectures”, *Angew. Chem. Int. Ed.* **49**, 2700–2704 (2010).
- [187] A.-P. Eskelinen, R. J. Moerland, M. A. Kostianen, P. Törmä, “Self-Assembled Silver Nanoparticles in a Bow-Tie Antenna Configuration”, *Small* **10**, 1057–1062 (2014).

- [188] L. Weller, V. V. Thacker, L. O. Herrmann, E. A. Hemmig, A. Lombardi, U. F. Keyser, J. J. Baumberg, “Gap-Dependent Coupling of Ag–Au Nanoparticle Heterodimers Using DNA Origami-Based Self-Assembly”, *ACS Photonics*, DOI: 10.1021/acsp Photonics.6b00062 (2016).
- [189] Y.-D. Stierhof, B. M. Humbel, H. Schwarz, “Suitability of different silver enhancement methods applied to 1 nm colloidal gold particles: An immunoelectron microscopic study”, *J. Electron. Microsc. Tech.* **17**, 336–343 (1991).
- [190] T. A. Taton, C. A. Mirkin, R. L. Letsinger, “Scanometric DNA Array Detection with Nanoparticle Probes”, *Science* **289**, 1757–1760 (2000).
- [191] M. Pilo-Pais, S. Goldberg, E. Samano, T. H. LaBean, G. Finkelstein, “Connecting the Nanodots: Programmable Nanofabrication of Fused Metal Shapes on DNA Templates”, *Nano Lett.* **11**, 3489–3492 (2011).
- [192] A. K. Samal, L. Polavarapu, S. Rodal-Cedeira, L. M. Liz-Marzán, J. Pérez-Juste, I. Pastoriza-Santos, “Size Tunable Au@Ag Core–Shell Nanoparticles: Synthesis and Surface-Enhanced Raman Scattering Properties”, *Langmuir* **29**, 15076–15082 (2013).
- [193] B. Aswathy, G. Sony, K. G. Gopchandran, “Shell Thickness-Dependent Plasmon Coupling and Creation of SERS Hot Spots in Au@Ag Core-Shell Nanostructures”, *Plasmonics* **9**, 1323–1331 (2014).
- [194] S. Hong, X. Li, “Optimal Size of Gold Nanoparticles for Surface-Enhanced Raman Spectroscopy under Different Conditions”, *J. Nanomater.* **2013**, 790323 (2013).
- [195] P. T. Yin, S. Shah, M. Chhowalla, K.-B. Lee, “Design, Synthesis, and Characterization of Graphene–Nanoparticle Hybrid Materials for Bioapplications”, *Chem. Rev.* **115**, 2483–2531 (2015).
- [196] J. M. Yun, K. N. Kim, J. Y. Kim, D. O. Shin, W. J. Lee, S. H. Lee, M. Lieberman, S. O. Kim, “DNA Origami Nanopatterning on Chemically Modified Graphene”, *Angew. Chem. Int. Ed.* **51**, 912–915 (2012).
- [197] N. Severin, M. Dorn, A. Kalachev, J. P. Rabe, “Replication of Single Macromolecules with Graphene”, *Nano Lett.* **11**, 2436–2439 (2011).
- [198] Y. Moon, J. Shin, S. Seo, J. Park, S. R. Dugasani, S. H. Woo, T. Park, S. H. Park, J. R. Ahn, “Nanoscale topographical replication of graphene architecture by artificial DNA nanostructures”, *Appl. Phys. Lett.* **104**, 231904 (2014).
- [199] G. Zhang, S. P. Surwade, F. Zhou, H. Liu, “DNA nanostructure meets nanofabrication”, *Chem. Soc. Rev.* **42**, 2488–2496 (2013).
- [200] X. Ling, L. Xie, Y. Fang, H. Xu, H. Zhang, J. Kong, M. S. Dresselhaus, J. Zhang, Z. Liu, “Can Graphene be used as a Substrate for Raman Enhancement?”, *Nano Lett.* **10**, 553–561 (2010).
- [201] X. Ling, L. G. Moura, M. A. Pimenta, J. Zhang, “Charge-Transfer Mechanism in Graphene-Enhanced Raman Scattering”, *J. Phys. Chem. C* **116**, 25112–25118 (2012).
- [202] X. Ling, J. Zhang, “First-Layer Effect in Graphene-Enhanced Raman Scattering”, *Small* **6**, 2020–2025 (2010).

- [203] F. Rana, “Graphene Terahertz Plasmon Oscillators”, *IEEE Trans. Nanotechnol.* **7**, 91–99 (2008).
- [204] T. M. G. Mohiuddin, A. Lombardo, R. R. Nair, A. Bonetti, G. Savini, R. Jalil, N. Bonini, D. M. Basko, C. Galotis, N. Marzari, K. S. Novoselov, A. K. Geim, A. C. Ferrari, “Uniaxial strain in graphene by Raman spectroscopy: *G* peak splitting, Grüneisen parameters, and sample orientation”, *Phys. Rev. B* **79**, 205433 (2009).
- [205] M. Huang, H. Yan, C. Chen, D. Song, T. F. Heinz, J. Hone, “Phonon softening and crystallographic orientation of strained graphene studied by Raman spectroscopy”, *Proc. Natl. Acad. Sci. USA* **106**, 7304–7308 (2009).
- [206] A. O. Govorov, H. H. Richardson, “Generating heat with metal nanoparticles”, *Nano Today* **2**, 30–38 (2007).
- [207] H. H. Richardson, M. T. Carlson, P. J. Tandler, P. Hernandez, A. O. Govorov, “Experimental and Theoretical Studies of Light-to-Heat Conversion and Collective Heating Effects in Metal Nanoparticle Solutions”, *Nano Lett.* **9**, 1139–1146 (2009).
- [208] Y. C. Cao, R. Jin, C. A. Mirkin, “Nanoparticles with Raman Spectroscopic Fingerprints for DNA and RNA Detection”, *Science* **297**, 1536–1540 (2002).
- [209] S. Yang, X. Dai, B. B. Stogin, T.-S. Wong, “Ultrasensitive surface-enhanced Raman scattering detection in common fluids”, *Proc. Natl. Acad. Sci. USA* **113**, 268–273 (2016).
- [210] M. Endo, Y. Yang, H. Sugiyama, “DNA origami technology for biomaterials applications”, *Biomater. Sci.* **1**, 347–360 (2013).
- [211] Q. Jiang, C. Song, J. Nangreave, X. Liu, L. Lin, D. Qiu, Z.-G. Wang, G. Zou, X. Liang, H. Yan, B. Ding, “DNA Origami as a Carrier for Circumvention of Drug Resistance”, *J. Am. Chem. Soc.* **134**, 13396–13403 (2012).

## **Declaration**

Hiermit versichere ich, die vorliegende Arbeit selbst verfasst und keine anderen Quellen und Hilfsmittel als hier angegeben verwendet zu haben. Diese Arbeit wurde weder einer anderen Prüfungsbehörde vorgelegt noch veröffentlicht.

Potsdam - Golm, August 2016

\_\_\_\_\_  
Julia Prinz